The inner structure of ΛCDM halos

Power, Christopher Brian James

Abstract

We have used high resolution N-body simulations to investigate the internal properties of Cold Dark Matter (CDM) halos with virial masses of $M_{200} \sim 10^{10}\,\mathrm{M}_{\odot}$ at $z = 0$, comparable to those of dwarf galaxy halos, forming in the ΛCDM cosmology. In particular, we have focused on providing accurate constraints on the mass distribution in these objects at $\sim 1\%$ of the virial radius, r_{200}.

After a brief introduction (chapter 1), the first part of this thesis is concerned with establishing the conditions under which the distribution of mass in simulated CDM halos is unaffected by finite numerical resolution. In chapter 2, we present results from a comprehensive set of simulations of a single galaxy mass halo in which numerical parameters have been varied systematically in order to determine their impact on the spherically averaged mass profile. Based on these results, we have defined a set of convergence criteria that allow us to identify the radial extent over which the spherically averaged circular velocity profile can be considered reliably resolved to better than 10%. In chapter 3, we have examined the abundance of substructure found in three sets of "converged" simulations, and quantified the effect of increasing mass resolution on the number of resolved subhalos of a given mass.

The second part of this thesis is concerned with the detailed analysis of the internal structure and kinematics of the simulated dwarf galaxy halos in our sample. In chapter 4, we analyse the structure and kinematics of the dwarfs for possible redshift dependence, and investigate whether these halos could sustain a gaseous disk. In chapter 5, we concentrate on mass dependent trends by performing a detailed comparison with galaxy and cluster mass halos.

Finally, chapter 6 provides a summary of the main findings of this work and highlights aspects that may prove rewarding for further study.

The Inner Structure of ΛCDM Halos

by Christopher Brian James Power

A thesis submitted to the University of Durham
in accordance with the regulations for
admittance to the Degree of Doctor of Philosophy.

Department of Physics
University of Durham
4th August 2003

Contents

List of Figures

List of Tables

Preface

The work described in this thesis was undertaken between October 1999 and September 2002 whilst the author was a research student under the supervision of Prof. Carlos Frenk and Dr. Adrian Jenkins in the Department of Physics at the University of Durham. Chapter 2 has been published in the form of a paper,

- **Power C.**, Navarro J.F., Jenkins A.R., Frenk C.S., White S.D.M., Springel V., Stadel J. & Quinn T. 2003, MNRAS, 328, 1039

None of the material in this thesis has been submitted previously to a degree at the University of Durham or at any other university. The work of others has been duly acknowledged.

Acknowledgements

"Two things fill the heart with ever renewed and increasing awe and reverence, the more often and the more steadily we meditate upon them: the starry firmament above and the moral law within."

Critique of Practical Reason, Immanuel Kant

It has never really occured to me to think of my Ph.D. thesis as "a means to an end". By the end of what was fundamentally a tortuous process - at least in the psychological sense - I could see the logic in this piece of advice that seemed to be so freely offered by so many people, and at times, I found myself wishing that I could rewire myself, force myself to adopt a more pragmatic mindset. However, more often than not I floundered, quite simply overwhelmed by what seemed like my limitless ignorance. It wasn't so much the starry firmament above that caused me my "problem", but the moral law within.

"Once upon a time, I dreamt I was a butterfly, fluttering hither and thither. Suddenly I awakened, and there I lay, myself again. Now I do not know whether I was then a man dreaming I was a butterfly, or whether I am now a butterfly dreaming I am a man."

The Chuang-Tzu

The time I have spent in Durham surely ranks as the happiest period of my life, and there are so many people I feel a sense of obligation towards as a result; to Carlos, who gave me the opportunity to do this Ph.D. in the first place and who often displayed a remarkable degree of understanding at times when I would have been suffering hair loss; to Adrian, a great teacher and good friend; to Peder, a great friend and probably the most eccentric office mate I will ever encounter; to Mike, a dear fellow traveller who helped me to clear my ears of all that sand; to Carlton, the ultimate football coach cosmologist; to Joy, the cookie monster extraordinaire; to Dajana, from whom I learnt the art of semaphore; to Nelson and Ale, two of the nicest people I know; to Pete, Natalie and Adam, who at times felt like my second family; to Phonsie, who taught me the importance of "chill!"; to Emma, who always knew when to snip those "wires to the Moon"; to Daibhid, a true

gentleman and friend; and to Adam, Amaya, Ben, Dave, Dorothy, Graham, John, Lydia, Marc, Rich, Rowena, Sally, Shaun, Stephen, Vicent, Vince and Volker.

Invariably I have forgotten to mention someone. If you stumble upon this thesis and feel a strong sense of aggrievement through your conspicuous absence, I offer you my sincerest apologies and recommend that you strike me off your Christmas card list.

Without a doubt, my Mum and Dad have been two pillars of strength for me over the years; they have always believed in me, always ensured that I have had the opportunities, sometimes at great personal sacrifice. I can't think of any compliment that could fully convey my sense of gratitude and love for them other than to hope that Bethan will grow up to feel the same way about Beverley and myself as I feel about them. I never really thought about it when I lived at home, but I draw so much strength from my family; thanks to my sister, brother and A.B.

Finally, Bev initially burst into my world as a noisy but lovable girl who lived two doors down the hall in Palatine House, but it didn't take me long to realise that she was so much more. Every time I look at our daughter Bethan, I know what it means to love two people unconditionally. Soppy, but true. This thesis is for Bev and Beth, more than anyone else, perhaps even more than for myself. You'll ask me why, but I just want to say, "Thank you".

Chapter 1 | *Introduction*

1.1 Prologue

The last century has witnessed a revolution in our understanding of how the structures that we see in the Universe today formed. Indeed, some of the most profound and fundamental discoveries of cosmology have been made within the last twenty five years.

Perhaps the most influential of these discoveries was made in 1992 by COBE when it detected small temperature fluctuations in the Cosmic Microwave Background (CMB). The measured fluctuations are consistent with the view that they arose from small amplitude Gaussian perturbations to the primordial density field, imprinted during an earlier epoch of inflation. These seeds of structure grew by gravitational instability, initially taking part in the expansion of the Universe before decoupling, collapsing and virialising, forming a dark matter halo. Such dark matter condensations merged and accreted material, and importantly, gas settled in the dense central regions of the halos, cooling and eventually forming stars.

This simple and elegant picture represents the current paradigm for how galaxies form. We live in a Universe in which structure grows hierarchically, whose principal matter component is some form of non-baryonic Cold Dark Matter (**CDM**), and in which baryonic matter, such as gas and stars, constitutes a small fraction of the overall mass density. Furthermore, there is compelling evidence that an additional component - some form of *dark energy* (Λ) - dominates the global dynamics of the present day Universe.

The ΛCDM model has been particularly impressive in its ability to make accurate predictions on scales of order $\gtrsim$ Mpc. In many cases these predictions are in excellent agreement with a wide and varied range of observations, such as measurements of the redshift-luminosity relation for distant supernovae (e.g. Perlmutter et al. (1999), Riess et al. (1999)), the present day abundance of galaxy clusters (e.g. Eke et al. (1998), Bahcall & Fan (1998)), the shape and amplitude of the matter power spectrum as inferred from studies of the Lyα forest (e.g. Croft (1999), CMB anisotropies and galaxy redshift surveys (e.g. Percival et al. (2001), and the shape and amplitude of galaxy clustering patterns (e.g.

Peacock et al. (2001)). However, it is on the scale of individual galaxies - $\lesssim$ Mpc - that ΛCDM's predictive power has encountered problems.

High resolution dark matter simulations are an established tool in modern cosmology and have played a pivotal role in providing accurate predictions that have contributed to the success of the ΛCDM model. Simulations of individual galactic and cluster dark matter halos, following the formation and evolution of the halo in a fully cosmological setting, predict divergent central density *cusps*. This result contrasts sharply with mass models fitted to the observed rotation curves of late-type dwarf galaxies and low surface brightness (LSB) galaxies, systems where the dark matter gravitational potential dominates over that from the gaseous and stellar disk. These mass models imply finite densities or *cores* in the central regions of these galaxies (e.g. Bolatto et al. (2002), Weldrake et al. (2003), Simon et al. (2003)).

While the *cusp-core problem* has focused attention on late-type dwarfs and low surface brightness galaxies, there is evidence that the problem may also be manifest in galaxies where the luminous material dominates the dark matter within the optical radius (e.g. Borriello & Salucci (2001)). The rotation curves of bright galaxies are often well fitted by *maximum disk* models in which circular velocities within the optical radius can be completely accounted for by the mass of the luminous bulge and disk alone (Sellwood & Kosowsky (2001)). In these cases, the analysis implies that dark matter does not contribute to the inner rotation curve at all!

Furthermore, it has been noted that,

- high resolution simulations appear to produce an *overabundance* of dark matter substructure halos (or subhalos) (Moore et al. (1999a), Klypin et al. (1999a); but see Stoehr et al. (2002)). If these subhalos are associated with the hosts of galactic satellites, it would appear that there are over two orders of magnitude too many in excess of the number observed around our own Galaxy. This is commonly referred to as the *substructure problem* or the *missing satellites problem.*

- simulations of galaxy formation in the ΛCDM cosmology that incorporate hydrodynamical processes such as star formation and feedback also indicate that galactic disks are an order of magnitude smaller - the *angular momentum problem* (e.g. Sommer-Larsen et al. (1999)) - and fainter, by one to two magnitudes for a given rotational velocity, than observed (Navarro & Steinmetz (2000); but see Eke, Navarro

& Steinmetz (2001)).

It is possible that both the missing satellites problem and the angular momentum problem could be resolved as progress is made in gaining a more complete understanding of the astrophysical processes that govern galaxy formation. Feedback, the injection of energy into the galaxy by its own stars and external radiation fields, will greatly impact upon the ability of gas to cool, regulating star formation and perhaps even suppressing the formation of the galaxy. Recent observations suggest that the Universe was reionized early in its history (Becker et al. (2001)). Semi-analytical calculations indicate that such an event could have prevented galaxies from forming in many galactic substructure halos, apparently resolving the problem of missing satellites (Benson et al. (2002), Bullock et al. (2001a), Somerville (2002)). Simulations of galaxy formation that incorporate increasingly sophisticated formulations of feedback appear to produce galactic disks more consistent with observations (Thacker et al. (2001)).

On the other hand, the cusp-core problem appears to present a more serious concern for the ΛCDM model, however. Divergent central halo densities are a generic feature of any structure formation model in which the dark matter particles are cold; the absence of any primordial phase space constraints on the density of dark matter implies that the density in the central region of halos is unconstrained (Tremaine & Gunn (1979)). However, it has been argued that high resolution rotation curves of nearby dwarf galaxies appear to be poorly fit by cuspy profiles (e.g. de Blok et al. (2001b)), which has led to speculation concerning the kind of astrophysical processes that could lower the central concentrations of dark matter halos, for example, scattering of the dark matter by a stellar bar (Weinberg & Katz (2002)), by gravitational slingshot from a central black hole (Merritt et al. (2001)) or explosive stellar feedback (e.g. Navarro et al. (1996), but see Gnedin & Zhao (2002)). While bar formation and gravitational scattering by black holes may prove to be effective mechanisms for lowering the dark matter density in normal galaxies, it is unlikely that these processes apply in systems where the discrepancies are most pronounced - the late-type dwarfs and LSB galaxies.

There are those - the *optimists* - who believe that these difficulties can be resolved within the context of the model and can be overcome by astrophysical solutions. Then there are also those - the *pessimists* - who believe that these problems highlight significant shortcomings in the assumption that the dark matter is cold, and instead seek solutions

by changing the way it behaves, prompting a flurry of interest in self-interacting dark matter (Spergel & Steinhardt (2000)), warm dark matter (Bode et al. (2001)), fluid dark matter (Peebles (2000)), etc... Finally, there are those - the *radicals* - who believe that these problems require dark matter to be discarded completely in favour of, for example, modified gravity (e.g. Milgrom (1983), McGaugh & de Blok (1998)) or magnetic fields (Battaner et al. (1992)).

It should be clear from the preceding discussion that ΛCDM's difficulties on galactic scales has presented the model with its sternest challenge to date. However, it would be instructive to step back for one moment and consider some important caveats.

1. Obtaining precise and well resolved rotation curves for late-type dwarfs and LSB galaxies is a delicate task, beset with systematic errors than can complicate interpretation of the data. For example, radio measurements of the HI 21-cm line have finite spatial resolution and so it is important to properly account for this *beam smearing* when constructing the HI rotation curve. If not, circular velocities will appear artificially suppressed (e.g. van den Bosch et al. (2001a)). Optical measurements of rotation curves are often troublesome because of the paucity of a stellar disk. Furthermore, it has been noted that optical Hα rotation curves of low surface brightness galaxies appear to rise more steeply than measurements of HI 21-cm line velocities would suggest (van den Bosch & Swaters (2001)).

2. In the limiting case of rotation curve data that is both well resolved and free from systematic errors, it is necessary to determine which mass models provide the best fit. This is in itself an onerous task, and assumptions must be made about the functional form of each mass component. Typically, late-type dwarf galaxies and LSB galaxies are assumed to have an exponential thin disk of neutral HI, an exponential thick stellar disk, and a spherically symmetric dark matter halo. Furthermore, the stellar disk is assumed to have a negligible mass-to-light ratio. However, there are cases where the physical situation departs significantly from the assumptions made (e.g. the clumpy gas distribution of DDO 154; see van den Bosch & Swaters (2001)) and in such cases it would appear sensible to reanalyse the data and review the conclusions drawn from the best fits.

3. The discrepancy between the predicted mass distribution of CDM halos and that inferred from the rotation curves of late-type dwarfs and LSBs was based on the halo

structure found in simulations of galaxy clusters and galaxies. However, there are as yet no published results on high resolution dark matter simulations of individual dwarf galaxy halos probing mass scales of $\sim 10^{10}M_{\odot}$, and therefore no quantitative predictions that can be tested against observations.

4. Observational constraints tend to be strongest where the luminous galactic material resides - near the centres of dark matter halos. Unfortunately, theoretical predictions from high resolution simulations are least robust in these regions where measured overdensities can exceed 10^6. In this regime, a typical dark matter particle can be expected to complete several thousand orbits over the course of a Hubble time. Understanding the effects of numerical approximations - the choice of timestep integrator, force softening, mass resolution, etc... - and separating these effects from the true predictions of CDM becomes a complex (and potentially hazardous!) operation.

This thesis will address key issues raised in points 2, 3 and 4. By performing a series of high resolution simulations of dwarf galaxy dark matter halos, capable of resolving masses $\sim 10^4M_{\odot}$ and probing the inner $\sim$ 300 pc, we have been able to investigate the properties of halos of the type a typical late-type dwarf galaxy would be expected to occupy today (3). Furthermore, we have been able to use these simulations to critically review the assumption of a static, spherically symmetric dark matter component made by those who perform mass decomposition on observational rotation curves (2). Before these simulations were possible, however, it was necessary to carry out a rigourous and comprehensive convergence study examining numerical effects such as gravitational softening, mass resolution, timestepping and starting redshift on the central mass distribution of the dark matter halo (4).

The remaining sections of this introductory chapter can be outlined as follows. In § 1.2, we review the current observational evidence for the ΛCDM model and briefly discuss constraints on the cosmological parameters, before highlighting some successful predictions. In § 1.3, we present observational evidence for the presence of massive extended dark matter around galaxies; this leads to a discussion of rotation curve studies in § 1.4, with particular emphasis placed on dark matter dominated systems such as late-type dwarfs and LSBs. In § 1.5, we review the predictions of the CDM model for the structure of galaxies and define some of the notation and conventions that are used in this thesis in § 1.5.1. Finally, we present an overview of the remaining chapters in this

thesis in § 1.6.

1.2 Dark Matter in the Universe

Recent observations strongly suggest that we live in a Universe with a low matter density that is spatially flat.

- Several different, unbiased approaches - in the sense that they do not require a mean mass-to-light ratio to be assumed - have been used to constrain the mean matter density of the Universe, $\Omega_{\rm m}$, expressed in units of the critical density

$$\Omega_{\rm m} = \frac{\bar{\rho}_{\rm m}}{\rho_{\rm crit}} \tag{1.1}$$

Values determined by the various methods are consistent with a low $\Omega_{\rm m}$, and it would appear that we are converging on a value of $\Omega_{\rm m} \simeq 0.3$.

Measurements of the baryonic mass fraction in clusters can be used to evaluate the cosmological ratio of mean baryon density to mean matter density, $f_{\rm b}=\Omega_{\rm b}/\Omega_{\rm m}$, because clusters are assumed to be representative of the universal baryon fraction (White et al. (1993)). X-ray measurements of intracluster gas density and temperature (e.g. Mohr et al. (1999), Ettori & Fabian (1999)) and gas densities inferred from observations of the Sunyaev-Zeldovich effect* combined with X-ray temperatures (Grego et al. (2001)) both yield consistent estimates of the baryon fraction, $f_{\rm b} \sim 0.12$. It is possible to determine precisely the mean baryon density (see below); together with a baryon fraction of $f_{\rm b} \sim 0.12$, this implies a mean matter density $\Omega_{\rm m} \simeq 0.33$.

The shape and amplitude of the matter power spectrum can be used to place constraints on the value of $\Omega_{\rm m}$ in the context of the CDM model. Combined measurements of temperature fluctuations in the CMB, clustering in the galaxy distribution, and the present day abundance of rich clusters have been used to place limits on both the shape and amplitude or *normalisation* on large ($\sim$ 1000 Mpc), intermediate ($\sim$ 100 Mpc) and small ($\sim$ 10 Mpc) scales respectively. A matter power spectrum normalised to match the observed CMB fluctuations and the abundance

*The scattering of CMB photons by energetic electrons in the intracluster gas.

of rich clusters has been found to be inconsistent with an $\Omega_m = 1$ Standard CDM cosmology and instead favours low Ω_m models, such as ΛCDM and Open CDM. These measurements indicate that either $\Omega_m \simeq 0.3$ or a change in the model is required, for example, the introduction of extra relativistic particles.

Other methods, such as evolution in the abundance of rich clusters (Bahcall & Fan (1998), Eke et al. (1996, 1998)), weak lensing by large scale structure (van Waerbeke et al. (2001)), large scale bulk flows (Strauss et al. (1999)), and analysis of CMB anisotropies (e.g. de Bernardis et al. (2000), Balbi et al. (2000)) combined with power spectrum measurements (Efstathiou et al. (2002)) also suggest a low value for Ω_m although with greater uncertainties.

- Measurements of the primeval abundance of deuterium (O'Meara et al. (2001)) have been combined with theoretical predictions of light element abundances based on Big Bang nucleosynthesis (Burles et al. (2001)) to determine precisely a value of $\Omega_b = 0.039 \pm 0.0075$ (assuming $h = 0.7$) for the mean baryon density of the Universe. This value is consistent with tentative estimates of Ω_b extracted from "baryon bumps" in the matter power spectrum as determined by the 2dF Galaxy Redshift Survey (Percival et al. (2001)), and the ratio of odd-to-even peak amplitudes in the CMB anisotropy power spectrum (Pryke et al. (2002), Netterfield et al. (2002)). It should be noted that this value of Ω_b and the resulting cosmological baryon fraction, $\Omega_b/\Omega_m (\simeq 0.12)$, implies that **non-baryonic dark matter is present in the Universe**, even if it does not constrain its interaction properties.

- Results from the Supernova Cosmology Project (Perlmutter et al. (1999)) and the High-Z Supernova Search (Riess et al. (1999)) show that distant supernova ($0.3 \lesssim z \lesssim 0.9$) are fainter than would be expected if the expansion rate of the Universe was decelerating, and instead indicate the presence of some dark energy component with negative pressure. Assuming a flat $\Omega_m + \Omega_\Lambda = 1$ cosmology, best fit results to the combined data of the two studies suggest $\Omega_\Lambda = 0.75 \pm 0.1$.

  This conclusion is supported by analysis of CMB anisotropies; the location and amplitude of the first acoustic peak in the angular power spectrum has been very well determined by several independent experiments - BOOMERANG (de Bernardis et al. (2002)), MAXIMA (Balbi et al. (2000)) and DASI (Pryke et al. (2002)) - and it implies $\Omega_m + \Omega_\Lambda \simeq 1$, suggesting a value of $\Omega_\Lambda \simeq 0.7$.

The ΛCDM model is widely regarded as a success on large scales, and it has made an impressive number of predictions that are in excellent agreement with a diverse range of observations (Bahcall et al. (1999)). Notable successes include;

- The present day abundance of rich galaxy clusters and its evolution as a function of redshift (Eke et al. (1996, 1998), Bahcall & Fan (1998)).
- The shape and amplitude of the matter power spectrum as inferred from studies of the Lyα forest (Croft et al. (1999)) and the combined analysis of CMB anisotropies and galaxy redshift surveys (Percival et al. (2001)).
- The redshift-luminosity relation for distant supernovae (Riess et al. (1998), Perlmutter et al. (1999)).
- The age of the oldest stars in the Galaxy (Krauss & Chaboyer (2003)).

Thus we have clear and unambiguous evidence that most of the matter in the Universe exists in the form of non-baryonic dark matter, widely assumed to be CDM, and that the dynamics of expansion is currently dominated by some peculiar dark energy, possibly vacuum energy - the *cosmological constant* (e.g. Carroll & Mersini (2001)) - or a scalar field - as favoured by *quintessence* (Caldwell et al. (1998, 2003)).

1.3 Dark Matter in Galaxies

The first evidence for significant amounts of dark matter within individual galaxies came as early as 1939. Babcock (1939) obtained long slit spectra of M31, the Andromeda galaxy, and found that the outer regions were rotating with an unexpectedly high circular velocity. Based on his observations, he concluded that either the outer parts of M31 were dominated by objects with a very high mass-to-light ratio, or its light had been severely attenuated because of strong dust absorption.

Subsequently, Oort (1940) studied the rotation and surface brightness of the edge-on S0 galaxy, NGC 3115. He found that "the distribution of mass in this object appears to bear almost no relation to that of the light" and concluded that the large mass-to-light in the outer parts of the galaxy must be interpreted in terms of a stellar mass distribution heavily weighted towards very faint M-type dwarfs.[†]

[†]Interestingly, neither Babcock nor Oort cite the previous work of Zwicky (1933) or Smith (1936) who pondered over the absence of large amounts "missing mass" in the Coma and Virgo clusters respectively.

Further evidence in favour of dark matter on galactic scales continued to accumulate. Page (1952, 1960) noted that pairs of elliptical galaxies had high mass-to-light ratios, implying that either the members of the binary had massive halos, or they were embedded in a common halo. Finzi (1963) showed that the orbtial motion of distant globular clusters around our own Galaxy required roughly three times as much interior mass as was implied by the rotation of the inner Galactic disk.

In spite of the substantial observational evidence, dark matter was not widely considered to be a viable explanation for discrepancies between observed luminous mass and gravitational mass until the mid-1970s. Roberts & Rots (1973) surveyed neutral HI gas in several nearby giant spirals and found that the rotation curves became flat at large radii. Similarly, Roberts & Whitehurst (1975) measured HI 21-cm line circular velocities in M31, extending the optical rotation curve of Babcock (1939) and Rubin & Ford (1970) well beyond the optical radius ($\sim$ 30 kpc). These observations did not show the expected Keplerian fall-off with increasing radial distance, but instead remained flat out to the last measured data point, corresponding to a galactocentric distance of $\sim$ 30 kpc ($\sim$ 10 disk scale lengths). This behaviour unequivocally implied that the interior mass is continuing to grow well beyond the optical radius of the galaxy, even if its luminosity is not. Roberts & Whitehurst concluded that the mass-to-light ratio in the outer parts of M31 was $\sim$ 200 and interpreted this result (like Oort before them) in terms of a significant number of faint M-type dwarfs populating the outermost regions of the galaxy.

These results were historically significant; at about the same time, Ostriker & Peebles (1973) and Ostriker, Peebles & Yahil (1974) published influential papers that, combined with the rotation curve data, first convinced the majority of the astronomical community that *missing mass* existed (van den Bergh 1999). Ostriker & Peebles noted that bar instabilities in spiral galaxies could be suppressed if the galactic disk is embedded in a massive spherical halo, although they supposed that the unseen component was a population of faint, low mass stars[‡]. Ostriker, Peebles & Yahil reviewed the observational evidence for missing mass in spiral galaxies within the Local Group, in the field and in the Virgo and Coma clusters. They found consistent evidence for significant amounts of dark matter out to a radius of $\sim$ 1 Mpc and noted that "*within the current observational uncertainties*

It certainly appears that no connection was made between the high mass-to-light ratios inferred in the both the galaxies and clusters.

[‡]Sellwood (1985) and Kalnajs (1987) have since contested this result.

the masses associated with ordinary spiral galaxies may make a cosmologically interesting contribution".

This shift in consensus coincided with a burgeoning interest in galaxy formation within the context of a hierarchically clustering cosmology. Press & Schechter (1974) showed how, assuming a Friedmann cosmology, gravitational clustering alone could explain the distribution of mass on all scales, while both Binney (1977) and Silk (1977a,b) considered the effects of dissipative physics on the formation of a galaxy. White & Rees (1978) extended this earlier work and argued that galaxies could not have formed as a result of purely dissipationless physics; rather, they asserted that gas condenses in potential wells provided by the dark matter, some of which is incorporated into luminous galaxies, the rest remaining uncondensed in intergalactic space. The presence of dark matter halos around galaxies is a *natural* consequence of structure formation in a cosmological context.

Subsequent comparisons of gravitational mass with luminous mass for a range of morphological types revealed systematic evidence for associated dark matter halos. Rubin et al. (1980) conducted a survey of 21 late-type spirals and found evidence for non-Keplerian behaviour in their rotation curves at large radii. Similar results were found by Bosma (1981) using the HI 21-cm line. Faber & Lin (1983) noted that the tidal masses of dwarf Spheroidals around our Galaxy implied very high mass-to-light ratios. Romanishin et al. (1982) found that "the mass and light distributions in disk galaxies are not well coupled" when considering the rotation curve of the LSB galaxy NGC 5963. Studies of ellipticals and lenticular (S0) galaxies are less conclusive, however, but the general conclusion is that these galaxies also have dark matter halos (Maoz & Rix (1993), Davis & White (1996), van Driel & van Woerden (1997)), although they may be somewhat smaller than those associated with spirals (Danziger (1997)). Zaritsky & White (1994) used the dynamics of a sample of satellite galaxies to constrain the mass within their orbits and used these data to demonstrate the existence of extended massive dark halos around spirals.

Thus, there is sound observational footing for the existence of extended massive dark matter halos around galaxies. On the other hand, placing constraints on the distribution of mass in the objects has proven to be more challenging.

1.4 Rotation Curve Studies of Late-Type Dwarfs and LSBs

In normal late-type spirals such as M31, the inner rotation curve appears to be dominated by the gravitational potential of the luminous disk and bulge, implying that the dark matter is not dynamically important inside the optical radius. The *maximum disk hypothesis* supposes that the mass-to-light ratio of the disk and bulge is unconstrained and can be varied freely to fit the inner rotation curve; deviations at large radii between the circular velocity produced by this maximum disk and the measured rotation curve are attributed to the dark matter. Although such an argument requires that galaxies occupy *hollow halos*, that is, halos in which the dark matter is completely absent from the innermost parts where the galaxy resides, it has gained considerable support, principally because minor features in the rotation curve appear to be correlated with the light distribution, e.g. "wiggles" due streaming motions in spiral arms (Sellwood & Kosowsky (2001)). However, the most widely used mass models assume that the dark matter halo has a finite central density and can be treated as spherically symmetric with a radial density profile described by the *pseudo-isothermal sphere*

$$\rho(r) = \frac{\rho_0}{(1 + (r/r_c)^2)} \tag{1.2}$$

where ρ_0 is the central density of the halo and r_c is the core radius, typically of order $\sim$ 10 kpc for normal luminous spirals. The central density ρ_0 is constrained generally using r_c and the asymptotic[§] circular velocity;

$$\rho_0 = \frac{v_{max}^2}{4\pi G r_c^2} \tag{1.3}$$

That is, galactic dark matter halos appeared to have a soft, constant density core in their innermost parts.

Unfortunately, the presence of the luminous disk and bulge considerably complicates attempts to extract structural information about the dark matter halo from the observed rotation curve. Lake & Feinswog (1989) considered optical and HI rotation curves from over fifty galaxies and found that while the central density of the fitted isothermal halo could be well determined, its core radius r_c and peak circular velocity, $v_{\rm peak}$, were not.

On the other hand, it was noted that systems dominated by dark matter would not suffer from such complications. Carignan & Freeman (1988) identified the late-type dwarf,

[§]Effectively the peak value

DDO 154, as such a system and showed that "there exist galaxies where the luminous matter (stars and gas) is only a *minor* component of the total galaxy mass". They found that 90% of the mass at 7.6 h^{-1}kpc is contributed by the dark component.

These *dark* late-type dwarf spirals are ideally suited for precise studies of their inner mass distribution - their negligible stellar bulge contributions allow for reduced uncertainties in rotation curve measurements. This is particularly important because the sensitivity of rotation curves to the exact density profile is quite low, so data must be of the highest sensitivity and highest resolution if meaningful comparisons are to be made with theory (Blais-Ouellette et al. (1999)).

As theoretical predictions for the inner structure halos of galactic scale dark matter halos became available, it was noted that the steep central density profiles predicted by high resolution simulations were in conflict with the observed soft central cores (e.g. Flores & Primack (1994), Moore (1994), Burkert (1994)).

Flores & Primack (1993) examined HI rotation curve data for two well studied gas-rich dwarfs, DDO154 and DDO168, and found in both cases that the data were inconsistent with cuspy profiles, instead favouring isothermal profiles with cores; Moore (1994) arrived at a similar conclusion. Burkert (1995) examined HI rotation curve data for seven well studied dwarf spirals and found that the implied mass profiles could be well fit by a phenomenological universal density profile

$$\rho(r) = \frac{\rho_0 \, r_0^3}{(r + r_s)(r^2 + r_s^2)} \tag{1.4}$$

where ρ_0 is the (finite) central density of the halo, and r_s is the scale radius, analogous to the core radius of a pseudo-isothermal sphere.

Further, higher resolution studies (e.g. de Blok & McGaugh (1997), McGaugh & de Blok (1998), Blais-Ouellette et al. (1999), Kravtsov et al. (1998)) continued to infer central cores in the dark matter distribution of dwarfs and LSBs. However, it has been claimed that these studies were compromised by finite spatial resolution (van den Bosch & Swaters (2001), van den Bosch et al. (2001a)); van den Bosch and Swaters (2000) concluded that when the effects of beam smearing were accounted for, "at best weak limits on cosmological parameters and/or the nature of the dark matter can be obtained".

The most recent published observations of dwarfs and LSBs now have sufficiently

high spatial resolution to reliably probe the innermost parts of their rotation curves (e.g. Swaters et al. (2000), de Blok et al. (2001a,b)), and so we might expect the results of mass modelling to be more discriminating. Unfortunately, although the quality of the data has improved, the interpretation of these data and the conclusions that can be drawn from mass modelling are still the subject of heated debate.

Swaters et al. (2000) studied the mass distribution in LSBs and noted that, even with high spatial resolution, "it is difficult to get useful constraints on the dark matter properties", finding that their data are consistent with both the cuspy halos predicted by CDM and halos with soft central cores. Swaters et al. (2003) reached a similar conclusion based on fits to high resolution Hα dwarf and LSB rotation curves. On the other hand, de Blok et al. (2001a), de Blok & Bosma (2002) and Weldrake et al. (2003) have found that their best resolved data are best described by halo profiles with a central kpc-sized constant density core. de Blok et al. (2003) performed a series of simulated observations and found that the "implied observational signature of CDM halos is strong and if present should be easily seen", even in the presence of systematic errors.

It is difficult to draw any firm conclusions from these results. However, erring on the side of caution, we might regard the findings of Swaters et al. (2000) and Swaters et al. (2003) as the most conservative reflection of the subject at present; that is, the high resolution data are still insufficient to constrain the structure of the underlying dark matter halo. As a result, the comparison of observational data with the predictions of CDM must be tentative at best.

1.5 The Structure of Cold Dark Matter Halos

Early analytical studies of gravitational instability in an expanding universe appeared to reject the notion that galaxies could form by such a process (e.g. Lifshitz (1946)). However, the discovery of the CMB radiation by Penzias & Wilson in 1965 prompted a revision of the assumptions made by earlier workers, resulting in Peebles' assertion that gravitational instability could play a key role in galaxy formation based on his analysis of the growth of small matter density fluctuations in an expanding universe (Peebles (1967)).

Subsequently, Gunn & Gott (1973) and Gunn (1977) considered the density distribution of collapsed objects based on the spherically symmetric *secondary infall* of matter onto seed perturbations. This work was extended by Hoffmann & Shaham (1985),

who allowed for Gaussian perturbations in their initial conditions, Fillmore & Goldreich (1984), who considered similarity solutions for planar, cylindrical and spherical collapse, and Bertschinger (1985), who obtained similarity solutions for secondary infall onto an accreting centre in a flat (Ω_m=1) Einstein-de Sitter universe.

These idealised studies provided a theoretical framework for understanding how such halos might form and the kind of density structure one could expect. The theoretically motivated expectation was for power law behaviour within the virialised regions of halos, $\rho(r) \propto r^{\alpha}$ with $\alpha \sim 2$, the exact slope dependent on cosmological parameters, principally the initial power spectrum of density fluctuations. Such a density distribution appeared to be in good agreement with the observed structure of galaxies as inferred from rotation curves, which implied $\rho(r) \propto r^{-2}$.

However, gravitational clustering is a highly nonlinear problem and so progress in understanding the structure of dark matter halos requires direct simulation. As numerical data became available from the earliest N-body work on hierarchical cosmologies, it was possible to follow the formation of halos in the nonlinear regime and to study their structure (e.g. Frenk et al. (1985)); for example, both Frenk et al. (1988) and Efstathiou et al. (1988) reported departures from power law behaviour in their best resolved halos ($\sim 1,000$ particles).

Dubinski & Carlberg (1991) were among the first to perform large enough N-body simulations ($\sim 300,000$ particles) to be able to resolve the inner parts of dark matter halos where galaxies form (but see also, e.g. Katz (1991), Warren et al. (1992)). They observed that halo density profiles had gently curving logarithmic slopes that continued to increase inside their resolution limit, and could be well described by the *Hernquist* profile (Hernquist (1990)),

$$\rho(r) = \frac{M}{2\pi} \frac{r_s}{r} \frac{1}{(r + r_s)^3} \tag{1.5}$$

where M is the total mass of the halo and r_s is the scale radius. The inner slope varies as $\rho(r) \propto r^{-1}$ at small radii and asymptotes to $\rho(r) \propto r^{-4}$ at large radii[¶].

Subsequently, in a series of seminal papers, Navarro, Frenk & White (1995. 1996, 1997) (hereafter NFW) carried out an extensive set of simulations of dark matter halos, extend-

[¶]It should be noted that Dubinski & Carlberg approximated the external tidal field by a first-order tidal tensor and used a spherical particle distribution, centred on the initial perturbation, with vacuum boundary conditions.

ing from galaxy to cluster mass scales in a variety of hierarchical clustering cosmologies. They were able to resolve individual halos with $\sim 10,000$ particles and used a *multimass method* (Porter (1985); Katz & White (1993)) to accurately model the tidal field. Based on analysis of their data, they observed that virialised dark matter halos could be well described by a *universal* density profile:

$$\rho(r) = \frac{\rho_{\rm crit}\ \delta_{\rm c}}{r/r_{\rm s}(1+(r/r_{\rm s}))^2}. \tag{1.6}$$

Here, $\rho_{\rm crit}$ is the critical density of the Universe, $\delta_{\rm c}$ is the characteristic density contrast of the halo, dependent on its mass and $r_{\rm s}$ is the scale radius (see § 1.5.1). The inner slope varies as $\rho(r) \propto r^{-1}$ but asymptotes to $\rho(r) \propto r^{-3}$ at large radii. NFW concluded that dark matter halos have the same shape, independent of halo mass, initial density fluctuation spectrum or values of the cosmological parameters.

Higher resolution studies with sufficient mass and force resolution to resolve the innermost regions of dark matter halos indicate that, while the NFW provides a good fit to down to $\sim 5-10\%$ of the virial radius, r_{200}[‖], the central asymptotic slope of the density profile appears be steeper than predicted by NFW. Fukushige & Makino (1997), Moore et al. (1998) and Ghigna et al. (1998) carried out simulations of galaxy clusters, resolving halos with $\sim 10^6$ particles, and found that the inner density profile diverged as $\rho(r) \propto r^{-1.5}$. Moore et al. (1999) suggested that the following functional form provided a better fit to the inner density profiles of cluster and galaxy mass halos;

$$\rho(r) = \frac{\rho_s}{(r/r_{\rm s})^{3/2}(1+(r/r_{\rm s})^{3/2})}, \tag{1.7}$$

where ρ_s is some characteristic density and r_s is some characteristic radius. These conclusions were confirmed in further simulations at still higher resolution ($\sim 3 \times 10^6$ particles) by Moore et al. (1999b), Ghigna et al. (2000), Fukushige & Makino (2001, 2003) and Klypin et al. (2001).

On the other hand, Jing & Suto (2000) analysed a sample of high resolution galaxy and cluster mass halos, and claimed that the shape of dark matter density profile is not universal but instead depends upon mass, steepening with decreasing mass scale. They found that the central slope of the density profile varied between -1.1 on cluster mass scales to ~ -1.5 on galaxy scales. Klypin et al. (2001) have questioned this result, however, highlighting the fact that such behaviour can be explained by the change in concentration between the different mass scales - more concentrated systems tend to have

[‖]See § 1.5.1

steeper profiles at a fixed fraction of the virial radius.

We may conclude that dark matter halos forming in high resolution simulations of CDM cosmologies can be well described by density profiles that are shallower than isothermal in their centres, with an inner slope $-1.5 \lesssim \alpha \lesssim -1$, before smoothly rolling over and approaching an asymptotic slope of $\alpha \to 3$ in their outer parts.

1.5.1 Analytic Profiles

For the purpose of this thesis, we define a *dark matter halo* to be a spherical overdense virialised region whose mean interior density is 200 times the critical density of the Universe, $\rho_{\rm crit}$, at the given redshift. We define the *virial mass*, M_{200}, to be the mass enclosed within this overdense region;

$$M_{200} = \frac{4\pi}{3} 200\, \rho_{\rm crit}\, r_{200}^3, \tag{1.8}$$

where r_{200} corresponds to the *virial radius.*

The NFW Profile

The NFW profile (1995, 1996, 1997) has the form

$$\rho(r) = \frac{\rho_{\rm crit}\ \delta_{\rm c}}{r/r_{\rm s}(1+(r/r_{\rm s}))^2} \tag{1.9}$$

where $\rho_{\rm crit}$ is the critical density of the Universe, r_s is a characteristic scale radius, and $\delta_{\rm c}$ is a characteristic overdensity. The scale radius, r_s, is related to the virial radius of the halo, r_{200}, through the *concentration* parameter, $c = r_{200}/r_s$. The characteristic overdensity can be written in terms of the concentration as,

$$\delta_c = \frac{200}{3} \frac{c^3}{\ln(1+c) - c/(1+c)} \tag{1.10}$$

As $r \to 0$, the density diverges as $\rho(r) \propto r^{-1}$.

The enclosed mass within a given radius r can be expressed as

$$M(r) = 4\pi \rho_{\rm crit} \delta_c r_s^3 \left(\ln(1+cx) - cx/(1+cx)\right). \tag{1.11}$$

where c is the concentration and $x = r/r_{200}$ is the radius normalised to the virial radius, r_{200}; note that $cx = r/r_s$.

The circular velocity profile can be expressed as

$$V_c(r) = \left(\frac{GM(r)}{r}\right)^{1/2} = V_{200}\left(\frac{1}{x}\frac{\ln(1+cx) - cx/(1+cx)}{\ln(1+c) - c/(1+c)}\right)^{1/2} \tag{1.12}$$

where V_{200} is the circular velocity at the virial radius.

The logarithmic slope, $S(r)$, at radius r can be expressed as

$$S(r) = -\frac{d\log\rho}{d\log r} = \frac{1+3(r/r_s)}{1+r/r_s} \tag{1.13}$$

We note that $S(r) = 2$ at r_s.

The Moore et al. Profile

The Moore et al. profile (Moore et al. (1999)) has the form

$$\rho(r) = \frac{\rho_s}{(r/\tilde{r}_s)^{3/2}(1+(r/\tilde{r}_s)^{3/2})} \tag{1.14}$$

where, as before, ρ_s is some characteristic density and $\tilde{r}_s$ is a characteristic scale radius. We can define a *concentration* parameter for this model, $\tilde{c} = r_{200}/\tilde{r}_s$, and we can rewrite ρ_s in terms of $\rho_{\rm crit}$ and a characteristic overdensity, similar to equation 1.10;

$$\tilde{\delta}_c = \frac{100\tilde{c}^3}{\ln(1+\tilde{c}^{3/2})} \tag{1.15}$$

As $r \to 0$, the density diverges as $\rho(r) \propto r^{-1.5}$.

The enclosed mass within a given radius r can be expressed as

$$M(r) = \frac{8\pi}{3}\rho_{\rm crit}\tilde{\delta}_c\tilde{r}_s^3\ln(1+(\tilde{c}x)^{3/2}). \tag{1.16}$$

where $x = r/r_{200}$ is the normalised radius; note that $cx = r/r_s$.

The circular velocity profile can be expressed as

$$V_c(r) = V_{200}\left(\frac{1}{x}\frac{\ln(1+(\tilde{c}x)^{3/2})}{\ln(1+\tilde{c}^{3/2})}\right)^{1/2} \tag{1.17}$$

where V_{200} is the circular velocity at the virial radius.

The logarithmic slope at radius r can be expressed as

$$S(r) = -\frac{d\log\rho}{d\log r} = \frac{3}{2}\frac{1+2(r/\tilde{r}_s)^{3/2}}{1+(r/\tilde{r}_s)^{3/2}}. \tag{1.18}$$

We note that $S(r) = 2.25$ at $\tilde{r}_s$.

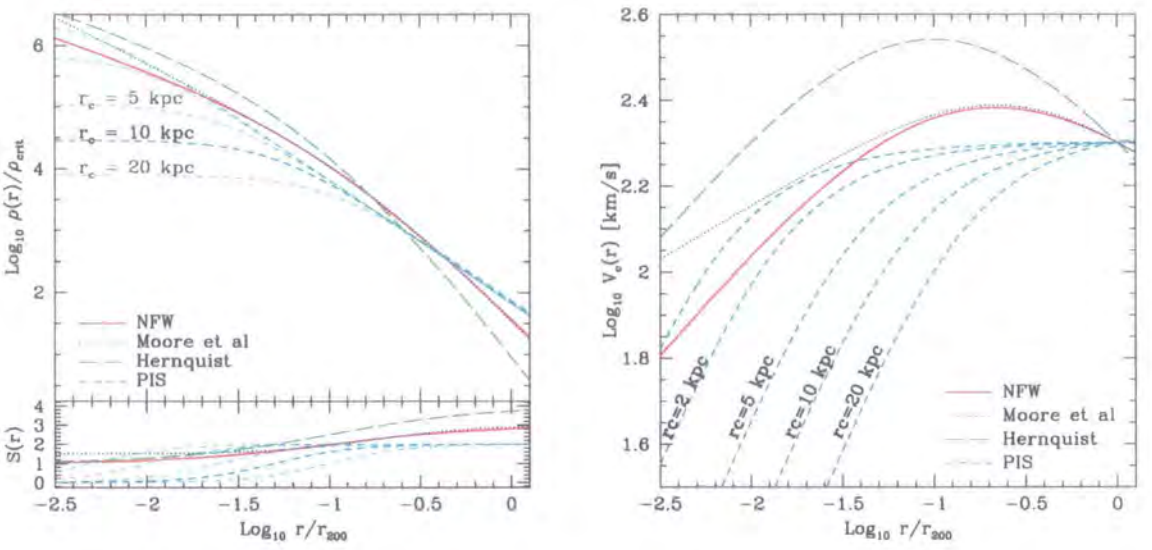

(a) Dark Matter Density Profiles

(b) Dark Matter Circular Velocity Profiles

Figure 1.1: **Comparison of Various Analytic Dark Matter Mass Profiles.** We compare the analytic NFW (solid red curves), Moore et al. (dotted blue curves), Hernquist (long dashed green curves) and pseudo-isothermal sphere (short dashed curves) mass profiles. The NFW and Moore et al. profiles have been normalised to have the same virial mass and the same radius of the maximum circular velocity. The upper panel in figure 1.1(a) shows the spherically averaged density profiles, while the lower panel shows the variation of logarithmic slope with radius. Figure 1.1(b) shows the spherically averaged circular velocity profiles. In the case of the pseudo-isothermal sphere, we have fixed the asymptotic circular velocity, $v_{\rm max}$, and highlight the effect of different core radii on the spherically averaged profiles.

We can relate the NFW and Moore et al. scale radii - r_s and $\tilde{r}_s$ - and therefore the concentrations by requiring that the circular velocity profiles of the respective models peak at the same location, $r_{\rm max}$. This occurs at $r_{\rm max} \simeq 2.16\, r_s$ for the NFW model, and $\simeq 1.24\, \tilde{r}s$ for the Moore et al. model; therefore we find that $\tilde{r}_s(\tilde{c}) \simeq 0.574\, r_s(c)$.

Figure 1.1 compares the density and circular velocity profiles for both the NFW and Moore et al. models, as well as those of the Hernquist profile (equation 1.5) and the pseudo-isothermal sphere (equation 1.2) for reference. We have normalised radii to r_{200}, the virial radius of the halo, set to $r_{200} = 200$ kpc, and we assume that the NFW concentration is $c = 10$, equivalent to that of a typical galaxy mass halo. The Hernquist scale radius, r'_s,

has been set to $r'_s = 20$ kpc. The asymptotic circular velocity of the pseudo-isothermal sphere has been chosen to be $v_{\rm max} = 200$ kms^{-1}.

1.6 The Inner Structure of ΛCDM Halos

This thesis can be divided into two parts;

- the first part is concerned with establishing the conditions under which the distribution of mass in dark matter halos forming in simulations of the ΛCDM cosmology is unaffected by finite numerical resolution;

  - In chapter 2, we have analysed the results from a comprehensive series of simulations of a single galaxy mass halo in which numerical parameters, such as the gravitational force softening, ϵ, timestep, δt, and particle number, N, have been varied in a systematic way in order to determine their impact on the spherically averaged mass profile. The results of this analysis have helped to define a set of convergence criteria with which we can identify the radial extent over which the spherically averaged circular velocity profile can be considered reliably resolved.

  - In chapter 3, we have examined the abundance of substructure halos in three sets of simulated halos, run with increasing mass and force resolution but deemed "converged" by the convergence criteria defined in chapter 3. By analysing the response of the subhalo mass function to variations in particle mass and softening, we have been able to estimate the minimum number of particles per subhalo required if substructure on a given mass scale is to be considered unaffected by mass and force resolution.

- the second part is concerned with the detailed analysis of the internal structure and kinematics of dwarf galaxy halos forming in high resolution simulations of the ΛCDM cosmology. In particular, we have focused on characterising the redshift and mass dependence of the spherically averaged density and circular velocity profiles; the associated concentration parameter (as defined in § 1.5.1); the spherically averaged radial velocity and velocity anisotropy profiles; the dimensionless spin parameter, λ; the shapes of isodensity surfaces; and the mass, abundance and spatial distribution of substructure.

- In chapter 4, we have analysed the various structural and kinematical properties of the dwarfs for trends that may reflect dependence on redshift. Furthermore, we have investigated whether these halos could sustain galactic disks by examining the symmetry and stability of their mean-field gravitational potential.
- In chapter 5, we have complemented our sample of dwarfs halos with a larger sample of galaxy and cluster mass halos, such that our combined sample spans ~ 5 orders of magnitude in mass, and compared their various structural and kinematical properties in order to identify trends that may reflect a dependence on mass.

Finally, in chapter 6, we provide a summary of the main findings of this work and highlight those sections of this thesis that may prove rewarding for further study.

Chapter 2

The Inner Structure of ΛCDM Halos: A Numerical Convergence Study

2.1 Introduction

Over the past few decades, cosmological N-body simulations have led to impressive strides in our understanding of structure formation in universes dominated by collisionless dark matter. Such simulations have provided an ideal test-bed for analytic theories of structure formation, and have been used to validate and motivate a variety of theoretical insights into the statistics of hierarchical clustering (e.g. Press & Schechter (1974), Bardeen, Bond, Kaiser & Szalay (1986), Bond, Cole, Efstathiou & Kaiser (1991), Lacey & Cole (1993), Mo & White (1996)) In particular, N-body simulations have played a pivotal role in providing a clear framework within which the CDM cosmogony may be compared with observation, and in establishing Cold Dark Matter (CDM) as the leading theory of structure formation (Davis et al. (1985)).

This work has led to the development of a robust theoretical framework which provides an accurate statistical description of structure growth through gravitational instability seeded by Gaussian primordial density fluctuations. It is now possible to predict with great accuracy, and based only on the initial power spectrum of the primordial fluctuations, a number of important statistics that characterise the large scale structure of the universe; e.g. , the mass function and clustering of dark matter halos and their evolution with redshift (e.g. Jing (1998), Sheth & Tormen (1999), Jenkins et al. (2001)) the non-linear evolution of the dark matter power spectrum and correlation functions (e.g. Hamilton et al. (1991), Peacock & Dodds (1996)), as well as the topological properties of

the large scale structure (e.g. Gott et al. (1987)).

The impact of such simulation work has been greatest in the non-linear regime, where analytic calculations offer little guidance. Recently, and as a result of the development of efficient algorithms and of the advent of massively parallel computers, it has been possible to apply N-body studies to the investigation of structure on small, highly non-linear scales. These studies can now probe scales comparable to the luminous radii of individual galaxies, thus enabling direct comparison between theory and observation in regions where luminous dynamical tracers are abundant and easiest to observe. Predicting the structure of dark matter halos on kpc and sub-kpc scales, where it can be compared directly with observations of galactic dynamics, is one of the premier goals of N-body experiments, and there has been steady progress in this area over the past few years.

Building upon the early work of Frenk et al. (1985, 1988), Quinn et al. (1986), Dubinski & Carlberg (1991) and Crone et al. (1994), Navarro, Frenk & White (1996, 1997, hereafter NFW) found that, independently of mass and of the value of the cosmological parameters, the density profiles of dark matter halos formed in various hierarchical clustering cosmogonies were strikingly similar. This 'universal' structure can be characterised by a spherically-averaged density profile which differs substantially from the simple power law, $\rho(r) \propto r^{-\alpha}$, predicted by early theoretical studies (Gunn & Gott (1972), Fillmore & Goldreich (1984), Hoffman Y. & Shaham J (1985), White & Zaritsky (1992)). The profile steepens monotonically with radius, with logarithmic slopes shallower than isothermal (i.e. $\alpha < 2$) near the centre, but steeper than isothermal ($\alpha > 2$) in the outer regions.

NFW proposed a simple formula,

$$\frac{\rho(r)}{\rho_{\rm crit}} = \frac{\delta_c}{(r/r_s)(1+r/r_s)^2}, \tag{2.1}$$

which describes the density profile of any halo with only two parameters, a characteristic density contrast*, δ_c, and a scale radius, r_s. Defining the mass of a halo as that contained within r_{200}, the radius of a sphere of mean density contrast 200, there is a single adjustable parameter that fully describes the mass profile of halos of given mass: the 'concentration' ratio $c = r_{200}/r_s$.

*We use the term 'density contrast' to denote densities expressed in units of the critical density for closure, $\rho_{\rm crit} = 3H^2/8\pi G$. We express the present value of Hubble's constant as $H(z=0) = H_0 = 100\,h$ km s^{-1} Mpc^{-1}

For the sake of this discussion, the two main points to note from the work of NFW are the following: (i) the density profile in the inner regions of the halo is shallower, and in the outer regions steeper, than isothermal, and (ii) there is no well defined value for the *central* density of the dark matter, which can in principle climb to arbitrarily large values near the centre.

Conclusion (i) is important, since it is a feature of dark halo models that is required by observations. For example, it implies that the characteristic speeds of dynamical tracers may be lower near the centre than in the main body of the system, as observed in disk galaxies, where the velocity dispersion of the bulge is lower than indicated by the maximum rotation speed of the surrounding disk, as well as in galaxy clusters, where the velocity dispersion of stars in the central cluster galaxy is lower than that of the cluster as a whole. Conclusion (ii) is also important, since there have been a number of reports in the literature arguing that the shape of the rotation curves of many disk galaxies rules out steeply divergent dark matter density profiles (Flores & Primack (1994), Moore (1994), de Blok et al. (2001), but see van den Bosch & Swaters (2001)), a result that may signal a genuine crisis for the CDM paradigm on small scales (e.g. Sellwood & Kosowsky (2000), Moore (2001)).

These general results of the work by NFW have been confirmed by a number of subsequent studies (Cole & Lacey (1996), Fukushige & Makino (1997), Huss, Jain & Steinmetz (1999), Moore et al. (1998), Jing & Suto (2000)), although there is some disagreement about the innermost value of the logarithmic slope. Moore et al. (1998), Ghigna et al.(2000), and Fukushige & Makino (1997, 2001) have argued that density profiles diverge near the centre with logarithmic slopes considerably steeper than the asymptotic value of $\alpha = 1$ in NFW's formula. Kravtsov et al. (1998), on the other hand, initially obtained much shallower inner slopes ($\alpha \sim 0.7$) in their numerical simulations, but have now revised their conclusions; these authors now argue that CDM halos have steeply divergent density profiles but, depending on evolutionary details, the slope of a galaxy-sized halo at the innermost resolved radius may vary between -1.0 and -1.5 (Klypin et al. (2001)).

Since steep inner slopes are apparently disfavoured by rotation curve data it is important to establish this result conclusively; if confirmed, it may offer a way to falsify the CDM paradigm on small scales. Unfortunately, observational constraints are strongest just where theoretical predictions are least trustworthy. For example, the alleged disagree-

ment between observed rotation curves and cuspy dark halo models is most evident for sub-$L_\star$ galaxies on scales of $\sim 1\,h^{-1}$ kpc or less. For typical circular speeds of ~ 100 km s^{-1}, this corresponds to regions where the density contrast exceeds $\sim 10^6$. Orbital times in these regions are of order 10^{-3} of the age of the universe, implying that N-body codes must be able to follow particles accurately for several thousand orbits. Few cosmological codes have been tested in a systematic way under such circumstances. Furthermore, the cold dark matter halos that host typical disk galaxies are thought to extend out to a few hundred kpc, implying that the ~kpc scale probed by observations involves a very small fraction of the mass and volume of the dark halo. As a consequence, these regions are vulnerable to numerical artifacts in N-body simulations stemming, for example, from the gravitational softening or the number of particles.

Extreme care is thus needed to separate numerical artifacts from the true predictions of the CDM model. In order to validate or 'rule out' the CDM cosmogony one must be certain that model predictions on the relevant scales are accurate, robust, and free of systematic numerical uncertainties. Although there have been some recent attempts at unravelling the role of numerical parameters on the structure of simulated dark matter halos, notably in the work of Moore et al. (1998), Knebe et al. (2000), Klypin et al. (2001) and Ghigna et al. (2000), the conclusions from these works are still preliminary and, in some cases, even contradictory.

To cite an example, Moore et al. (1998) argue that the smallest resolved scales correspond to about half the mean inter-particle separation within the virial radius, and conclude that many thousands of particles are needed to resolve the inner density profile of dark matter halos. Klypin et al. (2001), on the other hand, conclude that mass profiles can always be trusted down to the scale of the innermost ~ 200 particles, provided that other numerical parameters are chosen wisely. Ghigna et al. (2000) suggest an additional convergence criterion based on the gravitational softening length scale, and argue that convergence is only achieved on scales that contain many particles and that are larger than about ~ 3 times the scale where pairwise forces become Newtonian. Understanding the origin of such disparate conclusions and the precise role of numerical parameters is clearly needed before a firm theoretical prediction for the structure of CDM halos on ~kpc scales may emerge.

Motivated by this, we have undertaken a large series of numerical simulations designed

to clarify the role of numerical parameters on the structure of simulated CDM halos. In particular, we would like to answer the following question: what regions of a simulated dark matter halo in virial equilibrium can be considered reliably resolved? This question is particularly difficult because of the lack of a theory with which the true structure of dark halos may be predicted analytically, so the best we can do is to establish the conditions under which the structure of a simulated dark halo is independent of numerical parameters. This is the question which we endeavour to answer in this paper.

There is a long list of considerations and numerical parameters that may influence the structure of simulated dark halos:

- the N-body code itself
- the procedure for generating initial conditions
- the accuracy of the force computation
- the integration scheme
- the initial redshift
- the time-stepping choice
- the gravitational softening
- the particle number

Clearly the list could be substantially longer, but the items above are widely considered the most important concerning the structure of simulated dark halos.

Before we proceed to analyse their role, we must decide which properties of a dark matter halo we will assess for numerical convergence. Because, as mentioned above, disk galaxy rotation curves seem to pose at present one of the most pressing challenges to the CDM paradigm on small scales, we have decided to concentrate on the spherically-averaged mass profile, as measured by the radial dependence of the circular velocity, $V_c(r) = \sqrt{GM(r)/r}$, or, equivalently, by the inner mean density profile, $\bar{\rho}(r) = 3M(r)/4\pi r^3$.

We note that the convergence criteria derived here apply strictly only to these properties, and that others, such as the three-dimensional shape of halos, their detailed orbital structure, or the mass function of substructure halos, may require different convergence criteria.

The basic philosophy of our convergence testing procedure is to select a small sample of halos from a cosmological simulation of a large periodic box and to resimulate them varying systematically the parameters listed above, searching for regions in parameter space where the circular velocity curves are independent of the value of the numerical parameters, down to the smallest scales where Poisson uncertainties become important, i.e., roughly down to the radius that contains ~ 100 particles.

Overall, this is a fairly technical chapter of interest mostly to practitioners of cosmological N-body simulations. Readers less interested in numerical details may wish to skip to § 2.7, where we discuss in detail the converged inner mass profile of the galaxy-sized ΛCDM halo used in our convergence study. The more technical sections include:

- a discussion of the N-body codes used in this work, initial conditions setup and analysis procedure (§ 2.2)
- a general discussion of the consequences of discreteness effects on simulations of dark matter halos, including a derivation of "optimal" choices (for given particle number) of the timestep and the gravitational softening (§ 2.4)
- a comparison between single- and multi-timestepping techniques (§ 2.5)
- a discussion of the role of the gravitational softening, the initial redshift, the force accuracy, and the particle number on the inner mass profile of simulated halos (§ 2.6)

Finally, a worked example of how to choose optimal parameters for a high-resolution simulation is presented in § 2.6.5. We summarise our main conclusions in § 2.8.

2.2 Numerical Methods

2.2.1 N-body Codes

Most simulations reported in this chapter have been performed with the parallel N-body code `GADGET`, written by Volker Springel, and available from `http://www.mpa-garching.mpg.de/gadget` (Springel et al. (2001)). In order to test the dependence of our results on the particular algorithmic choices made in `GADGET`, we have also used `PKDGRAV`, a code written by Joachim Stadel and Thomas Quinn (Stadel (2001)). As we discuss in § 2.4 and § 2.6, the two codes give approximately the same results for appropriate choices of the numerical parameters. We have not attempted to carry out a detailed comparison of the relative efficiency or speed of the codes; such comparison is heavily dependent on the

particular architecture of the hardware used, and on a variety of optimisation and tuning procedures. We do note, however, that neither code seems obviously to outperform the other when our strict numerical convergence criteria are met.

The two N-body codes share a number of similarities. They both evaluate accelerations ('forces') on individual particles due to all others using a hierarchical tree data structure (Barnes & Hut (1986), Jernigan & Porter (1989)), and (optionally) use individually adaptive time-stepping schemes to advance the integration of each particle. Periodic boundary conditions are handled in both codes via Ewald's summation technique (Hernquist, Bouchet & Suto (1991)), although the implementation of the algorithm in each code is different.

Gravitational softening is introduced in the form of a 'spline' mass distribution (see, e.g., Hernquist & Katz (1989), Navarro & White (1993)) which, unlike the more traditional 'Plummer' softening of the early generation of N-body codes (e.g. Aarseth (1985)), converges for pairwise interactions exactly to the Newtonian regime at a finite radius. The length scale of the spline kernel, ϵ_i, can be chosen individually for each particle in PKDGRAV. GADGET, on the other hand, allows for different softenings to be chosen for up to six different particle 'species'. We quote the values of ϵ_i so that gravitational interactions between two particles are fully Newtonian for separations larger than $2\,\epsilon_i$.

The codes differ substantially in their implementation of the tree construction, in the force-evaluation algorithms and in the integrator scheme. Whereas PKDGRAV uses a spatial binary tree for gravity calculations, GADGET uses a version of the Barnes-Hut geometric oct-tree. Distant tree-node contributions to the force calculations include up to quadrupole expansion terms in GADGET, but up to hexadecapole in PKDGRAV. The tree is rebuilt every timestep in the version of PKDGRAV that we tested (although this is not the case in the most up-to-date version), whereas we rebuild the tree in GADGET dynamically after $\sim 0.1\,N_{tot}$ force computations since the last full reconstruction. (N_{tot} is the total number of particles in the simulation.)

Finally, GADGET uses a simple second-order DKD (drift-kick-drift) leap-frog integrator scheme with expansion factor as the integration variable, whereas PKDGRAV adopts a cosmic time-based KDK (kick-drift-kick) algorithm. All integrations are carried out in comoving coordinates. Details of these codes may be found in Springel et al. (2001), and in Stadel (2001). In the following subsections we describe the numerical setup used for

the two codes.

GADGET

GADGET has been the main simulation code used in this study, and it evolved as the project unfolded from the first public release v1.0 to the latest available release v1.1. All of the results presented here have been obtained with the latest version of the code.

GADGET presents the user with a number of options regarding time-stepping choices and the accuracy of the force calculations. In all cases we have used the tree node-opening criterion recommended by Springel et al. (2001), where a Barnes-Hut opening criterion with $\theta = 0.6$ is used for the first force computation and a dynamical updating criterion is used subsequently. In this criterion, a node is opened if $G\,M\,l^4 > f_{\rm acc}\,a_{old}\,r^6$, where G is the Gravitational constant, M is the mass of the node, l is the node-side length, and a_{old} is the acceleration that the particle experienced in the previous timestep. The parameter $f_{\rm acc}$ (called `ErrTolForceAcc` in GADGET's parameter list) is set to 10^{-3} in our standard calculations. This condition can be overridden if the `-DBMAX` compile-time flag is activated. Enabling this flag imposes an additional condition for node-opening: multipole expansion of a node is only used if, in addition to the previous condition, the particle is *guaranteed* to lie outside the geometric boundaries of the node in question[†]. The results reported in § 2.6.3 indicate that these choices are important to ensure convergence: resolving the inner structure of dark halos requires highly accurate forces.

We note that enabling `-DBMAX` guards against those rare, pathological situations where the treecode fails to force further subdivision of the cell in which the particle resides, in which case the cell is opened and large force inaccuracies result. Such a situation can arise if the particle lies close to the edge of the cell whose centre of mass is located at the opposite edge; the particle will have contributed to both the mass and the centre of mass coordinates of the cell and so its self acceleration is included, resulting in a spuriously large acceleration. Similar behaviour arises if the Barnes-Hut opening criterion is adopted and $\theta \simeq 1$ (Hernquist (1987)).

GADGET uses an integrator with completely flexible timesteps. The code carries, for each particle, a time, t_i, position, $\mathbf{r}_i$, velocity, $\mathbf{v}_i$, acceleration, $\mathbf{a}_i$, gravitational softening, ϵ_i, and, optionally, a local density, ρ_i, and a local one-dimensional velocity dispersion, σ_i. From these quantities, timesteps, Δt_i, can be computed for each particle according to

[†]A similar condition is activated by default in PKDGRAV

several possible choices:

$$\Delta t_i = \begin{cases} \eta_{a\epsilon}\sqrt{\epsilon_i/a_i}, & \text{if DtCrit=0;} \\ \eta_a/a_i, & \text{if DtCrit=1;} \\ \eta_{a\sigma}(\sigma_i/a_i), & \text{if DtCrit=2;} \\ \eta_\rho(G\rho_i)^{-1/2}, & \text{if DtCrit=3;} \\ \eta_{\sigma\rho}\min[(G\rho_i)^{-1/2},(\sigma_i/a_i)], & \text{if DtCrit=4,} \end{cases} \tag{2.2}$$

where `DtCrit` refers to the runtime input parameter `ErrTolIntAccuracy` in `GADGET`, and η is a dimensionless constant that controls the size of the timesteps (except for η_a, which has dimensions of velocity)[‡]. For ease of reference, we shall refer to the various choices for `DtCrit` using the following mnemonic shorthand: `EpsAcc` for `DtCrit=0`; `VelAcc` for `DtCrit=1`; `SgAcc` for `DtCrit=2`; `SqrtRho` for `DtCrit=3`; and `RhoSgAcc` for `DtCrit=4`, respectively

We report below results obtained with several of these choices. Unless specified, a maximum timestep was imposed so that all particles took *at least* 200 timesteps during the whole integration. In practise, this limit affects a very small fraction of the particles in a typical run: resolving the inner structure of dark halos requires typically several thousand timesteps.

PKDGRAV

In the `PKDGRAV` runs reported below we have only explored variations in two parameters: the time-stepping parameter, η, and the gravitational softening, ϵ_i. We note, however, that `PKDGRAV` is a very flexible code that includes a number of choices for the integrator scheme and time-stepping, and we have by no means explored all of its options. `PKDGRAV` was mainly used in this study to verify that the results obtained with `GADGET` are independent of the code utilised.

All `PKDGRAV` simulations that used individual timesteps were evolved to $z = 0$ using 50 system timesteps. The system timestep, ΔT, is the maximum allowed for any particle. Individual particle timesteps are binned in a hierarchy so that $\Delta t_i = \Delta T/2^n$, where n was allowed to take any value in the range (0,20). This allows particles to take up to $\sim 10^8$ timesteps in a run, which means that in practise no significant restrictions have been placed on the minimum timestep.

[‡]For convenience we have defined $\eta_{a\epsilon}$ to be directly proportional to the size of the timestep in all cases. For `DtCrit=0`, $\eta^2_{a\epsilon} = 2 \times$ `ErrTolIntAccuracy`

Individual particle timesteps were chosen in **PKDGRAV** runs in a manner analogous to **GADGET**'s **EpsAcc** criterion, i.e., $\Delta t_i \leq \eta\sqrt{\epsilon_i/a_i}$, although quantitatively accelerations differ because of the choice of integration variables. The parameter η specifies the size of the timesteps and, consequently, the overall time accuracy of the integration.

Finally, the force accuracy in **PKDGRAV** is controlled by θ, a redshift-dependent opening-node criterion. We have chosen for all runs $\theta = 0.55\,(z > 2)$ and $\theta = 0.7$ for $z < 2$.

2.2.2 The Initial Conditions

Setting up initial conditions that faithfully represent the cosmogony one wishes to investigate is a *crucial* step in the simulation process and, despite the popularity of cosmological N-body simulations, there is surprisingly little detail in the literature regarding how this is tackled by different groups. The major references on this topic in the refereed literature are the work of Efstathiou et al. (1985) and the recent papers by Bertschinger & Gelb (1991), Pen (1997), and by Bertschinger (2001; see also `http://arcturus.mit.edu/cosmics` and `http://arcturus.mit.edu/grafic`).

Our particular procedure follows closely that described in Efstathiou et al. (1985) and is described in detail in appendix A.1. It aims to provide a particle realisation of a Gaussian density field with the chosen primordial power spectrum, $P(k)$, on scales and at redshifts where linear theory is applicable.

We adopt the ΛCDM cosmological model, a low-density universe of flat geometry whose dynamics is dominated at present by a cosmological constant, $\Omega_0 = 0.3$, $\Omega_\Lambda = 0.7$ and $h = 0.65$. We shall assume that the initial power spectrum is Harrison-Zel'dovich ($P(k) \propto k$), modified by an appropriate cosmological transfer function, $T(k)$. For ΛCDM simulations we have chosen to use the analytic representation of the transfer function proposed by Bardeen et al. (1986) with shape parameter $\Gamma = 0.2$.

Our simulations proceed in two stages. Firstly, a large, low-resolution, periodic box is run to $z = 0$ and used to select halos targeted for resimulation at much higher resolution (consult the appendix A.1 for details). For the first step, we have generated a Fourier representation of the fluctuation distribution on a 128^3 mesh and have computed displacements for 128^3 particles initially arranged on a cubic grid. The displacements assume an initial redshift of $z_i = 49$ in the ΛCDM cosmogony and are normalised so that at $z = 0$ the linear rms amplitude of mass fluctuations on spheres of radius $8\,h^{-1}$ Mpc

is $\sigma_8 = 0.9$. The size of the box is $L_{\rm box} = 32.5\,h^{-1}$ Mpc (comoving), and the particle mass is $m_p = 4.55 \times 10^9\,\Omega_0\,h^{-1} M_\odot$. The dashed curve in figure 2.1 shows that the power spectrum computed from the displaced positions of the 128^3 particles within this box is in very good agreement with the theoretical power spectrum (dotted lines).

The second stage of the initial conditions generating procedure involves selecting a small region within the large periodic box destined to collapse into a halo selected for resimulation at higher resolution. In the case we consider here, this region is a box of $L_{\rm sbox} = 5.08\,h^{-1}$ Mpc on a side. The advantage of this procedure is that one can in principle include many more particles in the high-resolution box than were present in the parent simulation (we use $N_{\rm sbox} = 256^3$ in the case we consider here, giving a highest-resolution particle mass of $6.5 \times 10^5\,h^{-1}\,M_\odot$). A new Fourier representation of the theoretical power spectrum is then generated, retaining the phases and amplitudes of the Fourier components in the parent simulation and adding waves of higher frequency, periodic in the high-resolution box, up to the Nyquist frequency of the high-resolution particle grid. The solid line in figure 2.1 shows that the power spectrum measured directly from particle displacements in the high-resolution box is again in good agreement with the theoretical expectation.

Figure 2.1 thus demonstrates that the power spectrum is reproduced well by both the parent simulation and the resimulated region. Altogether, the power spectrum is fit well over nearly three decades in wavenumber and seven decades in power. The maximum difference between the theoretical power spectrum and the measured power spectra is less than 0.05 dex, except at low wavenumbers where the small number of modes makes the variance of the measurement large.

Outside the high-resolution box, we resample the particle distribution in the parent simulation in order to provide for the tidal forces which act on the high resolution particles. The resampling procedure bins particles into cells whose size varies approximately in proportion to their distance from the high resolution patch, greatly reducing the total number of tidal particles needed to represent the tidal field. Not all particles in the high-resolution box will end up near the system of interest, so the location on the original grid of selected particles is used to identify an 'amoeba-shaped' region within the cube that is retained at full resolution. Regions exterior to the 'amoeba' are coarse sampled with particles of mass increasing with distance from the region of interest (figure 2.2).

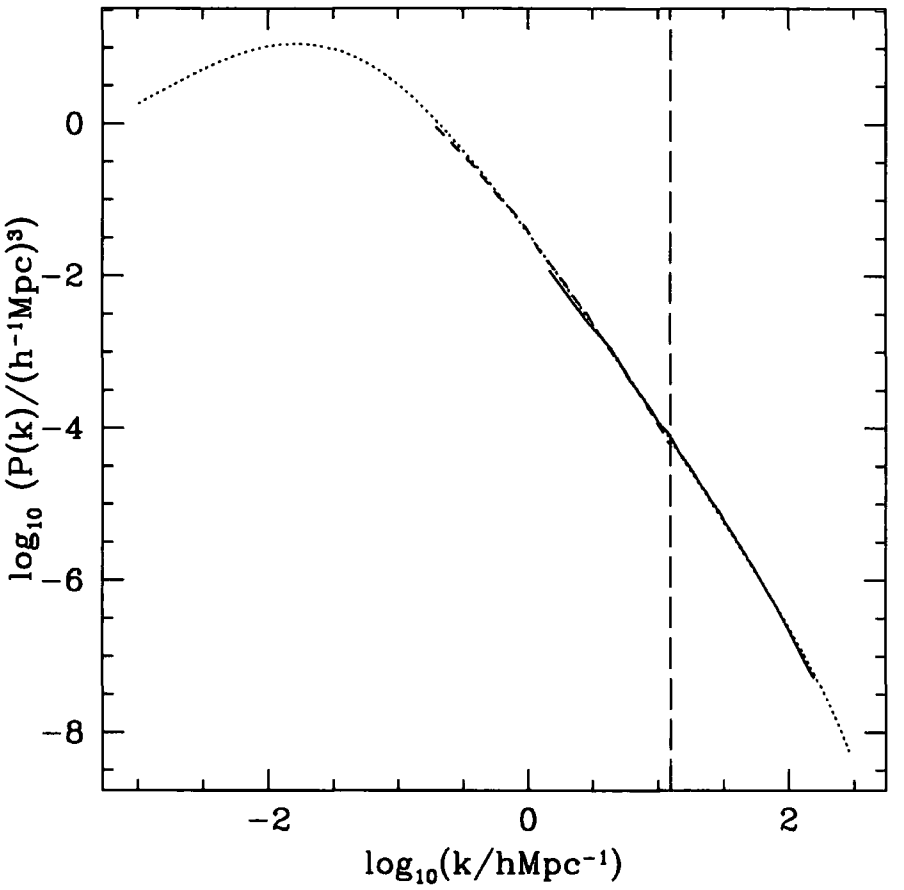

Figure 2.1: **The ΛCDM Power Spectrum at Redshift** $z = 49$. The dotted line shows the theoretical ΛCDM power spectrum at redshift $z = 49$. The short dashed curve shows the measured power spectrum from the initial conditions of the parent simulation ($L_{\rm box} = 32.5\,h^{-1}$ Mpc, $N_{\rm box} = 128^3$). The solid line shows the power spectrum within the high-resolution box selected for resimulation ($L_{\rm sbox} = 5.08\,h^{-1}$ Mpc, $N_{\rm sbox} = 256^3$). The agreement with the theoretical power spectrum is good over nearly three orders of magnitude in wavenumber and seven decades in amplitude. Significant departures are expected for both curves at low k as the number of long-wavelength modes is small. The charge assignment scheme causes a small drop at high-k for both curves. The vertical long dashed line marks the scale in the resimulated initial conditions which corresponds to the transition between the long waves which are present with the same phase and amplitude as the parent simulation and the additional short waves added to improve the resolution. See appendix A.2 for more details of the computation of the power spectrum.

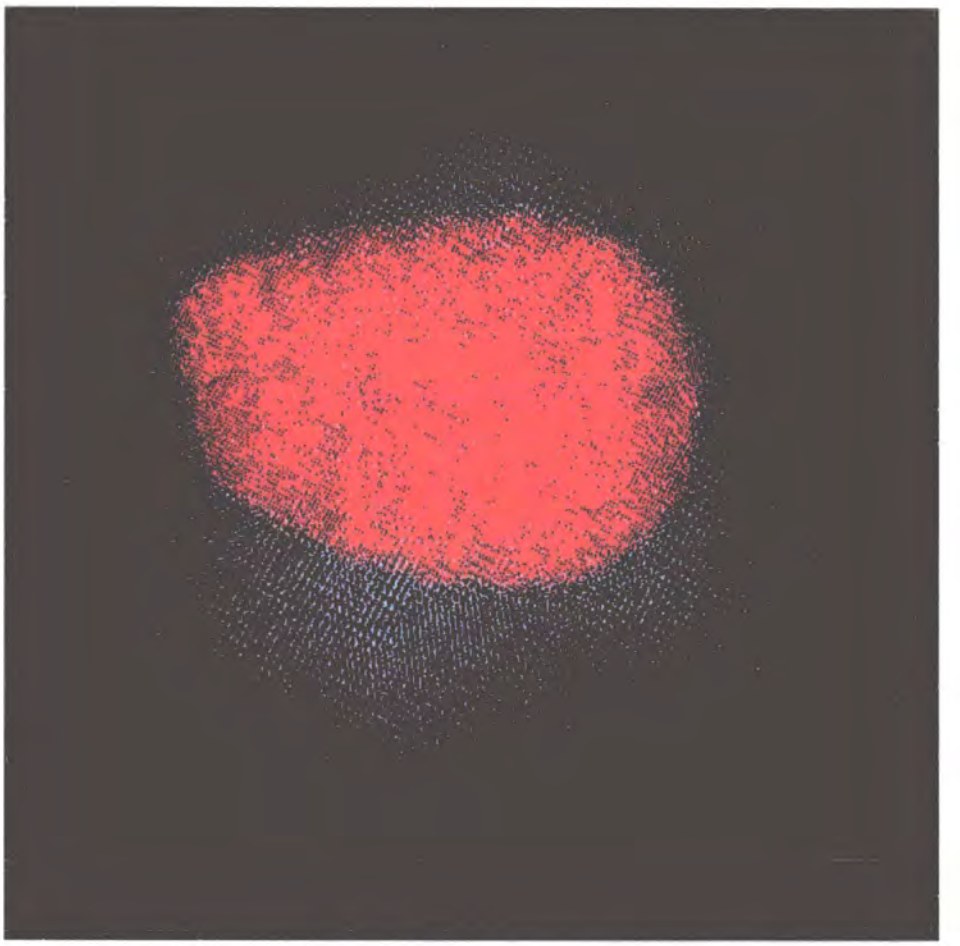

Figure 2.2: **Particle distribution in the initial conditions of our 128^3 runs at $z_i = 49$.** Clearly seen is the 'amoeba'-shaped region containing the highest resolution particles, which is embedded within the $5.08\,h^{-1}$ Mpc high-resolution cube used for the resimulation. Beyond the boundaries of the high-resolution cube lie massive particles that coarsely sample the entire volume of the $32.5\,h^{-1}$ Mpc periodic box.

2.3 The Simulations

The initial conditions file containing the displacement field for $N_{\rm sbox} = 256^3$ particles generated in the way described in § 2.2.2 can be easily rescaled to generate realisations of each system with varying particle number or starting redshift. To modify the starting redshift, we simply rescale the displacements and velocities according to the linear growth factor. To reduce the particle number, we average successively displacements in the high-resolution box over 8 neighbouring cubic cells. We refer to these 'reduced' initial conditions using the total number of particles in the high-resolution box: 256^3, 128^3, 64^3, and 32^3, respectively (Table 2.1).

These realisations may be used to test how numerical parameters affect the equilibrium structure of the dark halo at $z = 0$. Since runs with 32^3 particles are relatively inexpensive, we have used them for a large series of simulations varying systematically all the numerical parameters under scrutiny. This series (which contains several hundred runs) allows us to survey the large available parameter space and to draw preliminary convergence criteria that are then confirmed with a series of runs with 64^3 particles. The 128^3 and 256^3 simulations are too expensive to allow a full convergence study, so fewer of them were carried out, typically using values of the numerical parameters close to convergence. These are used mainly to test the dependence of our results on the total number of particles in the simulations.

2.3.1 The Halo

We concentrate our analysis on a single halo selected from our sample, although similar runs on two other halos confirm the conclusions presented here. The mass accretion history of this system is presented in figure 2.3. The halo accretes half of its present-day mass by $z \approx 0.66$ (expansion factor $a = 0.6$), when it undergoes a major merger. The last significant merger event occurs at $z \approx 0.4$ ($a = 0.71$), when the system accretes the last 20% of its final mass. After this the system remains relatively undisturbed and by $z = 0$ it is close to virial equilibrium. The virial radius, also shown in figure 2.3, changes by less than 7% after $z \approx 0.4$. The mass in the inner regions of the halo is assembled much earlier. Half of it is already in place by $z \approx 5$ ($a \approx 0.17$) and after $z \sim 1$ substantial fluctuations occur only during major mergers. (See the triangles in figure 2.3, which track the mass in the innermost 20 (physical) kpc.)

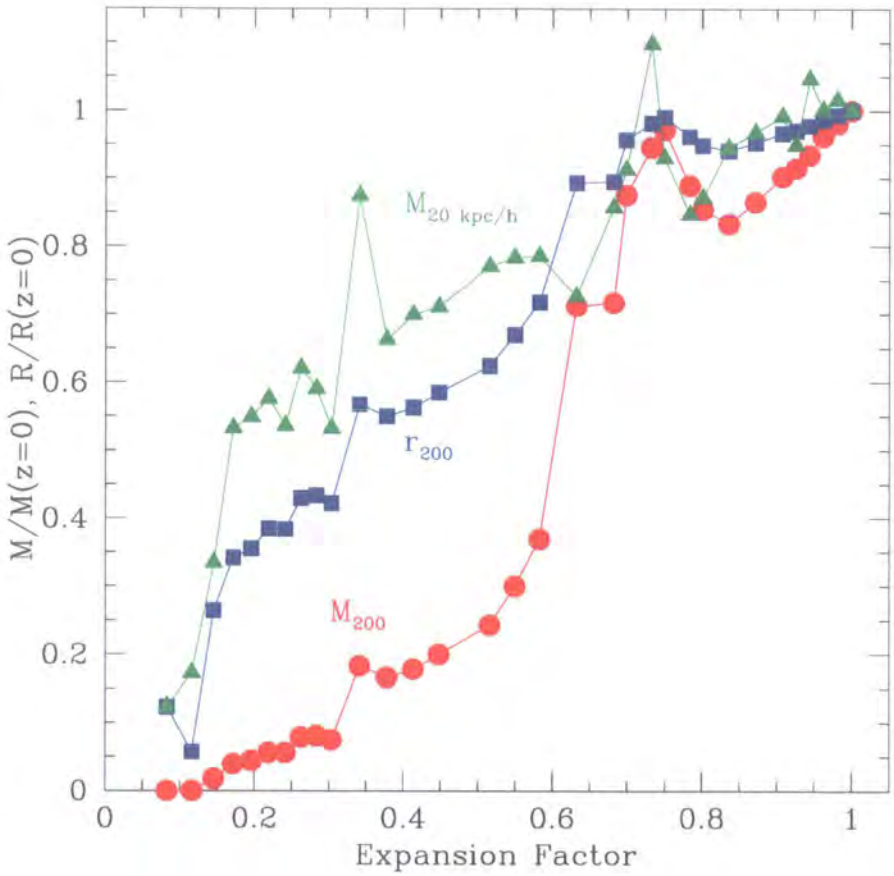

Figure 2.3: **Growth of virial mass and radius as a function of expansion factor.** Evolution of the virial radius of the main progenitor of the system, r_{200}, of the mass contained within that radius, M_{200}, and of the mass within the innermost $20\,h^{-1}$ (physical) kpc. Data are normalised to values at the present day. For the virial radius the ratio of the values in *comoving* units is shown. The system undergoes its last major merger at $z \sim 0.66$, accretes little mass afterwards and is close to virial equilibrium at $z = 0$. The mass within the inner $20\,h^{-1}$ kpc is assembled earlier than the rest, and is only affected seriously during major mergers.

2.3.2 The Analysis

We focus our analysis on the spherically averaged mass profile at $z = 0$. This is measured by sorting particles in distance from the centre and binning them in groups of 100 particles each. The cumulative mass within these bins, $M(r)$, is then used to compute the circular velocity profile of each halo, $V_c(r) = \sqrt{GM(r)/r}$, and the cumulative density profile, $\bar{\rho}(r) = 3\,M(r)/4\pi r^3$, which we shall use in our analysis.

It is important to choose carefully the halo centre, especially since the halos are not spherically symmetric. The centre of each halo is determined using an iterative technique in which the centre of mass of particles within a shrinking sphere is computed recursively until a convergence criterion is met. At each step of the iteration the centre of the sphere is reset to the last computed barycentre and the radius of the sphere is reduced by 2.5%. The iteration is stopped when a specified number of particles (typically either 1000 particles or 1% of the particles within the high-resolution region, whichever is smaller) is reached within the sphere. Halo centres identified with this procedure are quite independent of the parameters chosen to initiate the iteration, provided that the initial sphere is large enough to encompass a large fraction of the system. In a multi-component system, such as a dark halo with substructure, this procedure isolates the densest region within the largest subcomponent. In more regular systems, the centre so obtained is in good agreement with centres obtained by weighting the centre of mass by the local density or gravitational potential of each particle. We have explicitly checked that none of the results presented here are biased by our particular choice of centring procedure.

2.4 The Relationship between Particle Number, Softening and Timestep

The main goal of this study is to identify the conditions under which the structure of simulated halos, in particular their circular velocity profile, is independent of numerical parameters. We start with a brief discussion of the relationship between three of the main parameters: the number of particles, N, the gravitational softening, ϵ, and the timestep, Δt (§ 2.4.1). We proceed then (§ 2.4.2) to verify numerically the scalings expected between these quantities through a series of runs where the timestep for all particles is kept fixed and constant throughout the evolution.

2.4.1 Analytic Estimates

Modelling the formation of dark matter halos with N-body simulations entails a number of compromises dictated by limited computing resources. The choice of particle number, timestep, and gravitational softening may all affect, in principle, the reliability of the structure of simulated halos. We explore here the various limitations imposed by these numerical parameters. The analysis assumes, for simplicity, a steady-state system with circular speed, $V_c(r)$; enclosed mass, $M(r) = r\,V_c(r)^2/G$; enclosed particle number, $N(r)$; and orbital timescale, $t_{\rm circ} = 2\,\pi\,r/V_c$. The specific energy of a typical orbit at radius r is $E(r) \approx v^2 \approx V_c(r)^2$.

N and Collisional Relaxation

When a finite number of particles is used to represent a system, individual particle accelerations will inevitably deviate from the mean field value when particles pass close to each other. Even when orbits are integrated with perfect accuracy, these 'collisions' lead to changes of order unity in energy on the relaxation timescale (e.g. Binney & Tremaine (1987)),

$$\frac{t_{\rm relax}}{t_{\rm circ}} \sim \frac{N(r)}{\ln\left(r/\epsilon\right)}. \tag{2.3}$$

Thus energy changes due to two-body effects after integration time t_0 are given by

$$\frac{\delta E}{E} \sim \left(\frac{t_0}{t_{\rm relax}}\right)^{1/2} \sim \left(\frac{t_0}{t_{\rm circ}(r)}\,\frac{\ln(r/\epsilon)}{N(r)}\right)^{1/2} \tag{2.4}$$

Two-body effects first become important in the inner core of the system. Suppressing these effects is primarily a condition on the number of particles and depends only weakly on ϵ. The timestep, of course, does not appear explicitly in this criterion. We shall return to the limitations imposed by collisional relaxation in § 2.6.4.

Timestep and Integration Accuracy

Accurate integration of the equations of motion of dark matter particles requires a careful choice of the timestep adopted to evolve the system. A second-order accurate integration with timestep Δt induces a relative error in position, velocity, and energy which scales as

$$\frac{\delta r}{r} \propto \frac{\delta v}{v} \propto \frac{\delta E}{E} \propto \left(\frac{v\Delta t}{r}\right)^3 \propto \left(\frac{\Delta t}{t_{\rm circ}}\right)^3. \tag{2.5}$$

Note that this error depends only on the size of Δt, and that it is independent of N and of ϵ, consistent with our assumption of a smooth, collisionless system.

If errors on subsequent timesteps add incoherently, then the error at the end of a total integration time, t_0, is

$$\frac{\delta E}{E} \propto \left(\frac{t_0}{\Delta t}\right)^{1/2} \left(\frac{\Delta t}{t_{\rm circ}}\right)^3 \propto \frac{(t_0 \Delta t^5)^{1/2}}{t_{\rm circ}^3}. \tag{2.6}$$

For a given Δt, then, we expect orbits to be reliably modelled only at radii exceeding a certain value $r_{\rm conv}$ defined by,

$$\frac{t_{\rm circ}(r_{\rm conv})}{t_0} \propto \left(\frac{\Delta t}{t_0}\right)^{5/6}. \tag{2.7}$$

Timestep and Discreteness Effects

Finite-N systems are not smooth, and errors in the integration will also occur during close encounters between particles. The effects of such encounters will be incorrectly treated by the simple integrators used in **PKDGRAV** and **GADGET** whenever the predicted separation at mid-step between a particle and a near neighbour satisfies $|\mathbf{s}| = s < v\Delta t$. The error in velocity at the end of the step induced by this 'unexpected' encounter is, then,

$$\delta \mathbf{v} \sim \Delta t \frac{Gm\mathbf{s}}{(s^2+\epsilon^2)^{3/2}} \tag{2.8}$$

assuming Plummer softening. Such encounters occur with probability

$$p(s)\,ds \sim 4\pi s^2 ds\,\frac{\rho}{m} \sim \frac{s^2}{r^2}\,\frac{ds}{Gm/v^2}. \tag{2.9}$$

where ρ is the mean matter density at the point of encounter, and m is the particle mass. The maximum possible size of this error is

$$(\delta v)_{\rm max} \sim \frac{Gm\Delta t}{\epsilon^2} \tag{2.10}$$

The average velocity change obtained by integrating equation 2.8 over the particle distribution is just that due to the mean density field of the system. However, averaging the specific energy change over the discrete particle distribution gives a positive second-order contribution in excess of that expected along the mean-field orbit. For a single step,

$$\delta E \sim \frac{Gm\Delta t^2}{\epsilon r^2} \tag{2.11}$$

where the simplification arises because the integral is dominated strongly by contributions at $s \sim \epsilon$. After integration time t_0 the total energy change is then,

$$\frac{\delta E}{E} \sim \frac{t_0}{\Delta t} \frac{Gm\Delta t^2}{\epsilon r^2} \sim \frac{1}{N(r)} \frac{r}{\epsilon} \frac{t_0 \Delta t}{t_{\rm circ}^2} \tag{2.12}$$

For a given Δt, then, we expect orbits to be reliably modelled at radii larger than a certain $r_{\rm conv}$ defined by the following condition,

$$\frac{t_{\rm circ}(r_{\rm conv})}{t_0} \approx \left(\frac{\Delta t}{t_0}\right)^{1/2} \frac{(Gm/\epsilon)^{1/2}}{V_c(r_{\rm conv}).} \tag{2.13}$$

Since V_c does not change dramatically with radius in CDM halos, we see by comparing equation 2.7 with equation 2.13 that, in the presence of discreteness effects, the number of timesteps required for convergence increases as ϵ^{-1}. Economy reasons thus dictate the use of large softenings to minimise the number of timesteps. On the other hand, large softenings compromise the spatial resolution of the simulations. These competing effects suggest the existence of an 'optimal' softening choice, $\epsilon_{\rm opt}$, which maximises resolution whilst at the same time avoiding discreteness effects and thus minimising the number of timesteps required. We turn our attention to the softening next.

Softening and Discreteness Effects

When accelerations are softened, the *maximum* stochastic acceleration that can be caused by close approach to an individual particle is roughly $a_{m\epsilon} = Gm/\epsilon^2$, where m denotes the particle mass. It is useful to compare this with the *minimum* mean field acceleration, which occurs at the outer (virial) radius of the system, $a_{\rm min} \approx GM_{200}/r_{200}^2$. The condition $a_{m\epsilon} \lesssim a_{\rm min}$ sets a lower limit to the softening needed to prevent strong discreteness effects,

$$\epsilon > \epsilon_{\rm acc} \approx \frac{r_{200}}{\sqrt{N_{200}}}, \tag{2.14}$$

where $N_{200} = M_{200}/m$ is the total number of particles within r_{200}. When this condition is satisfied, discreteness causes only small changes in particle accelerations, and so does not significantly affect the timestepping in integration schemes with an acceleration-based timestep criterion.

Note that this condition is typically more restrictive than the usual requirement that large-angle deflections be prevented during two-body encounters. The latter is given by $\epsilon > \epsilon_{2b} = Gm/\sigma^2$, where σ is the characteristic velocity dispersion of the system (White (1979)). Since $\sigma^2 \approx GM_{200}/2r_{200} = Gm N_{200}/2r_{200}$, then this condition requires that

forces be softened on scales smaller than $\epsilon_{2b} \approx 2\,r_{200}/N_{200}$, which is usually smaller than $\epsilon_{\rm acc}$.

We shall determine the relationship between $\epsilon_{\rm acc}$ and the 'optimal softening' $\epsilon_{\rm opt}$ referred to in § 2.4.1 empirically in § 2.4.2.

2.4.2 Runs with Constant Timestep

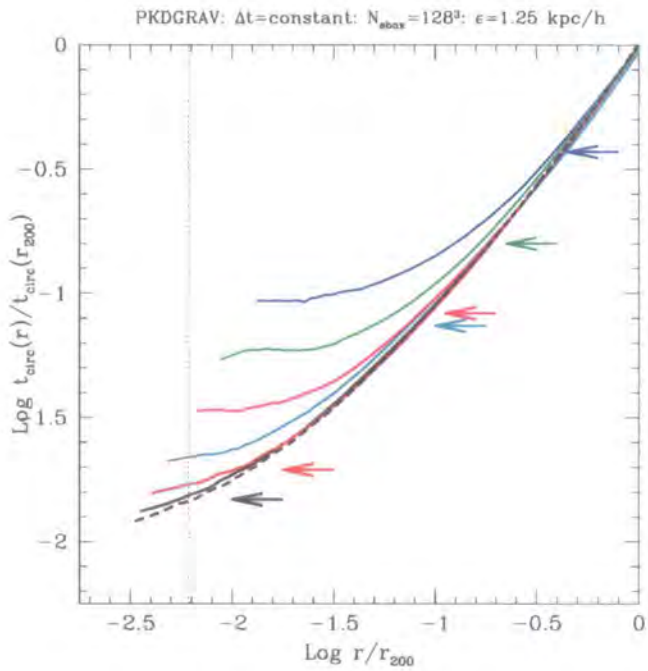

Figure 2.4: **Circular orbit timescale as a function of radius for a series of runs with constant timestep.** All runs have 128^3 particles within the high-resolution box, $\epsilon = 1.25\,h^{-1}$ kpc (shown with a dotted vertical line), and have been run with PKDGRAV. The total number of timesteps used in each run increases from the top down, from $N_{\Delta t} = 100$ to $N_{\Delta t} = 6400$ for the dashed curve at the bottom. From top to bottom, arrows mark the smallest radius where convergence, relative to the smallest-timestep run, is achieved in each case.

In order to validate the scalings derived in the previous subsection and to determine empirically the optimum values of the softening and timestep we have carried out a series of convergence tests where the timestep has been kept constant and is shared by all particles. Disabling the multi-timestepping capabilities of the codes allows us to concentrate on the role of the timestep size, rather than on the virtues or shortcomings of scaling it in various ways for individual particles.

The structure of the dark matter halo chosen for our study at $z = 0$ is illustrated in Figure 2.4, where we show the circular orbit timescale, $t_{\rm circ}(r) = 2\pi r/V_c(r)$, as a function of radius. Timescales are measured in units of $t_{\rm circ}(r_{200}) = 0.2\,\pi\,H_0^{-1}$, which is of the order of the age of the universe, t_0. Radii are measured in units of the virial radius, $r_{200} \approx 205\,h^{-1}$ kpc. The gravitational softening, shown by a vertical dotted line, was kept constant in these runs,which had 128^3 high-resolution particles ($\sim 4 \times 10^5$ within r_{200}) and were run with **PKDGRAV**. The innermost point plotted in each curve corresponds to the radius that contains 100 particles. From top to bottom, the curves in Figure 2.4 illustrate how the mass profile of the simulated halo changes as the total number of timesteps increases, by successive factors of 2, from $N_{\Delta t} = 100$ (top curve) to $N_{\Delta t} = 6400$ (bottom dashed curve).

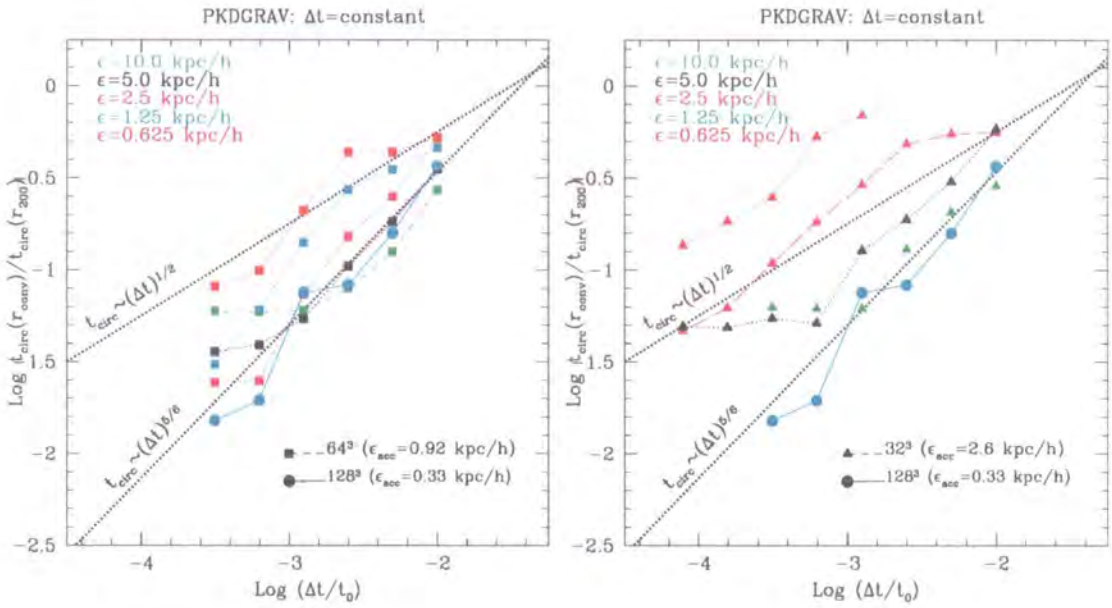

Figure 2.5: **Circular orbit timescale at the smallest 'converged' radius as a function of the timestep** for **PKDGRAV** runs, as illustrated by arrows in figure 2.4. Left panel shows the results for $N_{\rm sbox} = 64^3$, right panel for $N_{\rm sbox} = 32^3$. In both panels the results corresponding to $N_{\rm sbox} = 128^3$ are shown with filled circles. As the timestep decreases, radii where the orbital timescales are shorter become well resolved. This 'saturates' when the radius becomes comparable to the softening and flattens the curves horizontally in some cases. Note also that as the softening is reduced the number of timesteps required for convergence increases substantially. Refer to text for a thorough discussion.

The halo becomes more centrally concentrated as $N_{\Delta t}$ increases, and approaches a 'converged' structure for $N_{\Delta t} \gtrsim 3200$. Runs with fewer timesteps than this still converge to the right mass profile but at increasingly larger radii. It is interesting to explore how the radius where convergence is achieved, $r_{\rm conv}$, depends on the number of timesteps. We find $r_{\rm conv}$ by identifying the radius at which systematic departures greater than 10% in the circular timescale profile first become noticeable, gauged against the run with the largest number of timesteps. This is easily read off the profiles presented in figure 2.4. Arrows in this figure indicate $t_{\rm circ}(r_{\rm conv})$ for each choice of $N_{\Delta t}$.

Filled circles in figure 2.5 show the converged timescales thus determined as a function of the size of the timestep. Converged circular times follow closely the $\Delta t^{5/6}$ dependence expected from equation 2.7, suggesting that the choice of softening in this series is such that discreteness effects are negligible. This is perhaps not surprising, as $\epsilon = 1.25$ kpc/h is about 4 times larger than the lower limit estimated in equation 2.14, $\epsilon_{\rm acc} = r_{200}/\sqrt{N_{200}} = 0.32$ kpc/h (for $N_{\rm sbox} = 128^3$).

Solid squares in figure 2.5 (left panel) correspond to the same exercise carried out for several choices of the softening when the number of high-resolution particles is reduced to 64^3. For the same softening, $\epsilon = 1.25$ kpc/h, achieving convergence with 64^3 particles requires significantly smaller timesteps than with 128^3, as expected since discreteness effects become more important as the number of particles is reduced. It is also clear from figure 2.5 that the dependence of $t_{\rm circ}(r_{\rm conv})$ on Δt changes as ϵ decreases, shifting gradually from $\Delta t^{5/6}$ to $\Delta t^{1/2}$. This transition is precisely what is expected from the analytic estimates in § 2.4.1 (see equations 2.7 and 2.13).

There is further supporting evidence in figure 2.5 for the validity of the analytic estimates. Consider for example the right panel, where we present the results of runs with 32^3 high-resolution particles. The trends are similar to those in the left panel, but the transition to the discreteness-dominated regime ($t_{\rm circ}(r_{\rm conv}) \propto \Delta t^{1/2}$) occurs for even larger values of ϵ.

It is possible to use these results to estimate the softening above which discreteness effects become unimportant for the various series. From figure 2.5, we find that, for 64^3 particles, this 'optimal' softening is somewhere between 2.5 and 5 kpc/h, while for 32^3 particles it is of order ~ 10 kpc/h. Our 128^3 runs suggest that $\epsilon_{\rm opt} \approx 1.25\,h^{-1}$ kpc for this series. The optimal softening appears thus to scale with N just as suggested by our

discussion of equation 2.14. The simple empirical rule,

$$\epsilon_{\rm opt} \approx 4\,\epsilon_{\rm acc} = \frac{4\,r_{200}}{\sqrt{N_{200}}}, \tag{2.15}$$

appears to describe the numerical results well.

The reason why $\epsilon_{\rm opt}$ is about a factor of 4 larger than $\epsilon_{\rm acc}$ is likely related to the fact that, when softening is chosen to optimise results for halos at $z = 0$, the choice is not optimal for their progenitors at earlier times. Indeed, $r_{200}(M,z) \propto (\Omega(z)/\Omega_0)^{1/3} M^{1/3}(1+z)^{-1}$, which implies that, for softenings fixed in comoving coordinates, $\epsilon/\epsilon_{\rm opt}(N,z) \propto N(z)^{1/6}$. Small-$N$ progenitors thus have smaller softenings than optimal and may be subject to discreteness effects. The dependence on the number of particles is weak, however, and it is possible that the factor of 4 in equation 2.15 may act as a 'safety factor' to ensure that discreteness effects are negligible at all times.

A number of other predictions from the analytic scalings presented in § 2.4.1 are also confirmed by the data in figure 2.5. For example, when discreteness effects dominate, converged timescales are expected to scale as $\epsilon^{-1/2}$ (equation 2.13). This is in good agreement with the results of the 32^3-particle runs; for given timestep, $t_{\rm circ}(r_{\rm conv})$ is seen to increase by roughly a factor of 2 when ϵ decreases by a factor of 4, from $\epsilon = 2.5$ to 0.625 kpc/h.

Finally, the analytic estimates suggest that the timestep choice should be independent of N and ϵ when discreteness effects are unimportant. This is also reproduced in the simulation series: for $\epsilon \gtrsim \epsilon_{\rm opt}$, all runs, independent of N, lie along the *same* dotted line that delineates the

$$t_{\rm circ}(r_{\rm conv}) \approx 15 \left(\frac{\Delta t}{t_0}\right)^{5/6} t_{\rm circ}(r_{200}) \tag{2.16}$$

scaling. This confirms that the size of the timestep is the most important variable when discreteness effects are unimportant; roughly 400, 7000, and 110000 timesteps are needed to resolve regions where $t_{\rm circ}$ is, respectively, $\approx$ 10%, 1% and 0.1% of the orbital timescale at the virial radius.

2.4.3 Convergence and integrator schemes

So far these conclusions are based on runs carried out with PKDGRAV. Are they general or do they depend on the particular choice of integrator scheme? We have explored this by performing a similar series of constant-timestep runs with GADGET, which uses a different integrator (§ 2.2.1). There is another difference between the GADGET series and the one carried out with PKDGRAV: GADGET integrates the equations of motion using the expansion factor, a, as the time variable. Constant-timestep runs carried out with GADGET were therefore evolved using a fixed expansion-factor step, Δa. Comparing GADGET and PKDGRAV runs with the same *total* number of steps, GADGET takes shorter time steps than PKDGRAV at high-redshift, longer ones at moderate z and similar ones at $z \approx 0$.

We compare the results of the two series in figure 2.6, where we plot, at $z = 0$, the radii containing various mass fractions of the halo as a function of the number of timesteps, $N_{\Delta t}$. The three series shown correspond to runs with 128^3 high-resolution particles; two were run with GADGET and one with PKDGRAV. The choice of softening in each case is indicated in the figure labels. The four radii shown contain, from bottom to top, 0.025%, 0.2%, 1.6%, and 12.8% of the mass within r_{200}, respectively.

Convergence is approached gradually and monotonically in PKDGRAV runs (solid circles in figures 2.5 and 2.6). For $N_{\Delta t} \sim 3200$ convergence is achieved at all radii containing more than $\sim$ 100 particles; fewer timesteps are needed to converge at larger radii, as discussed in the previous subsection.

Convergence also occurs gradually, but *not* monotonically, in the case of GADGET (solid squares and triangles in figure 2.6). For the same number of steps, GADGET results typically in mass profiles that, near the centre, are more concentrated than PKDGRAV's, as shown by the systematically smaller radii that contain the same mass fraction. The effect is particularly noticeable for $N_{\Delta t} \approx 800$, when the central density profile is actually *steeper* than the 'converged' result achieved for $N_{\Delta t} \gtrsim 3200$.

Further runs with different softenings and numbers of particles suggest that the presence of these 'cuspy cores' in systems evolved with poor time resolution is inherent to Δa =constant GADGET runs, and not just a fluke. On the other hand, the artificial cusps only occur in regions well inside the convergence criterion derived from the PKDGRAV series. Outside the convergence radius delineated by equation 2.16 both GADGET and PKDGRAV

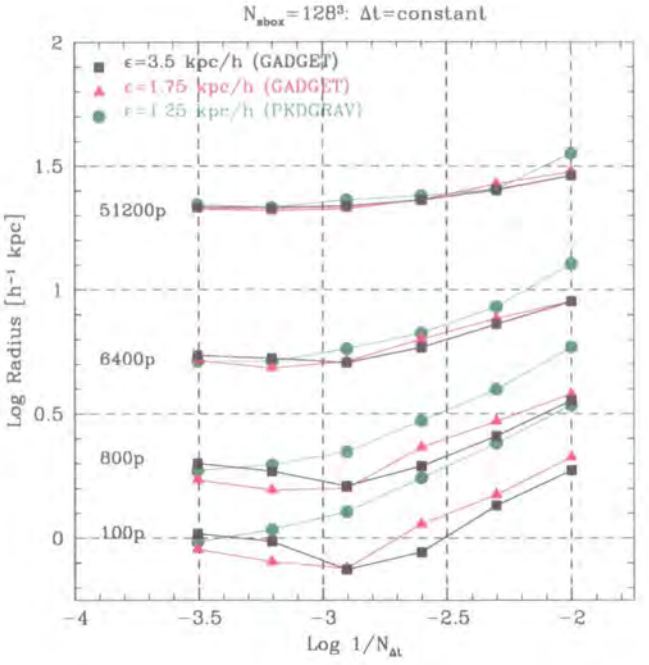

Figure 2.6: **Radii enclosing various numbers of particles as a function of the total number of timesteps.** Results shown correspond to runs with 128^3 particles in the high-resolution box and were run with PKDGRAV and GADGET, as labelled. PKDGRAV runs approach convergence progressively and monotonically. On the other hand with poor time resolution GADGET can produce artificially dense 'cuspy' cores, most noticeable when $N_{\Delta t} = 800$. These 'cuspy cores' seem to be inherent to the integrator and stepping schemes chosen in GADGET. Note, however, that both codes need approximately the same number of timesteps for full convergence.

results appear safe: one may conclude that GADGET and PKDGRAV require approximately the same number of timesteps to resolve the whole system.

To summarise, the central densities of systems evolved with poor time resolution may be over- or under-estimated, depending on the integrator scheme adopted. Such sensitivity to the integrator scheme emphasises the vulnerability of the central regions to numerical artifact and the need for detailed convergence studies such as the one presented here before firm conclusions can be reached regarding the inner density profiles of CDM halos.

2.4.4 Summary

The agreement presented above between numerical results and analytic estimates gives us confidence that it is possible to achieve convergence in the mass profiles of simulated dark halos down to scales which contain as few as 100 particles or where the gravitational softening starts to dominate. A few prescriptions for an efficient and accurate integration seem clear:

- choose gravitational softenings so that $\epsilon \gtrsim \epsilon_{\rm opt} = 4\,r_{200}/\sqrt{N_{200}}$ (equation 2.15) to minimise the number of timesteps needed, and
- regard as converged only regions where circular orbit timescales exceed $\approx 15\,(\Delta t/t_0)^{5/6}$ in units of $t_{\rm circ}(r_{200})$ (equation 2.16).

One problem with these prescriptions is that, in a large cosmological N-body simulation, where systems of different mass and size form simultaneously, it is possible to choose optimal values of the numerical parameters only for systems of roughly the same mass. Also, resolving the inner density profiles, where orbital timescales can reach a small fraction of the age of the universe, may prove impractical with a constant timestep, as the number of timesteps is then dictated by the densest region of the system, which may contain only a small fraction of the total number of particles. It is therefore important to learn how the structure of simulated dark halos is affected when non-optimal choices of numerical parameters are made as well as when multi-timestepping integration techniques are adopted. We turn our attention to these topics in the following sections.

2.5 Adaptive Multistepping Techniques

In order to improve efficiency, many cosmological N-body codes use individual timesteps that can vary with time and from particle to particle. This allows the time integration scheme to adapt spatially so as to achieve high accuracy across the whole body of non-linear structures. The two codes used in this study, `PKDGRAV` and `GADGET`, can use individual timesteps, although, as discussed in § 2.2.1, they differ significantly in the choice of integration scheme.

Evaluating the efficiency gain is not straightforward, since computing resources in most parallel environments do not scale in simple ways with the total number of particles and

of timesteps, and the latter is ill-defined when individual adaptive timesteps are adopted. We shall assume, for simplicity, that the bulk of the computational work is invested in computing individual accelerations ('forces'), and shall deem efficient timestepping choices that achieve 'full convergence'[§] whilst minimising the total number of force computations, $N_{\rm ftot}$.

For the integrators used in **PKDGRAV** and **GADGET** forces are computed once every time the position (or velocity) of a particle is advanced, so that $\bar{N}_{\Delta t} = N_{\rm ftot}/N$ can be thought of as the average number of timesteps in a run. $N_{\rm ftot}$ is an imperfect measure of the total computational work, since it neglects the overhead that stems from tree construction, neighbour searching (if required by the timestepping choice), synchronisation, and communication between nodes, but is nonetheless a useful guide for assessing the efficiency of various timestepping techniques.

2.5.1 Comparison of Timestep Criteria

GADGET allows for five different ways of setting the timestep, and we have explored extensively four of them. Our main results are illustrated in figure 2.7, which is analogous to figure 2.6 but for runs with 32^3 high-resolution particles. The radii shown enclose 1.6%, 3.2%, 6.5%, 12.9%, and 25.8% of the mass within the virial radius, respectively, and are shown as a function of the timestep parameter, η (§ 2.2.1). We adopt for this series a softening of $7\,h^{-1}$ kpc, close to the 'optimal' value for this number of particles (see table 2.1). For convenience, we have scaled η by a factor f (listed in the labels of figure 2.7) chosen so that, for given $f\,\eta$, all runs in this figure incur approximately the same total number of force computations. CPU consumption is lowest for **EpsAcc** and **VelAcc**, $\sim 25\%$ higher for **SgAcc**, and highest (by $\sim 60\%$) for **RhoSgAcc** because the neighbour search required by the latter two criteria imposes a significant overhead.

The main conclusion to be drawn from figure 2.7 is that all timestepping choices appear to converge for approximately the same value of $f\,\eta \lesssim 0.2$ or, equivalently, for the same $N_{\rm ftot}$. For $f\eta \approx 0.2$, $N_{\rm ftot} \approx 2.2 \times 10^7$, which implies that on average a minimum of ~ 650 timesteps is required for full convergence. This is comparable to the number of *constant* timesteps needed for full convergence (see figure 2.5).

For $f\,\eta > 0.2$, deviations from convergence are obvious in all cases. Deviations are monotonic in the case of **PKDGRAV** and **RhoSgAcc** runs; densities at all radii increase

[§] We use the term 'full convergence' when it extends down to the scale containing as few as 100 particles or the gravitational softening, whichever is larger.

Table 2.1: **Properties of the Simulated Halo at $z = 0$.** We show (1) the virial radius, r_{200}, in units of h^{-1} kpc, (2) the circular velocity at r_{200}, V_{200}, in units of km/s, (3) the virial mass, M_{200}, in units of $10^{10}h^{-1}\mathrm{M}_{\odot}$, (4) the effective number of particles in the high resolution box, N_{sbox}, (5) the number of particles interior to r_{200}, N_{200}, (6) the characteristic softening length, ϵ_{acc}, and (7) the 'optimal' softening length, ϵ_{opt}, both of which are expressed in units of h^{-1} kpc.

	r_{200} $[h^{-1}$ kpc$]$	V_{200} [km s^{-1}]	M_{200} $[10^{10}$ M$_{\odot}]$	N_{sbox}	N_{200}	ϵ_{acc} $[h^{-1}$ kpc$]$	ϵ_{opt} $[h^{-1}$ kpc$]$
Halo 1	205	205	200	256^3	3.17×10^6	0.12	0.46
				128^3	3.97×10^5	0.33	1.30
				64^3	4.96×10^4	0.92	3.68
				32^3	6.20×10^3	2.60	10.4

gradually as the timestep decreases and converge for $f\,\eta \lesssim 0.2$. On the other hand, the behaviour of the inner mass profile in the case of other criteria is clearly non-monotonic: the central shells dip well below the converged value before bouncing back to convergence as $f\,\eta$ approaches 0.2. This is reminiscent of the artificially cuspy cores discussed in § 2.4.3, but it seems to affect radii well beyond the softening.

Note that these artificial 'cuspy cores' affect runs with GADGET's EpsAcc criterion as well, which is formally the same as used in PKDGRAV. The monotonic approach to convergence seen in PKDGRAV runs thus suggest that the presence of 'cuspy cores' in runs with poor time resolution is an artifact related to GADGET's integrator scheme rather than to the timestepping choice. Artificially cuspy cores are an undesirable feature in large cosmological simulations, because dense cores may survive the hierarchical assembly of structure and lead to artifacts in the density profiles of systems formed by the merger of affected progenitors. This kind of subtle artifact again demonstrates that careful convergence studies of the kind presented here are needed to guarantee that the inner mass profiles of dark matter halos can be robustly measured in N-body simulations.

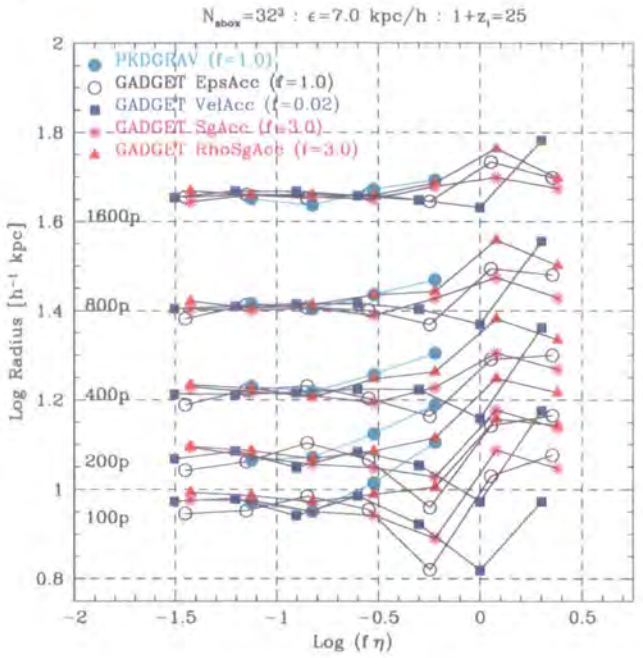

Figure 2.7: **Radii enclosing various numbers of particles as a function of the timestepping parameter, η.** See figure 2.6. The number of timesteps decreases linearly with η (§ 2.2). The values of η shown in the figure have been scaled by an arbitrary factor, f, so that for given $f\,\eta$ all runs have similar number of total force computations, $N_{\rm ftot}$. Values of f are given in the figure labels.

2.5.2 The Dependence on Softening

According to the analysis presented in § 2.4.1, the timestep required for convergence is independent of the softening when discreteness effects are unimportant (i.e., when $\epsilon \gtrsim \epsilon_{\rm opt}$, see equation 2.7) but should become increasingly short as ϵ decreases below the optimal value (see equation 2.13). Since optimal softenings can only be adopted for systems of roughly the same mass in a large cosmological simulation, optimising the choice for massive clumps leads to less-than-optimal softenings in low-mass halos. For such systems, keeping the values of η found to give convergence in the last subsection (i.e. $f\,\eta \approx 0.2$ with the values of f given in figure 2.7) may not guarantee convergence unless the timestepping criterion scales appropriately with softening. For fixed η, timesteps decrease as $\epsilon^{1/2}$ in `PKDGRAV` and for the EpsAcc criterion of `GADGET`, but are unchanged as the softening decreases for the other `GADGET` criteria.

The effects of this are illustrated in figure 2.8, which shows the result of adopting $f\,\eta \sim 0.2$ whilst gradually reducing the softening to values almost two orders of magnitude

below optimal. For **RhoSgAcc**[¶] (solid triangles), $f\eta = 0.15$ seems appropriate for ϵ close to or slightly smaller than $\epsilon_{\rm opt} \approx 10\,h^{-1}$ kpc, but an artificially low density core clearly develops for softenings well below the optimal value. This behaviour is not seen in the case of **EpsAcc**, where convergence appears firm even for values of ϵ approaching the large angle-deflection limit, ϵ_{2b}.

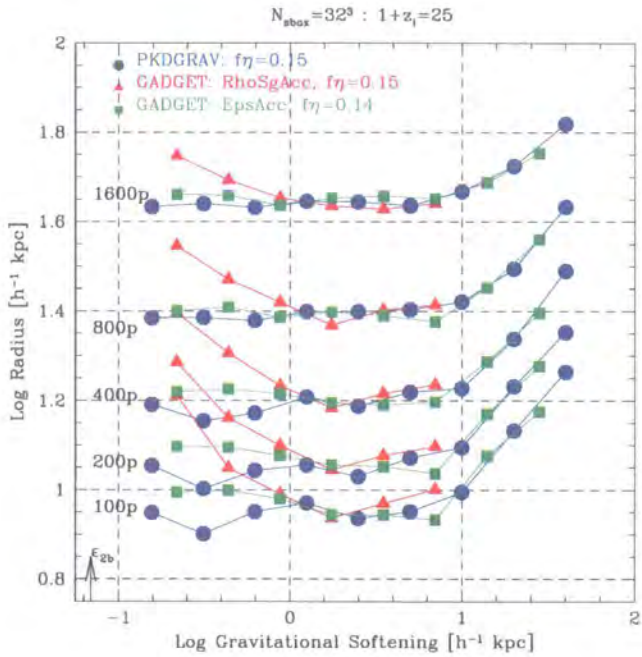

Figure 2.8: **Radii enclosing various mass fractions measured at $z = 0$ in our 32^3 simulations as a function of the gravitational softening scale length, ϵ.** Pairwise interactions become Newtonian at distances exceeding $2\,\epsilon$. The virial radius of the halo is $r_{200} = 205\,h^{-1}$ kpc and the total number of particles within this radius is $N(r_{200}) \approx 6200$. Note that for **PKDGRAV** and **EpsAcc** runs the mass profile is independent of softening for $\epsilon < 6\,h^{-1}$ kpc, provided that the softening remains larger than ϵ_{2b}, the minimum needed to prevent large-angle deflections during particle collisions (§ 2.4.1). For **RhoSgAcc**, the choice $f\eta = 0.15$ leads to convergence for $\epsilon > 1\,h^{-1}$ kpc, but results in large deviations for smaller softenings. See § 2.5.2 for details.

We emphasise that this does *not* signal a failure of the **RhoSgAcc** criterion; rather, it implies that the timesteps chosen with $f\eta \sim 0.2$ are not short enough to achieve convergence when $\epsilon \ll \epsilon_{\rm opt}$.

Indeed, choosing **RhoSgAcc** and $f\eta \approx 0.2(\epsilon/\epsilon_{opt})^{1/2}$ for small softenings eliminates the artificially low density core shown in figure 2.8 at a cost in total number of timesteps,

[¶]For simplicity, we discuss here only **RhoSgAcc**; similar results apply to **VelAcc**.

$N_{\rm ftot}/N$, not very different from that required by **EpsAcc**. This demonstrates clearly the need to take smaller timesteps when $\epsilon \ll \epsilon_{\rm opt}$.

How should timesteps scale with ϵ? Equation 2.13 suggests a linear dependence when discreteness effects dominate, $\Delta t \propto \epsilon$, although the firm convergence seen for **EpsAcc** in figure 2.8 indicate that a gentler dependence, $\Delta t \propto \epsilon^{1/2}$, may actually suffice. This is because the actual individual timesteps in this criterion are determined by the ratio, $(\epsilon/a_i)^{1/2}$, and accelerations are high during close encounters when softenings are small. As a result, the 'effective' size of **EpsAcc** timesteps scales roughly linearly with softening when $\epsilon \ll \epsilon_{\rm opt}$. We have verified this by comparing the 'maximum' number of timesteps, defined by the total number of timesteps taken by a hypothetical particle which, at all times, has the minimum timestep of all particles in the system, with the minimum number of *constant* timesteps required for convergence (see § 2.4.2). The agreement is quite good.

2.5.3 Adaptive versus Constant Timestep

Finally, we investigate the computational gain/loss associated with adopting a constant or adaptive time stepping technique when a criterion such as **EpsAcc** is selected. Again, we shall assume that the bulk of the computational work is invested in computing individual accelerations, although this measure neglects the cost of tree construction. Ordinarily, tree-making contributes a small fraction of the CPU budget, but this is not necessarily the case in multiple timestepping schemes when a full tree structure is recalculated every time particles in the smallest time bin are advanced. This is the case in the version of **PKDGRAV** that we tested. **GADGET**, on the other hand, recomputes trees only after a certain number of interactions have been computed (§ 2.2.1), so the comparison is not straightforward.

We have chosen for the comparison maximally-converged **PKDGRAV** runs, i.e., those requiring the minimum number of timesteps for full convergence. The main conclusion may be gleaned from table 2.2, where we list the total number of force computations, $N_{\rm ftot}$, for runs with 32^3 high-resolution particles[‖] and three different choices for the gravitational softening; $\epsilon = 10\,h^{-1}$ kpc ($\approx \epsilon_{\rm opt}$), as well as $\epsilon = 2.5$ and $0.625\,h^{-1}$ kpc. The number of constant timesteps needed for full convergence depends sensitively on softening, as discussed in § 2.4; $N_{\Delta t}$ climbs from 800 to 25600 as ϵ decreases from 10 to $0.625\,h^{-1}$ kpc.

[‖]For ease of comparison, we have not reduced in this series the number of high-resolution particles through the 'amoeba' procedure described in the appendix A.2 for runs listed in this table 2.2.

The total number of force calculations is directly proportional to $N_{\Delta t}$, and increases from 2.6×10^7 to 8.4×10^8.

Table 2.2: **Properties of maximally-converged runs (PKDGRAV).** See text for details.

$N_{\rm sbox}$	ϵ $[h^{-1}$ kpc]	$N_{\Delta t}$ (constant)	$N_{\rm ftot}$ (constant)	$\bar{N}_{\Delta t}$ (multiple)	$N_{\rm ftot}$ (multiple)
32^3	10.0	800	2.6×10^7	640	2.1×10^7
	2.5	1600	5.2×10^7	1342	4.4×10^7
	0.625	25600	8.4×10^8	2777	9.1×10^7
64^3	2.5	3200	8.4×10^8	1754	4.6×10^8
128^3	1.25	3200	6.7×10^9	2956	6.2×10^9

Table 2.2 shows that, when adaptive multiple timesteps are allowed, the total number of force calculations needed is comparable when $\epsilon \sim \epsilon_{\rm opt}$, but far fewer when the softening is well below the 'optimal' value. This demonstrates that the small timesteps required when the softening is well below the 'optimal' value are only needed briefly by a small subset of particles undergoing close encounters. Adaptive multi-stepping schemes vastly outperform the fixed timestep approach when $\epsilon \ll \epsilon_{\rm opt}$.

2.5.4 Summary

To summarise, we find that all timestepping criteria we have considered can deliver convergence at comparable cost. However, the **EpsAcc** criterion is the one that suffers least from overheads related to computing values for individual timesteps, and thus appears to be the most efficient of the criteria explored in this study. We emphasise, however, that this choice is primarily empirical; further investigation may very well lead to better and more efficient alternatives than any of the ones considered here.

Further, for softenings close to the 'optimal' value, the computational gain that results from adopting multi-stepping schemes is rather modest, especially considering that the implementation of multi-stepping incurs a non-negligible cost in terms of memory usage and bookkeeping.

Smaller softenings increase the importance of discreteness effects and lead to integrations with very small timesteps dictated by occasional encounters. Multi-stepping

schemes are strongly favoured under these circumstances.

2.6 The Role of other Numerical Parameters

Proper convergence requires, of course, that appropriate choices be made for *all* relevant parameters. We now turn to the analysis of the separate role of other numerical parameters. Unless explicitly stated, we will undertake the analysis of each parameter using only runs for which all other parameters take 'converged' values. This can only be done after a large parameter space search since the effects of combinations of some parameters may be subtle. For example, a timestep that is adequate for some gravitational softening may be inadequate when the softening is substantially modified. Because of this restriction, the results in the following subsections contain, for clarity, only a small fraction of all runs performed.

2.6.1 The Gravitational Softening

Large cosmological simulations generally use a single particle mass and thus resolve systems of different mass with different numbers of particles. This implies that it is possible to choose 'optimal' values of the softening only for a small range of halo masses, since $\epsilon_{\rm opt} \propto r_{200}/N_{200}^{1/2} \propto N_{200}^{-1/6}$. This may not be too restrictive for the resimulations we discuss here, since they focus on one system at a time, but it does affect significantly large cosmological simulations. If, for example, an optimal softening choice is made for the most massive system expected to form at, say, $z = 0$, it will be smaller than the optimal value for less massive systems present at the same time (see equation 2.15). How are their mass profiles affected and what regions in such systems may be considered converged?

To address this question, we have undertaken a large series of simulations where the softening, ϵ, was varied systematically while choosing 'converged' values of all other parameters. We have explicitly checked that, for example, doubling or halving the number of timesteps (or the initial redshift) has no appreciable effect and that, for given number of particles, the results discussed in this subsection depend only on ϵ.

We show the results of this series in figure 2.8, where radii enclosing various mass fractions are shown as a function of ϵ in simulations with 32^3 high-resolution particles. Since $r_{200} \approx 205\,h^{-1}$ kpc, the radii shown in figure 2.8 probe a large fraction of the halo's radial extent, between 4% and 22% of the virial radius. For this system, $\epsilon_{2b} = 0.066\,h^{-1}$

kpc $\approx 3.2 \times 10^{-4}\, r_{200}$ and $\epsilon_{\rm opt} \sim 10\, h^{-1}$ kpc $\approx 4.9 \times 10^{-2}\, r_{200}$.

As figure 2.8 shows, the mass profiles obtained with the two codes agree to better than 20% (i.e., to better than 10% in circular velocity) even for radii containing as few as 100 particles. Full convergence is achieved for a wide range of softening scales, provided that $\epsilon_{2b} < \epsilon \lesssim 6h^{-1}$ kpc. The mass profiles are essentially unchanged even as the softening is varied by almost two orders of magnitude.

A second important point to note in figure 2.8 is that for $\epsilon \sim 12\, h^{-1}$ kpc (only slightly larger than $\epsilon_{\rm opt}$) the profile deviates from the converged one even as far out as $60\, h^{-1}$ kpc; i.e., more than 5 times the softening length. This contrasts with the results for $\epsilon \sim 6\, h^{-1}$ kpc, where the mass profile appears to have converged down to almost one softening length scale. Clearly, assuming that mass profiles are affected out to a certain multiple of the softening length is an oversimplification that is *not* supported by these results.

What determines the smallest converged radius for a given softening length scale? Since softenings introduce a characteristic acceleration on small scales, it is instructive to consider the mean acceleration that particles experience as a function of the distance from the centre of the system. This radial acceleration profile, $a(r) = GM(r)/r^2 = V_c^2(r)/r$, is shown in figure 2.9 for two series of runs where the gravitational softening has been varied systematically by two orders of magnitude. The values of the softening in each run are shown with small vertical arrows near the bottom of the figure. Solid and dashed curves correspond to runs with 64^3 and 32^3 particles in the high-resolution box, respectively. As the softening is decreased from $\epsilon \sim 0.1\, r_{200}$ by successive factors of two, the acceleration profiles become steeper and converge to a unique profile for $\epsilon \lesssim 0.03\, r_{200} \approx 6\, h^{-1}$ kpc, as shown in figure 2.9. The convergent profile is well approximated by a NFW profile with concentration $c = 10$, shown by a dotted line in figure 2.9.

We note two interesting features of the acceleration profiles shown in figure 2.9. The first is that the effects of softening on the acceleration profile depend rather weakly on the number of particles used; for given ϵ, the profiles corresponding to runs with 32^3 and 64^3 particles agree reasonably well, and they approach the same 'converged' profile for $\epsilon \lesssim 0.03\, r_{200}$. The second feature is that acceleration profiles deviate from the 'converged' profile near the centre for larger values of the softening. Interestingly, deviations occur at radii where the acceleration exceeds a 'characteristic' acceleration,

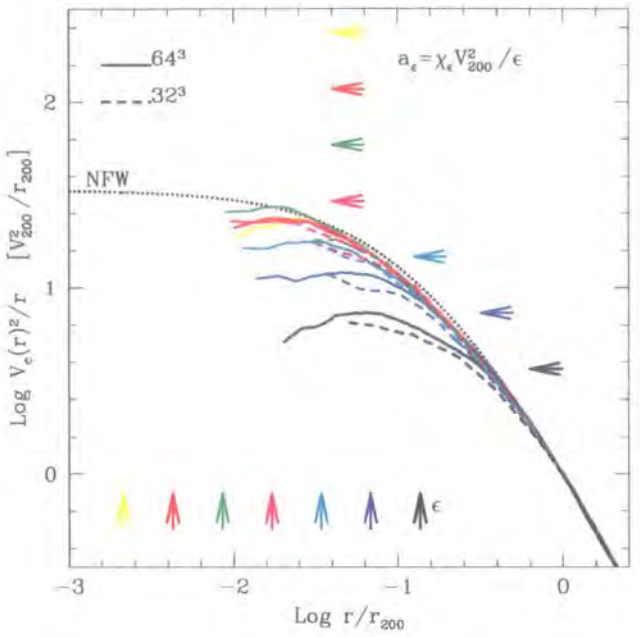

Figure 2.9: **Spherically-averaged 'acceleration' profiles** ($V_c^2(r)/r$) for 64^3 and 32^3 runs, shown for several choices of the softening scalelength, ϵ. The dotted line corresponds to the acceleration profile of a NFW model with concentration $c = 10$. The vertical arrows denote the value of the softening parameter, ϵ, for each run. The profiles line up, from bottom to top, in order of decreasing ϵ. As ϵ approaches $\sim 0.01\, r_{200}$, the acceleration profiles converge to a solution similar to the fiducial NFW curve. Profiles significantly affected by the softening deviate from the converged result at a radius where the acceleration matches the characteristic acceleration associated with the circular velocity of the halo, V_{200}, and ϵ: $a_\epsilon = \chi_\epsilon V_{200}^2/\epsilon$, with $\chi_\epsilon \approx 0.5$. The values of a_ϵ corresponding to each adopted value of ϵ are shown by the horizontal arrows.

$$a_\epsilon = \chi_\epsilon V_{200}^2/\epsilon, \tag{2.17}$$

which depends only on the circular velocity of the halo and on the value of the softening adopted. This characteristic acceleration is shown (for $\chi_\epsilon \approx 0.5$) with horizontal arrows in figure 2.9. The mass profile of a simulated halo becomes unreliable for accelerations exceeding a_ϵ.

This result suggests an empirical interpretation of the effects of softening on the mass profile of a simulated halo: the choice of gravitational softening imposes an effective limit on the accelerations that may be adequately reproduced in the system. This is interesting, since for systems with density profiles similar to that proposed by NFW,

there is a *maximum* acceleration that particles may experience. Indeed, $a(r) = V_c^2/r$ tends to a well-defined maximum,

$$a_{\rm max} = \frac{c^2/2}{\ln(1+c) - c/(1+c)} \frac{V_{200}^2}{r_{200}} \tag{2.18}$$

as r approaches zero. If ϵ is such that

$$a_\epsilon \gtrsim a_{\rm max}, \tag{2.19}$$

then it appears to impose no substantial restriction on the mass profile. For example, figure 2.6 shows that the converged mass within $\sim 1h^{-1}$ kpc appears not to change as ϵ varies between 1.25 and $3.5h^{-1}$ kpc. At face value, this would appear to imply that the mass profile can be trusted down to almost one third of the softening length scale when the condition expressed in equation 2.19 is satisfied. In order to be conservative, however, we shall hereafter assume that converged radii cannot be less than ϵ.

How does the upper limit on ϵ dictated by this constraint compare with $\epsilon_{\rm opt}$, the minimum needed to prevent discreteness effects and minimise the number of timesteps? The answer depends on the number of particles, as well as on the concentration of the system, and imposes an effective lower limit on the number of particles needed to satisfy both conditions simultaneously, $N_{200} \gtrsim (2c)^4/(\ln(1+c) - c/(1+c))^2$. For $c \approx 10$, we find that roughly 70,000 particles within the virial radius are needed to carry out a simulation where the softening is small enough not to restrict significantly the resolution of the inner mass profile and large enough to prevent discreteness effects from hindering the computational efficiency of the calculation.

To summarise, provided that all other numerical parameters are chosen appropriately, the effect of the softening on the spherically-averaged mass profile is to impose a maximum acceleration scale above which results cannot be trusted. The mass profile of a simulated halo converges at radii where the mean acceleration does not exceed a characteristic value imposed by the softening, $a(r) = V_c^2(r)/r \lesssim a_\epsilon = \chi_\epsilon V_{200}^2/\epsilon$, where χ_ϵ is empirically found to be ~ 0.5 if ϵ is expressed as a spline-softening scalelength.

2.6.2 The Initial Redshift

The starting redshift, z_i, determines the overall initial amplitude of density fluctuations in the simulation box. If z_i is too low, small scales may already be in the non-linear

regime, invalidating the assumptions of the procedure outlined in § 2.2.2. Initial redshifts cannot be chosen to be too high either, since the more uniform the periodic box, the more difficult the task of evaluating accurate forces in treecodes such as the ones we employ here becomes. A compromise must therefore be struck between these competing demands and we derive in this section a simple empirical prescription that ensures convergence in the mass profiles of simulated CDM halos at $z = 0$.

Figure 2.10(a) shows the radii of various mass fractions (at $z = 0$) as a function of the initial redshift of the simulation. Top and bottom panels refer to the same halo, using two different particle numbers in the high-resolution box: 32^3 (bottom), and 64^3 (top). Each curve is labelled by the enclosed number of particles. The inner mass profile of the halo converges as the initial redshift is increased. Convergence to better than 10% at all radii is achieved for $25 < 1 + z_i < 100$, and even for the highest z_i tested there is no clear departure from convergence. We have checked explicitly that this result does not depend on the particular time-stepping choice; a similar series with the `SgAcc` criterion gives similar results.

The data in figure 2.10(a) also suggest that convergence may be achieved at lower z_i when 32^3 particles are used rather than 64^3. A possible explanation for this is presented in figure 2.10(b), where we plot, for each radial shell, the deviations from the converged value as a function of the (theoretical) rms mass fluctuation on the smallest resolved mass scale at z_i, $\sigma(m_p, z_i)$ (m_p is the mass of one high-resolution particle). In terms of this variable, the 32^3 and 64^3 results are indistinguishable, showing convergence down to the 100-particle mass shell when z_i is chosen so that $\sigma(m_p, z_i) \lesssim 0.3$. This is a simple empirical rule for choosing the starting redshift that we shall adopt hereafter.

One advantage of this rule is that, for power spectra such as CDM, $\sigma(m_p)$ is only weakly dependent on mass on small scales, so the initial redshift can be chosen almost independently of the number of particles. For example, even for the highest number of particles considered in our study ($N_{\rm sbox} = 256^3$, $m_p = 6.5 \times 10^5\, h^{-1} M_\odot$) the starting redshift condition is satisfied for $1 + z_i \gtrsim 42$, so that $1 + z_i = 50$ could be safely used for all of our simulations, regardless of N.

2.6.3 Force Accuracy

Accurate forces are an obvious requirement for numerical convergence, and we investigate here the role of force accuracy parameters in the mass structure of dark halos. This is

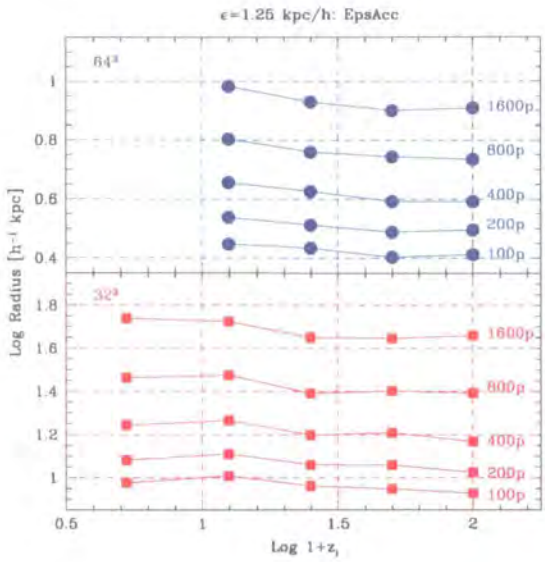

(a) Radii enclosing various mass fractions measured at $z = 0$ as a function of initial redshift

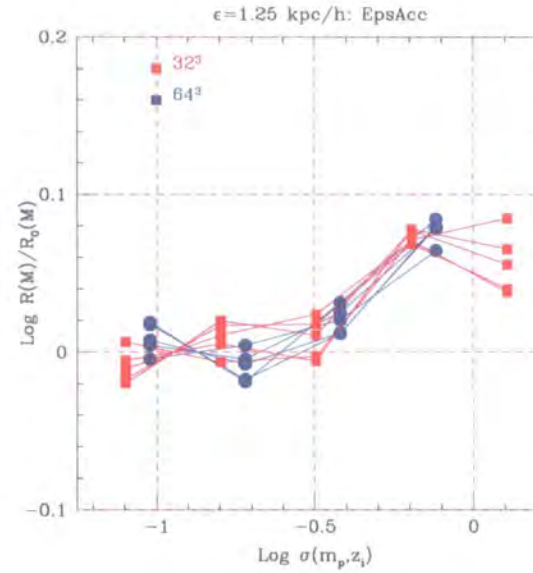

(b) Radii enclosing various mass fractions measured at $z = 0$ as a function of initial redshift, normalised to converged value.

Figure 2.10: In figure 2.10(a), we show **radii enclosing various mass fractions measured at $z = 0$ in our 32^3 and 64^3 simulations as a function of the initial redshift of the simulation, z_i.** Convergence is seen for $z_i \gtrsim 25$ in the 32^3 runs and for $z_i \gtrsim 49$ in the 64^3 runs. Starting at lower initial redshifts causes halo mass profiles to develop an artificially low density core. In figure 2.10(a), we show the radii of various mass shells as in figure 2.10(a), but normalised to the 'converged' value of the radius for each shell as a function of $\sigma(m_p, z_i)$, the linear rms fluctuation on the scale of the particle mass at $z = z_i$. Note that convergence is achieved at all radii when $\sigma(m_p, z_i) \lesssim 0.3$.

important since treecodes are based on approximate multipole expansion-based methods that are vulnerable to inaccuracies in the force calculations. Although accuracy can always be improved by adopting, for example, stricter node-opening criteria, this comes usually at the cost of substantial loss in computational efficiency. It is therefore important to determine what is the minimum force accuracy needed to achieve convergence in order to maximise the efficiency of the simulation.

Force accuracy is controlled in `GADGET` (in the configuration used in this study, see § 2.2.1) through two main parameters: a compile-time flag, `-DBMAX`, which, if enabled, restricts node opening to a list of cells *guaranteed* not to contain the particle under consid-

eration, and by the parameter $f_{\rm acc}$ (named `ErrTolForceAcc` in `GADGET`'s parameter file), which controls dynamically the updating of the tree-node opening criterion (Springel et al. (2001)). Figure 2.11 shows the radii of various mass shells in our standard halo as a function of $f_{\rm acc}$. Filled squares show the results obtained without setting the `-DBMAX` option in `GADGET`. Convergence is achieved in this case for quite small values of the accuracy parameter, $f_{\rm acc} \lesssim 0.003$. The reason behind the slow convergence seen in figure 2.11 appears to be related to rare but substantial errors incurred in `GADGET`'s tree walking procedure when the boundaries of open nodes are *not guaranteed* to exclude the particle under consideration (Salmon & Warren (1993), Hernquist (1987)), for the reason described in § 2.2.1. Disallowing this possibility (i.e., enabling `-DBMAX` during compilation) leads to much improved convergence relative to the parameter $f_{\rm acc}$, as can be seen from the filled circles in figure 2.11. There is almost no systematic trend with $f_{\rm acc}$ when `-DBMAX` is enabled, even for $f_{\rm acc} \approx 1$.

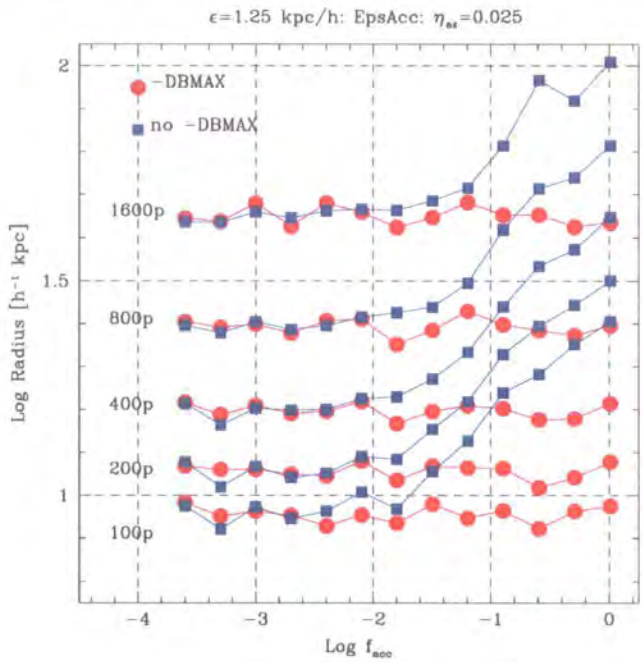

Figure 2.11: **Radii enclosing various mass fractions measured at $z = 0$ in our 32^3 simulations as a function of the force accuracy parameter, $f_{\rm acc}$.** Here $f_{\rm acc}$ is the `GADGET` force accuracy parameter, `ErrTolForceAcc` in `GADGET`'s parameter file. Filled squares show results without enabling the extra-accuracy flag `-DBMAX` during compilation. Filled circles show results enabling `-DBMAX`. When this flag is on, the effects of $f_{\rm acc}$ on the mass are mild, and good convergence is achieved even for rather large values of $f_{\rm acc}$. When `-DBMAX` is off, $f_{\rm acc} \lesssim 10^{-3}$ is needed to ensure convergence.

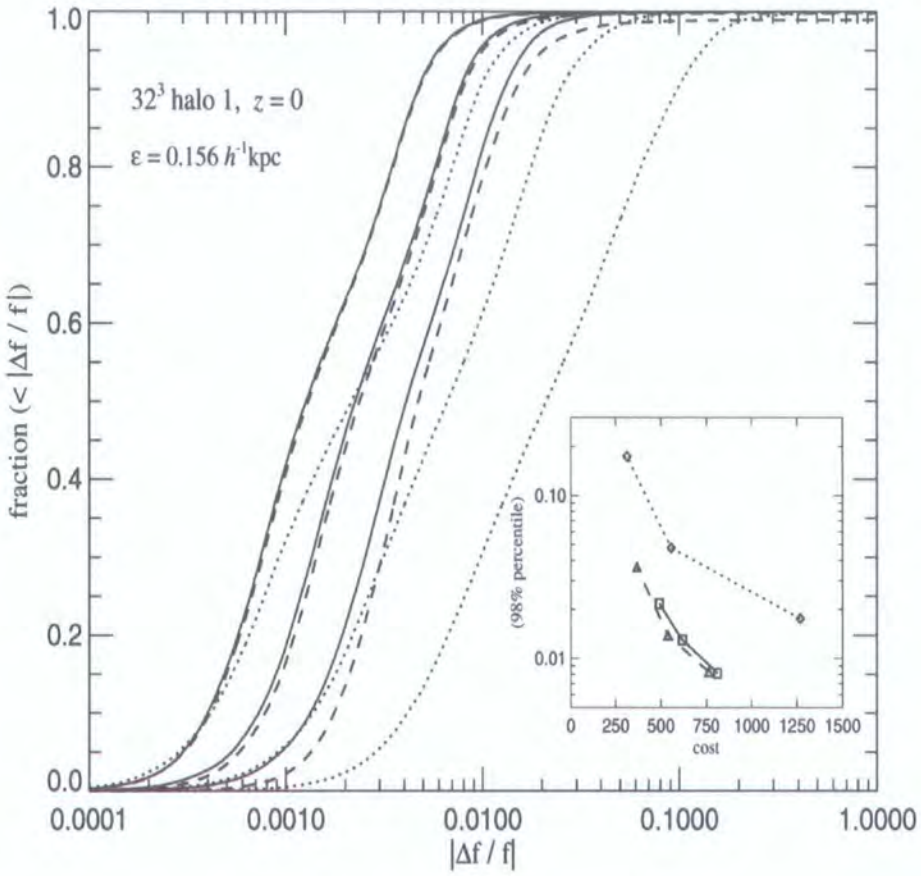

Figure 2.12: **Cumulative error distributions of GADGET's force computation for various choices of opening criterion and tolerance parameter.** We used the particle distribution of the z=0 snapshot of a run with 32^3 high-resolution particles and measured force errors by comparing to the result obtained by direct summation. Solid and dashed lines give the result of opening nodes with the 'relative' opening criterion proposed by Springel et al. (2001), with and without the `-DBMAX` option (solid and dashed lines, respectively). Results are shown for tolerance parameters $f_{\rm acc} = 0.001$, 0.003, and 0.01 (from left to right). Dotted lines show results for the traditional BH-opening criterion (dotted lines), with opening angles $\theta = 0.5$, 0.75, 1.0 (from left to right). The inset compares the accuracy obtained for all of these choices as a function of computational cost. See text for more details.

The main effect of enabling **-DBMAX** is to suppress a tail of large errors that, although rare, appear to have a significant effect on the final mass profile. This can be seen in figure 2.12 where we show the cumulative distribution of errors in accelerations computed on a $z = 0$ snapshot of a simulation with 32^3 high-resolution particles. Force errors were measured by comparing with the result obtained by direct summation. Solid and dashed lines give the result of opening nodes with the 'relative' opening criterion proposed by Springel et al. (2001), with and without the **-DBMAX** option (solid and dashed lines, respectively). In each case, results are shown for tolerance parameters $f_{\rm acc} = 0.001$, 0.003, and 0.01 (from left to right). We also show results for the traditional Barnes-Hut opening criterion (dotted lines), with opening angles $\theta = 0.5$, 0.75, 1.0 (from left to right).

We have chosen a rather small value of the softening in figure 2.12 to emphasise the point that a long tail of errors may exist when the **-DBMAX** option is not enabled; for example, errors of up to 100% or larger are present in this case when $f_{\rm acc} = 0.01$ (rightmost dashed line). Such errors are not present when **-DBMAX** is on (solid lines).

The inset compares the accuracy obtained for all of these choices as a function of the invested computational cost. 'Accuracy' is here taken as the 98% percentile force error, and the computational cost is measured in terms of the average number of node-particle interactions per force evaluation. For a given accuracy, the Barnes-Hut criterion results in higher cost than the criterion adopted in **GADGET**.

We conclude that enabling **-DBMAX** and adopting $f_{\rm acc} \lesssim 0.01$ is sufficient to study the inner structure of dark matter halos. Alternatively, adopting a redshift-dependent Barnes-Hut node opening criterion, such as in **PKDGRAV**, where $\theta = 0.55$ is used for $z > 2$ and $\theta = 0.7$ for $z < 2$, seems also to give adequate results.

2.6.4 The Number of Particles

The total number of particles is a critical parameter to choose when running a cosmological N-body simulation. Since the computation time will scale at best linearly with N, one must try and use as few particles as possible to achieve the goals of the programme. As mentioned in § 2.1, our main goal is to provide robust and accurate measurements of the circular velocity (or mass) profile of dark matter halos down to about the inner 1% of the virial radius. This corresponds to $\sim 2.2\,h^{-1}$ kpc in the case of the Milky Way if its halo has the same circular velocity as the disk. This is clearly the minimum resolution required for meaningful comparison with observed rotation curves.

In the preceding discussion we have determined the optimal choice of softening, time stepping, force accuracy, and starting redshift required to obtain repeatable and robust measurements of the circular velocity profile of a simulated CDM halo down to radii containing as few as 100 particles. Repeatability and robustness relative to these parameters are, of course, necessary conditions for convergence, but we must still demonstrate that the results do not depend on the total number of particles chosen.

How many particles must a region contain so that the circular velocity (or, equivalently, the mean inner density) converges?

We use the lessons from the preceding subsections to explore the dependence of the mass profile of simulated dark halos on the number of particles used. We consider only runs which meet the requirements discussed previously, so that, for each choice of N, we shall only present 'converged' results relative to other parameters. Our tests span an unprecedented range of 512 in particle number, from 32^3 to 256^3 particles in the high-resolution simulation cubes.

Our main results are summarised in figure 2.13, where we show, as a function of the enclosed number of particles, the mean inner density contrast measured at various radii from the centre of the halo. In this figure, for example, solid triangles show the mean inner density contrast measured at $\sim 20\%$ of the virial radius. From left to right, each group of filled triangles indicates the results of runs with 32^3, 64^3, 128^3, and 256^3 particles in the high resolution cube. These runs have 6200; 49600; 397000; and 3.2×10^6 particles within r_{200}, respectively. As the number of particles increases fewer runs are shown, because of the increasing computational cost. At the highest resolution, with 256^3 particles in the high-resolution cube, we have completed only one simulation. This run is comparable to the highest resolution simulations reported in the literature so far.

Figure 2.13 shows a number of important trends. Consider, for example, the radius corresponding to 2% of r_{200} (solid circles). In the 32^3 runs, this radius contains 1.6% of the halo mass (~ 100 particles). The mass within this radius is seen to increase significantly as the number of particles increases; the density contrast climbs from $\sim 1.2 \times 10^5$ (in the 32^3 runs) to $\sim 2.5 \times 10^5$ (in the 64^3 runs) before stabilising at $\sim 3 \times 10^5$ when $N_{\rm sbox}$ reaches 128^3 and 256^3. Clearly, 100 particles are *not enough* to trace reliably the mass profile of a simulated halo, in disagreement with the conclusions of Klypin et al. (2001), who argue that 100-200 particles suffice to resolve the inner mass profile when other parameters are

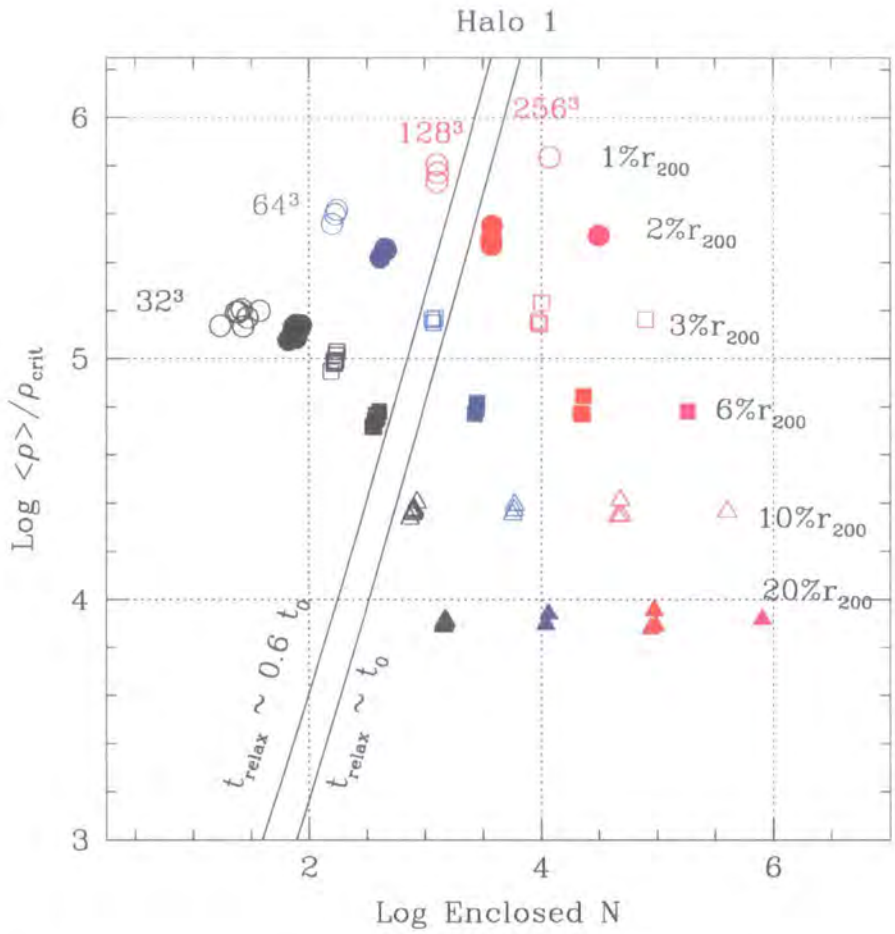

Figure 2.13: **Mean inner density contrast as a function of the enclosed number of particles** in 4 series of simulations varying the number of particles in the high-resolution box, from 32^3 to 256^3. Each symbol type corresponds to a fixed fraction of the virial radius, as shown by the labels on the right. The number of particles needed to obtain robust results increases with density contrast, roughly as prescribed by the requirement that the collisional relaxation timescale should remain longer than the age of the universe. According to this, robust numerical estimates of the mass profile of a halo are only possible to the right of the curve labelled $t_{\rm relax} \sim 0.6 t_0$.

chosen properly.

The situation is different for the 1000-particle radius in the 32^3 runs, which correspond to about 10% of the virial radius. The density contrast within this radius is $\sim 2.5 \times 10^4$, and remains essentially unchanged as the number of particles increases by a factor of 512. The data presented in figure 2.13 thus support the conclusions of Moore et al (1998): resolving regions closer to the centre, where the density contrast is higher, demands increasingly large particle numbers. Although 300 particles in the 32^3 runs are almost enough to resolve the 6% radius, they fall well short of what is needed to resolve the much higher overdensities characteristic of the 1% radius.

How many particles are needed to resolve a given radius? Moore et al. (1998) propose that converged regions are delineated by (one-half) the mean inter-particle separation within the virial radius, $0.5\,(4\pi/3N_{200})^{1/3}r_{200}$, whereas Fukushige & Makino (2001) suggest that the innermost resolved radius cannot be smaller than the radius where the two-body relaxation time becomes shorter than the age of the universe.

Our results appear to favour the latter interpretation. For example, the criterion of Moore et al. would predict that the 32^3 runs could be trusted down to 4.5% of the virial radius, but it is clear from Figure 2.13 that convergence in this case is achieved only for radii beyond 6% of r_{200}. On the other hand, all simulations can be seen to converge at radii larger than the radius where the average collisional relaxation time roughly matches the age of the universe. This is shown by the (almost vertical) line labelled $t_{\rm relax} \sim t_0$, where we define

$$\frac{t_{\rm relax}(r)}{t_{\rm circ}(r_{200})} = \frac{N}{8\ln N}\frac{r/V_c}{r_{200}/V_{200}} = \frac{\sqrt{200}}{8}\frac{N}{\ln N}\left(\frac{\bar{\rho}}{\rho_{\rm crit}}\right)^{-1/2}, \qquad (2.20)$$

$t_{\rm circ}(r_{200}) \sim t_0$, and $N = N(r)$ is the enclosed number of particles. For reference, the curve on the left indicates $t_{\rm relax} = 0.6\,t_{\rm circ}(r_{200}) \sim 0.6\,t_0$. As shown in figure 2.13, the density profile converges at radii that enclose enough particles so that $t_{\rm relax}(r) \gtrsim 0.6\,t_0$.

We emphasise that this criterion is mainly empirical, and does not necessarily imply that particles in regions where the relaxation time is shorter than $\sim 0.6\,t_0$ actually evacuate the central regions as a result of two-body encounters. Indeed, one would expect the inner mass profile to evolve as a result of collisions on the much longer 'evaporation' timescale, $t_{\rm evap} \approx 136\,t_{\rm relax}$ (Binney & Tremaine (1987)), a proposition that finds support in simulations of the evolution of isolated equilibrium N-body systems (Hayashi et al

(2002)). In addition, the heating rate near the centre is likely dominated by the presence of substructure rather than by particle-particle collisions, complicating the interpretation. Our result is thus reminiscent of the work of Weinberg (1998), who emphasises the difficulty of achieving the collisionless limit in N-body systems and the possibility that fluctuation noise may lead to relaxation effects important on all scales.

Despite this difficulty, it seems clear from figure 2.13 that resolving density contrasts exceeding 10^6 requires $\gtrsim 3000$ particles within that radius, or over 3 million particles within the virial radius. Providing robust numerical predictions of the mass structure of cold dark matter halos on scales that can be compared directly with observations of individual galaxies is thus a very onerous computational task.

2.6.5 Optimal parameters - a worked example

The many considerations discussed in the previous sections make the selection of optimal parameters for any given N-body run a delicate and complicated business. It may be helpful to go through how one might choose optimal parameters for a specific calculation, for example a simulation like the largest one ($N_{\rm sbox} = 256^3$) we consider in this paper.

This run has $\sim 3 \times 10^6$ particles within the virial radius at $z = 0$, and is the largest we can easily carry out with resources currently available to us. Figure 2.13 and the discussion in § 2.6.4 suggest that this number of particles should be sufficient to get converged results down to about $r_{conv} = 0.005\, r_{200}$. Equation 2.15 suggests that a softening parameter $\epsilon = 0.0025\, r_{200}$ will be near optimal for getting an efficient integration almost unaffected by discreteness effects. As figure 2.9 demonstrates, this softening is small enough relative to our target r_{conv} that it should not compromise the radial structure.

For these parameters, equation 2.16 and figure 2.4 then show that a single-timestep integrator should be able to converge in about 5000 equal steps, although we note that this depends on the detailed inner structure of the halo, which is what we are trying to measure. In practise, a series of runs where the number of particles is gradually increased, is desirable to fine-tune the choice of timestep. Alternatively, the discussion of § 2.5 implies that for our preferred multi-timestep integrator (`EpsAcc`) $\eta = 0.15$ should be small enough to ensure convergence. The discussion of § 2.6.2 shows that it should be safe to start the integration at $z_i = 49$.

2.7 The Circular Velocity Profile of a ΛCDM Halo

Finally, we use the convergence lessons derived above to analyse briefly the inner circular velocity profile of the ΛCDM halo considered here. The results of 'converged' runs are shown in figure 2.14. Each profile is shown only for radii considered converged according to the criteria discussed above. Plotted this way, all profiles, independent of the number of particles, seem to agree to within $\sim 10\%$ at all radii. The circular velocity increases from the virial radius inwards, reaches a maximum and then drops gradually towards the centre, following closely the dotted line that represents a NFW profile with concentration $c = 10$. This value of the concentration agrees reasonably well with the results of NFW and of Eke, Navarro & Steinmetz (2001), who find $c \approx 8$-9 for a halo of this mass. Near the centre, the profile is seen to deviate significantly from the steeply cusped profile approaching a central slope of $\beta = 1.5$ proposed by Moore et al. (1999), and agrees better with shallower central slopes such as that of the NFW model.

We emphasise that there is little evidence for convergence to a power-law density profile near the centre, and that the profile keeps getting shallower down to the innermost point that our procedure deems converged. Can our results be used to place meaningful constraints on the asymptotic inner slope? At $r_{\rm min} \sim 1\,h^{-1}$ kpc, the smallest radius resolved in our highest-resolution run ($N_{\rm sbox} = 256^3$), both the local and cumulative density profiles are robustly determined**: $\rho(r_{\rm min})/\rho_{\rm crit} = 9.4 \times 10^5$, and $\bar{\rho}(r_{\rm min})/\rho_{\rm crit} \approx 1.6 \times 10^6$. These values can be combined with the requirement of mass conservation to place an upper limit to the inner asymptotic slope of the density profile, $\alpha < 3(1 - \rho(r_{\rm min})/\bar{\rho}(r_{\rm min})) = 1.2$. In other words, there is not enough mass within $r_{\rm min}$ to support a power-law density profile with slope steeper than $\alpha = 1.2$. We note that this conclusion depends sensitively on our ability to resolve the innermost $1\,h^{-1}$ kpc. If $r_{\rm min}$ were just two or three times larger the same exercise would not be able to rule out slopes as steep as $\alpha = 1.5$.

In summary, our results argue strongly against the very steep central cusps advocated by Moore et al. (1998, 1999), Ghigna et al. (1998, 2000) and Fukushige & Makino (1997, 2001).

**Convergence in the local density actually extends to radii smaller than the minimum converged radius for the more stringent cumulative density.

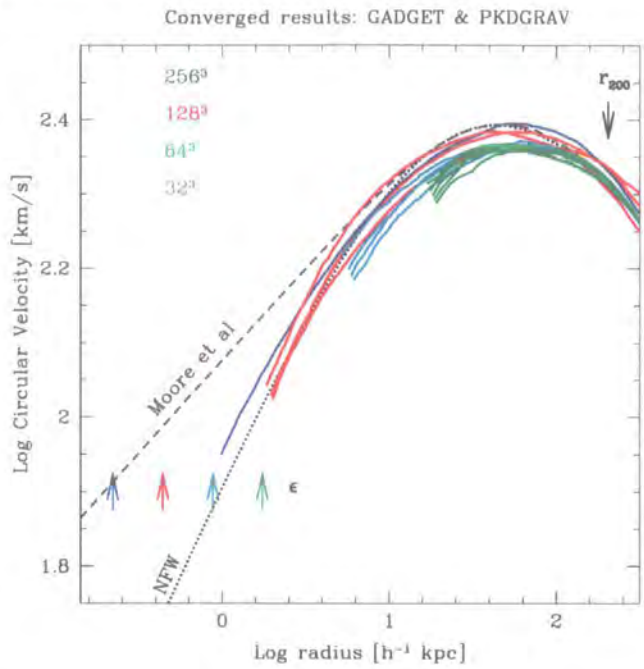

Figure 2.14: **The circular velocity profiles of 'converged' runs with different number of high-resolution particles.** Profiles are only plotted for radii where the convergence criteria derived in this chapter are satisfied. Several curves are shown for the cases of 32^3, 64^3, and 128^3 particles, corresponding to runs where all other numerical parameters take converged values. For clarity, a small selection of runs have been chosen; those with softenings indicated by the small vertical arrows. The convergent profile that emerges for this halo is roughly independent of the number of particles and resembles closely the model proposed by NFW, with $c = 10$. For this halo, steeply-cusped density profiles are disfavoured. The profiles labelled 'Moore et al' and 'NFW' have been matched at the peak of the circular velocity profile.

2.8 Conclusions

We have performed a comprehensive series of convergence tests designed to study the effect of numerical parameters on the structure of simulated cold dark matter halos. Our tests explore the influence of the gravitational softening, the time-stepping algorithm, the starting redshift, the accuracy of force computations, and the number of particles on the spherically-averaged mass profile of a galaxy-sized halo in the ΛCDM cosmogony. We derive, for each of these parameters, empirical rules that optimise their choice or, when those choices are dictated by computational limitations, we offer simple prescriptions to assess the effective convergence of the mass profile of a simulated halo. Our main results

can be summarised as follows:

1. *Timestep and Discreteness Effects.* The number of timesteps required to achieve convergence depends primarily on the orbital timescale of the region to be resolved, but may also be sensitive to the number of particles and the gravitational softening, unless these parameters are chosen so that discreteness effects are unimportant. This requires the gravitational softening to be large enough so that the maximum acceleration during two-body encounters does not exceed the minimum mean field acceleration in the halo, $\epsilon \gtrsim \epsilon_{\rm acc} = r_{200}/\sqrt{N_{200}}$. Empirically, we find that $\epsilon \approx \epsilon_{\rm opt} = 4\,\epsilon_{\rm acc}$ gives good results. When this condition is satisfied, the minimum converged radius, $r_{\rm conv}$, is given by the condition that the circular orbit timescale should be long compared to the timestep, $t_{\rm circ}(r_{\rm conv}) \approx 15\,(\Delta t/t_0)^{5/6}\,t_{\rm circ}(r_{200})$. *Substantially smaller* timesteps are needed if $\epsilon < \epsilon_{\rm opt}$. Dark matter densities at $r < r_{\rm conv}$ may be under- or over-estimated, depending on the integrator and timestepping schemes used. For example, constant-timestep **GADGET** runs develop artificially dense, 'cuspy' cores in poorly resolved regions, indicating that the approach to convergence is not always monotonic. This emphasises the importance of comprehensive convergence tests such as the ones presented here to validate the results of numerical studies of the inner structure of CDM halos.

2. *Fixed Timestep versus Adaptive Multi-Stepping.* Of the several adaptive, multiple time-stepping criteria that we considered, we have found best results when timesteps are chosen to depend explicitly on the gravitational softening and on the acceleration, $\Delta t_i = \eta_{a\epsilon}\sqrt{\epsilon_i/a_i}$, with $\eta_{a\epsilon} \sim 0.2$. Experiments with time-stepping choices that do not include explicitly the gravitational softening require the value of the corresponding η to be reduced as ϵ is reduced below the optimal value in order to obtain convergence. In terms of computational cost, we find that multi-time-stepping criteria significantly outperform the use of a single timestep for all particles only for softenings well below the optimal value.

3. *Gravitational Softening.* The choice of gravitational softening is found to impose a maximum acceleration scale above which simulation results cannot be trusted. This acceleration scale appears to depend mainly on the circular velocity of the halo and on the gravitational softening scale, and is given by $a_\epsilon = \chi_\epsilon\, V_{200}^2/\epsilon$, with $\chi_\epsilon \sim 0.5$. For *given particle number*, convergence to better than 10% in the mass

profile is obtained at radii greater than ϵ that also contain more than 100 particles and where the acceleration criterion is satisfied: $a(r) = V_c(r)^2/r \lesssim a_\epsilon$.

4. *Starting Redshift.* The mass profiles of simulated dark halos converge provided that the initial redshift is chosen so that the theoretical (linear) rms fluctuations on the smallest resolved mass scale, m_p (the mass of one high-resolution particle) is $\sigma(m_p, z_i) \lesssim 0.3$. Since $\sigma(m_p)$ is a weak function of mass on subgalactic mass scales for CDM-like power spectra, this criterion indicates that a modest starting redshift, such as $1 + z_i \approx 50$ is appropriate for particle masses as low as $m_p \sim 10^5\, h^{-1} M_\odot$ in the ΛCDM cosmogony.

5. *Force Accuracy.* The mass profiles of simulated CDM halos are quite sensitive to the accuracy of the force calculations, and convergence requires care in the choice of node opening criteria in the treecodes used in our study. Poor force accuracy leads to the development of artificially low density cores. In the case of **GADGET**, for example, we find that even occasional large errors in the forces may lead to noticeable deviations from converged profiles. To avoid this, it is necessary to choose tree-walking parameters that curtail drastically the tail of the most deviant force calculations, however rare. In **GADGET** this can be achieved by activating the compiler option **-DBMAX**. Using up to hexadecapole terms in the node potential expansion and setting a redshift dependent tree-node opening criterion, as in **PKDGRAV**, where $\theta = 0.55$ is chosen for $z > 2$ and $\theta = 0.7$ for $z < 2$, seems also to work well.

6. *Particle Number.* In order to achieve convergence in the mass profile, enough particles must be enclosed so that the average two-body relaxation timescale within the region is comparable or longer than the age of the universe. We find empirically that the condition, $t_{\rm relax}(r) \gtrsim 0.6\, t_0$, describes converged regions well. Since $t_{\rm relax}$ is roughly proportional to the enclosed number of particles times the local dynamical timescale, resolving regions near the centre, where density contrasts are high and dynamical timescales are short, requires substantially more particles than resolving regions more distant from the centre. Of order 3000 enclosed particles are needed to resolve regions where the density contrast reaches 10^6. On the other hand, density contrasts of order $10^{4.5}$ require only 100 enclosed particles for numerical convergence. Resolving radii of order 0.5% of the virial radius in the first case requires of order 3×10^6 particles within the virial radius.

For most simulations, the most stringent convergence criterion is the relaxation timescale condition on the number of particles. This implies that there is little choice but to strive for the largest possible N when studying the inner regions of dark matter halos. This limit is dictated by the available computer resources. Choosing the optimal softening for the adopted number of particles then minimises the number of timesteps needed to achieve convergence down to the radius where $t_{\rm relax}(r) \gtrsim 0.6\,t_0$. The precise number of timesteps cannot be determined ahead of time, since $t_{\rm relax}(r)$ depends on the detailed structure of the halo, which is what we are trying to measure. This implies that a series of simulations where the number of particles is increased gradually is advisable in order to ensure that optimal parameters are chosen for the highest-resolution run intended.

We have applied our convergence criteria to a ~ 205 km s^{-1} ΛCDM halo in order to investigate the behaviour of the inner slope of the density profile. We find that the slope of the spherically-averaged density profile, $\alpha = -{\rm d}\log(\rho)/{\rm d}\log(r)$, becomes increasingly shallow inwards, with little sign of approach to an asymptotic value. At the smallest radius that we consider resolved in our highest-resolution (256^3) simulation ($r_{\rm min} \sim 1\,h^{-1}$ kpc $\approx 0.005\,r_{200}$), the local and cumulative density contrasts are robustly determined, $\rho(r_{\rm min})/\rho_{\rm crit} = 9.4 \times 10^5$, and $\bar{\rho}(r_{\rm min})/\rho_{\rm crit} \approx 1.6 \times 10^6$. These values can be combined with the requirement of mass conservation to place an upper limit to the inner asymptotic slope of the density profile, $\alpha < 3\,(1 - \rho(r_{\rm min})/\bar{\rho}(r_{\rm min})) = 1.2$, although it is possible that the slope may actually become even shallower near the centre, as suggested recently by Taylor & Navarro (2001).

Our results thus argue against the very steep values for the asymptotic central slope ($\alpha \approx 1.5$) claimed recently by Moore et al. (1998, 1999), Ghigna et al. (1998, 2000), and Fukushige and Makino (1997, 2001). The reasons for this disagreement are unclear at this point, since there are substantial differences in the halo mass, numerical techniques, and cosmological model adopted, which hinder a direct comparison between our results and theirs. For example, the work of Moore et al. (1998) and Ghigna et al. (2000) differs from ours in mass scale (they simulated a galaxy cluster while we target a galaxy-sized halo) and in cosmology (they adopted an Einstein-de Sitter CDM cosmogony, whereas we adopt the ΛCDM model).

Finally, the difference between the conclusions from various authors may just reflect the fact that each group applies different criteria to the identification of the regions

deemed trustworthy. We note that models with the very steep ($\alpha \sim 1.5$) inner slopes proposed by the Moore et al group and with the shallower slopes that we find here are almost indistinguishable if we restrict our analysis to radii $\gtrsim$ 2% of the virial radius. Probing radii within the inner 1% of the virial radius seems required to shed light on this controversy.

Chapter 3

The Abundance of Substructure in ΛCDM Halos : Convergence at High Resolution?

3.1 Introduction

Over the last decade, considerable progress has been made in establishing the key predictions of the Cold Dark Matter (CDM) model on the scale of individual galaxies. Cosmological N-body simulations have proven to be a crucial tool in this highly non-linear regime, allowing the complex formation histories and structural properties of dark matter halos to be analysed in increasingly greater detail. Most notably, these investigations have revealed that CDM halos can be described by a *universal* mass profile (Navarro, Frenk & White (1996)), and that they contain an abundance of substructure halos (or *subhalos*) (Moore et al. (1999), hereafter M99; Klypin et al. (1999), hereafter K99). High resolution simulations of galaxy and cluster mass halos indicate that approximately 10% of the mass of a typical CDM halo is bound to substructure, and that the mass function of subhalos can be approximated by a power law with a slope $\alpha \simeq -2$ (e.g. Ghigna et al. (2000), hereafter G00).

We demonstrated in chapter 2 that the choice of numerical parameters used in a simulation can have a significant impact on how we interpret the structure of a dark matter halo, with particular emphasis on the effect on the spherically averaged circular velocity profile. This involved performing and analysing a comprehensive series of N-body simulations that were designed to clarify the role of numerical parameters on the structure of simulated CDM halos. Based on our analysis, we concluded that the spherically averaged

circular velocity profile could be considered reliably resolved at a given fraction of the virial radius of the halo provided the values of the gravitational softening, ϵ; timestep, δt; force accuracy, $f_{\rm acc}$; initial redshift, $z_{\rm i}$; and particle number, N satisfied certain convergence criteria. However, we found that it is the number of particles (i.e. the particle mass, $m_{\rm hres}$*) used in the simulation that provides the most stringent criterion - there is no alternative but to strive for as large a value of N as possible when investigating the detailed inner structure of CDM halos.

Thus it is clear that the distribution of mass within a simulated dark matter halo will be compromised by finite numerical resolution; the larger the choice of ϵ and $m_{\rm hres}$, the coarser the accuracy of the time integration (that is, the size of δt), the greater the radial extent of the regions affected by numerical artifacts. However, this result also suggests that the *abundance* of substructure within CDM halos will be as sensitive, if not more so, to the choice of numerical parameters.

If we apply the convergence criteria of chapter 2 to a typical subhalo, we find that the choice of parameters considered optimal to reliably resolve the central structure of the parent halo are insufficient to reliably resolve its central structure. The large ϵ and $m_{\rm hres}$ - relative to the "optimal" values for the subhalo - result in a diffuse system that will be more susceptible to disruption by the tidal forces it is exposed to in the denser environs of its parent. It follows that the lower the numerical resolution of the parent, the more unlikely the survival of all but the most massive subhalos.

This explains the difficulties encountered by early studies. The best resolved objects in simulations of cosmologically representative volumes - which used a single fixed value for the gravitational softening, particle mass and timestep - consisted of several hundred particles at most, and were featureless systems with little substructure (e.g. Frenk et al. (1988)). As techniques became available to simulate the formation of individual dark matter halos in a cosmological context (e.g. Porter (1985), Dubinski & Carlberg (1991), Katz & White (1993)), it became possible to resolve the structure of halos with relatively high spatial and mass resolution. This prompted several studies whose aim was to follow individual galaxy halos in rich galaxy clusters (Dubinski & Carlberg (1991), Carlberg (1994), Summers, Davis & Evrard (1995), Frenk et al. (1996)). However, only a handful of halos were found to survive in these simulations, in stark contrast to observed galaxy

*We use $m_{\rm hres}$ to denote particle mass because it is the mass of the high resolution particles in the simulation that is important.

clusters which boast several hundred galaxies.

This "overmerging" problem - the apparent inability of substructure to survive in dense environments - was first noted by White et al. (1987) and Frenk et al. (1988), and was understood to be a consequence of the limited numerical resolution of the simulations. It was initially thought that the inclusion of baryons was necessary to resolve the "overmerging" problem because the cooling of the baryons into the potential wells of the subhalos would increase their central densities and therefore increase their binding energies. As a result, the subhalos would be more robust to disruption by the tidal forces exerted in the dense environment of the parent.

However, Moore, Katz & Lake (1996) † noted that increasing the mass and spatial resolution of simulations should be sufficient to overcome the "overmerging" problem. They investigated the importance of numerical effects on the survival of subhalos by examining both physical *and* artificial mechanisms that could lead to mass loss and dissolution over a Hubble time. By assuming that subhalos could be treated as truncated isothermal spheres, they constructed equilibrium models and followed their structural evolution over several orbital timescales in an isothermal potential. These tests showed that halos dissolved rapidly once their limiting tidal radii - determined by the radius of their orbit within the parent halo - approached their core radii, imposed by the gravitational softening. In other words, too large a force softening or too few particles will produce a soft, diffuse halo that will be easily disrupted by tidal forces in a dense environment.

Subsequent high resolution studies (e.g. Ghigna et al. (1998), hereafter G98; M99; K99; G00; de Lucia et al. (2003), hereafter DKSW03) have vindicated the result of Moore, Katz & Lake (1996) and demonstrate that CDM halos contain an abundance of substructure. As we have already mentioned, approximately 10% of the mass of a typical CDM halo is bound to substructure (Tormen et al. (1998), G00; see also chapter 5), although this figure can fluctuate in response to recent merging history. The subhalo mass function can be approximated by a power law with a slope $\alpha \simeq -2$ (G00, DKSW03), while the distribution of subhalo peak circular velocities can be characterised as a power law with a slope $\alpha \simeq -4$ (K99, G00).

Interestingly, G98 found that subhalos follow quite eccentric orbits with a median apo-to-pericentre ratio of 6 : 1, in good agreement with the semi-analytical calculations of van den Bosch et al. (1999), who found a median radio $\sim 4 : 1$ for idealised models.

†But see also Klypin et al. (1999a)

This result suggests that many subhalos are exposed to the dense central regions of the parent.

However, relatively little attention has been paid to the robustness of quantities such as the subhalo mass fraction (i.e. the fraction of a halo's mass bound to substructure) or mass function to the choice of numerical parameters such as ϵ, $m_{\rm hres}$ and δt. G00 undertook a convergence study of sorts, analysing the properties of subhalos in two simulations of the same cluster mass halo (virial mass of $M_{200} \sim 2\times10^{14}h^{-1}{\rm M}_{\odot}$ at $z = 0$, forming in a SCDM cosmology) in which the mass and force resolution were increased. The higher resolution run had a factor of 8 more particles than the lower resolution run (G98), containing ~ 4 million particles within r_{200}, and the softening was a factor of 2 smaller ($0.5h^{-1}$ kpc) than in G98. They found good agreement between the subhalo mass fractions - 13% in G98 compared with 11% in G00 - and the distributions of subhalo masses and peak circular velocities agreed where both samples were complete, i.e. for masses $\gtrsim 5.6 \times 10^{10}h^{-1}{\rm M}_{\odot}$.

The results of G00 indicate that the global measures of substructure are relatively robust to the effects of finite numerical resolution when samples are complete, but we do not have any quantitative measure to judge at what mass scale a sample *is* complete. Moreover, we note that the choices of particle mass and gravitational softening in the high and low resolution simulations were chosen with the inner structure of the parent halo in mind.

A more thorough convergence study in the spirit of chapter 2 would fully explore the parameter space, systematically varying not only the particle mass and gravitational softening, but also the accuracy of the time integration, the criterion with which the timestep is chosen, the force accuracy and the starting redshift. Given the size of simulation needed to simply resolve a statistical sample of subhalos, it should be clear that such an enormous undertaking is well beyond the scope of this thesis!

Instead, the aim of this chapter is more modest and similar in spirit to G00 - to contrast the behaviour of the substructure mass fraction, the subhalo mass function and the spherically averaged number density profiles as the mass and force resolution of a simulation is increased. For this purpose, we have taken an existing set of simulations of three ΛCDM halos, which differ only in number of particles per parent, and analysed their subhalo populations. We note that the simulations were originally used to study the central structure of the spherically averaged mass profile, and so their numerical parameters were chosen according to the convergence criteria set out in chapter 2.

This chapter can be outlined as follows. In § 3.2, we present the simulations used in the proceeding analysis (§ 3.2.1) and discuss various approaches to the identification of substructure (§ 3.2.2), with particular emphasis on the **SubFind** algorithm used in this study. In § 3.3, we present the results of our analysis, while in § 3.4, we summarise our results and briefly discuss their implications.

3.2 Halo Substructure and its Identification

3.2.1 The Halos

We are interested in the studying the abundance of substructure in simulated CDM halos whose numerical parameters have been chosen according to the convergence criteria set out in chapter 2. In particular, we would like to understand the conditions under which selected global measures of the subhalo population can be considered converged when the mass resolution of a simulation is varied. We therefore require a sample of high resolution simulations that satisfy the convergence criteria of chapter 2 and for which we have realisations at lower resolution.

We have selected three sets of dark matter halos that satisfy our requirements - the dwarf galaxy halo **dH04** from the **dH** series of high resolution **d**(warf galaxy) **H**(alos), the galaxy halo **gH01** from the **gH** series of **g**(alaxy) **H**(alos) and the cluster halo **cl07** from the **cl** series of high resolution **cl**(uster halos). In the case of **gH01**, we have three levels of resolution. The converged numerical parameters used in these simulations are given in table 3.1. We note that the choice of mass resolution effectively sets the gravitational softening (see discussion in § 2.4).

We summarise the physical properties of the three sets of halos at $z = 0$ in table 3.2. Recall that it is our convention to define the virial radius, r_{200}, as the radius enclosing a spherical volume whose mean interior overdensity is 200 times the critical density of the Universe, $\rho_{\rm crit} = 3H^2/8\pi G$, at that redshift. z_f is defined following the convention of Lacey & Cole (1993) as the redshift at which the mass of the main progenitor first exceeds half the mass of the final $z = 0$ halo.

The algorithm used to identify substructure (**SubFind**, see below) generates a catalogue of subhalos sorted according to parent halo; however, in the particular implementa-

tion we use, the parent halo is defined to be a friends-of-friends (FOF) group. In general, FOF groups have ragged boundaries whereas we define the halo to be a spherical overdense region, and so it is possible that some halos that are on the peripheries of the parent FOF group but not linked to it may be absent from the subhalo catalogue. We overcome this by extending the subhalo catalogue to include *all* halos within r_{200} of the parent, including those on the peripheries of the parent group.

We show maps of the projected dark matter density distribution in and around each of the halos at $z = 0$ in the left hand panels of figures 3.1, 3.2 and 3.3. In each case, we have identified all particles within a cube of side $\sim 2\,r_{200}$ - corresponding to 0.1 h^{-1} Mpc, 1 h^{-1} Mpc and 3 h^{-1} Mpc in the cases of `dH04`, `gH01` and `c107` respectively - centred on the halos and estimated the local density at the position of each particle using the popular SPH spline kernel (Hernquist & Katz (1989)), where we have averaged over the nearest 64 neighbours. Particles are then convolved with a Gaussian kernel truncated at $5\,\sigma$, where σ is defined to be the distance to the 64th nearest neighbour; this has the effect of smoothing the mass of each particle over a volume determined by the local density - the lower the density a particle "sees", the larger the volume its mass is spread over. These smoothed particles are projected onto a 1024^2 mesh, and each mesh point (or pixel) is weighted according to the logarithm of its projected surface density. Thus, the "brighter" pixels correspond to regions of higher projected surface density. As we might expect, the centres of the halos tend to be the brightest regions in these maps, while the distinct bright knots correspond to substructure and orbiting halos in and around r_{200}.

The right hand panels of figures 3.1, 3.2 and 3.3 show the projected distribution of subhalos within r_{200} for each of the halos. Note that we show only those subhalos that lie *within* r_{200} and that we embed the projection within a cube $2.5\,r_{200}$ on a side. Each subhalo is represented by a circle whose radius is defined as

$$r_{\rm sub} = \frac{G m_{\rm sub}}{\sigma^2}, \tag{3.1}$$

where $m_{\rm sub}$ is the bound mass of the subhalo and σ represents the velocity dispersion of this material. We refer rather loosely to this radius as the "virial" radius of the halo, in the sense that we assume that the virial theorem applies. Radii are normalised to the virial radius of the parent, r_{200}.

Table 3.1: **Numerical Parameters of the Simulations.** We show for each of the simulations (1) the gravitational softening used for the high resolution particles, ϵ, in units of h^{-1} kpc, (2) the mass of the high resolution particles, $m_{\rm hres}$, in units of $h^{-1}{\rm M}_\odot$, and (3) the size of the simulation box, $\rm L_{box}$ in units of h^{-1} Mpc. Throughout we have assumed a ΛCDM cosmogony with $\Omega_\Lambda = 0.7$, $\Omega_0 = 0.3$, $h = 0.7$ and $\sigma_8 = 0.9$ except in the case of the galaxy runs where $h = 0.65$.

	ϵ $[h^{-1}$ kpc$]$	$m_{\rm hres}$ $[h^{-1}{\rm M}_\odot]$	$\rm L_{box}$ $[h^{-1}$ Mpc$]$
Dwarf (dH04)			
HIRES	0.0625	8.25×10^3	35.235
LORES	0.15625	1.05×10^5	
Galaxy (gH01)			
HIRES	0.15625	6.5×10^5	32.5
MEDRES	0.3125	5.2×10^6	
LORES	0.625	4.2×10^7	
Cluster (c107)			
HIRES	5.0	5.1×10^8	479.0
LORES	50.0	5.3×10^9	

Table 3.2: **Physical Properties of the Simulated Halos** We show for each halo (1) the virial radius, r_{200}, in units of h^{-1} kpc, (2) the virial mass, M_{200}, in units of $h^{-1}\mathrm{M}_{\odot}$, (3) the number of particles interior to r_{200}, N_{200}, (4) the mass in substructure, $M_{\rm sub}$, expressed as a percentage of M_{200}, (5) the number of subhalos interior to r_{200}, $N_{\rm sub}$, and (6) the redshift of formation, z_f, defined as the redshift at which the mass of the main progenitor first exceeds half the mass of the final ($z = 0$) halo.

	r_{200} [h^{-1} kpc]	M_{200} [$\mathrm{M}_{\odot}$/h]	N_{200}	M_{sub} [%M_{200}]	N_{sub}	z_f
Dwarf (dH04)						
HIRES	32.23	7.78×10^9	944047	6.37	310	1.9
LORES	33.26	8.56×10^9	81770	6.27	28	
Galaxy (gH01)						
HIRES	212.41	2.23×10^{12}	3429196	6.04	1415	0.7
MEDRES	214.08	2.28×10^{12}	438797	5.30	137	
LORES	210.95	2.18×10^{12}	52481	3.42	11	
Cluster (cl07)						
HIRES	1532.63	8.3×10^{14}	1634459	6.74	529	0.64
LORES	1548.37	8.63×10^{14}	161964	5.79	44	

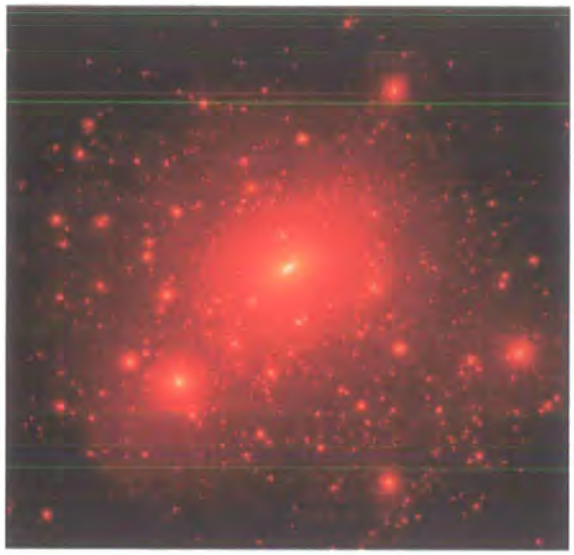

(a) High Resolution (HIRES)

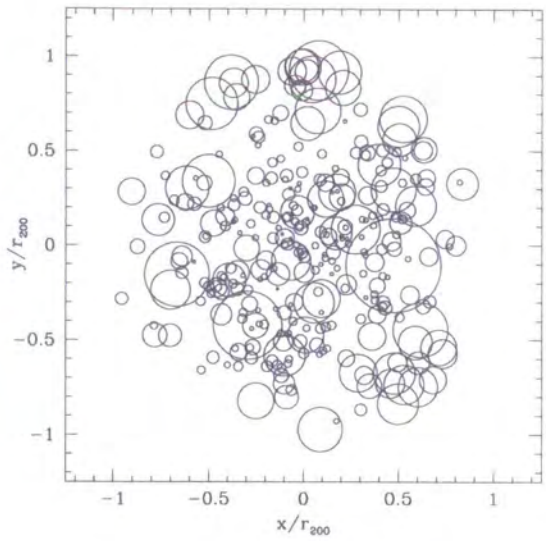

(b) Subhalo Distribution (HIRES)

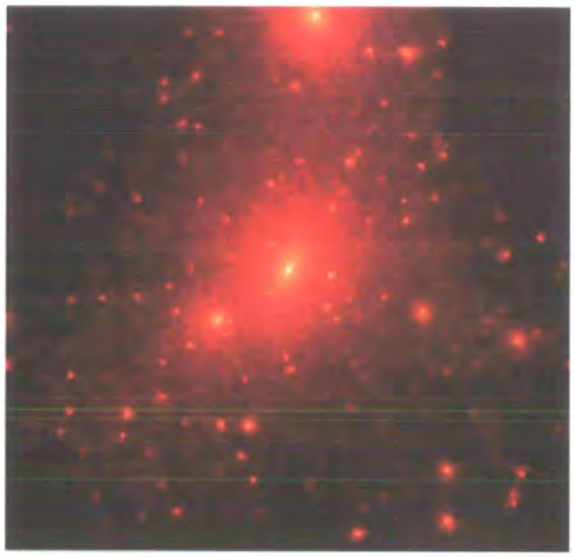

(c) Low Resolution (LORES)

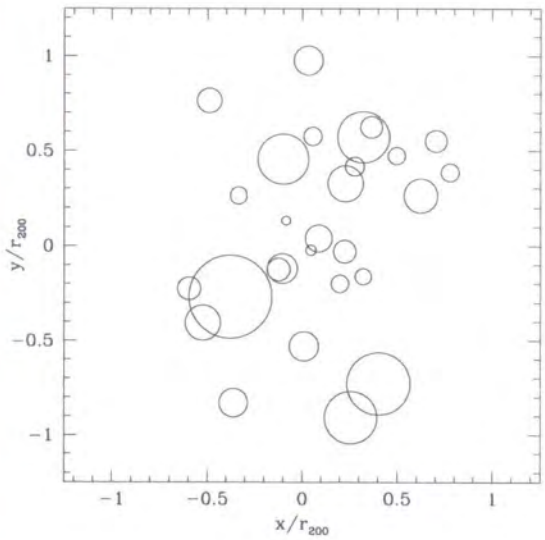

(d) Subhalo Distribution (LORES)

Figure 3.1: **Projected maps of the dark matter density and subhalo distribution in the dwarf halo dH04 at $z = 0$.** We show a projection of the smoothed dark matter distribution in a cube $0.1h^{-1}$ Mpc on a side onto a two dimensional (1024^2) mesh in figures 3.1(a) and 3.1(c); the brighter mesh points correspond to regions of higher projected density. Figures 3.1(b) and 3.1(d) highlight the projected distribution of subhalos; each subhalo is represented by a circle whose radius corresponds to its "virial" radius (in the sense defined in the text). Note that we have we have expressed radii in units of r_{200}, the virial radius of the parent.

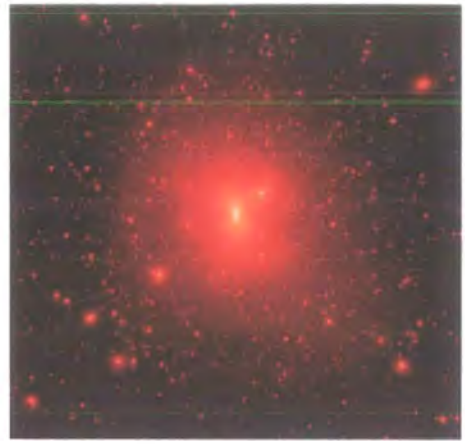

(a) High Resolution (HIRES)

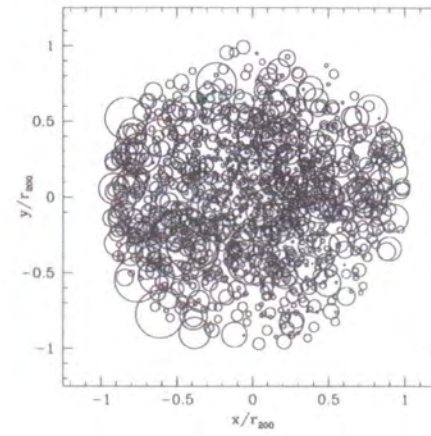

(b) Subhalo Distribution (HIRES)

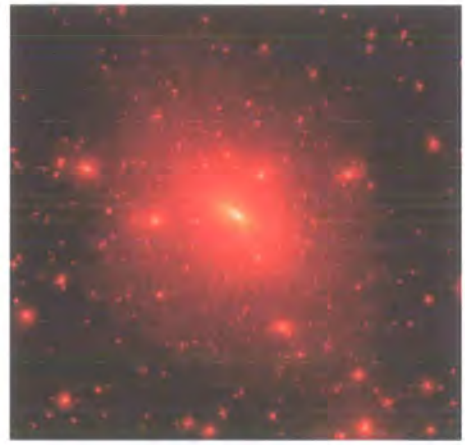

(c) Medium Resolution (MEDRES)

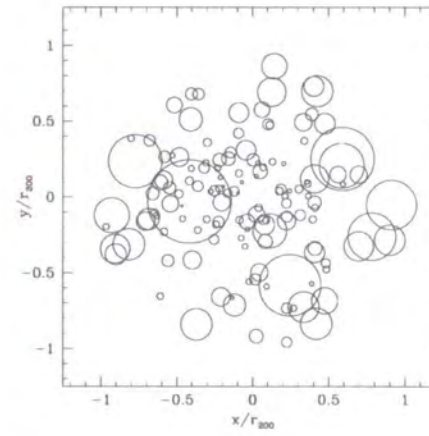

(d) Subhalo Distribution (MEDRES)

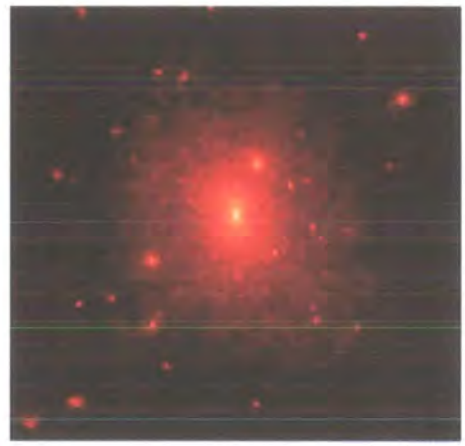

(e) Low Resolution (LORES)

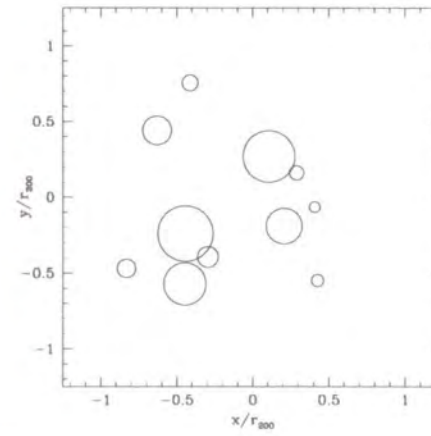

(f) Subhalo Distribution (LORES)

Figure 3.2: **Projected maps of the dark matter density and subhalo distribution in the galaxy halo gH01 at $z = 0$.** As in figure 3.1; see text for further details. We show a region $1h^{-1}$ Mpc on a side.

(a) High Resolution (HIRES)

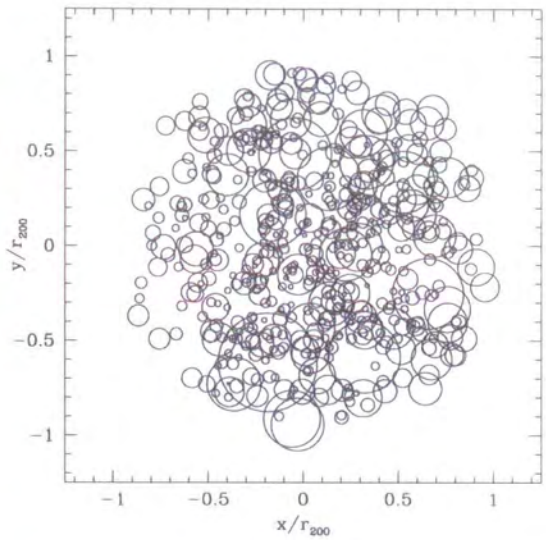

(b) Subhalo Distribution (HIRES)

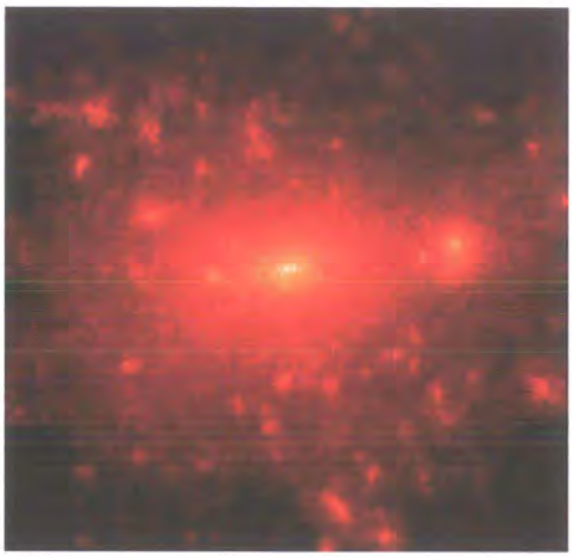

(c) Low Resolution (LORES)

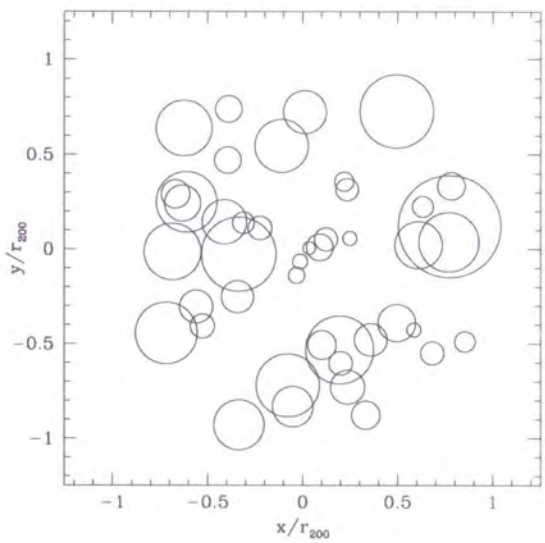

(d) Subhalo Distribution (LORES)

Figure 3.3: **Projected maps of the dark matter density and subhalo distribution in the cluster halo c107 at $z = 0$.** We show a region $3h^{-1}$ Mpc on a side. See text for further details.

3.2.2 Identification of Halo Substructure

Figures 3.1, 3.2 and 3.3 are useful, not only because they emphasise the wealth of substructure to be found within the virialised regions of CDM halos and the impact of increasing numerical resolution on the abundance of subhalos, but also because they confront us with the issue of how to identify dark matter substructure. We identify subhalos visually as concentrated overdense knots in the mass distribution of the parent halo, which promptly motivates the definition of a subhalo as any locally overdense region within a more massive parent halo that is *gravitationally bound.*

The requirement for the subhalo to be gravitationally bound is an important one. A typical subhalo represents a small fluctuation in the density field of the more massive host and so a substantial amount of mass can stream through the system without ever being gravitationally bound to it (see also Springel et al. (2001a)). Thus simply defining the subhalo as a local overdensity in the density field of the parent at a given instant would increase the chance of identifying spurious particle groups as "subhalos".

Several automated methods to identify substructure in dense environments have been developed and implemented with success. Some notable examples include

- The **Hierarchical Friends-of-Friends** method (Klypin et al. (1999a)), which is an extension of the basic friends-of-friends (FOF) method. The traditional FOF linking length is reduced in a sequence of steps, thus isolating groups of progressively higher overdensity. Results from each stage are combined and can be used to identify subhalos in dense regions. Note that this method does not require subhalos to be gravitationally bound.

- The **DENMAX** method (Gelb & Bertschinger (1994)), in which particles are moved along the local density gradient towards a local maximum. Eventually all particles are located in tight knots at maxima of the density field, at which point the FOF method is used to link them into groups. These groups are then checked to determine whether they are gravitationally bound are not, using an iterative procedure. The binding energy of each particle in the group is determined and the least bound particle is identified. If the particle is unbound, it is removed from the group list and the procedure is repeated until either the number of particles remaining drops below some critical threshold and the group is rejected, or the least bound particle is bound to the group. The **SKID** algorithm, developed by Stadel (2001), is similar

in principle to DENMAX but differs in its precise implementation; whereas densities are computed on a grid in DENMAX, SKID makes use of an adaptive kernel method.

- The **HOP** method (Eisenstein & Hut (1998)), in which each particle is associated with the particle with the highest density amongst its nearest neighbours, and then with that particle's densest neighbour and so on, until the particle which is its own densest neighbour - the local maximum of density - is reached. A density threshold is then applied, and particles with densities below this threshold are pruned. Further criteria can be applied to deal with cases where halos share a common boundary.

Although each of these methods have their merits, we have chosen to use a new algorithm developed by Volker Springel called `SubFind` (Springel et al. (2001a)). In this method, substructure halos are defined as locally overdense, self-bound particle groups within a larger parent group. Although there is some freedom in how parent groups are selected, we have adopted particle groups identified by the FOF algorithm, using a single *global* linking length set to the conventional value of $b = 0.2$ times the mean interparticle separation.

The principal features of the method can be summarised as follows:

- The three dimensional density field of the halo is constructed. This involves estimating the local density of each particle; an adaptive spline kernel is used for this purpose. The smoothing scale is set by the distance to the $N_{\rm dens}$th nearest neighbour, and the density is estimated by kernel interpolation over these neighbours. We have set $N_{\rm dens}$ to 32 particles.

- Locally overdense regions in this density field are identified. This involves the lowering of a global density threshold and extracting those regions enclosed by an isodensity contour that intersects saddle points in the density field. Particles within these regions constitute *subhalo candidates.*

- The binding energy of all subhalo candidates is computed and unbound particles are removed. This is an iterative procedure; the binding energy of each particle in a candidate is computed, and those particles with positive total energy are rejected until only bound particles remain.

- If the number of particles bound to the subhalo candidate exceeds a minimum threshold, N_{min}, the group of particles are collectively referred to as a **subhalo**.

We set the threshold N_{min} to 20 particles for the purposes of this study.

SubFind is attractive because it is intuitive, efficient and a version of code exists in which it has been implemented in parallel (essential when dealing with large numbers of particles).

3.3 Results

The discussion presented in § 3.1 emphasised the important relationship between mass and force resolution and the abundance of subhalos found in simulated CDM halos. We noted that subhalos naturally experience mass loss through physical processes such as exposure to tidal forces generated by the global potential of the parent and encounters with other subhalos, but limited numerical resolution greatly enhances this effect (Moore, Katz & Lake (1996), Klypin et al. (1999a)).

Increasing the resolution of a simulation leads to subhalos with higher central densities that are more robust to this tidal disruption. High resolution studies, such as M99, K99, G00 and our own analysis described in chapters 4 and 5, show that simulations which resolve CDM halos with $\gtrsim 10^6$ particles inside r_{200} and use gravitational softenings of order $\epsilon \sim 0.01 - 0.1\% r_{200}$ yield a wealth of substructure within the virialised region. This effect is readily apparent in the maps of the projected dark matter density and subhalo distributions shown in figures 3.1, 3.2 and 3.3. If we consider the particular case of the dwarf halo **dH04** (figure 3.1 and tables 3.1 and 3.2), the particle mass in **HIRES** is a factor of ~ 12 smaller than in **LORES**, but this leads to a factor of ~ 11 increase in the number of subhalos resolved within r_{200} in **HIRES** relative to **LORES**.

On the other hand, while increasing the mass resolution of a simulation enhances our ability to resolve low mass objects, it has little effect on the abundance of those objects that are already well resolved at lower resolution. For example, we find 10 of a possible 28 subhalos within r_{200} have masses $\gtrsim 8.6 \times 10^6 \mathrm{M}_\odot$ in the **LORES dH04** run , compared to 11 out of a possible 310 in the **HIRES** run.

These observations lead us to conclude that increasing the resolution of a simulation increases the number of subhalos resolved within the virialised region of a CDM halo but has little effect on the number of subhalos that are already well resolved in the lower resolution simulation. In the following subsections, we consider the implications of these

observations for the substructure mass fraction, $m_{\rm f}$, the subhalo mass distribution function, $N(M)$, and the spherically averaged number density profile, $n(r)$.

We begin by considering the impact of finite mass resolution on the proportion of a CDM halo's mass that is resolved in substructure - the substructure mass fraction, $m_{\rm f}$.

3.3.1 The Substructure Mass Fraction, $m_{\rm f}$

In figure 3.4(a), we show how the total subhalo mass fraction, $m_{\rm f}$, varies as the number of particles in the parent halo is increased. Red asterisks refer to the `HIRES` and `LORES` versions of the dwarf halo `dH04`, blue filled triangles refer to the `HIRES`, `MEDRES` and `LORES` versions of the galaxy halo `gH01` and the green filled squares correspond to the `HIRES` and `LORES` versions of the cluster halo `c107`.

There are two points worth noting in this figure. The first is that the fraction of a CDM halo's mass resolved in substructure is small, regardless of the resolution of the simulation. For the sample of halos we consider, we find that $3 \lesssim m_{\rm f} \lesssim 7\%$ - these values are consistent with the results of analysis that we shall present in chapter 5, which found that $m_{\rm f} \sim 3 - 10\%$ in a sample of high resolution simulations halos spanning ~ 5 orders of magnitude in mass.

The second is that $m_{\rm f}$ increases slightly with increasing mass resolution. In the most extreme case, the transition between the `LORES` and `HIRES` `gH01` runs, we find that reducing the particle mass, $m_{\rm hres}$, by a factor of 64 and the gravitational softening, ϵ, by a factor of 4 results in a dramatic increase in the abundance of substructure (from 11 to 1415 subhalos inside r_{200}, a factor of ~ 128) (c.f. tables 3.1 and 3.3). However, the subhalo mass fraction shows a meagre increase in response, rising by a factor of 1.75, from $\sim 3.4\%$ to $\sim 6\%$. In the three other cases, reducing $m_{\rm hres}$ by a factor of ~ 10 results in a factor of ~ 10 more resolved subhalos, whereas the mass fraction increases by a factor of 1.2 at most.

Here we have considered all subhalos within r_{200}. If we consider only those subhalos with masses greater than $M_{\rm lim}$, the threshold set in the lowest resolution simulation, we find that the trend is reversed in all the cases but one (see figure 3.4(b) and table 3.3). Such a reversal appears to be counterintuitive - we expect all subhalos with masses in excess of $M_{\rm lim}$ to be well resolved in the higher resolution simulations, and so we might expect the difference between $m_{\rm f}$ and $m_{\rm f}(> M_{\rm lim})$ to be accounted for by the subhalos

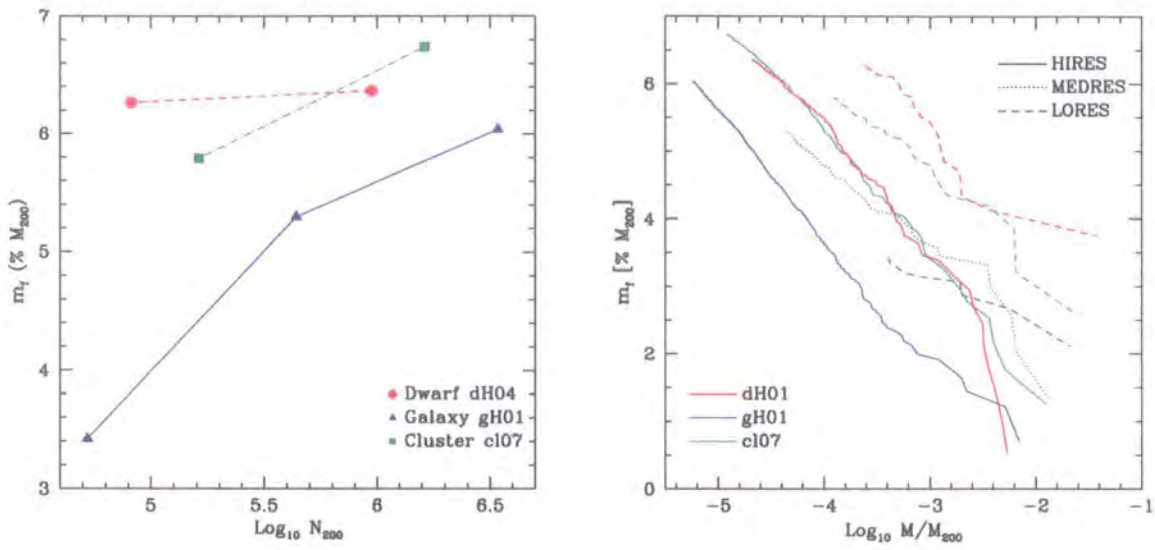

(a) Bound Substructure Mass Fraction : Total

(b) Bound Substructure Mass Fraction : Distribution

Figure 3.4: **Bound Substructure Mass Fraction at** $z = 0$. We have estimated m_f, the subhalo mass fraction for each of the halos in our sample, and express it as a percentage of the virial mass of the parent. The red asterisks, blue filled triangles and green filled squares correspond to the dwarf halo `dH04`, galaxy halo `gH01` and cluster halo `cl07` respectively. In figure 3.4(a), we plot the total mass fraction as a function of the number of particles in the parent halo, N_{200}. In figure 3.4(b), we plot the mass fraction in subhalos more massive than M expressed as a fraction of M_{200}, the virial mass of the parent halo.

with masses $M \lesssim M_{\rm lim}$ in the higher resolution simulations.

Figure 3.4(b) provides a convenient explanation for this behaviour. We show the mass fraction in subhalos more massive than a given fraction of the virial mass of the parent, M_{200}. The last (i.e. rightmost) plotted point represents the fraction of M_{200} that is bound to the most massive subhalo. If all subhalos with masses $M \gtrsim M_{\rm lim}$ were equally well resolved in both the `LORES`, `MEDRES` and `HIRES` simulations, then for any given halo, you would expect the `LORES` and `MEDRES` curves to overlap with the `HIRES` curves down to the mass limit, $M \sim M_{\rm lim}$.

This is not so, however; the `HIRES` curves (solid) are offset vertically from their lower resolution counterparts. This indicates that, as the mass resolution of the simulation is

Table 3.3: **The Impact of Mass Resolution on the Subhalo Mass Fraction**. We show for each of the halo's (1) the mass threshold, $M_{\rm lim} = N_{\rm min}\, m_{\rm lores}$, imposed by $N_{\rm min}$, the minimum number of particles per subhalo, and the particle mass in the LORES simulations, $m_{\rm lores}$, (2) the fraction of a halo's mass resolved in subhalos, $m_{\rm f}$, expressed as a percentage of M_{200}, and (3) $m_{\rm f}(> M_{\rm lim})$, the fraction of a halo's mass in subhalos more massive than $M_{\rm lim}$. In the case of gH01, the numbers in brackets correspond to the fraction of mass more massive than the value of $M_{\rm lim}$ imposed by the particle mass in the MEDRES simulation.

	$M_{\rm lim}$ $[h^{-1}{\rm M}_\odot]$	$m_{\rm f}$ $[\%M_{200}]$	$m_{\rm f}(> M_{\rm lim})$ $[\%M_{200}]$
Dwarf Halo dH04			
HIRES		6.37	4.56
LORES	2×10^6	6.27	6.27
Galaxy Halo gH01			
HIRES		6.05	2.4 (4.31)
MEDRES	10^8	5.3	4.07 (5.3)
LORES	8×10^8	3.42	3.42 (3.42)
Cluster Halo cl07			
HIRES		6.8	5.08
LORES	10^{11}	5.79	5.79

degraded, a larger proportion of the substructure mass is resolved in the few most massive subclumps. For example, if we consider only the fraction of a halo's mass in subhalos with masses $M \gtrsim 0.1\%\, M_{200}$, we find that $m_{\rm f}(M \gtrsim 0.1\%\, M_{200}) \sim 2 - 3.5\%$ in the HIRES simulations compared to $\sim 4 - 6\%$ in the LORES (MEDRES) counterparts.

Furthermore, if we compare the fraction of mass in subhalos more massive than $M \gtrsim 0.1\%\, M_{200}$ in the highest resolution simulation, the gH01 HIRES run, ($N_{200} \sim 3$ million particles, $\epsilon \sim 0.075\%\, r_{200}$) with the dH04 and cl07 HIRES, and gH01 MEDRES runs (($N_{200} \sim 0.5 - 1.5$ million particles, $\epsilon \sim 0.15 - 0.3\%\, r_{200}$), we find that $m_{\rm f}(M \gtrsim 0.1\%\, M_{200}) \sim 2\%$ in the former case, compared to $\sim 3.5\%$ in the latter. This is not a huge difference, but it is large enough to suggest that this quantity $m_f(> M)$ is unlikely to converge as N is increased.

3.3.2 The Substructure Mass Distribution Function, $N(M)$

The substructure mass distribution function, $N(M)$, (hereafter mass function) provides a convenient measure of the abundance of subhalos of a given mass. Previous studies (e.g. G00) and analysis presented in § 5.3 indicate that the subhalo mass function in a typical CDM halo at $z \sim 0$ can be approximated by a power law $N(M) \propto M^{-\alpha}$ with a slope $\alpha \simeq 2$; that is, the abundance of subhalos decreases with increasing mass.

As we mentioned earlier, we expect the effects of finite numerical resolution to be most readily apparent in the subhalo mass function. Consider the number of subhalos of mass M in a typical CDM halo simulated with increasing mass and force resolution, where M is chosen to be close to the subhalo mass limit ($M_{\rm lim}$, see table 3.4) in the lowest resolution simulation. We expect to find good agreement between the numbers of subhalos of mass M resolved in the highest resolution simulations (within Poisson errors). However, in simulations where the particle mass exceeds some threshold mass, these numbers become depressed and the lower resolution mass functions "peel off" the higher resolution mass functions. This behaviour reflects the impact that the reducing the mass and force resolution of a simulation has on the internal structure of subhalos.

G00 used an argument based on the tidal stripping of isothermal spheres in a larger isothermal potential (and described in G98) to estimate the mass above which a sample of subhalos could be considered unaffected by numerical resolution, i.e. complete. They expressed this limit in terms of the peak circular velocity, $v_{\rm c,max}$ of the subhalo and found that their sample was complete provided $v_{\rm c,max} \gtrsim 60$ kms^{-1} and $\gtrsim 100$ kms^{-1} in their high and low resolution runs respectively.

We have taken a complementary approach to that of G00 - we attempt to determine the fraction of the subhalo sample that is complete using $N(M)$ itself, and to identify the "converged" mass, $M_{\rm conv}$, at which the values of $N(M)$ measured in different resolution simulations can be considered converged. In particular, we express convergence in terms of the number of particles, $N_{\rm conv}$, in a subhalo whose mass is $M_{\rm conv}$.

We follow G00 and analyse the differential mass function, i.e. the number of subhalos per unit logarithmic mass interval per unit physical volume of the parent ($dN/d\log M$), as a function of subhalo mass for each of the halos in our sample. The results are shown in figure 3.5. The upper panels show subhalo mass functions for the dH04 runs and the

Table 3.4: **The Impact of Mass Resolution on the Subhalo Mass Function**. We show for each of the lower resolution simulations (1) the particle mass, $m_{\rm lres}$, (2) the mass threshold, $M_{\rm lim} = N_{\rm min}\, m_{\rm lres}$, imposed by $N_{\rm min}$, the minimum number of particles per subhalo, and $m_{\rm lres}$, (3) the converged mass, $M_{\rm conv}$, the subhalo mass at which the higher and lower resolution mass functions agree, and (4) the number of lower resolution particles corresponding to $M_{\rm conv}$, $N_{\rm conv}$. All masses are expressed in units of $h^{-1}{\rm M}_\odot$.

	$m_{\rm lres}$ $[h^{-1}{\rm M}_\odot]$	$M_{\rm lim}$ $[h^{-1}{\rm M}_\odot]$	$M_{\rm conv}$ $[h^{-1}{\rm M}_\odot]$	$N_{\rm conv}$
Dwarf Halo **dH04**				
LORES	1.05×10^5	2.1×10^6	5×10^6	~ 47
Galaxy Halo **gH01**				
MEDRES	5.2×10^6	5.2×10^6	5.2×10^6	~ 110
LORES	4.2×10^7	8.4×10^8	1.95×10^9	~ 46
Cluster Halo **c107**				
LORES	5.3×10^9	1.06×10^{11}	2.9×10^{11}	~ 55

gH01 runs, while the lower panel shows the results of **c107** runs. Blue, red and green solid curves represent the **LORES**, **HIRES** and **MEDRES** runs. We also show (Poisson) error bars for the **HIRES** and **MEDRES** runs.

There are two points to note here. The first is that all of the **HIRES** differential mass functions can be well approximated as power laws with slopes in good agreement with published results of $\alpha \simeq 1$ (G00, DKSW03). We find $\alpha \sim -0.8$ (**dH04**), ~ -1.1 (**gH01**) and -0.8 (**c107**). Furthermore, all of the runs agree (i.e. lie within the Poisson errors of the **HIRES** (**MEDRES**) runs) at the high mass end. However, we note that the **LORES** (**MEDRES**) mass functions begin to deviate (or "peel off") the **HIRES** mass functions at low-to-intermediate subhalo masses. This is precisely the kind of behaviour we predicted, and which we would like to exploit.

Using these figures, we may now ask, at what value of the subhalo mass do the **LORES** (**MEDRES**) mass functions begin to deviate *significantly* from the **HIRES** mass functions? The answer to this question defines $M_{\rm conv}$ and $N_{\rm conv}$, thus providing an estimate of the number of particles per subhalo required to ensure the completeness of the subhalo sample

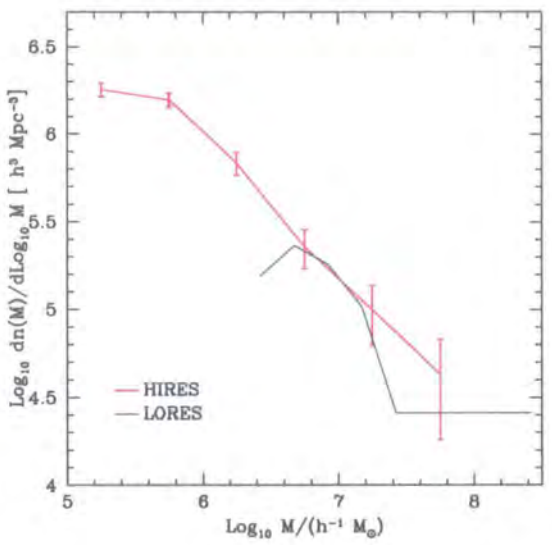

(a) Dwarf Galaxy Halo dH04

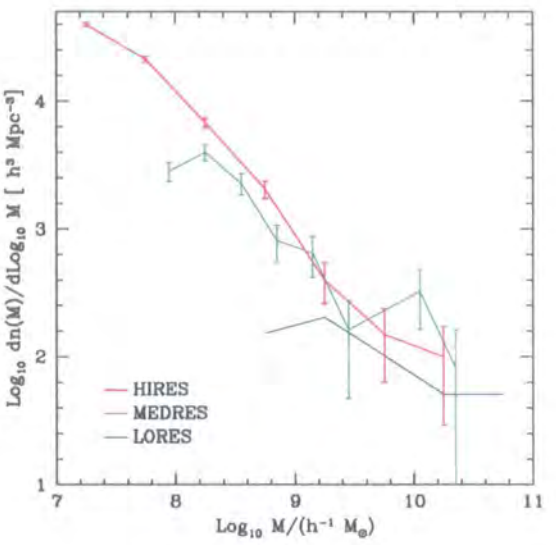

(b) Galaxy Halo gH01

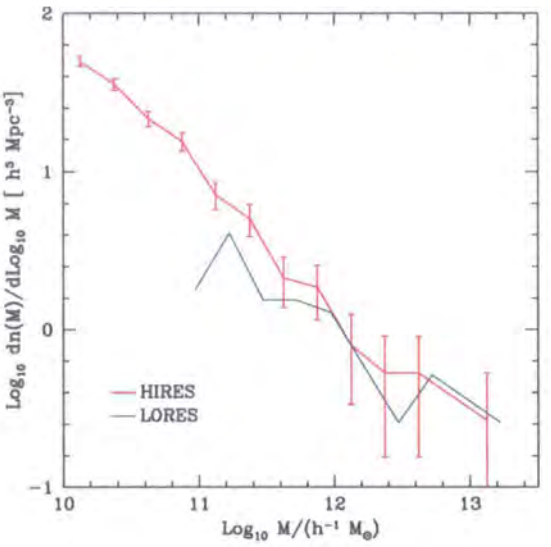

(c) Cluster Halo c107

Figure 3.5: **Differential Subhalo Mass Functions at** $z = 0$. We show differential subhalo mass functions for the each of the HIRES (red curves), LORES (blue curves) and, where appropriate, MEDRES (green curves) runs in our sample. The upper left and right hand panels show the results of the dH04 and gH01 runs; the lower panel shows the results of the c107 runs. The error bars represent 1σ Poisson errors on the number of subhalos per mass bin.

and a mass threshold above which the abundance of subhalos in a simulation can be considered converged.

We wish to identify the lowest subhalo mass at which a lower resolution mass function is considered to first deviate significantly from the higher resolution mass function. We define a *significant deviation* to be one in which the difference between the number of subhalos resolved in the higher and lower resolution mass functions exceeds the Poisson estimate of the fractional error in the higher resolution mass function. The lowest mass scale at which this first occurs corresponds to the converged subhalo mass for that simulation, $M_{\rm conv}$, from which we can estimate $N_{\rm conv}$.

To this end, we have made the simple assumption that the size of the Poisson errors in the higher resolution simulation smoothly varies with subhalo mass - if $N(M) \sim M^{-2}$, $\Delta N(M) \sim M^{-1}$ and so $\Delta N/N \sim M$. We can then estimate the lowest value of subhalo mass in the lower resolution mass function at which the deviation between the lower and higher resolution mass functions exceeds the Poisson error in the higher resolution mass function. For the purpose of this thesis, we have estimated by eye the point at which the lower resolution mass function peels off, and find consistent values for $N_{\rm conv}$.

In three of the four cases, we estimate that the subhalo sample is incomplete for subhalos with fewer than $N \lesssim N_{\rm conv} \simeq 50$ particles; in the case of the **MEDRES gH01** run, we find that $N_{\rm conv} \simeq 110$ particles. This value of $N_{\rm conv}$ corresponds to converged masses of $M_{\rm conv} \simeq 5.25 \times 10^6 h^{-1}\,{\rm M}_\odot, 2.1 \times 10^9 h^{-1}\,{\rm M}_\odot, 2.6 \times 10^8 h^{-1}\,{\rm M}_\odot$ and $2.6 \times 10^{11} h^{-1}\,{\rm M}_\odot$ for the **dH04**, **gH01** (**LORES** and **MEDRES**), and **c107** runs respectively.

We conclude that the sample of subhalos with $N \gtrsim N_{\rm conv} \simeq 50$ particles can be considered complete, imposing a mass threshold of $M_{\rm conv} \simeq N_{\rm conv} m_{\rm lres}$ (c.f. table 3.4).

3.3.3 The Spatial Distribution of Substructure

Finally, we consider the impact of increasing mass resolution on the spatial distribution of subhalos within their parent halos. In figure 3.6, we show normalised number density profiles of subhalos, $n(r)$, for each of the halos in our sample. We define the number density of subhalos at a given radius r to be the fractional number of subhalos (in units of N_{200}, the number of subhalos interior to r_{200}) in a spherical shell of radius r divided by the volume of that shell.

As in figure 3.5, we show the results for the **dH04**, **gH01** and **c107** runs in the upper left and right hand and lower panels; the blue long dashed, green short dashed and red

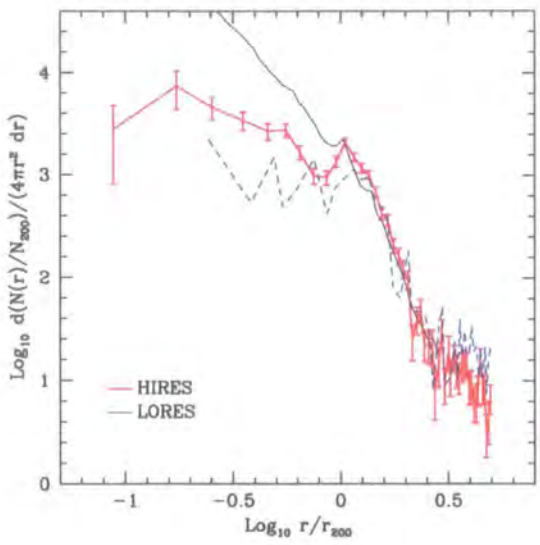

(a) Dwarf Galaxy Halo dH04

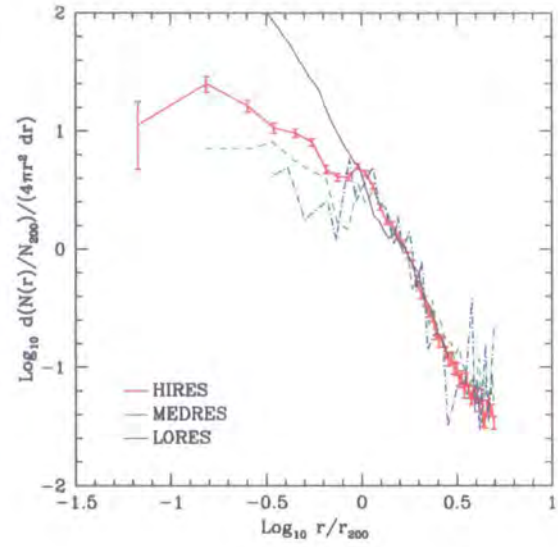

(b) Galaxy Halo gH01

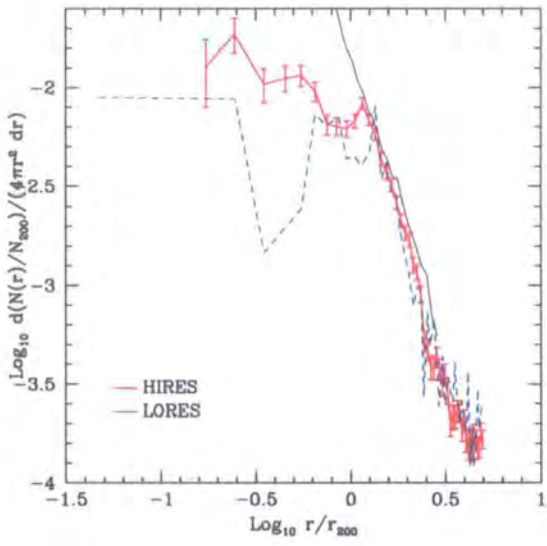

(c) Cluster Halo c107

Figure 3.6: **Fractional Number Density Profiles of Subhalos and Dark Matter Particles at $z = 0$.** We show normalised subhalo number density profiles for the subhalos for each of the HIRES (red curves), LORES (blue curves) and, where appropriate, MEDRES (green curves) runs in our sample. As in figure 3.5, the upper left hand, upper right hand and lower panels show results from the dH04, gH01 and c107 runs respectively. The heavy black solid curve in each panel corresponds to the normalised number density profile of the parent from the HIRES run. Error bars on the HIRES runs represent 1σ Poisson errors on the number of subhalos per mass bin. Radii are scaled to the virial radius of the parent, r_{200}.

solid curves curves represent the LORES, MEDRES and HIRES runs respectively. We also plot spherically averaged density profiles of particles in the parent for each of the halos (heavy black solid curves), computed for the HIRES case and normalised to allow direct comparison with the subhalo number density profiles. Error bars on the HIRES runs indicate 1σ Poisson errors on the number of subhalos per bin. Radii are scaled to the virial radius of the parent, r_{200}.

There are two main points to note in these figures. The first concerns the general shape of the number density profile; the second relates to the impact of increasing the mass resolution of a simulation.

All of the subhalo number density profiles are steep at large radii (for $r \gtrsim r_{200}$) and are in good agreement with the mass density profile of the underlying dark matter halo, suggesting that the subhalo number density profile shares a similar functional form with that of the dark matter in the outer parts, $n(r) \propto r^{-3}$. However, at radii $r \sim r_{200}$, the profiles roll over quite sharply and the slope of the profile is shallower at smaller radii, $r \lesssim r_{200}$; we find that $n(r) \propto r^{-\alpha}$ where $0.6 \lesssim \alpha \lesssim 0.8$ for our highest resolution halos. Relative to the dark matter particles, the number density of subhalos falls dramatically interior to r_{200}; at $\sim 50\% r_{200}$, the difference is nearly a factor of ~ 3 for our highest resolution runs.

If we consider the behaviour of the lower resolution number density profiles relative to those measured for the HIRES halos, we find that there is good agreement between each set at large radii (for $r \gtrsim r_{200}$); the lower resolution runs are within the 1σ error bars of the HIRES runs, and their profiles have a similar slope ($n(r) \propto r^{-3}$). However, interior to r_{200}, we note that the lower resolution profiles roll over more sharply than is the case for the HIRES runs, and their slopes are shallower; assuming $n(r) \propto r^{-\alpha}$, we estimate that $0 \lesssim \alpha \lesssim 0.2$. We also note that none of the subhalo profiles extend to radii smaller than $\sim 5\% r_{200}$, irrespective of mass resolution.

G00 quantified the observed difference in the number density of subhalos ($n_{\rm sub}(r)$) and dark matter particles ($n_{\rm part}(r)$) in terms of a bias parameter, b;

$$b(r) = n_{\rm sub}(r)/n_{\rm part}(r) \tag{3.2}$$

If this ratio increases with decreasing radius, the subhalos are said to be *biased* with respect to the smooth halo; otherwise, the subhalos are *antibiased*. The enhanced dis-

ruption and dissolution of subhalos in the inner parts of their parents as a result of finite numerical resolution tends to drive the system towards antibias. According to the results presented in figure 3.6, the subhalos in our three sets of halos are antibiased with respect to the underlying smooth halo, and the severity of this antibias is greater for lower resolution simulations.

3.4 Conclusions

The primary aim of this chapter has been to investigate the effect of increasing mass resolution on the abundance and spatial distribution of substructure halos (subhalos), with particular emphasis on the fraction of the parent halo's mass bound to these subhalos (the bound mass fraction, $m_{\rm f}$), the mass distribution function of the subhalos ($N(M)$) and the spherically averaged number density of subhalos as a function of radius ($n(r)$). For this purpose, we have analysed the subhalo populations in a sample of three existing sets of simulations that follow the formation and evolution of halos in the ΛCDM model, which differ only in number of particles per parent halo. The simulations were originally used to study the spherically averaged mass profile and so we note that we use the "converged" value for the gravitational softening in each case, set by the particle mass in accordance with the convergence criteria defined in chapter 2.

Based on our analysis, we conclude that

1. *increasing the mass resolution of a simulation results in an increase in the number of subhalos resolved within the virial radius of the parent halo, but the improved mass resolution has little impact on the abundance of subclumps that are already well resolved in the lower resolution simulation.* We noted that in the particular case of the halo **dH04**, reducing the particle mass by a factor of ~ 12 led to a factor of ~ 11 increase in the number of resolved subhalos within r_{200}; on the other hand, we found that the number of subhalos more massive than $\sim 0.001\, M_{200}$, where M_{200} is the virial mass of the parent halo, agreed to within 10% between the higher and lower resolution runs, well within the Poisson error on the count;

2. *the fraction of the parent halo's mass bound to substructure (the subhalo mass fraction, $m_{\rm f}$) is small, regardless of the mass resolution of the simulation.* For the halos in our sample, we find that $3\% \lesssim m_{\rm f} \lesssim 7\%$, in good agreement with the result of chapter 5;

3. *the mass fraction, m_f, appears to increase as the mass resolution of the simulation is increased, although it is a slight effect.* We found that reducing the particle mass by a factor of ~ 10 leads to a factor of ~ 10 increase in the number of resolved subhalos, but less than $\sim 20\%$ increase in the mass;

4. *an increasing proportion of a parent halo's mass is bound to the few most massive subclumps as the resolution of a simulation is degraded.* We noted that if we consider the fraction of a parent halo's mass bound to subclumps more massive than $M \gtrsim 0.1\% M_{200}$, the mass fraction $m_f(M \gtrsim 0.1\% M_{200}) \sim 2 - 3.5\%$ in our highest resolution simulations compared to $\sim 4 - 6\%$ in the lower resolution counterparts;

5. *the subhalo mass distribution function can be well approximated by a power law - $N(M) \propto M^{-\alpha}$ - with a logarithmic slope $\alpha \simeq 2$,* in good agreement with the results of previous studies (e.g. G00, DKSW03);

6. *reducing the mass resolution of a simulation causes lower resolution simulations to "peel" away from the highest resolution mass function* at intermediate-to-low subhalo masses. We estimated the lowest subhalo mass at which the lower resolution mass functions first deviated from the higher resolution mass functions by more than the fractional Poisson error in the higher resolution mass functions; this defined the converged subhalo mass, $M_{\rm conv}$, for the lower resolution simulation, from which we estimated $N_{\rm conv}$, the converged number of particles per subhalo. We found that $N_{\rm conv} \simeq 50$ in three of the four simulations;

7. *the spherically averaged number density profiles of subhalos measured for high and low resolution runs are in good agreement at radii $r \gtrsim r_{200}$, but reducing the mass resolution results in profiles that are depressed relative to the highest resolution case inside r_{200},* indicating the number of subhalos at a given radius falls as the mass resolution is decreased, that is, overmerging becomes an increasingly important effect in the lower resolution simulations. We found that all the subhalo profiles were *antibiased* with respect to the dark matter profile, but the antibias is more severe for lower resolution runs.

We noted in § 3.1 that the literature on this subject is relatively meagre. As we have already mentioned, Ghigna et al. (2000) performed a similar study, comparing the mass and velocity distribution functions, number density profiles and mass fractions in two simulations of the same cluster mass halo in which the mass and force resolution

were increased by factors of 8 and 2 respectively. They found good agreement between the subhalo mass fractions and the distributions of subhalo masses and peak circular velocities agreed where both samples were complete.

However, they defined completeness in terms of a model, developed in Ghigna et al. (1998), in which they assumed that subhalos could be treated as tidally stripped isothermal spheres orbiting in a larger isothermal potential, and identified a threshold *peak circular velocity* below which subhalos were likely to be compromised by numerical artifacts.

As a result, it is difficult to compare our result - that the abundance of subhalos with more than $N_{\rm conv} \simeq 50$ particles is unaffected by numerical resolution - with the Ghigna et al. (2000) result in detail; we could assume a concentration (derived from the Bullock et al. (2001) or the Eke, Navarro & Steinmetz (2001) prescriptions for concentration) to determine a peak circular velocity for a given subhalo bound mass, but invariably this concentration will be an underestimate. To paraphrase Ghigna et al. (1998), subhalos tend to be more concentrated than isolated counterparts with similar masses.

We conclude that a more comprehensive convergence study - similar in spirit to the convergence study of chapter 2 - which surveys the impact of gravitational softening, accuracy of timestepping, starting redshift, etc..., is required. Such a rigourous and exhaustive study would require many high resolution simulations with 128^3 runs providing the bulk of the *low resolution* simulations, similar to the workhorse 32^3 runs used in chapter 2; lower resolution simulations quite simply would not resolve sufficient numbers of subhalos and all but the most massive subhalos in these simulations would be susceptible to enhanced disruption due to finite resolution. However, such an undertaking seems necessary if we are to provide accurate convergence criteria for the abundance and perhaps the internal structure of the substructure.

Chapter 4

The Structure of ΛCDM Halos on Dwarf Galaxy Scales

4.1 Introduction

The Cold Dark Matter (CDM) model has come to represent one of the cornerstones of modern cosmology and is widely regarded as fundamental to any plausible theory of cosmological structure formation. Predictions based on this model, and in particular the ΛCDM variant in which the global dynamics of the Universe are dominated by some form of "dark energy" at the present epoch (for example, a cosmological constant (e.g. Carroll & Mersini (2001)) or quintessence (e.g. Caldwell et al. (2003))), are consistent with the results of a number of key observations. These include measurements of the shape and amplitude of temperature fluctuations in the Cosmic Microwave Background (e.g. de Bernardis et al. (2000), Balbi et al. (2000)), the inferred redshift-luminosity relation for distant supernovae (e.g. Riess et al. (1999), Perlmutter et al. (1999)) and the present day abundance of massive clusters (e.g. Eke et al. (1998), Bahcall & Fan (1998)). However, attempts to both clarify *and* verify the ΛCDM model's predictions on small scales, in the innermost parts of galaxies, have proven extremely challenging.

In this regime, gravitational clustering is a highly nonlinear problem and so high resolution cosmological simulations that follow the formation and evolution of individual dark matter halos from high redshift have been required to establish the predictions of the model (e.g. Navarro, Frenk & White (1996, 1997), hereafter NFW; Moore et al. (1999); Ghigna et al. (1998, 2000); Jing & Suto (2000); Klypin et al. (2001)). These studies robustly predict that the central densities of CDM halos increase without apparent limit as we probe smaller scales, i.e. $\rho \propto r^{-\alpha}$ where $1 \lesssim \alpha \lesssim 1.5$ as $r \to 0$ (e.g. NFW (1996), Moore et al. (1999)). Indeed, cuspy dark matter density profiles appear to be a generic

prediction of all CDM models (NFW (1997)). We conclude that placing observational constraints on the structure of the innermost parts of galactic dark matter halos should provide crucial evidence that can be used to establish the validity of the CDM paradigm.

However, attempts to determine the detailed spatial distribution of dark matter in the centres of halos are often dogged by uncertainty, which derives from degeneracies in fitting parameterised models for the galaxy's mass components. If we consider the particular case of mass decomposition of a galactic rotation curve, we find that, in the most general case, we must constrain the contribution of the stellar disk and bulge, gaseous disk and dark matter halo to the measured velocity at a given radius. The contribution of the gaseous component can be obtained by direct measurement and so is well constrained. On the other hand, the contribution of the stellar components is very uncertain because we have no absolute way of determining the amount of mass contained in stars, and therefore we must make fundamental assumptions about the stellar mass-to-light ratio, $\Upsilon_* = (M/L)$. Although we can estimate upper limits on Υ_* using population synthesis models (e.g. Bell & de Jong (2000)), it is clear that the freedom introduced by it introduces degeneracies when trying to uniquely determine a mass model for the halo.

Thus, while it is possible to derive strong constraints on the structure of the dark matter halo beyond the optical radius of the galaxy, the presence of the stellar disk effectively masks its structure within this radius. This is precisely the region that is of most interest for comparison with the predictions of the CDM model.

As a result, considerable attention has focused on the rotation curves of late-type dwarf spirals and low surface brightness galaxies (LSBs). These systems do not possess significant stellar bulges and it has been argued that their stellar disks are not dynamically important (e.g. de Blok & McGaugh (1996)); indeed, many late-type dwarfs are believed to be completely dominated by dark matter within their optical radii, as typified by the archetypal DDO 154 (Carignan & Freeman (1988)). Rotation curves are constructed by measuring the motions of their neutral hydrogen (HI) content. Thus the advantage of studying these "dark matter dominated" systems comes about because the ambiguity presented by uncertainty in Υ_* is removed and so mass decomposition should be a comparatively well defined exercise.

Initial studies suggested that the dark matter halos of dark matter dominated galaxies

could be well described by the pseudo-isothermal profile*,

$$\rho(r) = \frac{\rho_0}{1 + (r/r_c)^2} \tag{4.1}$$

where r_c is the core radius of the halo (typically ~ 1 kpc for a dwarf) and ρ_0 is the core density. In other words, halos with soft central cores, or in some cases very shallow cusps, appeared to provide a better fit to the data than the cuspy halos predicted by CDM, as noted by Flores & Primack (1994), Moore (1994), Burkert (1995), McGaugh & de Blok (1998) and Kravtsov et al. (1998), amongst others. However, both van den Bosch & Swaters (2001) and van den Bosch et al. (2001a) claimed that the data used to derive fits to mass models were compromised by insufficient spatial resolution, such as beam smearing in HI studies. This has the effect of "smearing out" velocity gradients in the centres of galaxies, resulting in a rotation curve that is artificially shallow on the scales that are of most interest for comparison with theory. As a result, once resolution effects were accounted for, the quality of the data were found to be insufficient to effectively discriminate between different mass models.

Recent published observations of dwarfs and LSBs now have sufficiently high spatial resolution to measure reliably the innermost parts of the rotation curves (e.g. Swaters et al. (2000, 2003), de Blok et al. (2001a,b), Weldrake et al. (2003), Bolatto et al. (2002), Simon et al. (2003)), and so we might expect the results of mass modelling to be more discriminating. Unfortunately, although the quality of the data has improved, the interpretation of these data and the conclusions that can be drawn from mass modelling are still the subject of heated debate. Swaters et al. (2000, 2003) have derived mass models from high resolution dwarf and LSB rotation curves and find that their data are consistent with both the cuspy halos predicted by CDM and halos with soft central cores. On the other hand, de Blok et al. (2003) performed a series of simulated observations using their own data and procedures, and found that the "implied observational signature of CDM halos is strong and if present should be easily seen", even in the presence of systematic errors.

The conflicting conclusions drawn by, most recently, Swaters et al. (2003) and de Blok et al. (2003), indicate that, while high resolution rotation curve data are available, ambiguities in the resulting interpretation of the data used in mass modelling render any comparison with the predictions of CDM tentative at best. Indeed, the lack of convergence

*See § 1.4 for further discussion.

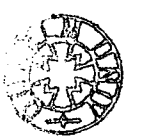

in the conclusions drawn from overlapping data (Hayashi et al. , in preparation) suggest that a convergence study, in the spirit of chapter 2, is necessary.

Nevertheless, the apparent discord between the structure of dark matter halos predicted by high resolution simulations of CDM cosmologies and the structure of dark matter halos implied by high resolution rotation curve studies has prompted discussion of a "small scale crisis" in the CDM model and kindled heated debate. Although substantial progress has been made recently in reconciling the predicted apparent overabundance of subhalos in galactic CDM halos with the observed abundance of satellite galaxies in the local group (e.g. Benson et al. (2002), Bullock et al. (2001a), Somerville (2002)) and understanding why simulations of galaxy formation in the ΛCDM cosmology produce galactic disks an order of magnitude smaller than observed (Thacker et al. (2001)), there continues to be speculation about the measures needed to reconcile the current paradigm for cosmological structure formation with observational evidence for soft, diffuse cores in the centres of galaxies. These measures have included astrophysical processes, such as explosive stellar feedback (e.g. Navarro et al. (1996), Gnedin & Zhao (2002)) and gravitational scattering by black holes (e.g. Milosavljevic & Merritt (2001), Merritt & Cruz (2001)) and stellar bars (e.g. Weinberg & Katz (2002)), alternative forms of dark matter, such as warm dark matter (Bode et al. (2001)) and self-interacting dark matter (Spergel & Steinhardt (2000)), and in some cases, the invocation of modified gravity (e.g. Milgrom (1983)), magnetic fields (e.g. Battaner et al. (1992)), etc...

However, we stressed in § 1.1 that it would be premature to discard the CDM model without fully investigating the predictions of the model on the scales of interest and questioning the validity of the assumptions that are made when comparing these predictions with observations. Recent studies such as Swaters et al. (2003), de Blok et al. (2003) and Weldrake et al. (2003) have addressed the impact of observational effects and assumptions made in mass decomposition on the results of mass model fitting to rotation curves, but as we noted above, these have offered conflicting results.

In contrast, the results presented in chapter 2 indicate that we now have a good understanding of the impact our choice of numerical parameters can have on the mass distribution of simulated CDM halos. We found that, provided the gravitational softening is chosen such that particle discreteness effects are negligible, we can achieve reproduce the spherically averaged circular velocity to better than 10% accuracy at radii where

- the timestep is much shorter than the local orbital timescale;

- the accelerations do not exceed a characteristic acceleration imprinted by the gravitational softening;

- enough particles are enclosed so that the collisional relaxation timescale is longer than the age of the universe.

In particular, we found that it is the number of particles that offers the most stringent criterion for convergence; of order ~ 1 million particles are needed to resolve the kind of overdensities ($\sim 10^6$) that we expect to measure at $\sim 1\% r_{200}$.

These convergence criteria have allowed us to address the principal aim of this thesis - to provide a sample of high resolution simulations of dark matter halos with masses $M \sim 10^{10} M_{\odot}$, comparable to those of dwarf galaxy halos, forming in ΛCDM cosmology. The mass and force resolution of these simulations has been sufficient to reliably resolve the mass distribution within the central few kiloparsecs of the halos and can, in turn, accurately predict the shape of the dark matter rotation curve on sub-kiloparsec scales, $\sim 1\% r_{200}$.

We present the results of our analysis of these simulations in this chapter. In particular, we focus on the properties of the halos between redshifts $0 \lesssim z \lesssim 3$, during which time between $50-80\,\%$ of the final (i.e. $z = 0$) mass is accreted, and address the following questions;

- When do dwarf galaxy halos form in the ΛCDM cosmology? What kind of mass accretion histories do they have?

- How do properties of their spherically averaged mass profiles, such as the central slope, shape and concentration, compare with theoretical predictions? In particular, do the NFW and Moore et al. profiles provide an adequate representation of the mass profiles?

- What kind of shapes do these objects have? How are these shapes supported? What do the spherically averaged kinematical profiles of these objects tell us about their dynamical state?

- Do dwarf galaxy halos contain a significant population of substructure halos? How much of their mass is bound to these substructures? How is this mass distributed amongst these substructure?

- What is the shape of gravitational potential? Is the potential symmetric and stable? By satisfying these two requirements, it is likely that the potential could support closed orbits and therefore a disk.

The question of whether there are any systematic differences between the mass profiles of dwarf galaxy halos and those of more massive systems such as galaxy and cluster halos is of obvious interest, and is addressed in considerable detail in chapter 5.

This chapter can be outlined as follows. In § 4.2, we present details of the technique that we used to generate initial conditions for the dwarfs, and the physical properties of the halos at various redshifts between $0 \leq z \lesssim 3$ are summarised. Key features of the methods used are sketched in § 4.3. We describe our results in some detail in § 4.4, including the spherically averaged mass and kinematical profiles, the shapes, the substructure content, and our analysis of the structure of the smooth gravitational potential within these galaxies. Finally, we present the principal results of our analysis in our conclusions in § 4.5.

4.2 The Simulations

4.2.1 The N-Body Code

All of the simulations described in this chapter have been performed using the parallel N-body code `GADGET` (Springel et al. (2001)), which is described in detail in § 2.2.1. Note that we have adopted the `DtCrit=0` criterion to evaluate individual, adaptive timesteps with which particle orbits are integrated; for each particle i,

$$\Delta t_i = \eta_{a\epsilon}\sqrt{\epsilon_i/a_i}, \tag{4.2}$$

where Δt_i, ϵ_i and a_i correspond to the particle's timestep, gravitational softening and magnitude of the gravitational acceleration, and $\eta_{a\epsilon}$ determines the accuracy of the time integration; we set $\eta_{a\epsilon} = 0.01$.

4.2.2 The Cosmological Model

We are interested in studying the properties of $10^{10}\mathrm{M}_{\odot}$ dark matter halos forming in the ΛCDM cosmology. Such a model presupposes that we live in a spatially flat Universe with low matter density, whose global dynamics are dominated at the present epoch by some

form of "dark energy". We have therefore chosen concordance values for the cosmological parameters - $\Omega_0 = 0.3$, $\Omega_\Lambda = 0.7$ and $h = 0.65$ - and assumed $\sigma_8 = 0.9$ at $z = 0$.

We have adopted a theoretical power spectrum, $P(k)T(k)$, consisting of the *Harrison-Zel'dovich* initial power spectrum $P(k) \propto k$, modified by the Bardeen et al. (1986) (BBKS) cosmological transfer function, $T(k)$;

$$T(k) = \frac{\ln(1+2.34q)}{2.34q}[1 + 3.89q + (16.1q)^2 + (5.4q)^3 + (6.71q)^4]^{-1/4}. \quad (4.3)$$

where

$$q = \frac{k/h\mathrm{Mpc}^{-1}}{\Gamma} \quad (4.4)$$

with a shape parameter $\Gamma = \Omega_\mathrm{m} h = 0.2$. Thus

4.2.3 The Initial Conditions

We have already described in some detail our procedure for setting up initial conditions (hereafter ICs) for high resolution cosmological simulations of individual dark matter halos in chapter 2. The procedure is well defined and can be summarised as follows;

1. *Perform a standard cosmological simulation of a representative volume.* A Fourier representation of a Gaussian random field characterised by the theoretical power spectrum is generated on a large cubic mesh and displacements and velocities are computed (using the Zel'dovich approximation assuming only growing modes are present) for N^3 particles initially arranged on a cubic grid. These constitute the initial conditions for a low resolution simulation of a sufficiently large cosmological volume (the "parent" simulation) and are evolved to $z = 0$. All particles have the same mass and gravitational softening.

2. *Select candidate halos for resimulation.* Candidate halos for resimulation are selected according to some criterion - typically mass or circular velocity - from catalogues of particle groups generated using an algorithm such as *friends-of-friends* (Davis et al. (1985)). Additional criteria may be applied, for example, the requirement that candidates be relatively isolated from massive neighbours, thus increasing the likelihood that they are in dynamical equilibrium.

3. *Define the high resolution region.* The positions of all particles within within $\sim 2 - 3\, r_{200}$ of the candidate at $z = 0$ are traced back to $z = \infty$. These positions are then used to define the extent of a "high resolution" region, a small cubic volume

within the original cosmological box that encompasses the region that collapses to form the final halo at $z = 0$.

4. *Create the displacement field for the high resolution particles.* A new Fourier representation of a Gaussian random field characterised by the theoretical power spectrum is generated within the high resolution region; this consists of recreating the original Fourier representation used in the parent simulation, retaining the phases and amplitudes of the original Fourier components, and adding additional waves in the high resolution region up to the Nyquist frequency of the high resolution particle grid.

5. *Capture the correct tidal effects.* The particle distribution outside of the high resolution region is coarsely sampled in order to accurately model the tidal forces that act on the high resolution particles; particles in the original low resolution simulation are binned into cells whose size varies in proportion to their distance from the high resolution cube.

   In addition, particles in the high resolution region that do not end up near the system of interest are coarse sampled in a similar manner to increase the yield - that is, the number of high resolution particles in the final object relative to the total number - and the efficiency of the simulation.

Although this approach has proven very successful for generating high resolution initial conditions for resimulations of larger mass objects such as galaxy and cluster mass halos, we have found that this approach needs to be modified when dealing with objects with masses similar to those of dwarf galaxy halos. We use as our parent simulation a box of length $L = 35.325h^{-1}$ Mpc (comoving) run in the ΛCDM cosmology; the resulting particle mass is $m_{\rm p} \sim 10^9 h^{-1}{\rm M}_\odot$, and implies that a typical dwarf galaxy halo in this simulation would be resolved with ~ 10 particles. We conclude that the mass resolution in our parent is insufficient to adequately resolve dwarf mass halos.

We overcome this by selecting a random spherical patch in the parent simulation whose mean enclosed density is close to the mean density of the Universe and resimulate it at higher resolution. The particle mass in our high resolution region is $m_{\rm p} \sim 5 \times 10^7 h^{-1}{\rm M}_\odot$, and we find that a typical dwarf galaxy halo will contain ~ 500 particles, which we consider adequately resolved.

We are then in a position to start selecting candidate dwarf halos for resimulation (as in step 2) and the procedure continues as in steps 2 to 5 above. This process is illustrated

in figure 4.1 where we show the stages involved in selecting a candidate dwarf (in this case, **dH04**) for resimulation. Details of the numbers of particles and the dimensions of the high resolution and parent cubes used in the simulation can be found in table 4.1.

4.2.4 The Halos

We wish to investigate the structural and kinematical properties of dark matter halos with masses $M \sim 10^{10}\mathrm{M}_{\odot}$ forming in the ΛCDM cosmological model. In particular, we are interested in the shape of the spherically averaged density and circular velocity profiles at radii of order $\sim 1\%$ of the virial radius, r_{200}. According to the convergence criteria set out in chapter 2, we require of order 10^6 particles within r_{200} if we are to reliably resolve the mass distribution on these scales. We present details of the principal numerical parameters used in these simulations, including the high resolution particle mass (m_{hres}) and gravitational softening (ϵ_{hres}), in table 4.1.

We show projected maps of the dark matter density distribution at $z = 0$ in and around the four halos in figure 4.2. We have smoothed the mass (particles) in cubes centred on the halos and containing all material within $\sim 2r_{200}$ - corresponding to a box of side $0.1h^{-1}$ Mpc - and projected the smoothed distribution onto a mesh. Each mesh point is weighted according to the logarithm of its projected surface density, and so the "brighter" the mesh point, the higher the projected surface density; see § 3.2.1 for further details. We notice that the centres of the halos tend to be the brightest points in these maps, although there are many distinct bright regions in and around the halo, corresponding to substructure within r_{200} and orbiting halos outside of r_{200}.

Physical properties of the halos at redshifts between $0 \leq z \lesssim 3$ are given in table 4.2; we give values for the halo's virial mass, M_{200}; virial radius, r_{200}; the circular velocity at r_{200}, V_{200}; the number of particles within r_{200}, N_{200}; its spin parameter, λ; and the virial ratio, $2\mathrm{T}/|\mathrm{W}|$.

Recall that we define the virial radius to be that radius that encloses a spherical volume whose mean overdensity is 200 times the critical density, $\rho_{\mathrm{crit}} = 3H^2/8\pi G$, at the given redshift. However, we might consider using the more general overdensity criterion of Δ_{vir} as determined for the spherical top-hat model (Lacey & Cole 1993, Eke et al. 1996) when computing the spin parameter and the virial ratio for a given halo; $\Delta_{\mathrm{vir}} \simeq 97(169)$ at $z = 0(2)$ for a ΛCDM cosmology. The virial radius, r_{vir}, defined in terms of Δ_{vir} is

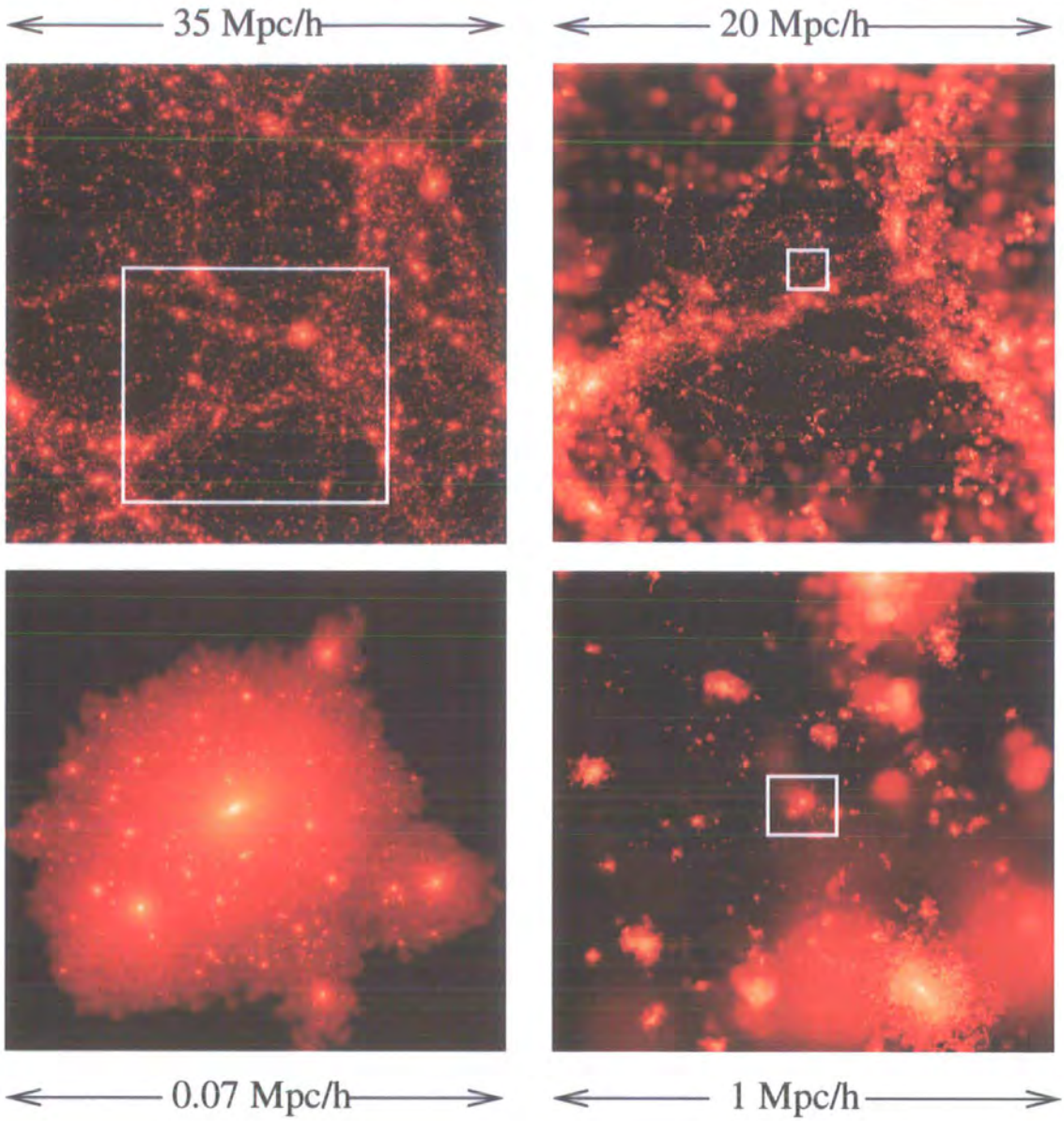

Figure 4.1: **Resimulating Dwarf Galaxy Halos at High Resolution.** This sequence of panels highlights the different stages in the resimulation process. The mass resolution of our original parent simulation (top left panel) is insufficient to resolve dwarf mass halos. The particle mass in this simulation was $m_{\rm p} \sim 10^9 h^{-1}{\rm M}_\odot$, implying that a typical dwarf galaxy halo would contain ~ 10 particles. We selected a random spherical volume (within the white box in parent) whose mean enclosed density was close to the mean density of the Universe and resimulated this at higher resolution (top right panel). After resimulating this region with a particle mass of $m_{\rm p} \sim 5 \times 10^7 h^{-1}{\rm M}_\odot$, we could resolve a typical dwarf galaxy halo with ~ 500 particles. Potential candidates are then selected from this region; we illustrate the case of `dH04`. The white box in the upper right hand panel corresponds to a projected cube of side $\sim 1h^{-1}$Mpc, shown in the bottom right hand panel; The friends-of-friends group corresponding to `dH04` at $z = 0$ is shown in the bottom left hand panel.

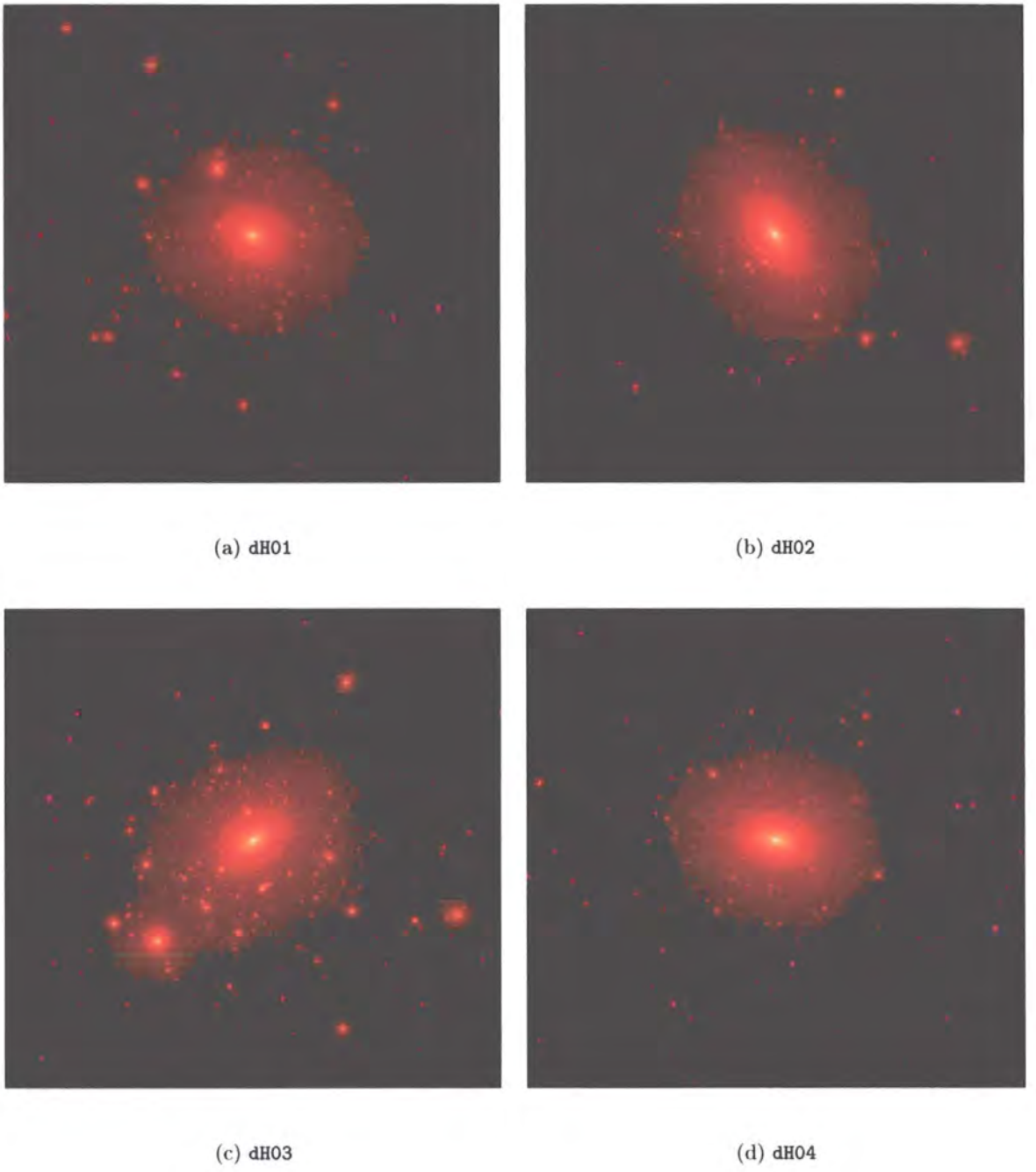

(a) dH01 (b) dH02

(c) dH03 (d) dH04

Figure 4.2: **Projected maps of the dark matter density distribution in our four dwarf galaxy halos at** $z = 0$. We have identified all the mass (particles) within a cube of $100\,h^{-1}$ kpc on a side, centred on the halo, and projected a smoothed distribution onto a two dimensional (1024^2) mesh. Particles were weighted according to their local density, determined using a SPH smoothing kernel computed over the nearest 32 neighbours. Each mesh point (or pixel) is weighted according to the logarithm of its projected mass density; the brighter the mesh point, the greater the projected density at that point.

expressed as,

$$r_{\rm vir} = \left(\frac{1}{\Delta_{\rm vir}} \frac{1}{\rho_{\rm crit}} \frac{3}{4\pi} M_{\rm vir} \right)^{1/3} ; \tag{4.5}$$

For completeness, we quote values for λ and $2T/|W|$ computed at both the general $r_{\rm vir}$ and at r_{200}.

Table 4.1: **Numerical Parameters of the Simulations.** Note that all simulations were run assuming a ΛCDM cosmogony with $\Lambda_0 = 0.7$ and $\Omega_0 = 0.3$ and $\sigma_8 = 0.9$. For each halo, we show (1) the size of the simulation box, $L_{\rm box}$ in units of h^{-1} Mpc (comoving), (2) the "effective" size of the high resolution cube, $L_{\rm sbox}$ in units of h^{-1} Mpc (comoving), (3) the number of particles in the simulation box, $N_{\rm box}$, (4) the number of particles in the high resolution region, $N_{\rm hres}$, (5) the mass of the high resolution particles, $m_{\rm hres}$, in units of $h^{-1}M_\odot$, (6) the gravitational softening of the high resolution particles, $\epsilon_{\rm hres}$, in units of h^{-1} kpc, (6) the minimum believable radius, $r_{\rm min}$, expressed as a percentage of r_{200}, and (7) the starting redshift of the simulation, z_i.

	$L_{\rm box}$ [h^{-1} Mpc]	$L_{\rm sbox}$ [h^{-1} Mpc]	$N_{\rm box}$	$N_{\rm hres}$	$m_{\rm hres}$ [$h^{-1}M_\odot$]	$\epsilon_{\rm hres}$ [h^{-1} kpc]	$r_{\rm min}$ [$\%r_{200}$]	z_i
dH01	35.325	2.5	5741027	3422221	9.97×10^3	0.0625	1.05	74
dH02	35.325	2.7	5084492	2710686	1.18×10^4	0.0625	1.09	49
dH03	35.325	1.6	3837889	2462551	8.24×10^3	0.0625	1.02	49
dH04	35.325	1.5	1943130	3505274	9.57×10^3	0.0625	0.92	49

Table 4.2: **Physical Properties of the Simulated Dwarf Halos at** $0 \leq z \lesssim 2$ For each of the dwarf halos and their most massive progenitors at redshift z, we show (1) the virial mass, M_{200}, in units of $h^{-1}\mathrm{M}_{\odot}$, (2) the virial radius, r_{200}, in units of h^{-1} kpc, (3) the circular velocity at r_{200}, V_{200}, in units of km/s, (4) the number of particles interior to r_{200}, N_{200}, (5) the dimensionless spin parameter, λ, and (6) the ratio of twice the kinetic energy to the potential energy of the halo, $2\mathrm{T}/|\mathrm{W}|$; we expect this ratio to approach unity if the halo is in virial equilibrium. Both λ and $2\mathrm{T}/|\mathrm{W}|$ have been evaluated at the virial radius, r_{vir}, but we also quote their values at r_{200} (in brackets) ; see text for further details.

	z	M_{200} $[\mathrm{h}^{-1}\mathrm{M}_{\odot}]$	r_{200} $[\mathrm{h}^{-1}$ kpc]	V_{200} [km/s]	N_{200}	λ	$2T/\lvert W\rvert$
dH01							
	0.0	0.781	32.26	32.3	783309	0.0649 (0.0627)	1.06 (1.08)
	0.51	0.703	25.89	34.19	704347	0.0677 (0.0699)	1.09 (1.11)
	0.99	0.621	20.54	36.11	619884	0.0683 (0.0725)	1.16 (1.17)
	1.51	0.443	15.17	35.47	443149	0.0582 (0.0569)	1.16 (1.19)
	2.01	0.322	11.56	34.66	323307	0.0453 (0.0395)	1.25 (1.35)
dH02							
	0.0	0.923	34.17	34.12	778369	0.0325 (0.0307)	1.03 (1.06)
	0.47	0.887	28.46	36.64	742587	0.0422 (0.0310)	1.15 (1.15)
	0.99	0.887	23.16	40.62	674574	0.0339 (0.0609)	1.78 (1.46)
	1.47	0.770	18.50	42.35	649109	0.0270 (0.0257)	1.22 (1.23)
	2.07	0.503	13.21	40.48	423358	0.0336 (0.0271)	1.16 (1.24)
dH03							
	0.0	0.778	32.23	32.25	944050	0.0222 (0.0153)	1.07 (1.15)
	0.47	0.611	25.15	32.34	738473	0.0205 (0.0230)	1.13 (1.17)
	0.99	0.518	19.37	33.95	627861	0.0276 (0.0218)	1.20 (1.16)
	1.47	0.398	14.84	33.98	482329	0.0313 (0.0304)	1.23 (1.16)
	2.07	0.354	11.75	36.02	429160	0.0425 (0.0373)	1.37 (1.25)
dH04							
	0.0	0.959	34.54	34.58	1000702	0.0349 (0.0329)	1.07 (1.08)
	0.47	1.025	29.78	38.51	1070352	0.0432 (0.0364)	1.36 (1.39)
	0.99	0.501	19.10	33.63	523870	0.0138 (0.0124)	1.07 (1.09)
	1.47	0.435	15.25	35.05	454671	0.0151 (0.0179)	1.09 (1.12)
	2.07	0.419	12.41	38.15	438086	0.0190 (0.0238)	1.17 (1.20)

4.3 Methods

4.3.1 Identification of the Halo

We have adopted an iterative method for determining the centre of the halo in which we recursively compute the average position of all particles within a shrinking spherical volume until either a convergence criterion is met or the number of particles has fallen below some predefined threshold value. Details of this method have been described already in chapter 2, but we recap the principal features here for the sake of completeness.

As an initial step we determine the extent of the particle distribution, rescale the particle coordinates in units of the box length and compute the average centre of all the particles within this region; that is, we compute

$$x^i_{\rm cen} = \frac{1}{N}\sum_j^N x^{i,j} \tag{4.6}$$

where $x^{i,j}$ is the Cartesian coordinate x^i of the jth particle, and N is the number of particles in the volume. If the number of particles in the region is less than the threshold n_{min}, which we set to be the minimum of 1% of the number of particles in the high resolution region or 1000 particles, we define $x^i_{\rm cen}$ to be the centre.

This average centre represents an initial guess for the centre of the shrinking sphere. We then iteratively compute the average centre for all particles within this sphere, resetting the centre of the sphere to the last computed centre at each step, and reducing its radius by 2.5%. The iteration is stopped when the number of particles remaining in the sphere falls below n_{min}. The final centre is then rescaled and expressed in the original length units.

As we noted in chapter 2, halo centres identified in this way are robust and do not depend on the initial parameters chosen to start the iteration, provided the initial sphere is large enough to encompass a large fraction of the system. In a multi-component system such as a dark matter halo with substructure, this procedure isolates the densest region within the largest subcomponent. In more regular systems, the centre returned by this procedure is in good agreement with centres obtained by weighting the centre by mass, local density or gravitational potential of each particle.

4.3.2 Identifying Bound Substructure within the Halo

Finding a reliable automated method for the identification of substructure within a dark matter halo has proven to be both technically challenging and computationally expensive. Several popular techniques have been developed, for example, the `DENMAX` algorithm (Gelb & Bertschinger (1994)) and its derivative `SKID` (Stadel (2001)), and some of these are briefly described in § 3.2.2. However, we have chosen to adopt the `SubFind` algorithm of Springel et al. (2001a) throughout our analysis. Details of the algorithm are presented in § 3.2.2, but it may be briefly summarised as follows;

- A friends-of-friends catalogue of parent halos is generated.
- Candidate substructure halos (hereafter subhalos) are identified as local overdensities in the density field of each of the parent halos.
- The binding energies of particles within each candidate subhalo are computed iteratively until only particles with negative binding energies remain.
- Of the remaining candidates, only those groups that contain $N \geq N_{min}$ particles are retained. These particle groups are then referred to as *subhalos*.

We have chosen to set the threshold N_{min} to 20 particles.

4.3.3 Measuring the Shapes of Halos

We have adopted a method similar in spirit to that used by Jing & Suto (2002) to determine the shapes of isodensity surfaces within dark matter halos. This involves isolating a given isodensity shell by selecting particles according to their local density (computed using a SPH style smoothing kernel), constructing the moment of inertia tensor for the particles in this shell and deducing the axis ratios and orientation of the principal axes by solving the secular equation. This is a particularly attractive approach to shape-finding because it is intuitive and relatively straightforward to implement.

Information about the shape of an object can be determined by taking moments of its mass distribution. The second moment corresponds to the *moment of inertia tensor*; for a collection of particles, this can be written as

$$I_{jk} = \sum_{i=1}^{N} m_i \left(r_i^2 \, \delta_{jk} - x_{i,j} \, x_{i,k} \right) \tag{4.7}$$

where m_i is the mass, r_i the radius and $x_{i,j}$ the Cartesian coordinates of the ith particle.

If we interchange indices j and k in equation 4.7, we notice that $I_{jk} = I_{kj}$, that is, the inertia tensor is symmetric. Furthermore, if we change the coordinate centre or the axis about which the moment is taken, it is clear that its components will change. The symmetry of I_{jk} implies that we can define a coordinate transformation (rotation) such that the moment of inertia tensor about an axis *through the centre of mass* is diagonal in this new frame of reference, that is, $I_{jk} = 0$ if $j \neq k$.

Such a coordinate transformation can be deduced by solving the secular equation,

$$|I_{jk} - \lambda I| = 0 \tag{4.8}$$

where λ represents the eigenvalues and in this particular instance, I is the unit matrix. The ordered eigenvalues, I_{xx}, I_{yy} and I_{zz}, correspond to the diagonal components or *principal moments of inertia*,

$$I_{xx} = \sum_{i=1}^{N} m_i(y_i^2 + z_i^2), \qquad I_{yy} = \sum_{i=1}^{N} m_i(x_i^2 + z_i^2), \qquad I_{zz} = \sum_{i=1}^{N} m_i(x_i^2 + y_i^2). \tag{4.9}$$

These can be related to $a \geq b \geq c$, the long, medium and short axes respectively. Note that the Cartesian coordinates (x_i, y_i, z_i) are defined with respect to the normalised eigenvectors, $\hat{e}_x$, $\hat{e}_y$ and $\hat{e}_z$, the *principal axes* in the diagonalised frame; x, y and z lie along the major, intermediate and minor axes respectively. If the principal moments of inertia of the object can be expressed in a closed analytic form, then it is often possible to relate these moments to its shape.

In the particular case of a thin ellipsoidal shell, it is straightforward to show that

$$I_{xx} = \frac{M}{3}\left(b^2 + c^2\right), \qquad I_{yy} = \frac{M}{3}\left(a^2 + c^2\right), \qquad I_{zz} = \frac{M}{3}\left(a^2 + b^2\right). \tag{4.10}$$

It follows that we can express the axis ratios of the ellipsoid in terms of the principal moments of inertia;

$$\frac{b}{a} = \sqrt{\frac{I_{xx} - I_{yy} + I_{zz}}{-I_{xx} + I_{yy} + I_{zz}}} \qquad \frac{c}{a} = \sqrt{\frac{I_{xx} + I_{yy} - I_{zz}}{-I_{xx} + I_{yy} + I_{zz}}}. \tag{4.11}$$

The general method we have just described should be suitable for determining the shapes of dark matter halos that form in cosmological N-body simulations, and suggests the following procedure for shape finding;

- Compute the local density for each particle within a volume encompassing the halo. For this purpose, we have made use of the code **smooth**.

  smooth was developed by the NASA HPCC ESS group at the University of Washington and it is freely available online[†]. It computes the local density at the position of particle i by spatially averaging over the particle's nearest N_n neighbours,

$$\rho(r_i) = \sum_{j=1}^{N_n} m_j \, W(r_{ij}; h); \tag{4.12}$$

  We have chosen to set N_n to 32 particles. $W(r, h)$ corresponds to the *smoothing kernel* and h is an adaptive *smoothing length* that varies according to the local number density. We have chosen to set $W(r, h)$ to be the symmetric smoothing kernel commonly used in SPH calculations,

$$W(r_{ij}; h) = \frac{1}{2} \left(W(r_{ij}, h_i) + W(r_{ij}, h_j) \right), \tag{4.13}$$

  which has a functional form

$$W(r_{ij}, h_i) = \frac{1}{\pi \, h_i^3} \begin{cases} 1 - \frac{3}{2}\left(\frac{r_{ij}}{h_i}\right)^2 + \frac{3}{4}\left(\frac{r_{ij}}{h_i}\right)^3 & 0 < r_{ij} < h_i, \\ \frac{1}{4}\left(2 - \frac{r_{ij}}{h_i}\right)^3 & h_i < r_{ij} < 2\,h_i, \\ 0 & 2\,h_i \leq r_{ij}, \end{cases} \tag{4.14}$$

  Here h_i is the smoothing length of particle i, and r_{ij} corresponds to the magnitude of the separation vector,$|\mathbf{r_i} - \mathbf{r_j}|$. Other functional forms are possible, but this particular choice has compact support - only particles within a given volume contribute to the sum.

- Sort particles according to local density and retain only those with densities satisfying some pre-defined criterion. In the limit of a smooth monolithic halo, we expect particles to be stratified in a series of concentric ellipsoidal shells. Therefore we identify particles with densities

$$\rho_{\rm s}^{(n)} = A^{(n)} \rho_{\rm crit}, \tag{4.15}$$

  where

$$A^{(n)} = 20 \times 5^{n-1} \quad \text{where} \quad (1 \leq n \leq 7) \tag{4.16}$$

  All particles that satisfy $0.97\,\rho_{\rm s}^{(n)} < \rho_i < 1.03\,\rho_{\rm s}^{(n)}$ are associated with these shells.

[†]The appropriate URL is **http://www-hpcc.astro.washington.edu/tools/smooth.html**

- Construct the moment of inertia tensor for each subset of particles (equation 4.7) and diagonalise by solving the secular equation (equation 4.8).

- Compute the axis ratios, b/a and c/a, using equation 4.11, and construct the rotation matrix, $\bar{R}$, which can be used to rotate the particle distribution into the principal axes frame.

Unfortunately, this straightforward approach implicitly assumes that the local density varies smoothly within the halo. However, high resolution dark matter halos contain a substantial amount of substructure, typically $\sim 10\%$ of the mass of the system, and this presents difficulties for the simple shape-finding procedure we have just described. If we try to identify particles with local densities in a given range, we isolate not only the iso-density surface of interest but also a multitude of disconnected dense knots, corresponding to particles in subhalos that satisfy the density threshold.

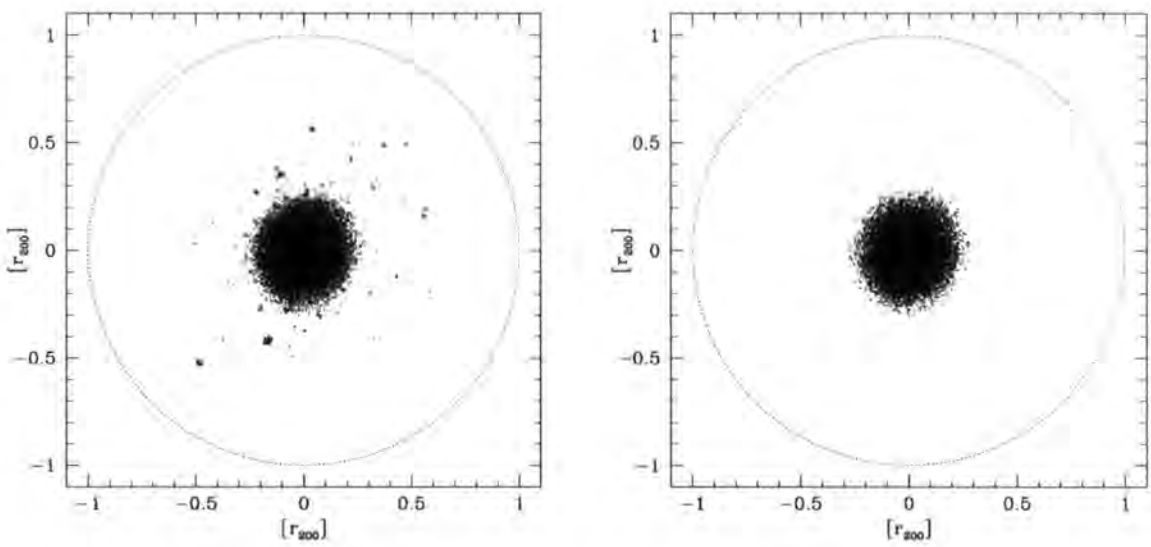

(a) With Substructure

(b) Without Substructure

Figure 4.3: **The Impact of Substructure on our Shape Finding Algorithm.** We show the projected particle distribution within r_{200} in dwarf halo `dH02` at $z = 0$. In figure 4.3(a), we retain the subhalos and show the projected distribution of all particles, whereas in figure 4.3(b), we show only those those particles with densities greater than $12500\,\rho_{\rm crit}$.

This is illustrated in figure 4.3(a) where we have plotted the projected particle distribution in halo `dH02` at $z = 0$; the particle distribution has been sampled to avoid

saturation. Figure 4.3(a) shows all particles within r_{200} with local densities greater than $12500\,\rho_{\rm crit}$. As expected, the bulk of these particles are concentrated in the centre of the halo, but there are also several tens of disconnected clumps containing high density particles scattered throughout the halo's volume - these correspond to subhalos.

Removing the substructure produces a much smoother halo, as we can see in figure 4.3(b); we show only those particles with local densities greater than $12500\,\rho_{\rm crit}$. All of the particles are now concentrated in the centre of the halo.

This clearly demonstrates that we must account for the presence of substructure in the halos when determining the shapes of isodensity shells. We therefore modify our original procedure as follows;

- Identify all bound substructure halos within the dark matter halo using the `SubFind` algorithm (§ 4.3.2) and remove them.
- Compute the local density at the position of each particle.
- Sort particles into shells determined by their local density. Estimate the mean radius and thickness (i.e. $5\,\sigma$) of the shell; if the separation between a particle and the shell exceeds some threshold value (typically several shell thicknesses), remove it from the shell. In general, these are particles associated with candidate subhalos that did not satisfy the criteria to be considered a subhalo, e.g. fewer particles than threshold $N_{\rm min}$.
- Construct the moment of inertia tensor for each isodensity shell and diagonalise it. The ordered eigenvectors correspond to the principal axes for that isodensity shell and the ordered eigenvalues can be used to compute the axis ratios. Further information, such as the orientation of these isodensity shells, can be derived from the eigenvectors.

The results of this method agree well with those of previous studies (e.g. Frenk et al. (1988), Katz (1991), Dubinski & Carlberg (1991), Warren et al. (1992), Jing & Suto (2002)).

4.3.4 Measuring the Smooth Gravitational Potential

We require a reliable and efficient method for computing a smooth estimate of the gravitational potential, $\Phi(\mathbf{r})$, at position $\mathbf{r}$ generated by a discrete set of particles, and so we

have adopted the *Self Consistent Field* method of Hernquist & Ostriker (1992). This approach involves solving Poisson's equation by expanding the density and potential in a set of basis functions. Although the method is described in considerable detail in Hernquist & Ostriker (1992), we highlight its principle features here.

We note that the Hernquist & Ostriker (1992) method has been implemented in the parallel N-body code described in Hernquist et al. (1995) and is publicly available[†], However, we have decided to implement the algorithm ourselves in a piece of serial code, specifically designed to for our own purposes.

The potential generated by an discrete mass distribution $\rho(\mathbf{r})$,

$$\rho(\mathbf{r}) = \sum_{i=1}^{N} m_i \delta(\mathbf{r} - \mathbf{r}_i), \tag{4.17}$$

can be expressed as

$$\Phi(\mathbf{r}) = -G \sum_{i=1}^{N} \frac{m_i}{|\mathbf{r} - \mathbf{r}_i|}. \tag{4.18}$$

where m_i is the mass of the ith particle and G is the gravitational constant. We seek a smooth estimate of this potential.

The *Self Consistent Field* method assumes that both the density and gravitational potential can be expanded as a set of *biorthogonal* basis functions, that is, the density and potential basis functions are mutually orthogonal[§]. Therefore we may express the local density and gravitational potential as

$$\rho(r) = \sum_{nlm} A_{nlm} \rho_{nlm}(r) \tag{4.19}$$

and

$$\Phi(r) = \sum_{nlm} A_{nlm} \Phi_{nlm}(r) \tag{4.20}$$

where n can be regarded as a radial *quantum* number, l,m are the corresponding angular *quantum* numbers and A_{nlm} represent the expansion coefficients. The assumption of biorthogonality ensures that there is a one-to-one relationship between the expansion coefficients of the density and the potential, and also that the individual harmonics ρ_{nlm} and Φ_{nlm} satisfy Poisson's equation

$$\nabla^2 \Phi_{nlm}(r) = 4\pi \rho_{nlm}(r) \tag{4.21}$$

[†]See `http://www.astro.psu.edu/users/steinn/src/scf.html` for details.

[§]More general formulations which do not require the functions to be biorthogonal are possible (Saha (1993)).

Dark matter halos are generally spheroidal systems and so it seems reasonable to expand in spherical coordinates and use spherical harmonics to characterise the angular dependence of the density and potential. Hence,

$$\rho(r,\theta,\phi) = \sum_{nlm} A_{nlm}\rho_{nl}(r)Y_{lm}(\theta,\phi) \tag{4.22}$$

and

$$\Phi(r,\theta,\phi) = \sum_{nlm} A_{nlm}\Phi_{nl}(r)Y_{lm}(\theta,\phi) \tag{4.23}$$

where $\rho_{nl}(r)$ and $\Phi_{nl}(r)$ are the radial basis functions, which will generally depend on both the radial and polar quantum numbers, and Y_{lm} are the familiar spherical harmonics.

We now require an analytic form for the basis function. The NFW profile defined in § 1.5.1,

$$\rho(r) = \frac{\rho_0}{r/r_s(1+r/r_s)^2}, \tag{4.24}$$

where ρ_0 is a characteristic density and r_s is the characteristic scale radius of the halo, appears to provide the obvious choice because it has been found to provide a good description of dark matter halos that form in cosmological simulations. However, it is not suitable as a basis function because of the form of the gravitational potential it generates,

$$\Phi_{\rm NFW}(r) = -\frac{v_{200}^2}{g(c)}\frac{\ln(1+cx)}{x}. \tag{4.25}$$

Here we have assumed that the halo has infinite radial extent; v_{200} corresponds to the circular velocity of the halo at the virial radius, r_{200}, $x = r/r_{200}$ is the radius normalised to r_{200}, c is the familiar concentration parameter (as defined in § 1.5.1), and $g(c)$ is the function

$$g(c) = \ln(1+c) - \frac{c}{1+c}. \tag{4.26}$$

The presence of the logarithmic term makes this an extremely unattractive basis function, and so we continue to follow Hernquist & Ostriker (1992) and use the spherically symmetric Hernquist profile (Hernquist (1990)),

$$\rho(r) = \frac{M}{2\pi}\frac{a}{r}\frac{1}{(a+r)^3}. \tag{4.27}$$

where a is the scale radius and M, the total mass, is related to the cumulative mass, $M(r)$, by the expression,

$$M(r) = M\frac{r^2}{(a+r)^2}. \tag{4.28}$$

It is straightforward to compute the gravitational potential,

$$\Phi(r) = -\frac{GM}{a+r}, \tag{4.29}$$

where once again we have assumed that the halo is of infinite extent.

With equations 4.27 and 4.29 in mind, we may write the zeroth order terms of the expansions as

$$\rho_{000} = \frac{1}{2\pi}\frac{1}{r}\frac{1}{(1+r)^3} \tag{4.30}$$

and

$$\Phi_{000} = -\frac{1}{a+r} \tag{4.31}$$

Angular dependence is captured by use of spherical harmonics, $Y_{lm}(\theta,\phi)$. Concentrating on the variation in Φ_{0lm}

$$\begin{aligned}\Phi_{0lm} &= \Phi_{000} \times 4\pi\frac{r^l}{(r+1)^{l+1}}Y_{lm}(\theta,\phi) \\ &= -4\pi\frac{r^l}{(1+r)^{2l+1}}Y_{lm}(\theta,\phi)\end{aligned} \tag{4.32}$$

This is motivated this by analogy with the usual multipole expansion; $\Phi_{0lm} \sim r^l Y_{lm}(\theta,\phi)$ as $r \to 0$ and $\Phi_{0lm} \sim r^{-(l+1)}Y_{lm}(\theta,\phi)$ as $r \to \infty$.

The corresponding mass density can be derived from equation 4.21 and is written as

$$\rho_{0lm} = \frac{1}{2\pi}\frac{(2l+1)(l+1)}{r}\frac{r^l}{(1+r)^{2l+3}}4\pi Y_{lm}(\theta,\phi). \tag{4.33}$$

The most general terms can be expressed as

$$\rho_{nlm}(r) = \frac{K_{nl}}{2\pi}\frac{r^l}{r(1+r)^{2l+3}}C_n^{(2l+3/2)}(\xi)\sqrt{4\pi}Y_{lm}(\theta,\phi) \tag{4.34}$$

and

$$\Phi_{nlm}(r) = -\frac{r^l}{(1+r)^{2l+1}}C_n^{(2l+3/2)}(\xi)\sqrt{4\pi}Y_{lm}(\theta,\phi) \tag{4.35}$$

where $C_n^{\alpha}(\xi)$ is an ultraspherical polynomial, a generalisation of the Legendre polynomials (Arfken & Weber (2000), p.699) and ξ is a radial variable. Both sets of functions are complete and so *any potential* that is *finite everywhere* can be *represented exactly* by summing over a sufficiently large number of the Φ_{nlm} basis functions.

The expressions for the basis functions in hand allow us to compute values for the expansion coefficients, A_{nlm}, in equations 4.22 and 4.23. Multiplying both sides of equation 4.22 by the complex conjugate of $\Phi_{nlm}(r)$ and integrating over the entire volume

isolates A_{nlm}:

$$A_{nlm} = \frac{1}{I_{nl}} \int \rho(\mathbf{r}) \Phi_{nlm}(\mathbf{r})^* d\mathbf{r} \tag{4.36}$$

where the coefficient I_{nl} is expressed as

$$I_{nl} = -K_{nl} \frac{4\pi}{2^{8l+6}} \frac{\Gamma(n+4l+3)}{n!(n+2l+3/2)[\Gamma(2l+3)]^2}, \tag{4.37}$$

and the coefficient K_{nl} can be determined from,

$$K_{nl} = \frac{1}{2} n(n+4l+3) + (l+1)(2l+1). \tag{4.38}$$

We have tested our implementation of this method, and the results shown in figure 4.4 demonstrate that it works well.

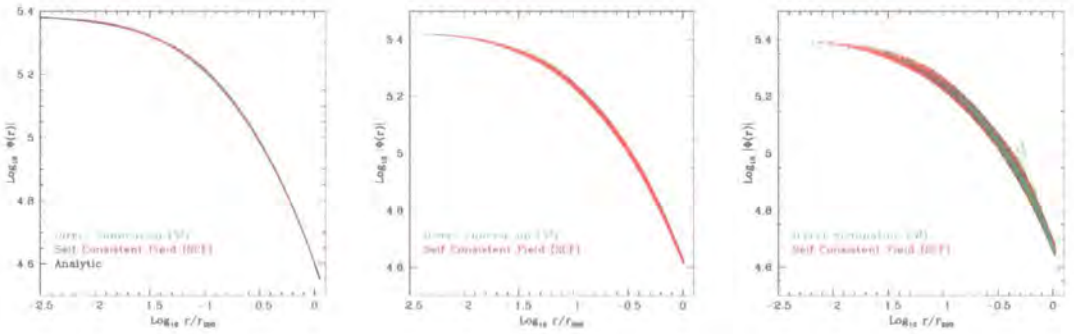

(a) Spherical NFW model (b) Triaxial NFW model (c) Galaxy Halo 1

Figure 4.4: **Tests of the SCF Method.** We show the radial variation of the gravitational potential for spherically symmetric and triaxial NFW models in figures 4.4(a) and 4.4(b), and for a simulated CDM galaxy mass halo in figure 4.4(c). Green points correspond to the potential estimated by the N^2 method; red points represent the results of the SCF method.

In figure 4.4(a), we have computed the gravitational potential as a function of radius for each particle in a spherically symmetric NFW model with concentration $c = 10$, realised with 10^5 particles interior to $r_{200} = 200$kpc. Only particles within the virial radius, r_{200}, are used in the calculation; this effectively truncates the model, which modifies the potential expressed in equation 4.25;

$$\Phi(r) = -\frac{v_{200}^2}{g(c)} \left(\frac{\ln(1+cx)}{x} - \frac{c}{(1+fc)} \right), \tag{4.39}$$

where $f = 1$ corresponds to the truncation radius, in units of $c = r_{200}/r_s$. Truncating the halo leads to the addition of a constant term, which raises the global potential.

Potentials computed using our implementation of the SCF method are represented by the red points; potentials computed using the N^2 direct summation method are coloured green; and the thick solid black curve corresponds to the exact analytic solution. There is excellent agreement between the potentials computed using both the SCF and N^2 codes and the expected potential for a NFW halo, as we would expect.

As in figure 4.4(a), we have computed the gravitational potential as a function of radius for a NFW model with concentration $c = 10$, realised with 10^5 particles interior to r_{200} in figure 4.4(b); how, we have introduced a coordinate transformation which results in a triaxial halo with axis ratios $b/a = 0.8$ and $c/a = 0.6$. The effect of triaxiality is to introduce a finite spread in the potential measured at any given radius; it follows that if we plotted $\Phi(r)$ against an effective radius, $r_{\rm eff} = (abc)^{1/3}$, we would recover the sharp spherically symmetric profile. We note that there is excellent agreement between the potentials evaluated using both the SCF and N^2 methods.

Finally, in figure 4.4(c), we have estimated the value of the gravitational potential as a function of radius for a simulated CDM halo - one of the converged 64^3 "Halo 1" runs used in the convergence study of chapter 2. We note that the profile is similar to that shown in figure 4.4(b), indicating that its mass distribution can be characterised as triaxial. Furthermore, we note that there is excellent agreement between the potentials evaluated using both the SCF and N^2 methods.

4.4 Results

In the following sections, we present the results of our analysis, reviewing their formation histories (§ 4.4.1), spherically averaged mass (§ 4.4.2) and kinematical (§ 4.4.3) profiles, their shapes (§ 4.4.4), substructure content (§ 4.4.5) and the symmetry and stability of the smooth gravitational potential (§ 4.4.6). Where it has been appropriate, we have considered data at various redshifts between $0 \leq z \lesssim 3$, during which time each of the halos has more than doubled in mass.

4.4.1 Mass Assembly History

We begin by considering the mass assembly histories of the four dwarfs in our sample of simulations. By following the growth of a halo's virial mass, M_{200}, as a function of redshift, we can determine the redshift at which the halo forms and identify events in its formation history that might correlate with dynamical state. For the purpose of this the-

sis, we follow the convention of Lacey & Cole (1993) and define the redshift of formation of a dark matter halo as the redshift at which the mass of its most massive progenitor first exceeds half the mass of the halo at $z = 0$.

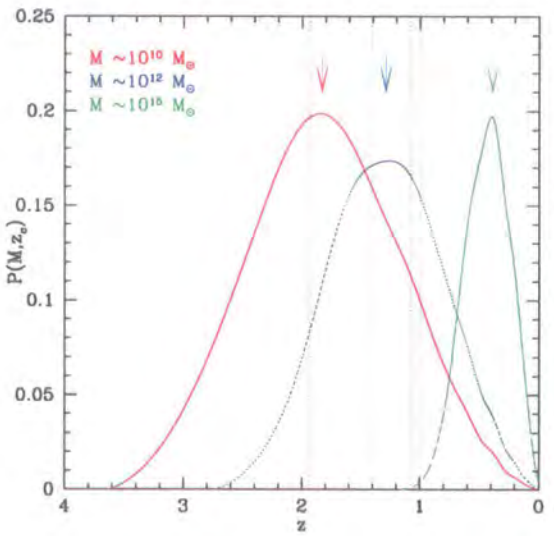

Figure 4.5: **Distribution of Formation Redshifts of Halos in the ΛCDM cosmology,** ($\Omega_m = 0.3$, $\Omega_\Lambda = 0.7$, $h = 0.7$, $\sigma_8 = 0.9$) as predicted by Extended Press Schechter (EPS) theory. We define the redshift of formation as the redshift at which the mass of the most massive progenitor first exceeds half the mass of the halo measured at $z = 0$. Curves are coloured according to mass scale - red, blue and green denote masses of order M $\sim 10^{10}\,M_\odot$, $10^{12}\,M_\odot$ and $10^{15}\,M_\odot$ respectively. The three sets of vertical dotted lines correspond to the median, upper and lower quartiles, while arrows indicate the most probable or *modal* values. See text for further details.

Hierarchical models such as CDM predict that the mass of a dark matter halo and its epoch of formation will be correlated, with lower mass halos typically forming at higher redshifts when compared to more massive counterparts. This expectation is confirmed by figure 4.5, in which we show the expected (normalised) probability distributions of formation redshifts for halos with virial masses of $10^{10}\,M_\odot$ (red curve), $2 \times 10^{12}\,M_\odot$ (blue curve) and $10^{15}\,M_\odot$ (green curve) at $z = 0$, as predicted by extended Press-Schechter (EPS) theory. These masses are typical of dwarf, galaxy and cluster mass halos respectively. In each case, we have generated the distribution from 10^5 realisations of the merger tree history of the halo, using the Monte Carlo method described in Lacey & Cole (1993) and implemented in the `merger_tree` software kindly provided by Shaun Cole.

Figure 4.5 confirms that, in the context of the ΛCDM variant of the CDM model, lower mass halos are more likely to form at higher redshifts relative to more massive halos. Here we have assumed a concordance ΛCDM cosmology, i.e. $\Omega_0 = 0.3, \Omega_\Lambda = 0.7, h = 0.7$, and $\sigma_8 = 0.9$. According to EPS, dwarf mass halos ($10^{10}\,M_\odot$) are most likely to form at $z \sim 1.9$, compared to $z \sim 1.3$ for galaxy mass halos ($2 \times 10^{12}\,M_\odot$) and $z \sim 0.4$ for cluster mass halos ($10^{15}\,M_\odot$). These modal values are indicated by coloured arrows. Alternatively, the median redshift of formation for dwarf halos is $z_{\rm med}$ 1.5, compared to $z_{\rm med}$ 1.1 and ~ 0.4 for galaxy and cluster halos respectively; the median, upper and lower quartiles of the distribution are indicated by light coloured dotted vertical lines.

On the other hand, we find that the formation times of dwarf mass halos are drawn from a relatively broad distribution, when compared with galaxy and cluster mass halos. Dwarfs can form as early as $z \sim 3.6$ and as late as $z \sim 0$, although such extremes have a low probability. In comparison, few clusters have formed by $z \sim 1$, while some may still be forming today.

We can determine the redshift of formation for each of the dwarf halos in our sample of simulations by tracking the mass of the most massive or *main* progenitor as a function of redshift and identifying the earliest redshift at which this mass exceeds half the mass of the halo measured at $z = 0$; the results are shown in figure 4.6. For reference, table 4.3 records virial masses and radii as a function of redshift for each of the four halos.

In figure 4.6, we follow the evolution of the main progenitor's virial mass, M_{200}, normalised to the virial mass of the halo at $z = 0$, with redshift. Red, green, blue and cyan curves correspond to the mass assembly histories of halos `dH01`, `dH02`, `dH03` and `dH04` respectively. For each halo, we identify the main progenitor at z by locating its centre using the iterative method outlined in § 4.3 and determining the radius at which the mean enclosed overdensity is 200 times $\rho_{\rm crit}(z)$, the critical density at that redshift.

The horizontal dashed line defines the threshold that the normalised mass must reach in order for the halo to be deemed formed. For ease of comparison with figure 4.5, we show the median, upper and lower quartiles of the EPS distribution of formation redshifts (light dotted lines). Formation redshifts determined from the simulation data appear to be perfectly consistent with the predictions derived from EPS theory. We find that `dH02` forms earliest, with half its mass in place by $z \sim 2.6$, followed by `dH04`, `dH01` and `dH05` at $z \sim 1.9$, ~ 1.8 and ~ 1.2 respectively. Three of the four halos - `dH04`, `dH01` and `dH05` - have formation redshifts that lie in the semi-interquartile range, while the formation

Table 4.3: **Virial masses and physical radii of halos at selected redshifts,** $0 \lesssim z \lesssim 3$

z	M_{200} $[10^{10}h^{-1}\mathrm{M}_\odot]$	r_{200} $[h^{-1}$ kpc$]$	z	M_{200} $[10^{10}h^{-1}\mathrm{M}_\odot]$	r_{200} $[h^{-1}$ kpc$]$
dH01			**dH02**		
0.0	0.781	32.26	0.0	0.923	34.17
0.51	0.703	25.89	0.47	0.887	28.46
0.99	0.621	20.54	0.99	0.887	23.16
1.51	0.443	15.17	1.47	0.770	18.50
2.01	0.322	11.56	2.07	0.503	13.21
2.80	0.120	6.70	2.98	0.285	8.55
dH03			**dH04**		
0.0	0.778	32.23	0.0	0.959	34.54
0.47	0.611	25.15	0.47	1.025	29.78
0.99	0.518	19.37	0.99	0.501	19.10
1.47	0.398	14.84	1.47	0.435	15.25
2.07	0.354	11.75	2.07	0.419	12.41
2.98	0.182	7.36	2.98	0.261	8.30

redshift of the remaining halo has a reasonable likelihood associated with it.

Perhaps of more interest for the subsequent analysis, we consider the mass accretion histories of our halos. Two of the halos - `dH01` and `dH02` - have gradually accreted mass at a steady rate with redshift up to $z = 0$. `dH01` has experienced continuous smooth accretion up to the present day, and its mass has grown by $\sim 20\%$ since $z = 1$. `dH02` experienced a minor merger between $1.5 \lesssim z \lesssim 2$, growing in mass by $\sim 30\%$ during that time, but has been relatively quiescent since $z \sim 1$, during which time it has accreted a further $\sim 10\%$ of its mass.

On the other hand, the remaining two halos - `dH03` and `dH04` - initially accreted mass steadily before experiencing violent, rapid major mergers (with mass ratios 1 : 3 and 1 : 2 respectively) at relatively late times. `dH03` experienced continuous smooth accretion between $0.3 \lesssim z \lesssim 3$, tripling its mass during that period, before undergoing a rapid major (1 : 3) merger that started at $z \sim 0.3$. The mass of the main progenitor initially

rose - or *overshot* - to $\sim 1.1\,M_{200}(z=0)$ at $z \simeq 0.1$ before falling. **dH04** experienced relatively little mass growth between $0.6 \lesssim z \lesssim 3$, although it doubled its mass during this period; however, beginning at $z \sim 0.6$, it underwent a violent, rapid major $(1:2)$ merger and as happened with **dH03**, the mass of the main progenitor initially overshot, reaching $\sim 1.1\,M_{200}(z=0)$ at $z \simeq 0.4$, before falling to $\sim 0.95\,M_{200}(z=0)$ at $z \simeq 0.2$ and then rising again. The mass overshooting suggests that these two halos are still undergoing mergers at $z = 0$, which may have implications for their structure.

The projected particle distributions shown in figures 4.7 to 4.10 can be considered complementary to figure 4.6, allowing the causes of features observed in the individual mass accretion histories to be investigated. For each of the four dwarf halos, we plot the projected distribution of particles within a cube of comoving side $500\,h^{-1}$ kpc at $z = 3, 2, 1.5, 1, 0.5$ and 0, centred on the main progenitor; the comoving lengths correspond to physical lengths of $125, 167, 200, 250, 333$ and $500\,h^{-1}$ kpc or $\sim 15\,r_{200}$ at the respective redshifts. At each redshift, we delineate the (projected) extent of the virialised region by a red circle.

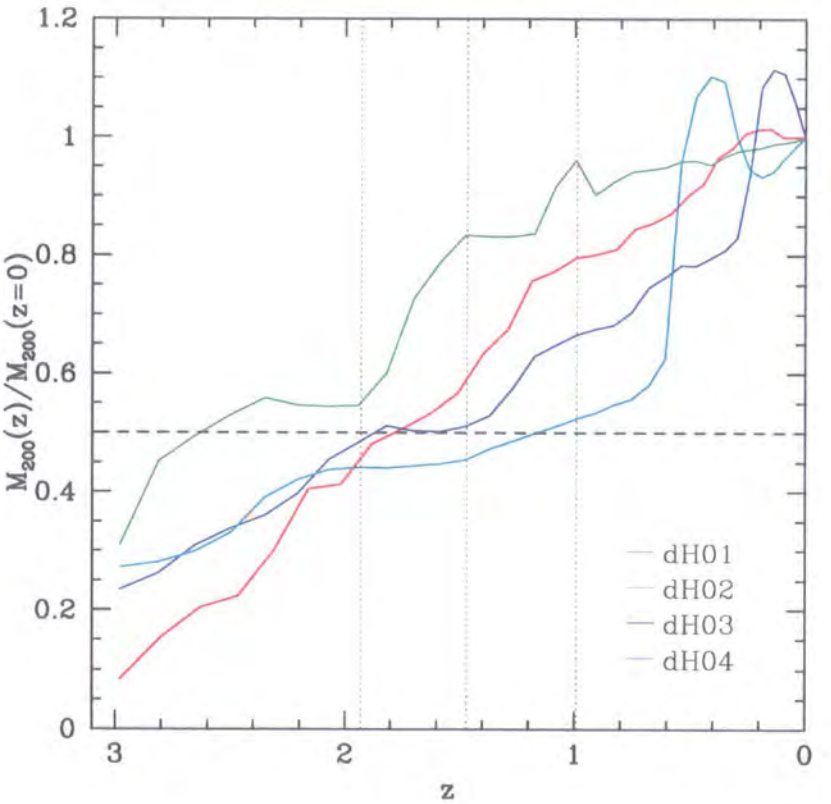

Figure 4.6: **Redshift Evolution of Mass Growth of Halos** This figure highlights the evolution of the virial mass, M_{200}, of the most massive progenitor as a function of redshift. Progenitor masses are normalised to the value of the virial mass of the halo at the present day, i.e. we show $M_{200}(z)/M_{200}(z=0)$. The horizontal dashed line indicates that $M_{200}(z) = 0.5\,M_{200}(z=0)$ and represents the threshold above which the halo is deemed to have formed, according to our definition. The median of the distribution of formation redshifts, computed using EPS theory, is indicated by the light dotted line at $z \simeq 1.5$; upper and lower quartiles are also shown. See text for further details.

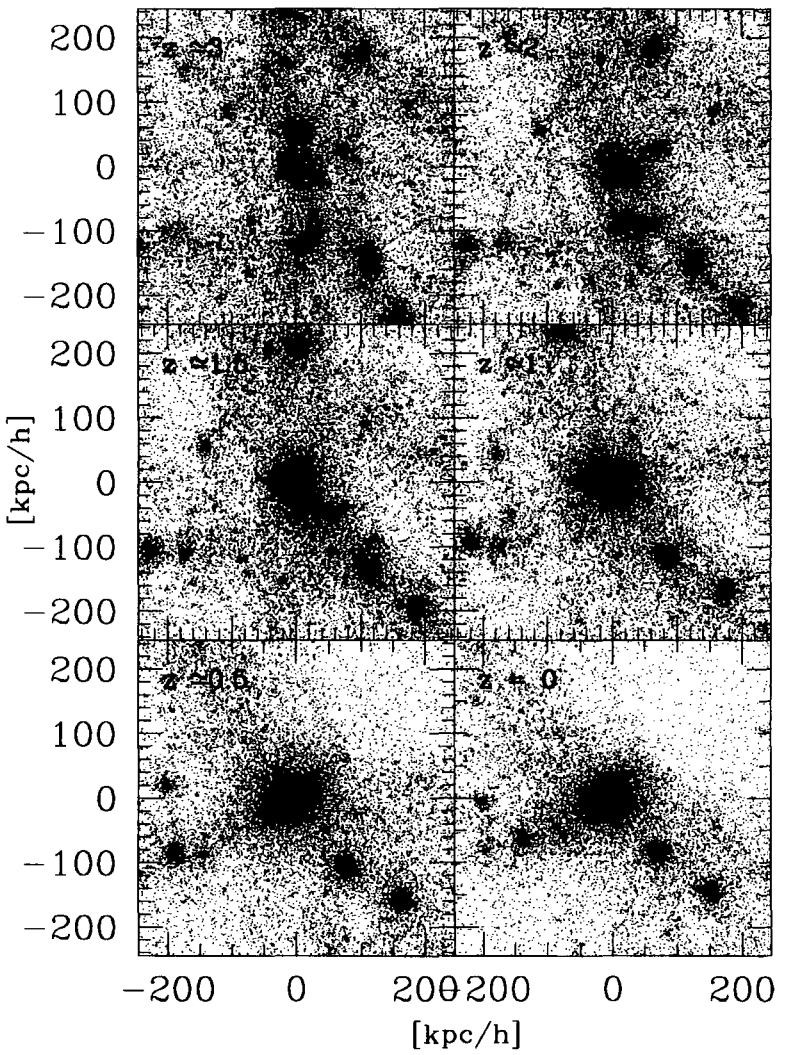

Figure 4.7: **Mass Assembly of dH01.** Here we illustrate the formation history of halo dH01 by plotting the projected distribution of particles within a cube of (comoving) side $500\,h^{-1}$ kpc at $z = 3, 2, 1.5, 1, 0.5$ and 0 (top left to bottom right panels), centred on the most massive progenitor at that redshift. At each redshift, the region bound by the red circle, centred on the main progenitor, corresponds to the projected volume enclosed by the virial radius of the halo, r_{200}. See text for further details.

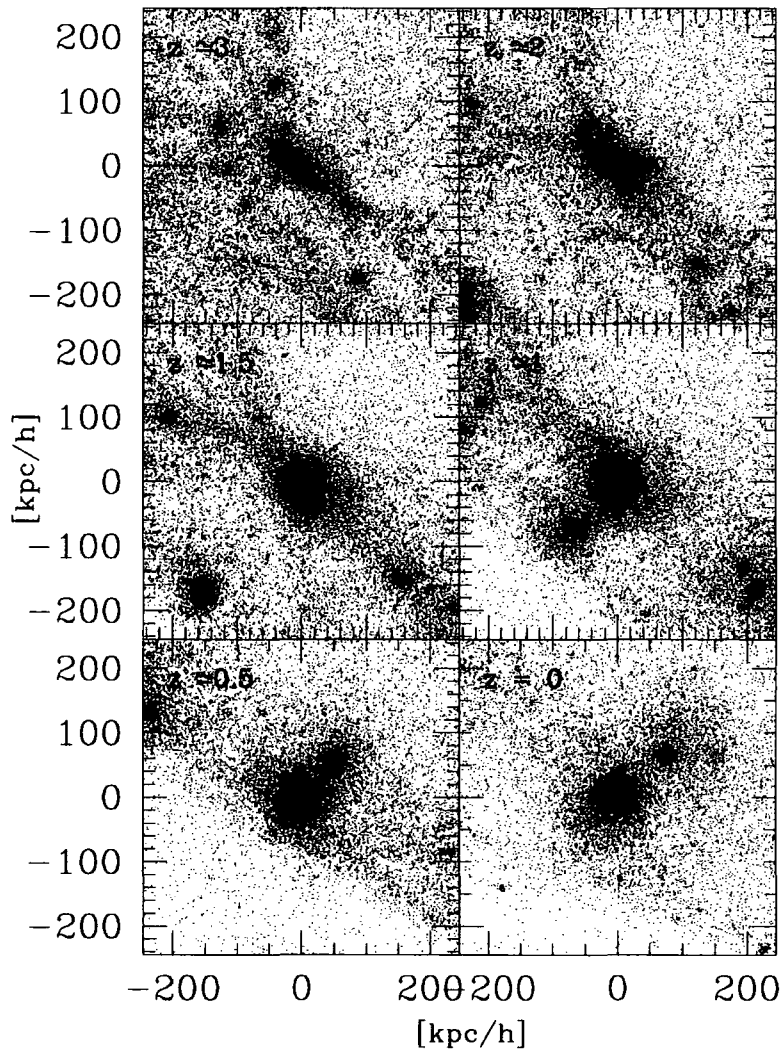

Figure 4.8: **Mass Assembly of dH02.** An illustration of the formation history of halo dH02; as in figure 4.7, we plot the projected distribution of particles within a cube of (comoving) side $500\,h^{-1}$ kpc at $z = 3, 2, 1.5, 1, 0.5$ and 0, centred on the most massive progenitor at that redshift. As before, the projected virial radius of the main progenitor at z at is indicated by the red circle.

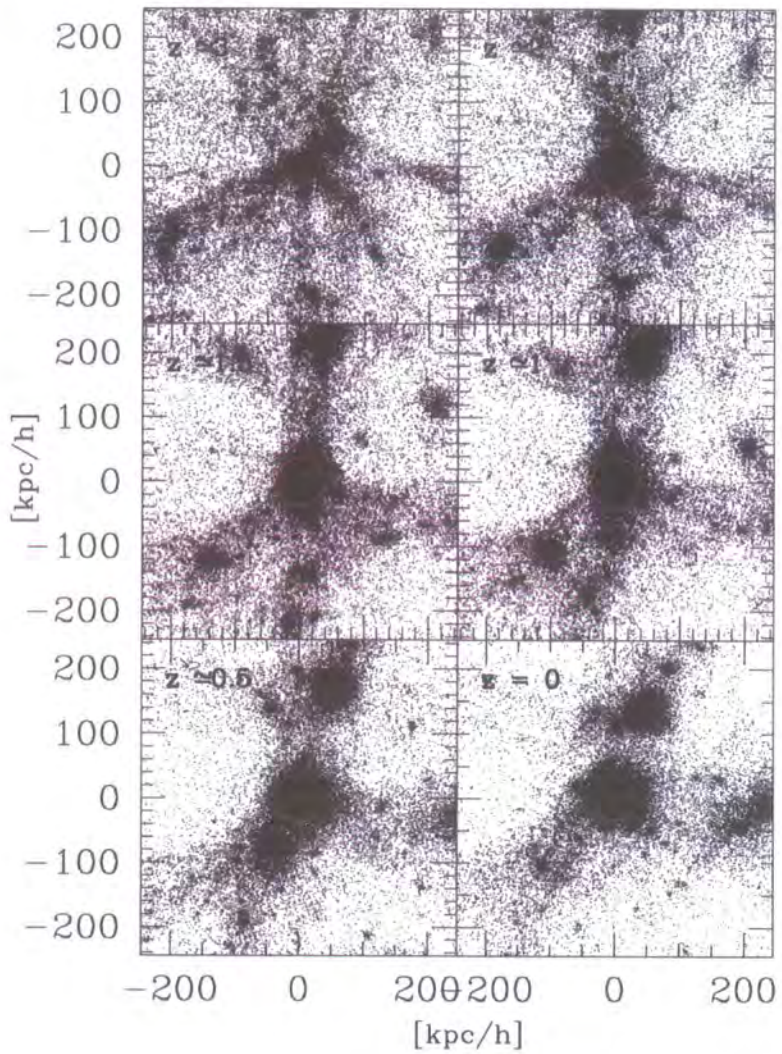

Figure 4.9: **Mass Assembly of dH03.** An illustration of the formation history of halo dH03; as in figure 4.7, we plot the projected distribution of particles within a cube of (comoving) side $500\,h^{-1}$ kpc at $z = 3, 2, 1.5, 1, 0.5$ and 0, centred on the most massive progenitor at that redshift. As before, the projected virial radius of the main progenitor at z at is indicated by the red circle.

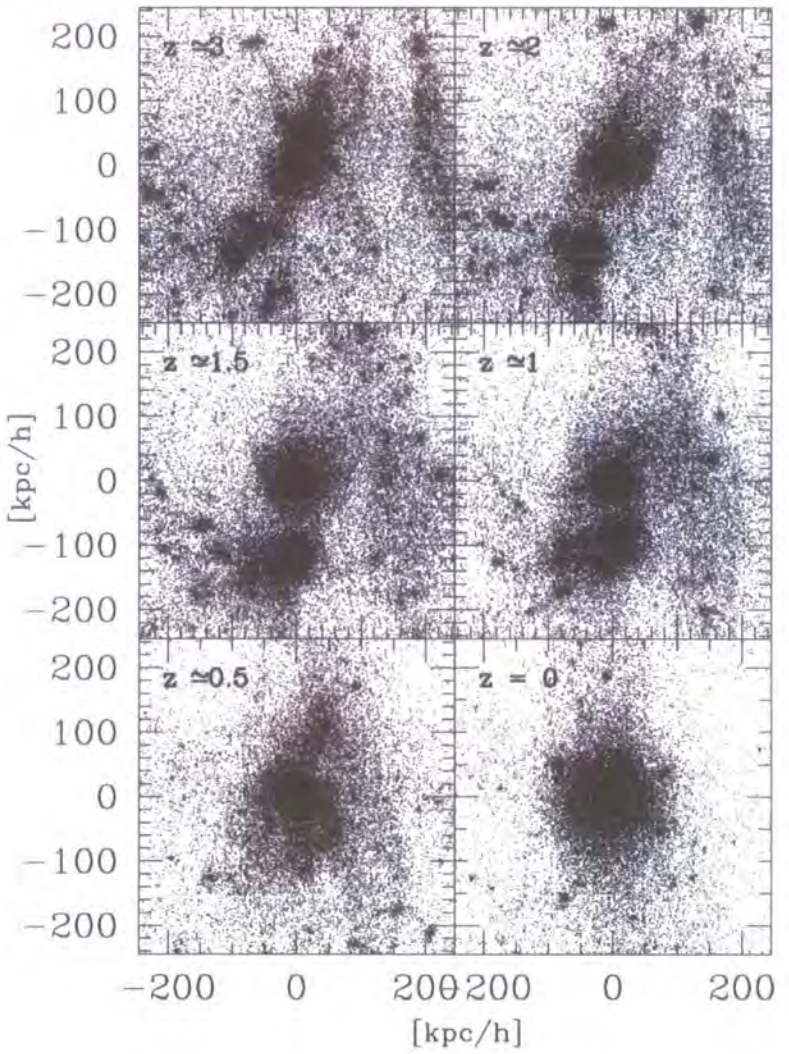

Figure 4.10: **Mass Assembly of dH04.** An illustration of the formation history of halo dH03; as in figure 4.7, we plot the projected distribution of particles within a cube of (comoving) side $500\,h^{-1}$ kpc at $z = 3, 2, 1.5, 1, 0.5$ and 0, centred on the most massive progenitor at that redshift. As before, the projected virial radius of the main progenitor at z at is indicated by the red circle.

4.4.2 Spherically Averaged Mass Profiles

The results presented in § 4.4.1 indicate that the dwarf halos in our sample have formation histories that are in good agreement with the predictions of EPS theory applied to the ΛCDM cosmology ($\Omega_m = 0.3$, $\Omega_\Lambda = 0.7$, $h = 0.7$ and $\sigma_8 = 0.9$); we found a median redshift of formation $z_{med} \simeq 1.8$, comparable to the predicted median ($z_{med} \simeq 1.5$) and within the interquartile range of the distribution. We also note that projected maps of the dark matter density distribution in and around each of the halos at $z = 0$ shown in figure 4.2 suggest that they are centrally concentrated objects with divergent densities in their innermost parts.

These observations and the results of previous studies (e.g. NFW (1996, 1997), Moore et al. (1998, 1999), Ghigna et al. (1998, 2000), Klypin et al. (2001), Fukushige & Makino (1997, 2001, 2003), Jing & Suto (2000)) lead us to suspect that there will not be any significant qualitative differences in the spherically averaged mass profile of the dwarf halos in our sample when compared with more massive systems such as galaxy and cluster mass halos. Therefore we expect that the "average" shape of the spherically averaged mass profile will be well approximated by a NFW profile, although the slope of the inner profile may be steeper, $\rho(r) \propto r^{-\alpha}$ with $1 \lesssim \alpha \lesssim 1.5$. We also expect the dwarfs to have higher concentrations than, say, a typical cluster halo (NFW (1997), Bullock et al. (2001), Eke, Navarro & Steinmetz (2001) (hereafter ENS)) given their higher relative redshift of formation.

We shall compare the structure of the dwarf halos in our sample with those of more massive systems in the next chapter, and so we defer any discussion of mass dependent trends until then. In this section, we investigate properties that may depend on redshift by focusing on the spherically averaged mass profiles of our halos between redshifts $0 \lesssim z \lesssim 3$, during which time $50 - 80\,\%$ of their final (i.e. $z = 0$) mass is accreted. In particular, we

- compare and contrast the shapes of profiles at redshifts $z = 0$ and $z \simeq 0.5$, $\simeq 1$ and $\simeq 1.5$.
- estimate characteristic measures of the density and circular velocity, and best fitting NFW and Moore et al. concentrations, comparing the observed redshift dependence with the predictions of the Bullock et al. and ENS models.
- measure fractional deviations in the density and circular velocity profiles relative to

the average, NFW and Moore et al. profiles at redshifts $z = 0$ and $z \simeq 0.5$, $\simeq 1$ and $\simeq 1.5$, discussing the performance of the model fits.

- place constraints on the maximum asymptotic slope, α, at the innermost believable radius.

Mass Profiles at Redshifts $0 \leq z \lesssim 1.5$

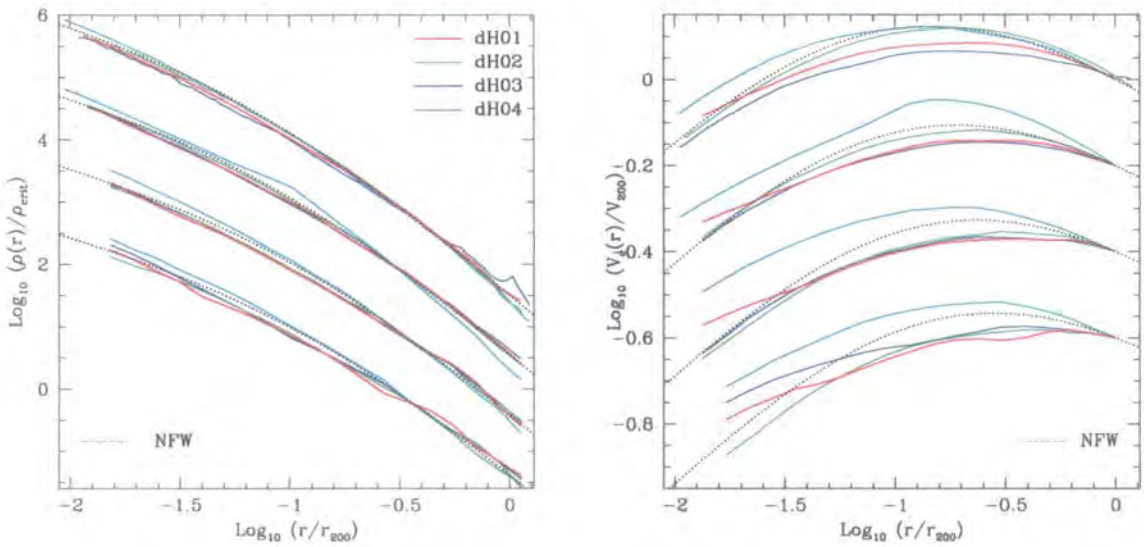

(a) Density Profiles : Comparison with Redshift

(b) Circular Velocity Profiles : Comparison with Redshift

Figure 4.11: **Spherically Averaged Mass Profiles** measured from the simulation data. In figures 4.11(a) (4.11(b)), we compare density (circular velocity) profiles for each dwarf halo in our sample, as measured at redshifts (from top) $z = 0$ and $z \simeq 0.5, 1$ and 1.5; a vertical offset of 1 (0.4) dex separates profiles measured at successive redshifts. Heavy solid red, green, blue and cyan curves correspond to halos `dH01`, `dH02`, `dH03` and `dH04` respectively. Light dotted curves represent NFW profiles for a *typical* halo at the appropriate redshift. All profiles are plotted from the innermost believable radius, $r_{\rm min}$, out to the virial radius, r_{200}. Radii are normalised to the virial radius at a given redshift z. See text for further details.

We begin by considering how the shapes of the density and circular velocity profiles of the four dwarf halos change with redshift. We show density and circular velocity profiles for each of the halos at $z = 0$ and for their most massive progenitors at $z \simeq 0.5, 1$ and 1.5 in figure 4.11. Profiles are constructed by sorting particles in order of ascending

radius from the centre of the halo (determined as described in § 4.3.1) and binning in shells equally spaced in $\log_{10} r$. Densities are expressed in units of $\rho_{crit} = 3H^2/8\pi G$, the critical density at redshift z, circular velocities in units of V_{200}, the circular velocity at r_{200}, and radii in units of r_{200}. All of the profiles are truncated at r_{min}, the innermost believable radius, as defined in § 4.2.4 - corresponding to the outermost radius for which the relaxation timescale, $t_{\rm relax} \lesssim 0.6\, t_0$, where t_0 is the Hubble time.

In figures 4.11(a) and 4.11(b), we separate density profiles (figure 4.11(a)) and circular velocity profiles (figure 4.11(b)) according to redshift. For clarity, we have introduced factors of 10 offset (1 dex) in density and ~ 2.5 (0.4 dex) in circular velocity between successive redshifts; thus the uppermost set of curves correspond to the halo profiles at $z = 0$. The light dotted curves represent the profiles we might expect a *typical* main progenitor to have at z, where we have used EPS theory to estimate the median mass of the most massive progenitor of a halo with a $z = 0$ mass of $10^{10}\mathrm{M}_\odot$, the ENS prescription for computing concentrations, and assumed that the mass profile of the progenitors can be described by the NFW profile. For reference, we give typical progenitor masses (M_{200}) and the corresponding concentrations (c_{200}), determined in the manner we have just described, in table 4.4.

Table 4.4: Typical progenitor masses and concentrations at redshift z, as predicted by extended Press Schechter theory and the ENS prescription respectively. See text for further details.

z	M_{200} $[10^{10}h^{-1}\mathrm{M}_\odot]$	c_{200}
0	1	11.7
0.5	0.87	10.7
1	0.65	8.3
1.5	0.49	7

Perhaps the main point to note in figures 4.11(a) and 4.11(b) is that the shapes of the profiles at any given redshift are similar. If we use the *root mean square* (r.m.s.) or $1\,\sigma$ deviation as a measure of the scatter in the profile relative to the mean, we find that the *maximum* deviation never exceeds $40 - 55\%$ in density or $15 - 20\%$ in circular velocity

at redshifts between $0 \leq z \lesssim 1.5$. The *mean* scatter is smaller, with a 1σ deviation of $\sim 20\%$ in density and $\sim 10\%$ in circular velocity at any given redshift.

We also note that the shape of the average mass profiles do not differ significantly from that predicted for the "typical" NFW profile, although the average density profile appears to have a steeper central slope than predicted at any given redshift. In other words, the average dwarf halo forming in our high resolution simulations appears to be more concentrated than our "typical" halo. This is confirmed by the shape of the average circular velocity profile, which indicates that there is more mass within a fixed fraction of the virial radius than we might expect if the inner profile is as shallow as $\rho(r) \propto r^{-1}$.

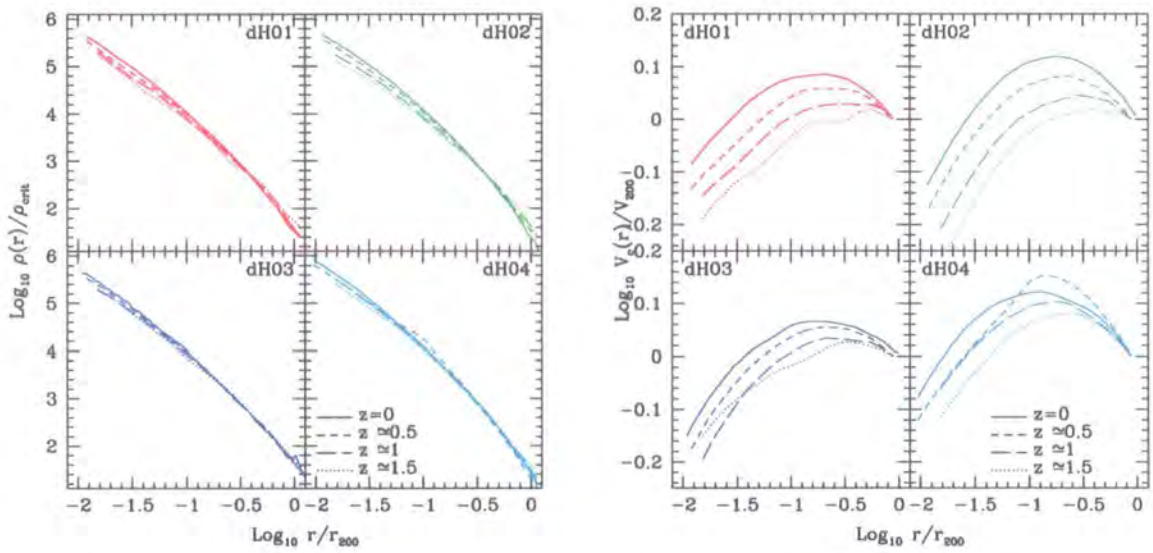

(a) Density Profiles (Normalised)

(b) Circular Velocity Profiles (Normalised)

Figure 4.12: **Spherically Averaged Mass Profiles (Normalised)** measured from the simulation data at $z = 0$ (solid curve), $z \simeq 0.5$ (short dashes), $z \simeq 1$ (long dashes) and $z \simeq 1.5$ (dots). In figure 4.12(a) (4.12(b))), we emphasise variations in the normalised density (circular velocity) profile of a given halo with redshift. All profiles are plotted from the innermost believable radius, $r_{\rm min}$, out to the virial radius, r_{200}.

In figures 4.12(a) and 4.12(b), we separate density profiles and circular velocity profiles according to halo, which should allow us to identify trends in profile shape as a function of redshift. Solid, short dashed, long dashed and dotted curves represent a halo's mass profile at $z = 0$ and $z \simeq 0.5, 1$ and 1.5 respectively. Note that the halos in our sample accrete between $\sim 20\%$ and $\sim 50\%$ of their final mass during $0 \leq z \lesssim 1.5$. As in figure 4.11, we

have expressed densities in units of ρ_{crit}, circular velocities in units of V_{200} and radii in units of r_{200}. All of the profiles are truncated at r_{min}, the innermost believable radius.

If we focus on the normalised density profiles shown in figure 4.12(a), it is quite noticeable, especially within the inner $\sim 10\% r_{200}$, that the profiles steepen with decreasing redshift at a fixed fraction of r_{200}. We find that the spherically averaged local overdensity at $r_{\rm min} \simeq 1.5\% r_{200}$ increases by a factor of $\sim 2-3$ between $z \simeq 1.5$ and $z = 0$. This suggests that the concentrations of our halos increase with decreasing redshift.

A similar conclusion may be drawn from the circular velocity profiles shown in figure 4.12(b). In general, the normalised circular velocity at a fixed fraction of r_{200} steadily grows with decreasing redshift, increasing by $\sim 25-40\%$ between $z \simeq 1.5$ and $z = 0$ at $r_{\rm min} \simeq 1.5\% r_{200}$.

We also note that the normalised radius at which the peak circular velocity ($v_{\rm c,max}$) occurs increases with increasing redshift, another signature of the fall in concentration. We expect the location of the peak circular velocity to depend on the concentration of a halo - the more concentrated the halo, the smaller the fraction of the virial radius at which the peak occurs.

In figures 4.13(a) and 4.13(b), we again separate our sample of profiles according to halo, but now compare profiles plotted in physical units; we express densities in units of $h^2 {\rm M}_\odot {\rm kpc}^{-3}$, radii in units of h^{-1} kpc and circular velocities in units of ${\rm kms}^{-1}$.

We find that the shapes and slopes of both the density and circular velocity profiles are in excellent agreement with each other at all redshifts in all of the cases but one - **dH04**, which experienced a major merger at $z \simeq 0.5$. If we consider the density profiles in figure 4.13(a) and exclude **dH04**, we find that the maximum 1σ deviation never exceeds $\sim 30\%$ relative to the mean profile (computed by stacking profiles from all redshifts for a given halo), whereas the mean deviation is $\sim 5\%$. If we include **dH04**, we find that this maximum deviation rises to a factor of ~ 3. Similarly, we find a maximum (mean) deviation in the circular velocity profile (excluding **dH04**) of $\sim 10\%$ ($\sim 2.5\%$). Including **dH04** causes the maximum deviation to rise to $\sim 30\%$.

The previous discussion suggests that the shapes of the spherically averaged mass profiles of our dwarfs are similar at redshifts in the range $0 \leq z \lesssim 1.5$. Although the profiles plotted in physical units proved useful for emphasising this similarity, these quantities are redshift dependent. We wish to find a way of scaling our profiles such that we can make

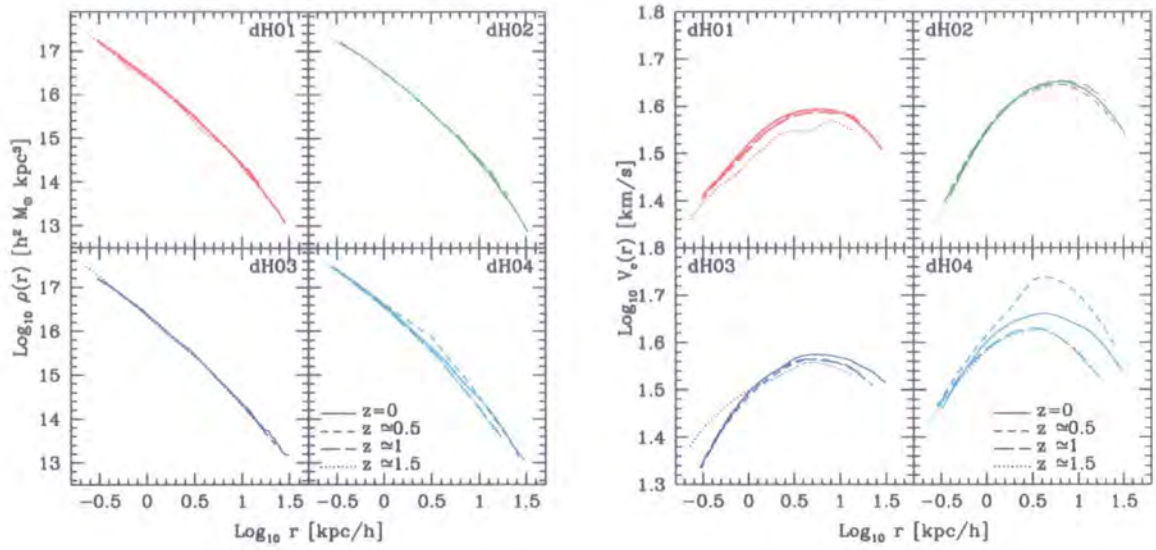

(a) Density Profiles (Physical)

(b) Circular Velocity Profiles (Physical)

Figure 4.13: **Spherically Averaged Mass Profiles (Physical)** measured from the simulation data at $z = 0$ (solid curve), $z \simeq 0.5$ (short dashes), $z \simeq 1$ (long dashes) and $z \simeq 1.5$ (dots). As in figure 4.12(a) (4.12(b))), we emphasise variations in the normalised density (circular velocity) profile of a given halo with redshift, whereas we plot the density (circular velocity) profile in physical units in figure 4.13(a) (4.13(b)). All profiles are plotted from the innermost believable radius, $r_{\rm min}$, out to the virial radius, r_{200}. See text for further details.

a direct comparison between profiles measured at different redshifts, and so we require characteristic measures of density and circular velocity.

For simplicity, we have chosen to use ρ_{-2}, the density at which the logarithmic slope of the density profile is -2, and r_{-2}, the radius at which this occurs as the the characteristic density and radius with which we can normalise our density profiles. It is relatively straightforward to compute r_{-2} and ρ_{-2} from simulation data; by using the location of the peak of the differential mass profile, ρr^2;

$$\frac{d}{dr}(\rho r^2) = \frac{d\rho}{dr} r^2 + 2\rho r = 0 \Rightarrow S(r) = \frac{d\log\rho}{d\log r} = -2 \quad . \tag{4.40}$$

This provides an estimate for the radius, r_{-2}. We may then invert the ρr^2 profile to give the local density, ρ_{-2}, at that point. We have found that ρr^2 can be quite flat around its maximum, which can lead to a fractional error in r_{-2} as large as 50% or 0.2 dex, or a factor of ~ 2.5 or 0.4 dex in ρ_{-2}.

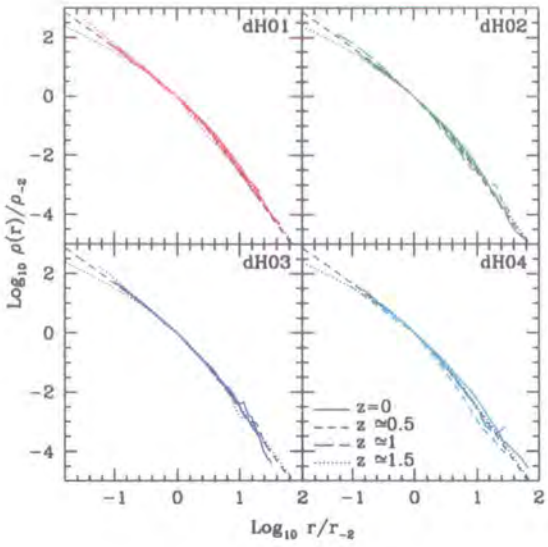

(a) Similarity of Density Profiles at $0 \leq z \lesssim 1.5$.

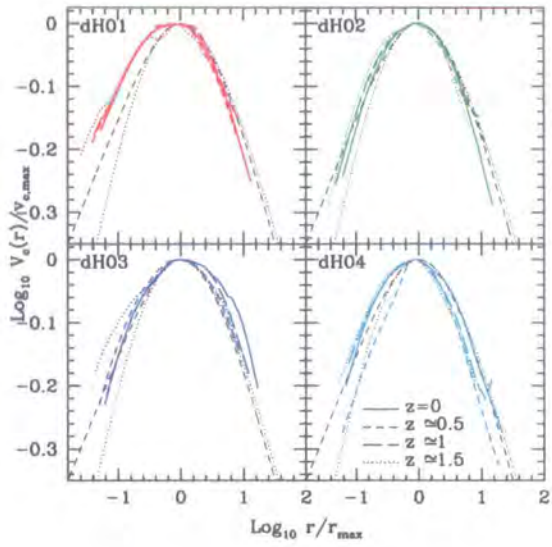

(b) Similarity of Circular Velocity Profiles at $0 \leq z \lesssim 1.5$.

Figure 4.14: **Similarity of Spherically Averaged Mass Profiles** measured at $0 \leq z \lesssim 1.5$. In figure 4.14(a), we have scaled the density profiles in radius by r_{-2}, the characteristic radius at which the slope of the logarithmic density profile is -2, and in density by ρ_{-2}, the spherically averaged density at this radius. We perform a similar operation in figure 4.14(b), where we show the circular velocity profile scaled by the peak circular velocity, $v_{\rm c,max}$, and radii at, $r_{\rm max}$, the radius at which the peak occurs. Solid, short dashed, long dashed and dotted curves represent the system at $z = 0$ and $z \simeq 0.5, 1$ and 1.5 respectively.

Similarly, we have chosen the peak circular velocity, $v_{\rm c,max}$, and the radius at which this occurs, $r_{\rm max}$, as the most natural characteristic scalings for our circular velocity profiles. $r_{\rm max}$ and $v_{\rm c,max}$ can be estimated in a similar manner to r_{-2} and ρ_{-2}, by locating the peak value of the circular velocity profile. While our method consistently finds $v_{\rm c,max}$ to better than $\sim 1\%$, the fractional error in $r_{\rm max}$ can be as large as 0.1 dex or 25%, reflecting the flatness of $v_c(r)$ around the peak in some cases.

It is worth noting that $r_{-2} = r_s^{\rm N}$ for a NFW profile and $r_{-2} = r_s^{\rm M}/2^{2/3}$ for a Moore et al. profile, where we have related the scale radii in the respective models by requiring that they both agree on the radius at which $r_{\rm max}$ occurs. For a NFW model, $r_{\rm max} \simeq 2.16\, r_s^{\rm N}$, while for a Moore et al. model, $r_{\rm max} \simeq 1.24\, r_s^{\rm M}$. Hence, it follows that $r_s^{\rm M} = 0.574\, r_s^{\rm N}$.

Density and circular velocity profiles normalised by these characteristic quantities are shown for each of the halos in our sample in the panels of figures 4.14(a) and 4.14(b). We also show rescaled NFW (dotted curves) and Moore et al. (dashed curves) profiles for comparison.

As before, we note that there is good agreement overall between the shapes of both sets of profiles measured at different redshifts. We find that the maximum deviation in the density profile relative to the mean can be as great as a factor ~ 2 (**dH04**), but such large deviations generally occur in the outer parts of the $r \gtrsim 5\,r_{-2}$ and on average, the mean 1σ deviation is between $\sim 30\%$ and $\sim 60\%$. Similarly, we find that the maximum 1σ deviation in the circular velocity profile never exceeds $\sim 10\%$ and is closer to $\sim 1-2\%$ on average.

Both the NFW and Moore et al. models appear to provide adequate representations of the simulated data down to $\sim 0.1\,r_{-2}$, but within this radius, we note that the normalised density profiles appear to be steeper than predicted for a NFW profile but and consistent with a Moore et al. profile in three of the four cases considered; in the other case, the profile does not extend to small enough values of r_{-2} to be able to discriminate between the profiles. The normalised circular velocity profiles also suggest that the dwarfs are more centrally concentrated than we might expect if their internal structure can be characterised by the NFW profile. In particular, **dH01** appears to be more concentrated than any of the other halos in our sample; at $\sim 0.1\,r_{-2}$, $V_c/v_{\rm c,max}$ is $\sim 20\%$ ($\sim 10\%$) greater than predicted by the NFW (Moore et al.) profile. On the other hand, the normalised Moore et al. profiles appear to provide a better fit to the simulated circular velocity profiles in general.

We conclude that the shapes of spherically averaged density and circular velocity profiles of simulated dwarf galaxy halos do not appear to vary with redshift; that their concentrations decrease with increasing redshift; and that in the majority of cases, the data appear to favour density profiles with central slopes steeper than those predicted by the NFW profile, but possibly consistent with the Moore et al. profile.

Characteristic Measures of Halo Structure

The characteristic measures of density - ρ_{-2} and r_{-2} - and circular velocity - $v_{\rm c,max}$ and $r_{\rm max}$ - should be sensitive to the form of the dark matter halo's underlying mass profile

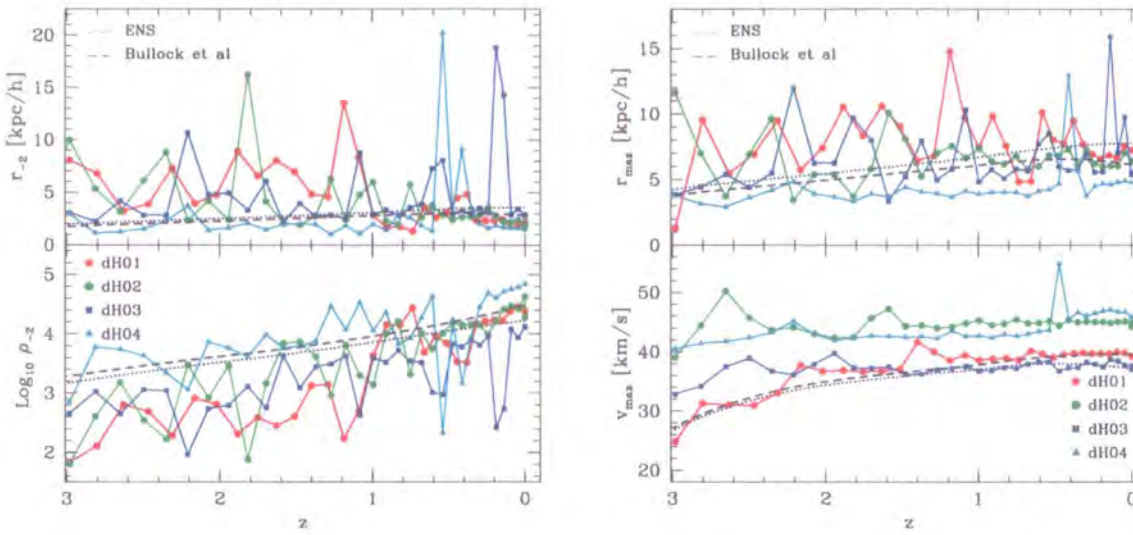

(a) Variation of r_{-2} and ρ_{-2} with Redshift

(b) Variation of $v_{\mathrm{c,max}}$ and r_{max} with Redshift

Figure 4.15: **Variation of scaling parameters with redshift.** We have computed r_{-2}, ρ_{-2}, r_{max} and $v_{\mathrm{c,max}}$ for each of the halos in our sample and show their variation with redshift (in the range $0 \leq z \lesssim 3$). We also compare these data with predictions based on the ENS (dotted curves) and Bullock et al. (dashed curves) prescriptions for concentration, assuming that the halo structure can be described by the NFW profile. In figure 4.15(a) we show how the characteristic radius r_{-2} (upper panel) and density ρ_{-2} (lower panel) depend on redshift, z. Similarly, in figure 4.15(b), we show how the radius at which the circular velocity peaks, r_{max}, and the peak circular velocity vary as a function z (upper and lower panels respectively).

and consequently its concentration. The redshift dependence of these quantities can be predicted in principle using the Bullock et al. and ENS prescriptions for the concentration, and the NFW and Moore et al. profiles. It is therefore interesting to compare the observed redshift variation of these characteristic measures with the model predictions.

In figure 4.15, we show the variation of ρ_{-2}, r_{-2}, $v_{\mathrm{c,max}}$ and r_{max} as a function of redshift for each of the halos in our sample. The data are represented by red asterisks (`dH01`), green filled circles (`dH02`), blue filled squares (`dH03`) and cyan filled triangles (`dH04`). In particular, we compare our data with the predictions of the ENS (dotted curves) and Bullock et al. (dashed curves) prescriptions for concentration with redshift, assuming (as a limiting case) that the mass profile can be described by the NFW profile.

Both the ENS and Bullock et al. models assume that the concentration of a halo is uniquely determined by its virial mass (M_{200}), and so we can estimate both r_{-2} and $r_{\rm max}$ at any given redshift by determining the typical progenitor mass at that epoch, estimating its concentration (c_{200}) and noting that $r_{-2} = r_s = r_{200}/c_{200}$ and $r_{\rm max} \simeq 2.16\, r_s = 2.16\, r_{200}/c_{200}$.

Furthermore, it is straightforward to derive analytic expressions for both ρ_{-2} and $v_{\rm c,max}$; for a NFW profile,

$$\rho_{-2} = \frac{1}{4}\rho_{\rm crit}\delta_c = \frac{50}{3}\frac{\rho_{\rm crit}\, c_{200}^3}{\ln(1+c_{200}) - c_{200}/(1+c_{200})} \tag{4.41}$$

and

$$v_{\rm c,max} = V_{200}\sqrt{\frac{g(f c_{200})}{g(c_{200})}} \tag{4.42}$$

where V_{200} is the circular velocity at the virial radius, $f = 2.16$ and the function $g(x)$ is given by

$$g(x) = \frac{\ln(1+x)}{x} - \frac{1}{1+x}, \tag{4.43}$$

Note that both the ENS and Bullock et al. models define the concentration to be the more general $c_{\rm vir} = r_{\rm vir}/r_s$, where

$$r_{\rm vir} = \left(\frac{1}{\Delta_{\rm vir}}\frac{1}{\rho_{\rm crit}}\frac{3}{4\pi}M_{\rm vir}\right)^{1/3}; \tag{4.44}$$

$\Delta_{\rm vir}$ is a cosmology dependent overdensity threshold, which for a ΛCDM cosmology is approximately $\Delta_{\rm vir} \simeq 97$ at $z = 0$(e.g. Eke et al. (1996)). We have used a fixed overdensity threshold of 200 for all redshifts, and so we correct the model predictions to obtain $c_{200} = r_{200}/r_s$.

In figure 4.15(a), we show the variation of r_{-2} (expressed in physical units, upper panel) and ρ_{-2} (expressed as an overdensity in units of $\rho_{\rm crit}$, lower panel) against redshift. The most striking aspect of this figure is that the data are very noisy; the value of ρ_{-2} can vary by as much as a factor of ~ 100 between halos at any given redshift, or a factor of ~ 30 between consecutive outputs for a given halo. Similarly, r_{-2} appears to vary by as much as a factor of ~ 10 between halos at any given redshift, and by a similar factor between consecutive outputs for a given halo. We noted earlier that we expect to incur fractional errors of $\sim 50\%$ in r_{-2} and a factor of ~ 2.5 in ρ_{-2}, which suggests that these large fluctuations are features in the differential mass profile ($\rho(r)r^2$) and are not solely the result of the procedure used to estimate them.

We also note that the average value of ρ_{-2} appears to decrease with increasing redshift, falling by a factor of ~ 100 between $0 \leq z \lesssim 3$, whereas r_{-2} does not appear to change at all.

It is difficult to make a meaningful comparison between the predicted relations for ρ_{-2} and r_{-2} with z and the simulation data because there are such large variations in the measured values at any given z. However, we note that both the ENS and Bullock et al. models tend to both underestimate r_{-2} and overestimate ρ_{-2} by a factor of $\sim 2-3$ if we compare "average" values at high redshifts. This suggests that the simulated halos are *less* concentrated than we might expect a typical progenitor to be at high redshifts - apparently at odds with the spherically averaged mass profiles shown in previous figures. On the other hand, there is reasonable agreement between the average values of r_{-2} and ρ_{-2} measured from the simulation data and the model predictions for redshifts $0 \leq z \lesssim 1.5$. At $z \simeq 1.5$, the models overestimate ρ_{-2} by $\sim 60\%$ and underestimate r_{-2} by $\sim 25\%$, and at $z \simeq 0$, we find that models underestimate ρ_{-2} by $\sim 20\%$ and overestimate r_{-2} by $\sim 20\%$. We also note that the slope of the predicted relation between ρ_{-2} and z appears to be in reasonable agreement with the average of the data.

In figure 4.15(b), we show the variation of the peak circular velocity, $v_{\rm c,max}$, (lower panel) and the radius at which this occurs, $r_{\rm max}$, (upper panel) with redshift.

We find that $r_{\rm max}$ is a noisy quantity, changing by as much as a factor of ~ 3 between successive outputs. This is in excess of the 25% relative error we expect to incur, and suggests that the variation in $r_{\rm max}$ is a real effect. Indeed, if we examine a series of circular velocity profiles as a function of radius, we note that $r_{\rm max}$ can change dramatically between consecutive outputs at early times ($z \gtrsim 1$) because of infalling clumps, whereas it can fluctuate by a factor of $2-3$ at late times because the circular velocity peak is quite broad and flat.

On the other hand, we find that $v_{\rm c,max}$ of a given halo does not change significantly over the interval $0 \leq z \lesssim 3$. The most dramatic rise - that of `dH01` - corresponds to an increase of $\sim 70\%$ in $v_{\rm c,max}$, from ~ 24 kms^{-1} to ~ 40 kms^{-1}; during this time, the halo accretes $\sim 80\%$ of its mass. Typically, the change is smaller - in the other three cases, it is $\sim 15-20\%$ over the same period. On the other hand, if we consider changes in $v_{\rm c,max}$ over the redshift interval $0 \leq z \lesssim 1.5$ - corresponding to the period over which a typical dwarf halo will have accreted half its mass (according to EPS theory) - we find that $\Delta v_{\rm c,max}/v_{\rm c,max} \lesssim 2.5\%$ for three of the four halos. As we have noted previously,

dH04 experienced a major merger at $z \simeq 0.5$ that resulted in an initial jump in $v_{\rm c,max}$ of $\sim 25\%$, and an overall increase of $\sim 10\%$ between $0 \leq z \lesssim 1.5$.

In general, the predicted value of $v_{\rm c,max}$ at any given z tends to underestimate the observed value of $v_{\rm c,max}$ (although we note that there is reasonable agreement between the predicted and observed relation for dH01 (red asterisks) and dH03 (blue filled squares) between $0 \leq z \lesssim 1.5$); this suggests that our halos are *more* concentrated than predicted for a typical progenitor, in keeping with the conclusions we drew from the mass profiles shown in the previous figures.

We conclude that, while estimates of ρ_{-2}, r_{-2}, $v_{\rm c,max}$ and $r_{\rm max}$ can provide an insight into halo structure, they are too sensitive to merging and mass accretion history to provide strong constraints on the form of the mass profile or concentration.

In figure 4.16(a), we compare best fit concentrations determined at redshifts between $0 \leq z \lesssim 3$ for each of the halos in our sample with the predictions of the NFW (upper panel) and Moore et al. (lower panel) models as a function of $1 + z$. Concentrations are obtained by performing a weighted χ^2 fit to the density profile; the weighting, σ, given to a shell is simply the Poisson error on the number of particles in that shell, i.e. $\sigma = \rho_{\rm shell}/N_{\rm shell}^{1/2}$, where $N_{\rm shell}$ is the number of particles per shell and $\rho_{\rm shell}$ is the density of the shell. Note that we only include data in the range $r_{\rm min} \leq r \leq r_{200}$, and that changing the outer limit does not change the estimated concentration by more than 10%.

Light dotted and solid curves highlight the expected variation of the concentration, c_{200}, with redshift, z, predicted by the ENS (solid curves) and Bullock et al. (dashed curves) models for a typical progenitor halo (as described above). Error bars correspond to the 1σ variation of $\Delta \log_{10} c_{\rm vir} = 0.18$ found by Bullock et al. (2001) for a statistical sample of halos forming in a large cosmological volume.

There are a few points worth noting in this figure. The first is that there is a definite trend in the simulation data, with halos at higher redshifts having lower concentrations. At $z = 0$, the median NFW (Moore et al.) concentration of our dwarfs is $c_{200}^{\rm N} \simeq 11$ ($c_{200}^{\rm M} \simeq 6$); this has fallen to $c_{200}^{\rm N} \simeq 5.9$ ($c_{200}^{\rm M} \simeq 2.8$) at $z \simeq 1.5$.

If we consider the average concentration at any given redshift (the heavy solid black curve shown in figure 4.16(b)), we see good agreement between the simulation data and the predictions for the typical progenitor. The mean curve never deviates by more than the 1σ errors from either of the ENS or Bullock et al. curves for any redshifts between

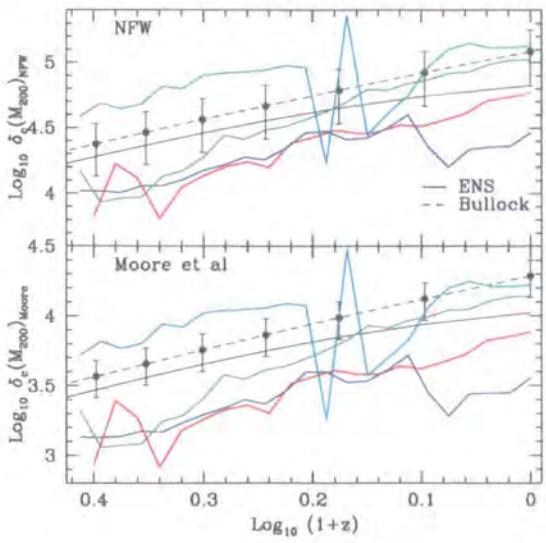

(a) Variation of c_{200} with Redshift

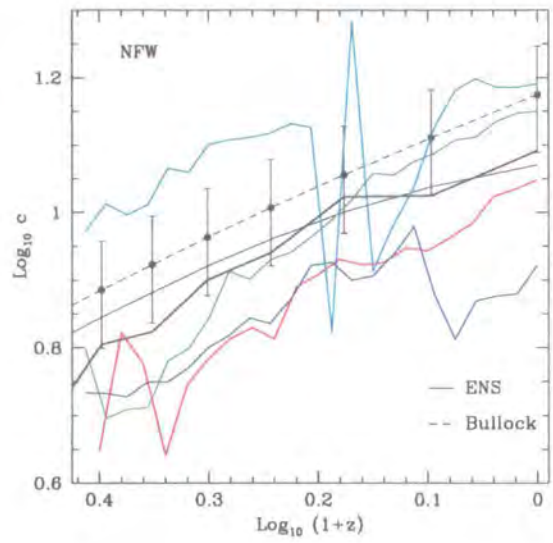

(b) Variation of Median (NFW) with Redshift

Figure 4.16: **Variation of concentration, c_{200}, with redshift, z.** We have determined best fit NFW (upper panel) and Moore et al. (lower panel) concentrations for all halos with redshifts in the range $0 \leq z \lesssim 3$, and we plot the resulting variation in figure 4.16(a). We have also computed the expected concentration for a "typical" halo at a given redshift using EPS (see text for details) and show the variation of concentration with redshift, as predicted by the ENS (solid curves) and Bullock et al. (dashed curves) prescriptions. Error bars correspond to the $1\,\sigma$ deviation in the median concentration found by Bullock et al. (2001) - $\Delta \log_{10} c_{\rm vir} \sim 0.18$. Figure 4.16(b) repeats the upper panel of figure 4.16(a), but highlights the average behaviour of the concentration (heavy solid black curve).

$0 \leq z \lesssim 1.5$.

On the other hand, if we consider the predicted behaviour of the median concentration with redshift by following the formation of a halo from high redshift using EPS theory to estimate the progenitor mass, we find that the models predict different rates of growth with redshift. The Bullock et al. relation is quite straight and grows approximately as $(1+z)^{0.45}$ with z, whereas the ENS relation curves gently from a $(1+z)^{0.5}$ relation between $1 \lesssim z \lesssim 1.5$ to a $(1+z)^{0.5}$ relation for $z \lesssim 0.25$.

The median concentration at any given redshift estimated from the simulation data agree with both the Bullock et al. and ENS models to within the 1σ deviation, but while the Bullock et al. model consistently overestimates the median concentration, the slope of the relation appears to provide a better match to that of our data ($(1+z)^{0.4}$).

The second point worth noting concerns the scatter in concentration. We find that there is a sizable spread in the best fit concentrations measured from the simulation data at all redshifts, larger than the $1\,\sigma$ deviation of $\log \Delta c \sim 0.18$ measured by Bullock et al. (2001). We estimate that the maximum deviation relative to the mean concentration never exceeds $\log \Delta c \sim 0.4$ or $\sim 40\%$ (at $z \simeq 1.5$), and is typically $25 - 30\%$ for redshifts $0 \leq z \lesssim 1.5$.

We conclude that the concentrations of the most massive progenitors at z of our dwarf halos at $z = 0$, in broad agreement with the theoretical models.

Characterising the Shape of the Mass Profile

We now consider the adequacy of the NFW and Moore et al. profiles as descriptions of simulated mass profiles by comparing spherically averaged mass profiles measured from the simulation data with the best fitting models as a function of radius at three different redshifts - $z = 0, 1.5$ and 3. By examining the fractional deviations in $\rho(r)$ and $V_c(r)$, $\Delta \log \rho(r)$ and $\Delta \log V_c(r)$, as a function of radius, we can gain insight into the radial extent over which the models provide an adequate description of the data and quantify deviations between the data and models.

We noted in figure 4.14 that both models provided an adequate representation of the simulation data for radii $r \gtrsim 0.15\, r_{-2}$, but that the Moore et al. profile appeared to be in better agreement with the observed steep inner profiles of the dwarfs. Therefore, we might expect the fractional deviations between the simulated data and the best fitting NFW and Moore et al. profiles to be small ($\lesssim 10\%$) for radii $r \gtrsim 2 - 3\% r_{200} \simeq 0.15\, r_{-2}$, and for deviations from the best fitting NFW profile to be larger at smaller radii.

As we mentioned earlier, spherically averaged profiles are constructed from shells equally spaced in $\log_{10} r$. For each of the profiles, we have estimated two sets of concentrations; one by means of a weighted fit to the density profile (hereafter ρ-fit), the other by an unweighted fit to the circular velocity profile (hereafter v_c-fit). We note that concentrations estimated from v_c-fits using both models are on average $\sim 30 - 40\%$ larger than those estimated from ρ-fits to the corresponding profile. Fractional errors in our weighted fits are greatest at small radii and therefore the fits tend to place most emphasis on intermediate to large radii; in contrast, the fractional errors are the same over the entire radial range in unweighted fits, which fit all parts of the halo to the same level of accuracy. This indicates that neither model fully captures the behaviour of the simu-

lated profiles, otherwise there should be no difference in the estimates of the concentration.

In figures 4.17 and 4.18, we show density and circular velocity profiles (top left hand panels) for each of our halos at redshifts $z = 0, 1.5$ and 3. We also plot the accompanying fractional deviations ($\Delta \log \rho(r)$ and $\Delta \log V_c(r)$) as a function of radius relative to the mean (top), best fitting NFW (middle) and best fitting Moore et al. profiles (bottom) at $z = 0$ (top right panel), $z \simeq 1.5$ (bottom left panel) and $z \simeq 3$ (bottom right panel). Curves are colour coded according to halo - red, green, blue and cyan correspond to **dH01**, **dH02**, **dH03** and **dH04** respectively.

As in figure 4.12, we have introduced factors of 10 offset (1 dex) in density and ~ 2.5 (0.4 dex) in circular velocity between successive redshifts in figures 4.17(a) and 4.18(a); thus the uppermost set of curves correspond to the halo profiles at $z = 0$. Light dotted curves represent the profiles we might expect a "typical" main progenitor to have at z, where we define typical in the sense described above - a halo with a median mass at z as determined by EPS theory, a concentration as estimated by the ENS model and a NFW mass profile.

Let us first consider the fractional deviations in the density profile (figure 4.17), and in particular, the performance of the best fitting NFW and Moore et al. models in describing the simulated profiles.

At $z = 0$, we note that both models provide acceptable fits (i.e. they agree with the simulated profiles to better than 10%) down to $\sim 5\% r_{200}$; deviations apparent close to r_{200} are the due to a massive subclump in the process of merging with **dH03**. However, inside $\sim 5\% r_{200}$, we find that both models tend to underestimate the density. At the innermost resolved point, the difference can be as great as 75% in the case of the NFW fit and 40% in the case of the Moore et al. fit to **dH03**. On average, the models tend to underestimate the density by $\sim 25\%$ (NFW) and 10% (Moore et al.), although we note that the NFW profile does appear to provide a good description of **dH02**'s profile, never differing by more than 10% between $r_{\rm min} \leq r \lesssim 80\% r_{200}$.

Deviations between the best fitting models and the simulated profiles are more pronounced at higher redshifts. At $z \simeq 1.5$ and $\simeq 3$, the best fit models agree with the simulated profiles to better than 10% on average down to about $\sim 10\%$ of r_{200}, although we note deviations can be as great as $\sim 20\%$ (e.g. **dH01**). Interior to $\sim 10\% r_{200}$, we find that both models tend to underestimate the density, as at $z = 0$. At the innermost

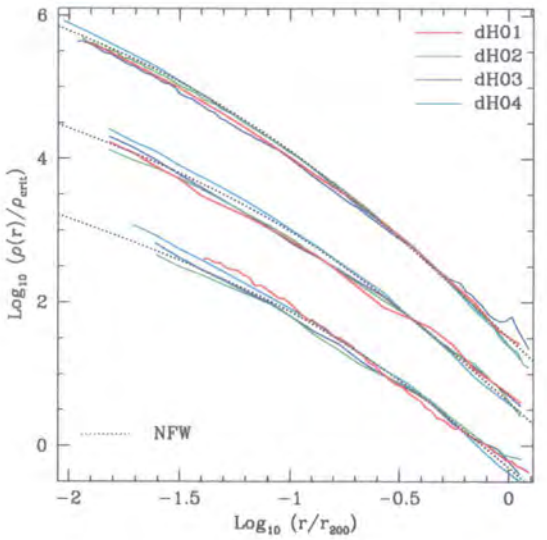

(a) Density Profiles at $z = 0,\ 1.5\,\&\,3$

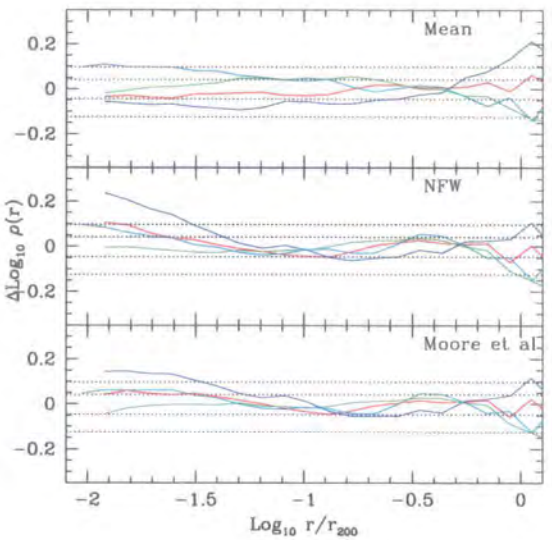

(b) Fractional Deviations in $\rho(r)$ at $z = 0$

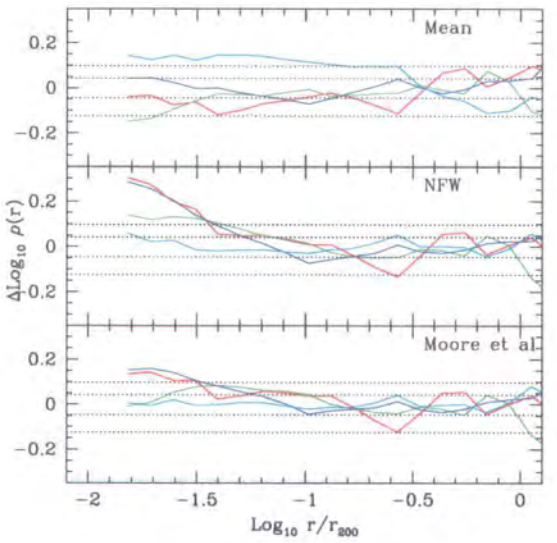

(c) Fractional Deviations in $\rho(r)$ at $z \simeq 1.5$

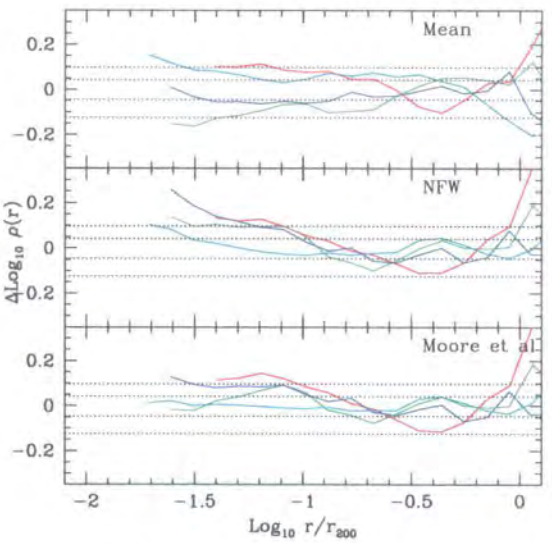

(d) Fractional Deviations in $\rho(r)$ at $z \simeq 3$

Figure 4.17: **Comparing the Shape of Density Profiles at** $z = 0,\ 1.5\,\&\,3$. In figure 4.17(a), we show density profiles for each dwarf halo in our sample, as measured at redshifts (from top) $z = 0, 1.5$ and 3.0; a vertical offset of 1 dex separates profiles determined at successive redshifts. Heavy solid red, green, blue and cyan curves correspond to halos `dH01`, `dH02`, `dH03` and `dH04` respectively. Light dotted curves represent NFW profiles for a *typical* halo at the appropriate redshift. In figures 4.17(b) through to 4.17(d), we plot the fractional deviation of each halo profile relative to the mean the mean, best fitting NFW and best fitting Moore et al. profiles at a given redshift (upper, middle and lower panels respectively). The sets of dotted lines correspond to deviations of 10% and 20%.

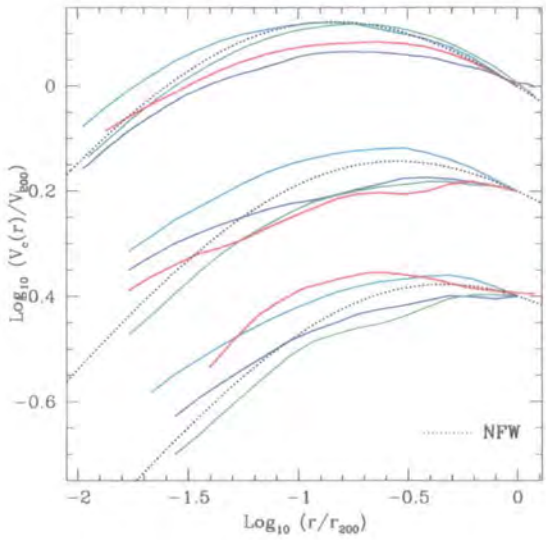

(a) Circular Profiles at $z = 0,\ 1.5\,\&\,3$

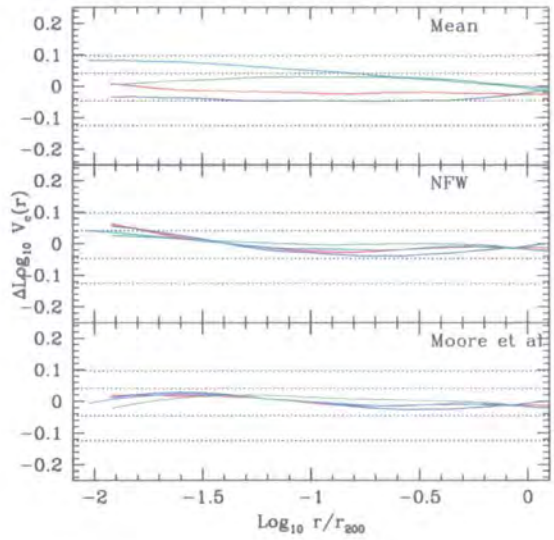

(b) Fractional Deviations in $V_c(r)$ at $z = 0$

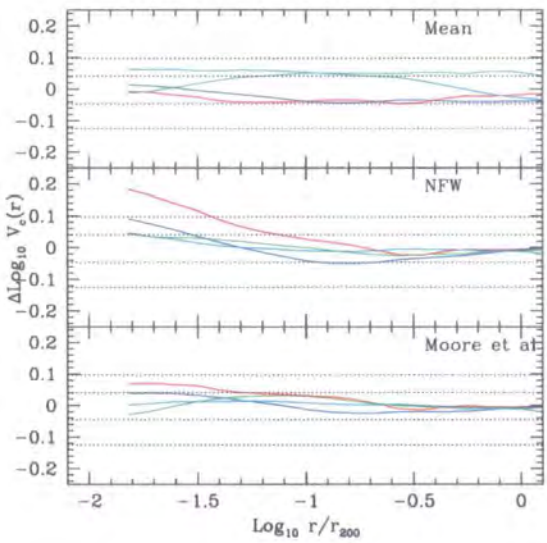

(c) Fractional Deviations in $V_c(r)$ at $z \simeq 1.5$

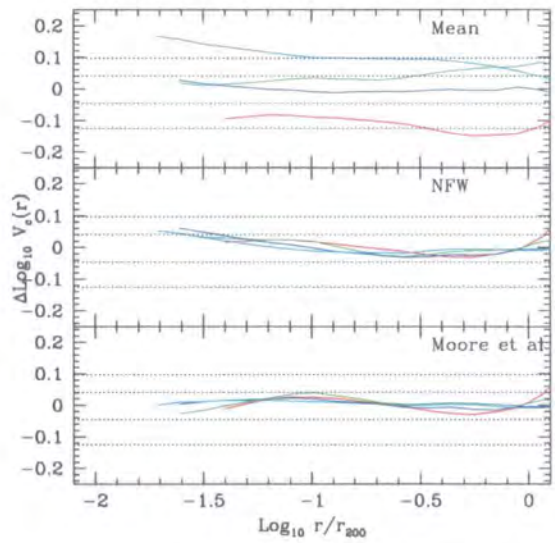

(d) Fractional Deviations in $V_c(r)$ at $z \simeq 3$

Figure 4.18: **Comparing the Shape of Circular Velocity Profiles at $z = 0,\ 1.5\,\&\,3$.** In figure 4.18(a), we show circular velocity profiles for each dwarf halo in our sample, as measured at redshifts (from top) $z = 0, 1.5$ and 3.0; a vertical offset of 0.4 dex separates profiles determined at successive redshifts. As before, the light dotted curves represent NFW mass profiles for a *typical* halo at the appropriate redshift. Figures 4.18(b) through to 4.18(d) show fractional deviations as a function of radius for each halo profile relative to the mean, best fitting NFW and best fitting Moore et al. profiles at a given redshift (upper, middle and lower panels respectively). The sets of dotted lines correspond to deviations of 10% and 20%.

resolved point, the predicted density can differ by as much as a factor of ~ 2 in the case of the NFW fit and 40% in the case of the Moore et al. fits to **dH01** and **dH03** at $z \simeq 1.5$. On average, the models tend to underestimate the density by $\sim 40\%$ (NFW) and 20% (Moore et al.), although we note that the Moore et al. profile appears to provide a good fit to **dH04**, never differing by more than 10% between $r_{\rm min} \leq r \lesssim r_{200}$.

We also note that the average fractional deviation relative to the best fitting models as a function of radius indicates that both models tend to underestimate the density at small radii and overestimate it at intermediate radii ($10\% r_{200} \lesssim r \lesssim 50\% r_{200}$), perhaps suggesting the need for a modified mass profile. This point shall be addressed in greater detail in the next chapter.

If we now consider figure 4.18, where we show how the fractional deviation in circular velocity varies as a function of radius, we find that both best fitting models are able to reproduce the circular velocity to better than 10% down to $\sim 5\% r_{200}$ at all redshifts.

At $z = 0$, both models fit the circular velocity to better than 10% down to $\sim 2\% r_{200}$. Inside $\sim 2\% r_{200}$, we find that the best fitting NFW can differ by as much as 15% (**dH01** and **dH03**), although on average it is closer to 10%. On the other hand, the best fitting Moore et al. profile never differs by more than 10%, down to the last reliably resolved data point.

At higher redshifts, we find that the deviations are greater than at $z = 0$, as we might expect upon consideration of the density profiles in figure 4.17. At $z \simeq 1.5$ and $\simeq 3$, both best fitting models agree with the simulated profiles to better than 10% on average down to about $\sim 5\%$ of r_{200}. Interior to $\sim 5\% r_{200}$, we find that the best fitting NFW can differ by as much as 60% at the innermost reliably resolved point (**dH01** at $z \simeq 1.5$), although on average the difference is closer to $15 - 20\%$. On the other hand, the best fitting Moore et al. profile never differs by more than 15% (**dH01** at $z \simeq 1.5$), and is closer to 10% on average.

We conclude that the best fitting NFW and Moore et al. profiles provide reasonably accurate descriptions - to better than 10% - of our simulated density profiles for radii $5\% r_{200} \lesssim r \lesssim r_{200}$ at redshifts between $0 \lesssim z \lesssim 3$. However, both models underestimate the value of the density in the centres of our halos, at radii $\lesssim 5\% r_{200}$; this discrepancy appears to be more serious for the NFW profile, which can underestimate the density by up to a factor of ~ 2 at $\sim 1\% r_{200}$. On the other hand, we find that both the best fitting

NFW and Moore et al. descriptions fit the circular velocity to better than 10% down to $\sim 2\% r_{200}$ at $z = 0$ and $\sim 5\% r_{200}$ at higher redshifts, whereas the Moore et al. profile appears to perform better close to the centre.

Constraining the Central Slope

We have seen in figures such as 4.14 that the dwarfs halos in our sample can be characterised by steep inner density profiles that appear to be at odds with the predictions of the NFW and Moore et al. models. Indeed, we have also noted that the *best fitting* NFW and Moore et al. models underestimate central densities by between $10 - 60\%$ on average, although deviations as large as a factor of ~ 2 were noted. However, we did not quantify this "steepness".

The logarithmic slope, $S(r)$, of the density profile (defined in § 1.5) can be used to estimate the slope, but this is inherently a noisy quantity (the derivative of a differential function) and our sample of halos is small. Instead, we have adopted the maximum asymptotic slope, $\alpha(r)$, as a measure of the slope of the density profile at radius r. In particular, $\alpha(r)$ defines an *upper limit* on the slope of the profile at that radius.

We can estimate the value of α by assuming that the halo is spherically symmetric and that the interior density profile can be characterised as a power-law, $\rho(r) \propto r^{-\alpha}$; it follows that

$$\alpha(r) = 3\left(1 - \frac{\rho(r)}{\overline{\rho(r)}}\right) \tag{4.45}$$

where $\rho(r)$ is the local density and $\overline{\rho(r)}$ is the mean interior density at radius r.

It is straightforward to derive analytic expressions for $\alpha(r)$ for both the NFW and Moore et al. profiles; for a NFW model,

$$\alpha(x) = 3 - \left(\frac{c^{\rm N}x}{1 + c^{\rm N}x}\right)^2 \frac{1}{\ln(1 + c^{\rm N}x) - c^{\rm N}x/(1 + c^{\rm N}x)}, \tag{4.46}$$

whereas the corresponding expression for the Moore et al. model is given by

$$\alpha(x) = 3 - \frac{3}{2}\left(\frac{(c^{\rm M}x)^{3/2}}{1 + (c^{\rm M}x)^{3/2}} \frac{1}{\ln(1 + (c^{\rm M}x)^{3/2})}\right) \tag{4.47}$$

In both cases, $x = r/r_{200}$ corresponds to the normalised radius and $c^{\rm N}$ and $c^{\rm M}$) correspond to NFW and Moore et al. concentrations respectively.

In figure 4.19, we show the variation of $\alpha(r)$ with radius for each of the four halos in our sample at $z = 0$ (upper panel), $z \simeq 1.5$ (middle panel) and $z \simeq 3$ (lower panel). For

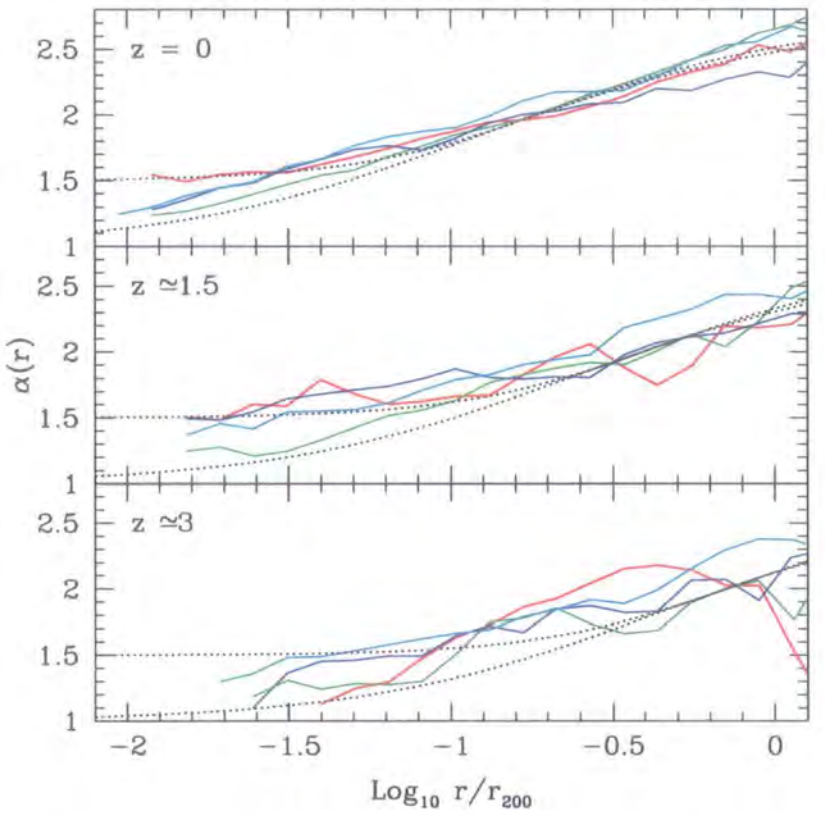

Figure 4.19: **The Maximal Slope, $\alpha(r)$, and its Variation with Redshift.** We have computed $\alpha(r) = 3\,(1 - \rho(r)/\overline{\rho}(r))$ for each of the halos in our sample and we show the radial variation of a selection of these profiles measured at $z = 0$ and close to $z \simeq 1.5$ and $\simeq 3$. Upper and lower dotted curves correspond to the expected behaviour of Moore et al. and NFW profile for a typical progenitor mass at the given redshift. Curves are colour coded according to halo - red, green, blue and cyan correspond to `dH01`, `dH02`, `dH03` and `dH04` respectively. See text for further details.

reference, we show also the radial variation of $\alpha(r)$ for a "typical" halo at z - as before, one whose mass has been determined using EPS theory and whose concentration has been estimated using the ENS model - predicted by the NFW (lower dotted curves) and Moore et al. (upper dotted curves) models.

There are a few important points worth commenting on in this figure. Although the curves become increasingly noisy with redshift, we note that they show little or no curvature; indeed, the average curve at each redshift falls roughly linearly with radius, down to the innermost believable point ($\sim 1\% r_{200}$ at $z = 0$, $\sim 3\% r_{200}$ at $z \simeq 3$). This behaviour would appear to rule out very steep central slopes and is in sharp contrast (especially at $z = 0$) with the prediction of the Moore et al. model, which achieves its asymptotic inner value of $\alpha = 1.5$ at a relatively large radius - between $\sim 3\% r_{200}$ at $z = 0$ and $\sim 10\% r_{200}$ at $z \simeq 3$.

Furthermore, the apparent lack of curvature in the profiles suggests that, even in our best resolved halos at $z = 0$, we have yet to see evidence for convergence to an asymptotic slope, similar to the conclusion we reached in chapter 2.

Finally, we note that the average value of the maximum asymptotic slope at the innermost reliably resolved radius, $\alpha(r_{\rm min})$, lies between the predictions of the NFW and Moore et al. models and does not appear to change significantly with redshift. At $z = 0$, $\alpha(r_{\rm min}) \simeq 1.25$ where $r_{\rm min} \simeq 1\% r_{200}$, while at $z \simeq 3$, $\alpha(r_{\rm min}) \simeq 1.3$ where $r_{\rm min} \simeq 3 - 4\% r_{200}$. This reflects the competing effects of the lowering of concentration and the growth in mass of the halo; although we expect the value of α at a fixed fraction of the virial radius to decrease with increasing redshift (because the concentration is decreasing), the halo is less massive at early times and therefore $\alpha(r_{\rm min})$ is evaluated at a larger fraction of the virial radius (because $r_{\rm min}$ is larger), at which point the value of α is larger.

4.4.3 Spherically Averaged Kinematics

The analysis performed so far has been concerned primarily with the spatial distribution of the dark matter within the halo, and in particular, spherically averaged quantities such as the density profile $\rho(r)$ and the related circular velocity profile $V_c(r)$. However, if the mass profiles we find in our simulations are representative of systems in dynamical equilibrium, it follows from simple consideration of the Jeans Equations (pp. 195-211, Binney & Tremaine, 1987) that the spatial and kinematical structures of CDM halos should be related. This duly leads us to consider the kinematics of dark matter in and around our

dwarf halos.

We have examined the behaviour of the radial velocity, v_r, the velocity anisotropy parameter, $\beta(r)$, and the ratio, $v_{\rm rot}/\sigma_r$, which measures the importance of the mean rotational velocity to radial velocity dispersion of dark matter as a function of radius; the results are shown in figures 4.20, 4.21 and 4.22. The upper and lower left hand panels show radial profiles for each of the halos at $z = 0$, 1.5 and 3.0, while the lower right hand panel highlight the mean behaviour (averaged over all the halos) at each of these redshifts. We also consider the degree to which the halos in our sample are supported by anisotropic velocity dispersion (or "anisotropy pressure") by computing the dimensionless spin parameter, λ, as a function of redshift in figure 4.23.

Note that we have computed the mean value (in physical units) for material in thin spherical shells centred on the centre of mass of the halo; velocities have been defined relative to the bulk centre of mass motion. We define the mean rotational velocity in terms of the angular momentum ($\vec{J}$) of material in the shell,

$$v_{\rm rot} = \frac{|\vec{J}|}{M\overline{R}}, \tag{4.48}$$

where M is the mass of the shell and $\overline{R}$ is the mean perpendicular distance from the axis defined by $\vec{J}$. The velocity anisotropy parameter is defined such that

$$\beta = 1 - \frac{1}{2}\frac{\sigma_t^2}{\sigma_r^2}, \tag{4.49}$$

where σ_r and σ_t represent the mean radial and tangential velocity dispersions respectively. According to our definition, $\beta = 0$ implies an isotropic velocity distribution, while $\beta \to 1/-\infty$ indicates that the velocities are preferentially radial/tangential.

Let us first consider the spherically averaged behaviour of the radial velocity of dark matter (figure 4.20), where we have expressed v_r in units of V_{200}, the circular velocity at r_{200}, for ease of comparison. We expect to find $v_r \simeq 0$ within r_{200} if the halo is dynamically relaxed, but $v_r < 0$ close to r_{200} because of the infall of material onto the halo.

At $z = 0$ (upper left hand panel), v_r is approximately zero within r_{200} of each of the systems, suggesting that our halos are dynamically relaxed systems at present. Somewhat surprisingly however, we find that v_r is negligible out to $\sim 2\,r_{200} \simeq 70\,h^{-1}$ kpc (roughly corresponding to the turnaround radius), contrary to expectation, but grows rapidly beyond this radius as the outer shells start to couple to the Hubble flow. The deviation

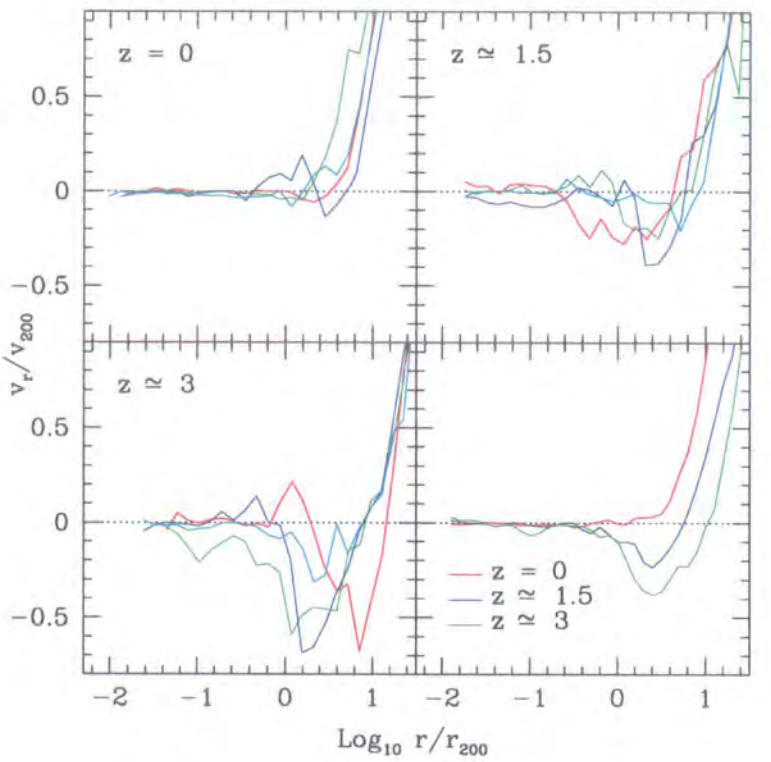

Figure 4.20: **Radial variation of radial velocity, v_r, at three different redshifts.** We show spherically averaged radial velocity profiles for dH01 (red curves), dH02 (green curves), dH03 (blue curves) and dH04 (cyan curves) at redshifts $z = 0$, 1 and 2 respectively. The curves are truncated at the innermost believable radius, $r_{\rm min}$ (see text). Average profiles for each of these redshifts are shown in the bottom right hand panel; note that in this instance red corresponds to $z = 0$, blue to $z \simeq 1.5$ and green to $z \simeq 3$. Radial velocities are expressed in units of V_{200}, the circular velocity at r_{200}, and radii are expressed in units of r_{200}.

apparent in the profile of dH03 close to r_{200} ($v_r > 0$, indicating that these shells are moving outwards) reflects the perturbing influence of a companion halo which appears to be on the outward part of an elongated orbit. On average, however, dwarf galaxy halos appear to experience little mass infall at $z = 0$.

At $z \simeq 1.5$ (upper right hand panel), individual profiles start to show the characteristic signatures of mass inflow and outflow - as we might have anticipated, given that this represents the median redshift of formation for these objects. For example, dH01, dH02 and dH03 all shows signs of mass accretion, while dH04 is relatively quiescent. On the other hand, if we consider the average behaviour of our sample as a whole, v_r is comparatively small within r_{200} - for $r \lesssim 0.1\, r_{200}$, $v_r \simeq 0$, while for $0.1\, r_{200} \lesssim r \lesssim r_{200}$, $|v_r| \lesssim 0.1\, V_{200}$.

This indicates that our halos are dynamically relaxed on average (see blue curve in bottom right hand panel), although the central parts are "more" relaxed, that is $v_r \simeq 0$, as we might expect. Beyond r_{200}, however, we now see a well defined mass infall pattern (peaking at $\sim 2.5\, r_{200}$).

Finally, at $z \simeq 3$ (lower left hand panel), it is clear that all of the halos are accreting material, showing the characteristic signatures of mass infall with pronounced peaks in $|v_r|$ between $r_{200} \lesssim r \lesssim 5\, r_{200}$. On average, v_r is negligible within $r < r_{200}$ - never exceeding $|v_r| \lesssim 0.1\, V_{200}$ - but we see stronger infall beyond r_{200} with a peak at $\sim 2.5\, r_{200}$.

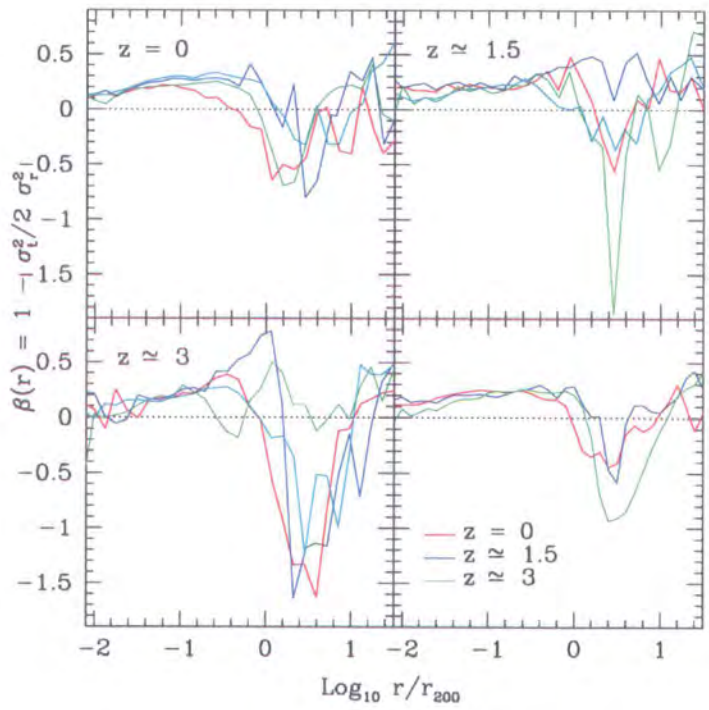

Figure 4.21: **Variation of velocity anisotropy, β, with halocentric radius at three different redshifts.** We have computed $\beta = 1 - 1/2\ \sigma_t^2/\sigma_r^2$ in a series of concentric spherical shells centred on the halos `dH01` (red curves), `dH02` (green curves), `dH03` (blue curves) and `dH04` (cyan curves) at redshifts $z = 0$, 1.5 and 3 respectively. According to our definition, $\beta = 0$ corresponds to an isotropic velocity distribution, while $\beta \to 1/-\infty$ indicates that the distribution is radial/tangential. As in figures 4.20 and 4.22, average profiles at each of these redshifts are shown in the bottom right hand panel. Curves are truncated at the innermost believable radius, $r_{\rm min}$. Note that we have scaled the radii by r_{200}.

The velocity anisotropy parameter, β, provides us with information that is comple-

mentary to that derived from the radial velocity profile, giving us a simple means of parameterising the spherically averaged velocity distribution of dark matter at a given radius. We have computed β as a function of radius at redshifts $z = 0, 1.5$ and 3 and we show the results in figure 4.21. If the velocity distribution is the same throughout the halo, we would expect $\beta \simeq$ constant for $r \lesssim r_{200}$. However, we might expect $\beta \simeq 0$ in the innermost parts, becoming more radial with increasing radius; this kind of behaviour is observed in higher mass systems (see § 5.3). We also expect $\beta \to 1$ for $r \gtrsim r_{200}$, that is, we expect the velocity distribution to become radial beyond $\sim 2\,r_{200}$, reflecting the coupling of material close to the turnaround radius and the Hubble flow.

At $z = 0$ (upper left hand panel), $\beta \simeq 0$ implies that the distribution is effectively isotropic within the central parts of all the halos. It then grows (or becomes more radial) in an almost linear fashion with increasing radius for $r \lesssim 0.1\,r_{200}$. The profiles plateau at an average of $\beta \simeq 0.3$ between $0.1\,r_{200} \lesssim r \lesssim 0.6\,r_{200}$, before rolling over and becoming negative (or tangential) at $\sim r_{200}$. β reaches its minimum at $r \simeq 2.5\,r_{200}$, at which point it begins to increase again; the velocity distribution becomes radial ($\beta > 0$) once again at $r \simeq 4\,r_{200}$ and β continues to rise with increasing radius, as we would expect.

Perhaps surprisingly, we do not see any significant differences in the average behaviour of β at higher redshifts. At both $z \simeq 1.5$ (upper right hand panel) and $z \simeq 3$ (lower left hand panel), the velocity distribution is preferentially radial within r_{200}, tangential at intermediate radii ($r_{200} \lesssim r \lesssim 6 - 10\,r_{200}$) and increasingly radial beyond this. The distribution is more tangential at intermediate radii at $z \simeq 3$ - > z_f - in the sense that β is more negative, but this can be attributed to the complicated orbits of clumps participating in the assemblage of the halo.

Figure 4.22 highlights the importance of rotation within the halo by showing the dependence of the ratio of $v_{\rm rot}/\sigma_r$, the mean rotational velocity to the radial velocity dispersion averaged over spherical shells, on halocentric radius. Previous studies (e.g. Cole & Lacey 1996) and our own investigations (§ 5.3) have found that dark matter halos are supported by anisotropic velocity dispersion; therefore we do not expect the rotation velocity to be significant.

The are two main points to note here. The first is that, in general, $v_{\rm rot}$ is small compared to σ_r within r_{200} at all redshifts; we find that, on average, $v_{\rm rot} \sim 0.05 - 0.4\,\sigma_r$, which suggests that rotation does not make a significant contribution to the support of the halo. The exception - **dH01** at $z \simeq 3$ in which $v_{\rm rot}/\sigma_r \to 1$ - can be explained by the proximity

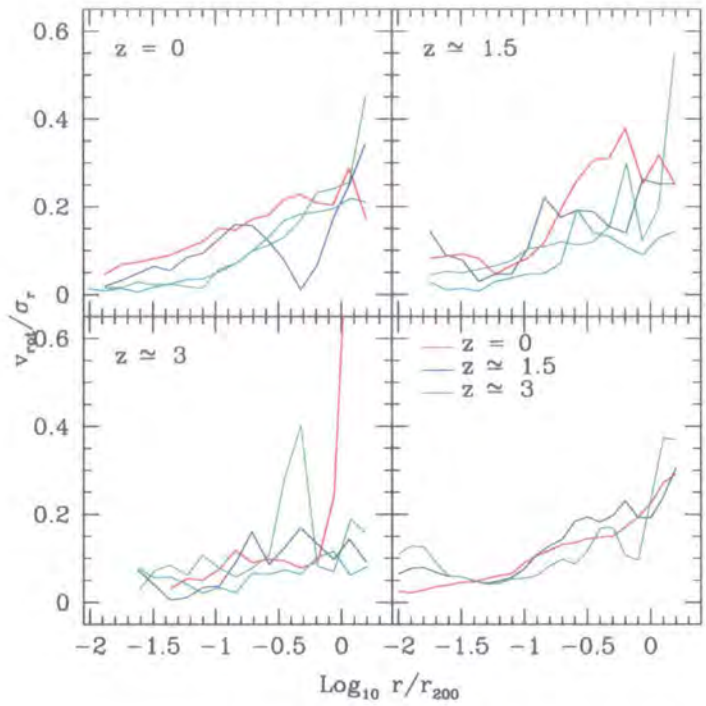

Figure 4.22: **Radial variation of the ratio $v_{\rm rot}/\sigma_r$ at three different redshifts.** We can quantify the degree to which the system is supported by anisotropic velocity dispersion by plotting the ratio of the mean rotational velocity to the radial velocity dispersion of the dark matter as a function of radius. We show $v_{\rm rot}/\sigma(r)$ computed for a series of concentric spherical shells centred on the halo for `dH01` (red curves), `dH02` (green curves), `dH03` (blue curves) and `dH04` (cyan curves) at redshifts $z = 0$, 1.5 and 3 respectively. As in the figures 4.20, we also show average profiles for each of these redshifts in the bottom right hand panel. Curves are truncated at the innermost believable radius, $r_{\rm min}$. Velocities and radii are scaled by V_{200} and r_{200} respectively.

of an infalling clump close to r_{200}. The second is that, in virtually all cases, $v_{\rm rot}/\sigma_r$ appears to increase with radius. At $10\%\, r_{200}$, $v_{\rm rot}/\sigma_r \simeq 0.1$, while at r_{200}, $v_{\rm rot}/\sigma_r \simeq 0.3$. The increase appears more "steady" (in the sense that it is effectively monotonic) at $z = 0$, while it is more abrupt at higher redshifts; at $z \simeq 1.5$, $v_{\rm rot}/\sigma_r \simeq 0.05$ between $0.01\, r_{200} \lesssim r \lesssim 0.1\, r_{200}$, before starting to rise, peaking at $0.5\, r_{200}$ ($v_{\rm rot}/\sigma_r \simeq 0.4$), and falling to $v_{\rm rot}/\sigma_r \simeq 0.3$ at r_{200}. On the other hand, at $z \simeq 3$, $v_{\rm rot}/\sigma_r \simeq 0.1$ between $0.01\, r_{200} \lesssim r \lesssim 0.1\, r_{200}$ and then shows a steady increase to $v_{\rm rot}/\sigma_r \simeq 0.25$ at r_{200}.

We conclude that isolated dwarf galaxy CDM halos at $z = 0$ are supported by anisotropy "pressure" ($v_{\rm rot}/\sigma_r \simeq 0.1 - 0.3$) and are in dynamical equilibrium ($v_r/V_{200} \simeq 0$

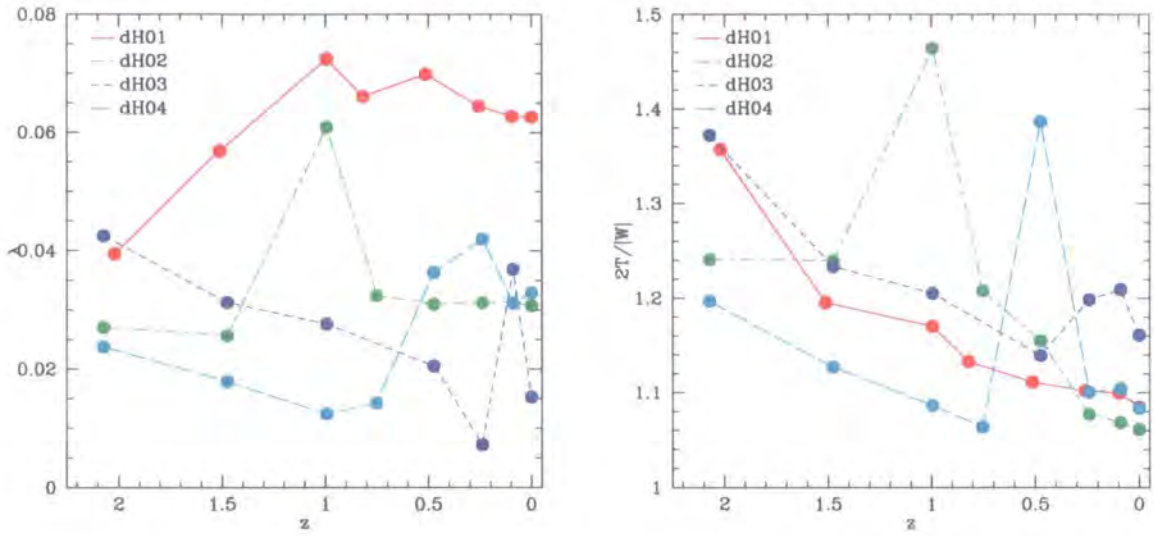

(a) λ : Variation with redshift

(b) 2T/|W| : Variation with redshift

Figure 4.23: **The Importance of Velocity Anisotropy Pressure.** Dwarf galaxy halos are supported by an anisotropic velocity dispersion tensor in general. This is borne out by the values of λ, the dimensionless spin parameter, presented in figure 4.23(a); $\lambda \simeq 0.04$, irrespective of redshift. Figure 4.23(b) indicates that the halos become more relaxed at later times. See text for further details

within r_{200}); they experience negligible mass infall ($v_r/V_{200} \simeq 0$ at $r \gtrsim r_{200}$) and their velocity distribution is mildly radial ($\beta \simeq 0.3$ or $\sigma_t \simeq 1.2\sigma_r$) within r_{200} but becomes tangential between $r_{200} \lesssim r \lesssim 4\, r_{200}$.

At higher redshifts, these systems continue to be "pressure" dominated but tend to be less dynamically relaxed than their $z = 0$ counterparts. Infall becomes appreciable ($|v_r| \simeq 0.3 V_{200} \simeq 10$ km/s) but there is little change in the overall velocity distribution.

Finally, we investigate the angular momentum content of our halos in figure 4.23, where we show the dependence of the spin parameter, λ, on the mass of the halo. This can be considered complementary to figure 4.22, in which we computed the related quantity $v_{\rm rot}/\sigma_r$ as a function of radius. The dimensionless spin parameter is defined as,

$$\lambda = \frac{J\,|E|^{1/2}}{GM^{5/2}} \tag{4.50}$$

where J, E and M are the total angular momentum, energy and mass of the virialised dark matter halo, and G is the gravitational constant. Physically, the spin parameter provides

a measure of the size of a halo's net rotational velocity, derived from its spin angular momentum, relative to its circular velocity, and indicates whether the halo is supported by anisotropy pressure or rotation. Previous studies have found that λ is generally small with a median value $\lambda_{\rm med} \simeq 0.04$ (e.g. Cole & Lacey 1996).

We have computed λ for all the halos in our sample at selected redshifts between $0 \lesssim z \lesssim 2$ and the results are shown in figure 4.23(a). Note that we have computed λ for all the material within $M_{\rm vir}$ instead of M_{200} in this instance , for consistency with previous studies. As usual, $M_{\rm vir}$ is defined as

$$M_{\rm vir} = \frac{4\pi}{3}\Delta_{\rm vir}\rho_{\rm crit}r_{\rm vir}^3 \tag{4.51}$$

where $\Delta_{\rm vir} \simeq 97(169)$ at $z = 0(2)$ (Eke et al. (1996)). We show values of λ computed for both $M_{\rm vir}$ and M_{200} in table 4.2. For reference, we also present values of the virial ratio, $2T/|W|$; these data are shown graphically in figure 4.23(b) and indicate that halos tend to be less dynamically relaxed at earlier times.

Perhaps the main point to note in this plot is that λ is comparable for all the halos in our sample, despite the range in redshift. Indeed, we find $\lambda_{\rm med} \simeq 0.035$ at $z = 0$ and $\lambda_{\rm med} \simeq 0.03$ at $z \simeq 2$, in good agreement with the findings of previous studies (e.g. Cole & Lacey (1996)). In common with our previous findings, we conclude that dwarf galaxy halos are supported by anisotropy pressure for redshifts between $0 \lesssim z \lesssim 2$.

4.4.4 The Shape of Dwarf Galaxy Halos

Projected maps of the density distribution in and around each of the dwarfs at $z = 0$, as shown in figure 4.2, indicate that that these objects can be described as triaxial ellipsoids, in common with the results of previous studies for more massive systems (e.g. Frenk et al. (1988), Cole & Lacey (1996), Thomas et al. (1998), Jing & Suto (2002)).

This observation is confirmed in figures 4.24 and 4.25, where we show two dimensional projections of the particle distribution in thin isodensity shells for two of the halos in our sample, **dH02** and **dH04**, at redshifts of $0 \leq z \lesssim 1.5$. The shells are defined such that they contain particles with densities in the range $0.97\,\rho_s < \rho < 1.03\,\rho_s$, where

$$\begin{aligned} \rho_s &= \tilde{\rho}^{(n)}\rho_{\rm crit}\ , \\ \tilde{\rho}^{(n)} &= 20 \times 5^{n-1}\ ,\ n = 1, 7. \end{aligned} \tag{4.52}$$

These densities correspond to shells with effective radii of 100%, 80%, 40%, 20%, 5% and 2% of the virial radius, r_{200}, where we define the effective radius of the shell to be

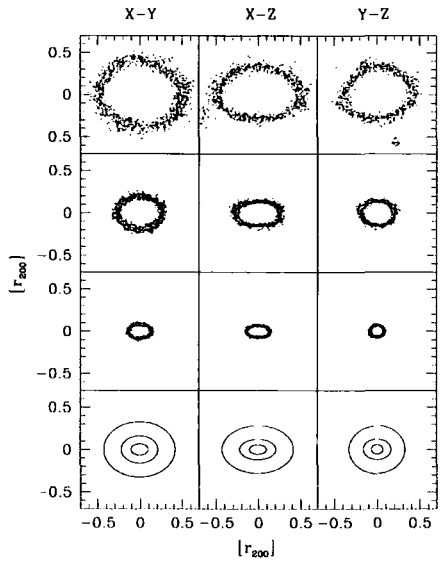

(a) $z = 0$

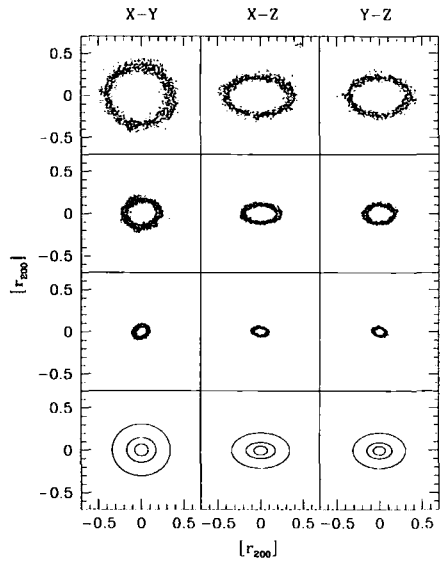

(b) $z = 0.5$

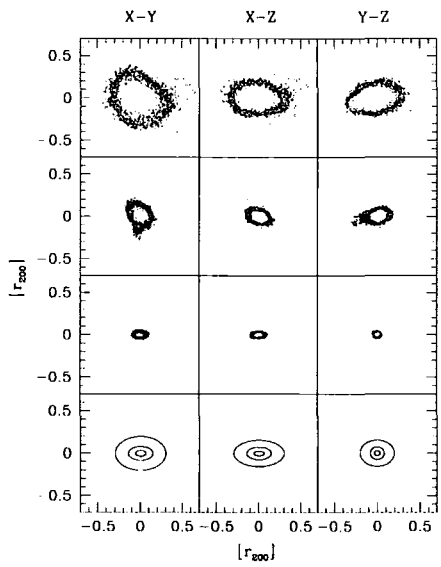

(c) $z = 1$

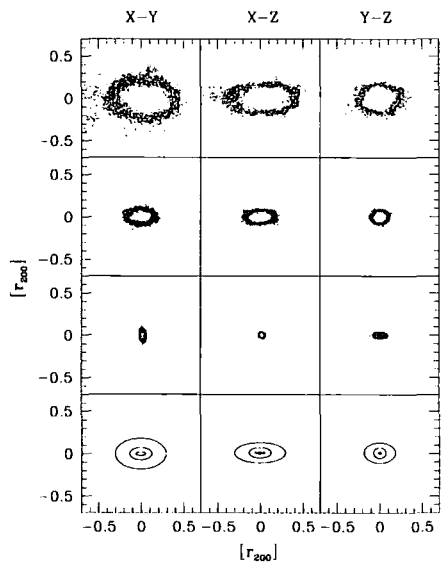

(d) $z = 1.5$

Figure 4.24: **Two dimensional projections of isodensity shells in dwarf halo dH02 at redshifts** $0 \leq z \lesssim 1.5$. We show two dimensional projections of the distribution of particles in slices through shells satisfying the density thresholds (from top) $\rho_s = 500$, 2500 and 12500 times $\rho_{\rm crit}$. Particle coordinates have been rotated into the diagonalised frame and scaled by the virial radius, r_{200}, of the halo at the given redshift. We show the particle distribution as projected onto the major-intermediate (X-Y), major-minor (X-Z) and intermediate-minor (Y-Z) planes. We also show the corresponding ellipsoidal fits to the isodensity surfaces in the bottom set of panels.

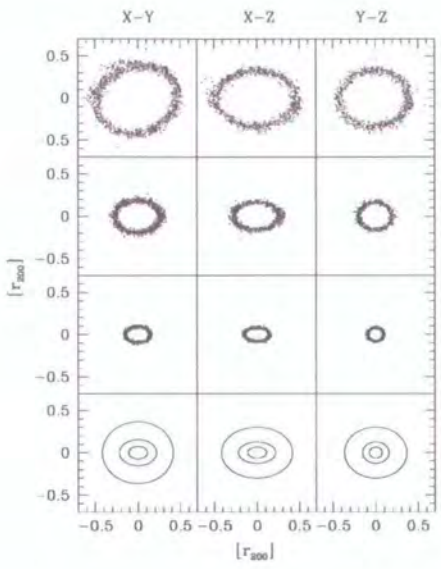

(a) $z = 0$

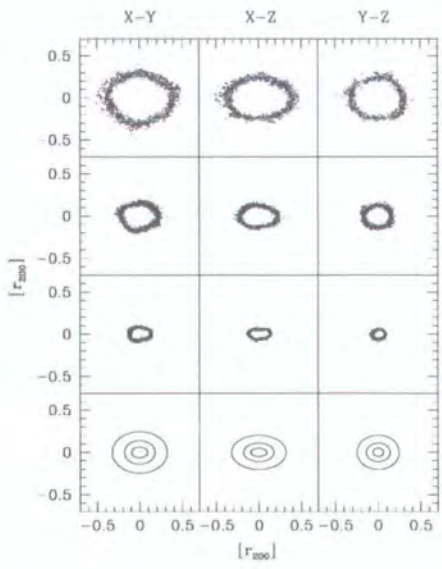

(b) $z = 0.5$

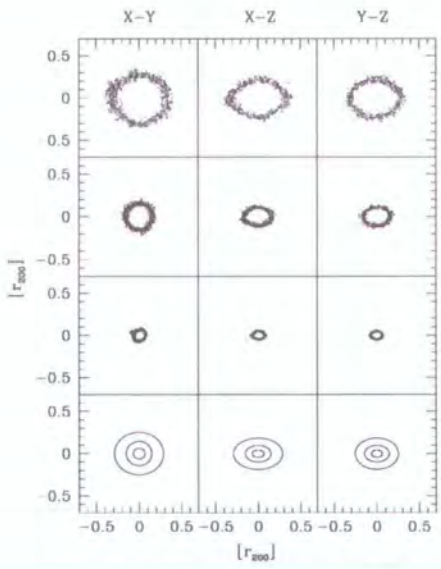

(c) $z = 1$

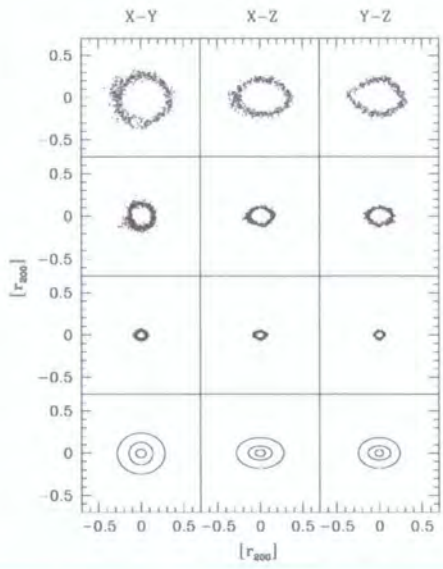

(d) $z = 1.5$

Figure 4.25: **Two dimensional projections of isodensity shells in dwarf halo dH04 at redshifts** $0 \leq z \lesssim 1.5$**.** We show two dimensional projections of the distribution of particles in slices through shells satisfying the density thresholds (from top) $\rho_s = 500$, 2500 and 12500 times $\rho_{\rm crit}$. Particle coordinates have been rotated into the diagonalised frame and scaled by the virial radius, r_{200}, of the halo at the given redshift. We show the particle distribution as projected onto the major-intermediate (X-Y), major-minor (X-Z) and intermediate-minor (Y-Z) planes. We also show the corresponding ellipsoidal fits to the isodensity surfaces in the bottom set of panels.

$r_{\rm eff} = (abc)^{1/3}$. We have chosen to show projections of the particle distribution in three of these shells - (from top) $\rho_s/\rho_{\rm crit} = 500$, 2500 and 12500.

For clarity, we have determined the orientation of the principal axes for each of the shells and rotated the particle coordinates into the diagonalised frame so that projections are onto the principal (or symmetry) planes. This procedure is described in detail in § 4.3.3. To emphasise the ellipticity of the shells, we have taken thin slices through the rotated shells with thicknesses corresponding to 10%, 5% and 2.5% of r_{200} for $\rho_s/\rho_{\rm crit} = 500$, 2500 and 12500 respectively. Furthermore, we show projections of equivalent ellipsoids for each of the shells in the bottom panels; axis ratios are estimated as described in § 4.3.3.

There are a few points worth noting in these two figures. The isodensity surfaces appear relatively regular and symmetric at all redshifts, although we do note deviations from symmetry in the outermost ($\rho_s = 500\,\rho_{\rm crit}$) shells of **dH02** at $z \geq 1$. At any given redshift, we note that the axis ratios inferred from isodensity shells at a fixed overdensity appear to be similar in the two halos. Furthermore, at any given overdensity, we find that the values of the axis ratios inferred from isodensity shells in the final halo and its progenitors do not appear to vary with redshift. Finally, we note that the axis ratios appear to decrease over the range of overdensities highlighted; this suggests that isodensity surfaces become more elongated in the innermost parts of the halos.

We can gain greater insight into the variation of a halo's shape with radius by calculating the ratio of the intermediate-to-major and minor-to-major axis ratios, b/a and c/a, for shells at progressively higher overdensities at all of the redshifts we have considered. In figure 4.26(a), we show the variation of b/a (solid lines) and c/a (dashed lines) for a series of thin isodensity shells of increasing overdensity at three different redshifts - $z = 0$ (upper left hand panel), $z \simeq 0.5$ (upper right hand panel) and $z \simeq 1$ (lower left hand panel) - for each of the halos in our sample. Curves are colour code according to halo - red, green, blue and cyan correspond to **dH01**, **dH02**, **dH03** and **dH04** respectively. We also highlight the average behaviour of the axis ratios with overdensity at each of these redshifts in the bottom right hand panel.

We note that both b/a and c/a decrease with increasing overdensity, ρ_s, at each of redshifts we have analysed. Focusing on the average behaviour (lower right hand panel), we find that b/a (c/a) falls from 0.85 (0.65) at $\rho_s = 10^3\,\rho_{\rm crit}$ to 0.75 (0.55) at $\rho_s = 10^4\,\rho_{\rm crit}$ at $z = 0$; from 0.8 (0.6) at $\rho_s = 10^3\,\rho_{\rm crit}$ to 0.7 (0.5) at $\rho_s = 10^4\,\rho_{\rm crit}$ at $z \simeq 0.5$; and from 0.7 (0.55) at $\rho_s = 10^3\,\rho_{\rm crit}$ to 0.7 (0.5) at $\rho_s = 10^4\,\rho_{\rm crit}$ at $z \simeq 1$. In general, it would

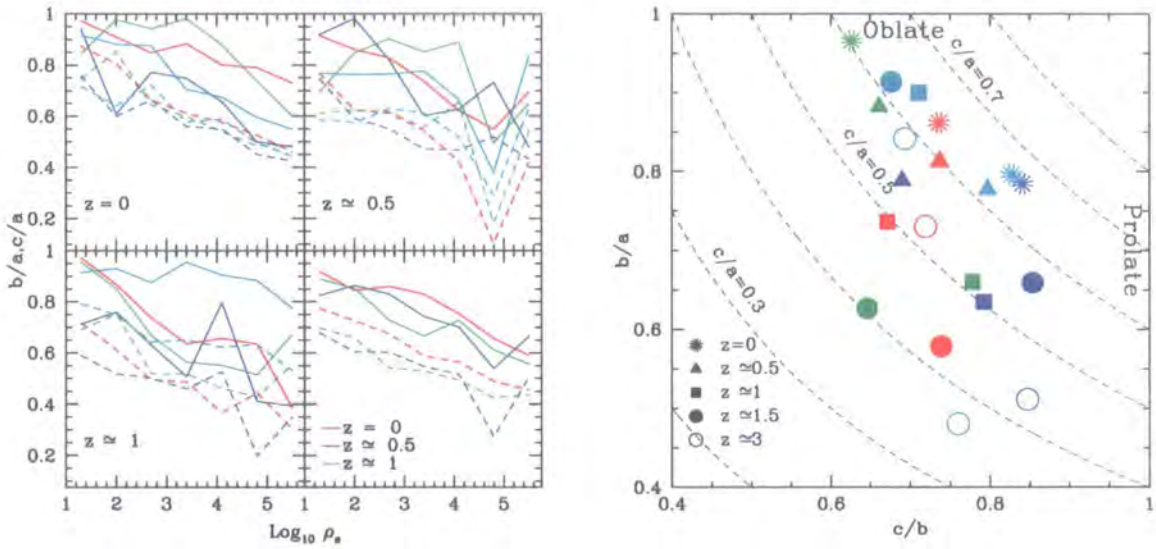

(a) Variation of Axis Ratios with Local Density

(b) Variation of Shape with Mass Scale

Figure 4.26: **Variation of Halo Shape with Overdensity, ρ_s, and Redshift, z.** Figure 4.26(a) illustrates how the axis ratios of isodensity shells change as we probe higher densities, corresponding to smaller radii, within the bulk of the dark matter halo. We show the variation of b/a (heavy solid lines) and c/a (heavy dashed lines) as a function of increasing density threshold, ρ_s, for the dwarf halos at $z = 0$ (upper left hand panel), $z \simeq 0.5$ (upper right hand panel) and $z \simeq 1$ (lower left hand panel). We directly compare the mean behaviour at each of these redshifts in the lower right hand panel. In figure 4.26(b), we show how a halo's shape depends on redshift by comparing the distribution of axis ratios, b/a and c/b, measured at the half-mass radius of the halo at $z = 0$ (asterisks), $z \simeq 0.5$ (filled triangles), $z \simeq 1$ (filled squates), $z \simeq 1.5$ (filled circles) and $z \simeq 3$ (open circles). Lightly dashed curves indicate how the value of c/a varies for a given c/b and b/a. Curves and symbols are colour coded according to halo - red, green, blue and cyan correspond to `dH01`, `dH02`, `dH03` and `dH04` respectively.

appear that the variation of both b/a and c/a with overdensity can be approximated by a power law that varies as $\rho_s^{-\alpha}$, where $\alpha \simeq 0.07$, independent of redshift.

We note also that b/a and c/a show a scatter that is relatively uniform with overdensity and redshift. If we use the 1σ deviations in the values of b/a and c/a relative to the mean to quantify the scatter, we find that the 1σ deviation in b/a (c/a) measured at $z = 0$ varies between $\sim 15\%$ ($\sim 4\%$) at $\rho_s = 10^3\,\rho_{\rm crit}$ and $\sim 20\%$ ($\sim 6\%$) at $\rho_s = 10^4\,\rho_{\rm crit}$. On the other hand, at $z \simeq 1$, we find that b/a (c/a) varies by as much as $\sim 20\%$ ($\sim 20\%$) at $\rho_s = 10^3\,\rho_{\rm crit}$ and $\sim 35\%$ ($\sim 40\%$) at $\rho_s = 10^4\,\rho_{\rm crit}$. In other words, the scatter increases with increasing redshift.

Figure 4.26 offers us a complementary means of quantifying the redshift dependence of halo shape. We compare the distribution of axis ratios, b/a and c/b, as measured at the half mass radius of each of the halos at redshifts $z = 0$ (asterisks), $z \simeq 0.5$ (filled triangles), $z \simeq 1$ (filled squares), $z \simeq 1.5$ (filled circles) and $z \simeq 3$ (open circles). We note that prolate objects have $a = b > c$ and oblate objects have $a > b = c$.

We find that the data points are distributed uniformly about $b/a = c/b$, suggesting that dwarf galaxy halos they can be characterised as general triaxial ellipsoids. However, we note that the halos appear to be preferentially oblate at later times ($z \lesssim 0.5$) - at $z \simeq 0.5$, all four halos have $b/a > c/b$ and at $z = 0$, two of the halos have $b/a \simeq c/b$ while the other two have $b/a > c/b$ - whereas at earlier times ($z \gtrsim 0.5$) there are equal numbers of prolate and oblate systems.

We conclude that dwarf galaxy halos can be characterised as general triaxial ellipsoids at all radii; that the axis ratios of these ellipsoids decrease with increasing overdensity in a way that can be characterised as a power law profile $b/a(c/a) \propto \rho_s^{-\alpha}$ where $\alpha \simeq 0.07$, independent of redshift; and that these systems appear to be preferentially oblate at late times ($z \lesssim 0.5$).

4.4.5 The Substructure Content of Dwarf Galaxy Halos

The analysis we have performed so far has focused either on spherically averaged properties of the dwarfs, which by definition smooth the mass distribution and wash out small scale irregularities, or on properties which assume that the mass density field varies smoothly within the halo (e.g. the shape of isodensity shells). However, projected maps of the dark matter distribution, such as those shown in figure 4.2, clearly demonstrate that

dwarf galaxy halos are not smooth monolithic systems but instead contain a wealth of substructure halos - or *subhalos* - within their virial radius. This observation is consistent with the findings of Moore et al. (1999) and Klypin et al. (1999) who found that many properties of the subhalo population in galaxy and cluster mass halos are similar.

Previous studies [¶] have noted that $\sim 10\%$ of a dark matter halo's virial mass, M_{200}, is bound to substructure, and that the distribution of subhalo masses can be described by a power-law. However, these results are based on analysis of galaxy and cluster mass halos and it is therefore interesting to ask whether we might expect lower mass systems such as dwarf galaxy halos to differ in any systematic way. A detailed comparison between dwarf, galaxy and cluster masses is deferred until chapter 5. Until then, we shall concentrate on those properties of the substructure population that may depend with time, and ask whether such time-dependent variations could be correlated with the merging history of the halos.

We now consider a few global properties of the substructure, namely, the relative amount of mass in bound substructures (*mass fraction*), the distribution of this mass amongst the substructures (*mass distribution function*) and the spherically averaged number density profile.

In figure 4.27, we track the variation of the bound substructure mass fraction, $m_{\rm f}$, with redshift, z, where we have expressed $m_{\rm f}$ as a percentage for the purpose of this plot. Halos `dH01`, `dH02`, `dH03` and `dH04` are represented by red filled circles, green filled triangles, blue asterisks and cyan filled squares respectively. Note that it is also instructive to refer to the mass accretion histories of each of the halos, presented in figure 4.6, and projections of the raw (i.e. unsmoothed) particle distribution, shown in figures 4.7 to 4.9, when examining this figure.

There are two main points to note in this figure. The first is that $m_{\rm f}$ is relatively small, typically $m_{\rm f} \simeq 2-10\%\, M_{200}$, although the precise value is sensitive to the few most massive subclumps in the halo. The second is that, in three of the four cases considered, $m_{\rm f}$ decreases with decreasing redshift; in the the fourth case, the halo appears to be in the process of merging, which we might expect to increase $m_{\rm f}$.

If we follow the formation history of a typical dark matter halo, we find that it is punctuated by a sequence of minor and major mergers. During these events, the halo

[¶]See also chapter 5

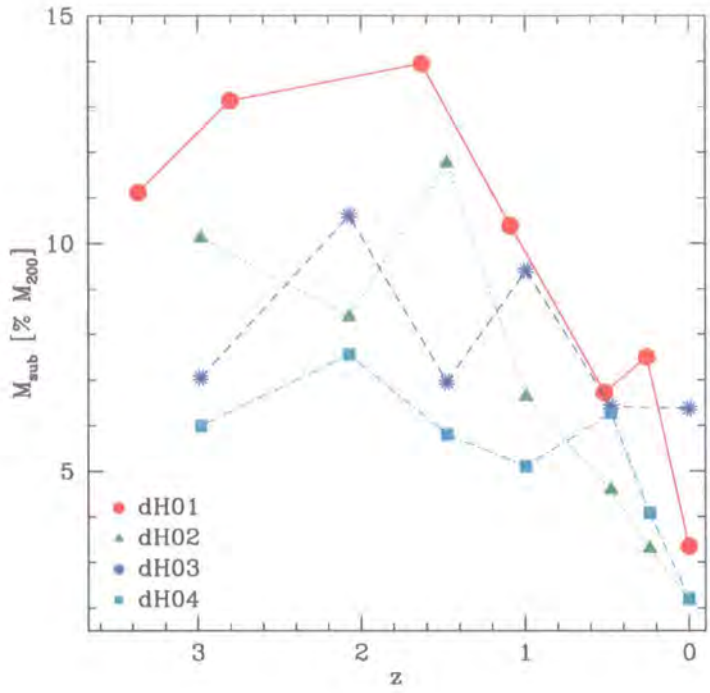

Figure 4.27: **Variation of the subhalo mass fraction, m_f, with redshift z.** This figure illustrates how the subhalo mass fraction (expressed as a percentage of M_{200}) varies with redshift. Filled red circles, green filled triangles, blue asterisks and cyan filled squares represent `dH01`, `dH02`, `dH03` and `dH04` respectively.

grows in mass and accretes other halos, and therefore it seems likely that there may be a correlation between the fraction of a halo's mass bound to substructure and its recent merging history. We can gain insight into any correlation between merging activity and m_f by comparing "jumps" in m_f with sudden changes in the mass of each of the halos in our sample.

At $z \simeq 3$, $\sim 11\%$ of `dH01`'s virial mass is bound to substructure; this figure increases to $\sim 14\%$ at $z \simeq 2$ before falling dramatically from $\sim 14\%$ at $z \simeq 1.5$ to $\sim 7\%$ at $z \simeq 0.5$. It then increases slightly to $\sim 8\%$ at $z \simeq 0.4$ before settling to $\sim 3\%$ at $z = 0$. Although `dH01` steadily accretes mass with redshift, we can see the reason for the dramatic decrease in m_f between $z \simeq 1.5$ and $z \simeq 0.5$ - several relatively massive orbiting clumps, which are readily apparent in the projected dotplots at $z \simeq 3.0$ and $z \simeq 2.0$, have been dragged inwards by dynamical friction and tidally disrupted, shedding a sizable fraction of their mass in the process.

Similarly, $\sim 10\%$ of `dH02`'s virial mass is bound to substructure at $z \simeq 3$, falling to $\sim 8\%$ at $z \simeq 2$, then increasing to 12% at $z \simeq 1.5$, before gradually declining to $\sim 2\%$

at $z = 0$. The dramatic jump of 50% between $z \simeq 2$ and $z \simeq 1.5$ coincides with a period during which the systems grows by $\sim 30\%$ in mass.

Both **dH03** and **dH04** experience mergers close to $z = 0$, as this is apparent by the sudden jumps - $\sim 30\%$ and $\sim 50\%$ respectively - in their virial masses. In the case of **dH03**, m_f fluctuates between $\sim 7 - 11\%$ between $0.0 \lesssim z \lesssim 3$; at $z \simeq 2\,(1)$, m_f increases by $\sim 60\,(30)\%$ while the overall mass of the system grows by $\sim 25\,(20)\%$. At $z = 0$, $m_f \simeq 6\%$. In the case of **dH04**, m_f remains relatively constant at $\sim 6 - 7\%$ between $0.5 \lesssim z \lesssim 3$, never increasing by more than $10 - 15\%$, but falls to $m_f \sim 2\%$ at $z = 0$. The small relative increase in m_f at $z \simeq 0.5$, appears to coincide with a time when the virial mass of the parent grows by $\sim 50\%$.

We conclude that the mass fraction does fluctuate in response to recent merging activity. During the initial stages of a capture of a clump, m_f can show a large fractional increase; however, as dynamical friction takes effect and the clump spirals in towards the centre of the halo, it is tidally disrupted and can suffer significant mass loss, resulting in a decrease in m_f.

The previous discussion indicated that dynamical friction is more effective when the mass ratio in a merger is of order unity, that is, the masses of the halos are similar. Orbits of massive subclumps are eroded and circularised by dynamical friction, exposing them to strong tidal forces for a larger fraction of their orbit. On the other hand, smaller, less massive subclumps experience relatively little dynamical friction in comparison, and their orbits remain eccentric. This combination of orbit erosion and their relatively low concentrations in comparison with less massive systems means that more massive subclumps are efficiently disrupted by tidal forces. Therefore, if we consider the abundance of subhalos with a given fractional mass relative to the host, we might expect to find many more low mass systems than high mass systems. Indeed, this would appear to be borne out by the results of high resolution simulations such as those of Ghigna et al. (1998, 2000), which have found that the distribution of subhalo masses at redshifts close to $z \simeq 0$ can be well described by a power-law. As we might expect, they found few relatively massive subhalos but many lower mass systems in a $10^{15} h^{-1} \mathrm{M}_{\odot}$ cluster halo forming in a SCDM cosmology. Although the mass scale and details of the cosmology differ, we do not expect this basic result to change.

In figure 4.28, we show the mass distribution function (MDF), defined as the number of subhalos per unit logarithmic mass interval per unit physical volume of the parent, for

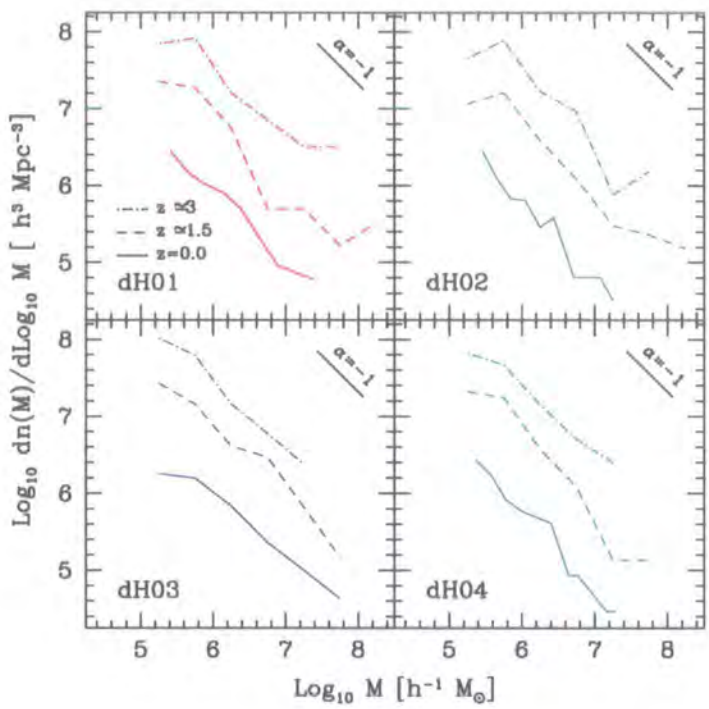

Figure 4.28: **Mass Distribution Functions (MDFs) of Subhalos.** We show mass distribution functions for subhalos in dH01 (red curves), dH02 (green curves), dH03 (blue curves) and dH04 (cyan curves) at redshifts $z = 0$ (solid curves), $z \simeq 1.5$ (dashed curves) and $z \simeq 3$ (dotted-dashed curves). The diagonal solid line in the top right hand corner of each panel corresponds to a power-law with index $\alpha = -1$.

each of our dwarf galaxy halos measured at $z = 0$ (solid curves), $z \simeq 1.5$ (dashed curves) and $z \simeq 3$ (dotted-dashed curves). Each of the four panels correspond to a single halo - from top left, dH01, dH02, dH03 and dH04.

Perhaps the main point to note in this figure is that the distribution does not show any significant change in slope with increasing redshift, indicating that the relation between abundance and subhalo mass holds.

Finally, we consider the spatial distribution of the subhalos in and around the parent halo. For simplicity, we compute the spherically averaged number density in shells of thickness $\Delta \log r = 0.1$. Results for each of the dwarf halos at $z = 0$ (solid curves), $z \simeq 1.5$ (dashed curves) and $z \simeq 3$ (dotted-dosed curves) are shown in figure 4.29. Error bars on the $z = 0$ profiles are computed assuming Poisson errors in the number of particles per bin. The light solid curves in each panel indicate the behaviour of the underlying dark matter density profile of the parent halo at $z = 0$.

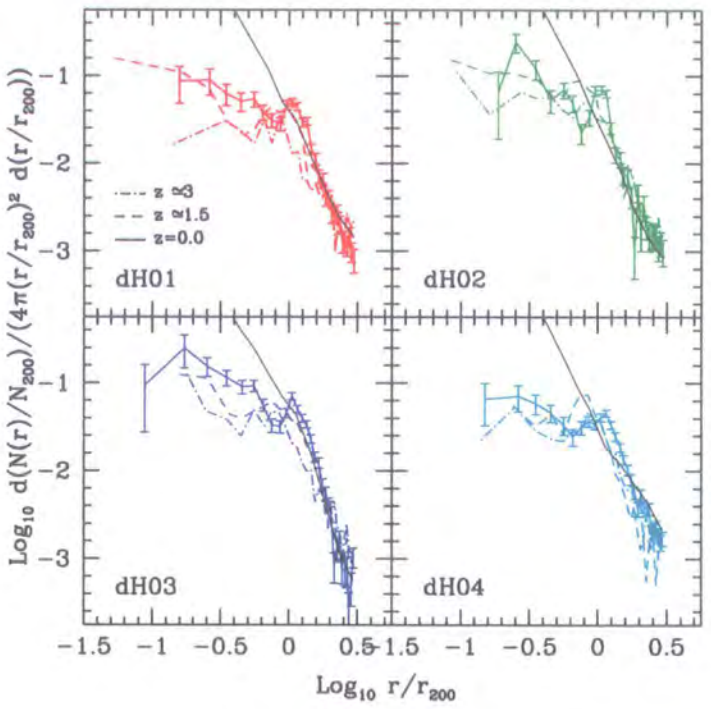

Figure 4.29: **Number Density Profiles of Substructure Halos.** Here we show spherically averaged number density profiles for all subhalos within r_{200}. Radii have been normalised to r_{200}. As before, we show the behaviour at $z = 0$ (solid curves), $z \simeq 1.5$ (dashed curves) and $z \simeq 3$ (dotted-dashed curves). The light solid curves in each panel indicate the behaviour of the underlying halo profile at $z = 0$.

All the profiles are steep in the outer parts (beyond r_{200}) at all redshifts, and all start to roll over and become shallower at $r \lesssim r_{200}$), irrespective of redshift. There do not appear to be any significant differences between the shapes of profiles at different redshifts, although in some cases (dH01 and dH03), those measured at $z \simeq 3$ do appear to be depressed relative to those at $z \simeq 1.5$ and $z = 0$, differing by as much as factor of ~ 4 at r_{200} (dH01). We also note that there is reasonable agreement between the profiles of the subhalos and the smooth component at $\sim r_{200}$ but the subhalo profile rapidly drops off for $r \lesssim r_{200}$, indicating that the subhalos distribution is less concentrated (or *antibiased*) with respect to the underlying smooth halo mass distribution. Indeed, we do not find any subhalos inside $r \leq 0.1\, r_{200}$, although this may in part be affected by enhanced disruption due to finite numerical resolution.

4.4.6 Symmetry and Stability of the Gravitational Potential

Perhaps the most interesting of the questions raised in § 4.1 concerned the symmetry and stability of the dwarf galaxy halos gravitational potentials at $z = 0$. In particular, we noted that an understanding of the structure of a halo's potential would allow us to place constraints on the kind of orbits we might expect to find and to investigate whether simulated CDM halos could support gaseous disks of the kind observed in rotation curve studies. If the gravitational potential of a halo is symmetric and is stable, that is, it neither rotates nor changes shape over several dynamical times, then we expect the probability will be enhanced that the halo can support closed, non-intersecting orbits of the kind required if a gaseous disk is to form and survive.

We noted in § 4.4.4 that the underlying dark matter distribution in our halos could be more accurately described as ellipsoidal and projections of slices through thin iso-density shells within r_{200} revealed that they were regular and symmetric. Therefore we expect to find ellipsoidal isopotential surfaces that are equally symmetric, albeit rounder. Moreover, it has been noted that cuspy ellipsoidal mass distributions generate ellipsoidal isopotential surfaces that become rounder with increasing distance from the centre of the halo (Binney& Tremaine (1987)).

We have used the *Self Consistent Field* of Hernquist & Ostriker (1992), described in § 4.3.4, to evaluate the smooth, mean-field gravitational potential in each of our dwarfs. We have also rerun each of the dwarfs from $z = 0.05$ to $z = 0$ - equivalent to ~ 10 circular orbital timescales at $1\% r_{200}$ for a $c_{200} = 11$ NFW halo - and sampled the particle distribution approximately once every quarter of a circular orbital timescale, thus allowing us to investigate whether the potential is stable.

As a preliminary, we show projections of the raw particle distribution between $0 \leq z \lesssim 0.04$ in figure 4.30, where we consider only those particles within r_{200} that satisfy the potential threshold,

$$\frac{\Delta\Phi}{\Phi_{\rm min}} = \frac{\Phi_i - \Phi_{\rm min}}{\Phi_{\rm min}} \leq 0.5; \tag{4.53}$$

here $\Phi_i = \Phi(\mathbf{r}_i)$ is the smooth gravitational potential at the position of particle i, $\mathbf{r}_i$, and $\Phi_{\rm min}$ is the minimum of the gravitational potential.

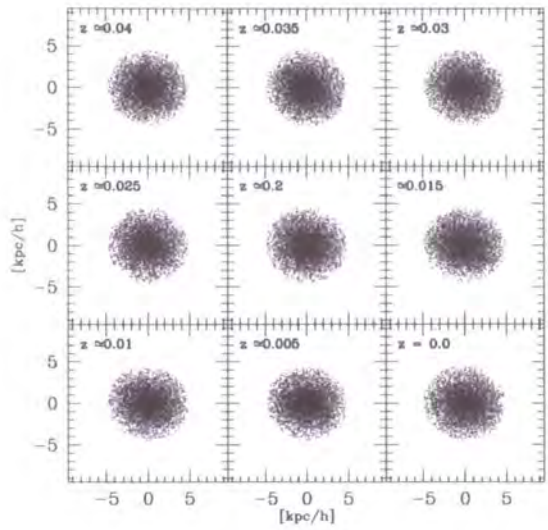

(a) dH01

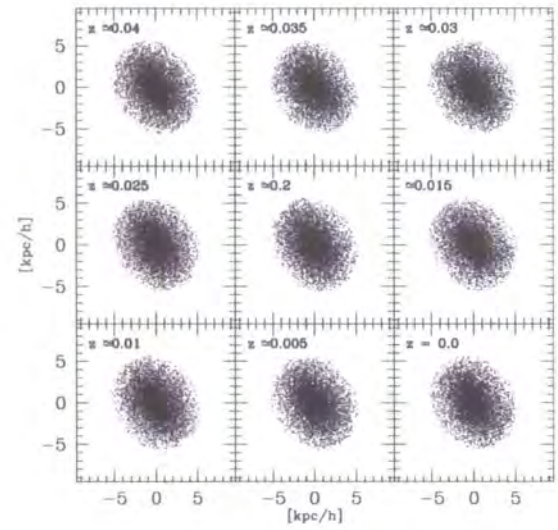

(b) dH02

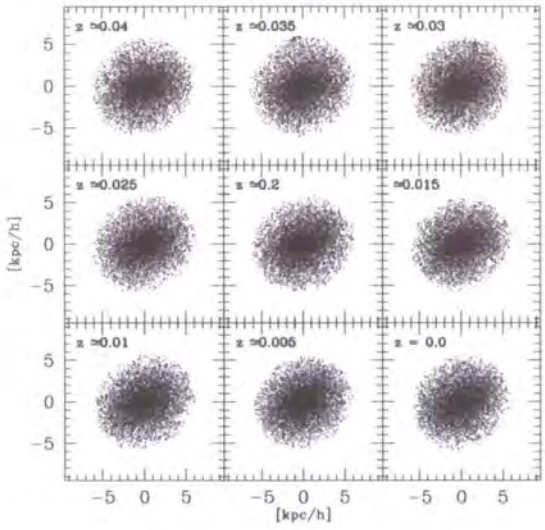

(c) dH03

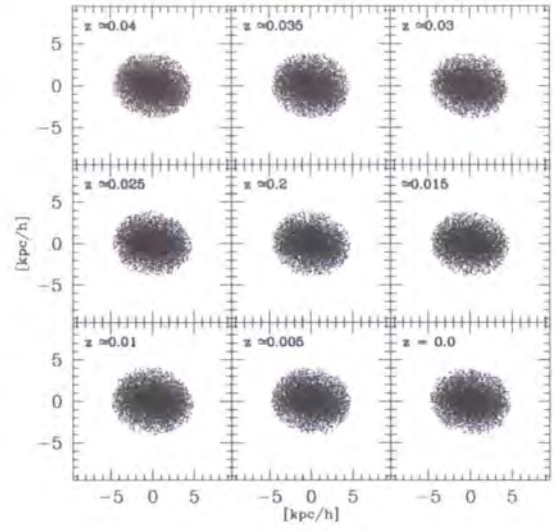

(d) dH04

Figure 4.30: **Two dimensional projections of the particle distribution selected according to gravitational potential** at redshifts $0 \leq z \lesssim 0.04$. We show only those particles that satisfy the potential threshold defined by equation 4.53.

As we anticipated, the isopotential surfaces appear to be smooth ellipsoids, although viewed from an angle; the ellipticities of these surfaces do not appear to change over the redshift range $0 \leq z \lesssim 0.04$ - equivalent to several circular orbital timescales - and the particle distribution shows no sign of rotation. Both of these observations indicate that the smooth gravitational potential is both symmetric and stable.

We investigate whether the potential is symmetric and stable in a more quantitative fashion below. In particular, we focus on isopotential contours in the principal planes of the ellipsoids we isolated in figure 4.30; previous analytic studies (e.g. Steiman-Cameron & Durisen (1982, 1984), David et al. (1984, 1985); see also Thomas et al. (1994)) indicate that gaseous disks are more likely to settle and survive in these principal planes.

Symmetry of the Potential

The projections shown in figure 4.30 indicate that the isopotential surfaces can be approximated as smooth ellipsoids, which suggests that we can identify the principal planes of the particle distribution by taking the second moment of the distribution, weighted by the gravitational potential. This is essentially the same procedure we adopted to estimate the axis ratios and principal planes of the mass distribution, adapted so that particles are weighted by their gravitational potential rather than their mass - see § 4.3.3 for details.

Particles are selected according to the potential threshold given by equation 4.53; this isolates an ellipsoidal volume of particles bounded by the isopotential surface on which equation 4.53 holds. We compute a modified "moment of inertia" tensor, replacing the mass of each particle by its smooth gravitational potential, Φ_i;

$$I_{jk} = \sum_{i=1}^{N} \Phi_i \left(r_i^2 \, \delta_{jk} - x_{i,j} \, x_{i,k} \right) . \tag{4.54}$$

Here r_i is the radius and $x_{i,j}$ are the Cartesian coordinates of the ith particle. Equation 4.54 can be diagonalised using standard techniques (see Press et al. (1995)), allowing us to compute values for the axis ratios (eigenvalues) and principal axes (eigenvectors) of the particle distribution. We can also construct a rotation matrix that can used to rotate the particle distribution into its diagonalised frame.

To emphasise the symmetry of the potential, we have taken halo `dH02` and estimated the gravitational potential at points on a fine (1024^2) mesh in two of the principal (symmetry) planes - the major-to-minor and intermediate-to-minor planes - at redshifts $z \simeq 0.04$

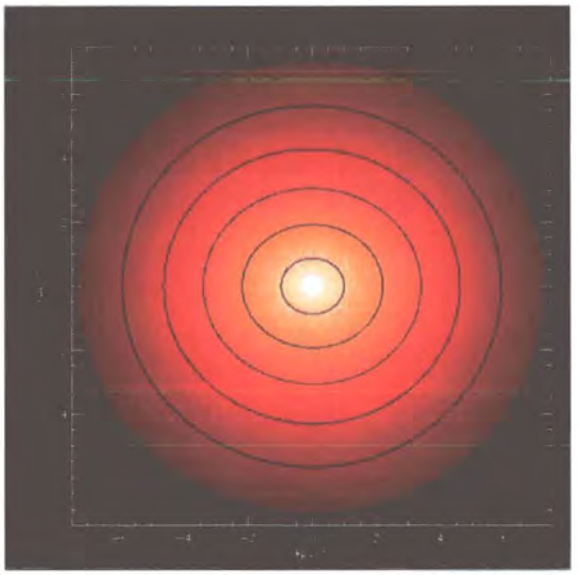

(a) Major-to-Minor Principal Plane, $z \simeq 0.04$.

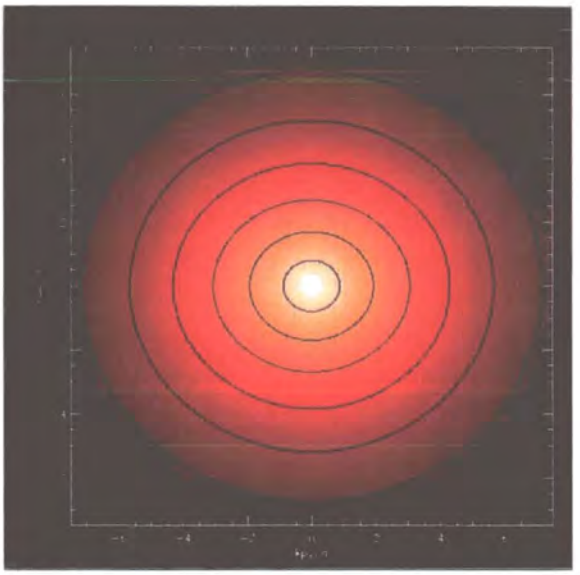

(b) Intermediate-to-Minor Principal Plane, $z \simeq 0.04$.

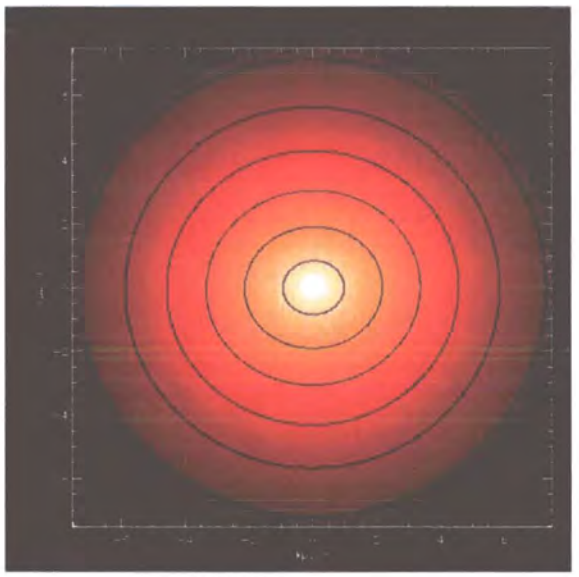

(c) Major-to-Minor Principal Plane, $z = 0$.

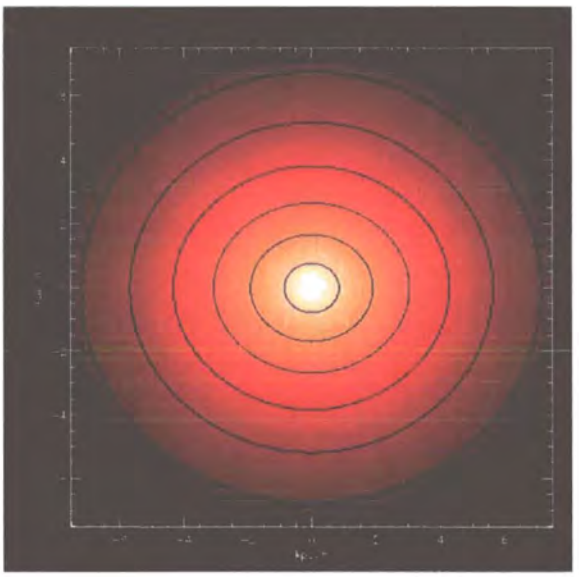

(d) Intermediate-to-Minor Principal Plane, $z = 0$.

Figure 4.31: **The Gravitational Potential is Symmetric.** We demonstrate symmetry by estimating the gravitational potential on a 1024^2 mesh embedded in the major-to-minor (left hand panels) and intermediate-to-minor (right hand panels) principal planes at $z \simeq 0.04$ (upper panels) and $z = 0$ (lower panels) for halo `dH02`. Heavy black ellipses correspond to isopotential contours in the respective planes.

and $z = 0$. The results of this operation are shown in figure 4.31, in which we also overplot the shape of the isopotential contours in these planes (heavy black ellipses). Bright regions correspond to mesh points where the gravitational potential is most negative.

The most noticeable aspects of figure 4.31 are the smoothness and symmetry of the gravitational potential. Although we have demonstrated this result for dH02, we find that it applies equally well to intermediate times and to the other halos. When applied to the other halos, the only discernible difference is in the value of the axis ratios of the isopotential contours.

Furthermore, we note that the isopotential contours in the symmetry planes can be well fit by ellipses, which suggests that the isopotential surfaces can be characterised as ellipsoids whose axis ratios increase with increasing effective radius (i.e. $r_{\rm eff} = (a\,b\,c)^{1/3}$). We note also that the axis ratios of the isopotential contours do not appear to have changed between $z \simeq 0.04$ and $z = 0$, which is equivalent to several dynamical times, as noted previously.

We can quantify this symmetry by rotating the particle distribution through 180° about the intermediate axis (in the case of the major-minor plane) and the major axis (in the case of the intermediate-minor plane), and recomputing the potential for these rotated distributions. The respective potentials can then be differenced. If the potential is symmetric, we expect that $\Delta\Phi/\Phi = 0$ at every point; we find that $\Delta\Phi/\Phi \lesssim 10^{-3}$. Once we account for the error in the method used to derive Φ, we conclude that Φ is symmetric.

Stability of the Potential

Having established that the potential is symmetric, we now determine whether it is stable. To do this, we investigate whether the axis ratios change as a function of redshift, which would indicate a change in the shape of the surface, and whether the relative positions of the principal axes of the halo change with redshift, which would indicate that the potential is rotating.

In figure 4.32, we plot the distribution of axis ratios, b/a and c/b, determined for isopotential shells with effective radii between $0.01\,r_{200} \lesssim r_{\rm eff} \lesssim 0.5\,r_{200}$, for several redshifts between $0 \leq z \lesssim 0.04$. If the shape of the surface remains constant over the course of several dynamical times, i.e. between $0 \leq z \leq 0.04$, we expect the points

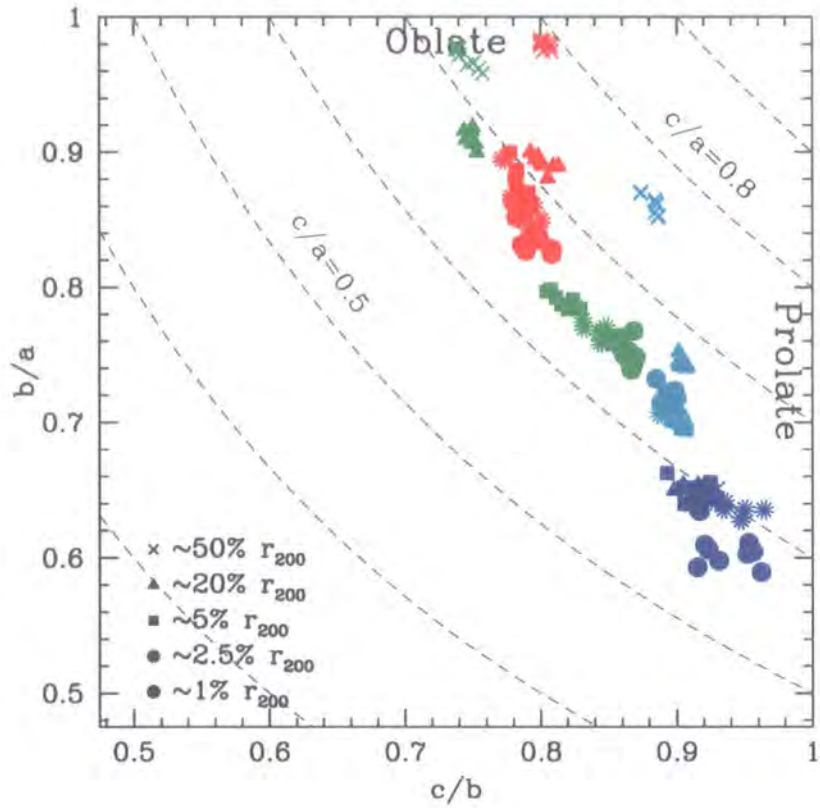

Figure 4.32: **Distribution of Axis Ratios** b/a **and** c/b for the second moment of the particle distribution, weighted by gravitational potential. Symbols are colour coded according to halo - red, green, blue and cyan correspond to halos `dH01`, `dH02`, `dH03` and `dH04`. Crosses, filled triangles, filled squares, asterisks and filled circles correspond to the shapes of isopotential surfaces with effective radii (defined as $r_{\rm eff} = (a\,b\,c)^{1/3}$) of $(\sim 50\%, 20\%, 5\%, 2.5\%, 1\%)\ r_{200}$.

measured for a given isopotential surface to cluster. We also expect the sets of points evaluated for the outer surfaces to separate from those corresponding to the inner surfaces, because we expect the isopotential surfaces to become rounder at larger effective radii (see Binney & Tremaine (1987), pp. 49-62).

The main point to note in this figure is that we see precisely the behaviour we expected - in three of the four cases. The outer isopotential surfaces belonging to `dH03` do not appear to differ in shape from the inner surfaces. However, further investigation reveals that the outermost surfaces occur at smaller fractional radii - the outermost surface has an effective radius of $r_{\rm eff} \simeq 25\% r_{200}$. This may be a result of the recent merging event it experienced (at $z \simeq 0.2$).

Otherwise, we conclude that the shapes of the surfaces do not change with time, at

least over the number of dynamical times we have considered - we find that $< b/a > \simeq 0.85$ and $< c/a > \simeq 0.65$ for $r_{\rm eff} \simeq 20\% r_{200}$ and $< b/a > \simeq 0.7$ and $< c/a > \simeq 0.6$ for $r_{\rm eff} \simeq 1\% r_{200}$ over the range of redshifts we have considered. The inner surfaces are of most interest, because they are older in terms of the number of dynamical times they have survived, and also because this is where the rotation curves are measured; we find that the measured axis ratios change by $\sim 5\%$ at most, indicating that the shapes are robust over the range of redshifts we have considered.

Finally, in figure 4.33, we investigate the alignment of the principal axes for each of the isopotential surfaces we have examined. In particular, we have inverted the dot product to obtain the change in angle, $\Delta\theta$;

$$\mathbf{e}_i \cdot \mathbf{e'}_i = |\mathbf{e}_i|\,|\mathbf{e'}_i| \cos(\Delta\theta), \tag{4.55}$$

where $\mathbf{e}_i$ and $\mathbf{e'}_i$ are the vectors corresponding to each of the major, intermediate and minor principal axes.

In figure 4.33, we show $\Delta\theta$, expressed in degrees, evaluated for the major and minor axes between successive outputs as a function of redshift for volumes bounded by isopotential surfaces with effective radii (from top) of $(\sim 50\%, 20\%, 5\%, 2.5\%, 1\%)\ r_{200}$. Green filled squares and red filled circles represent the values of $\Delta\theta$ for the minor and major axes at a given redshift.

We find that the change in angle between the principal axes measured at successive outputs is small; deviations can be as great as $\Delta\theta \lesssim 7.5^{\rm o}$, but on average we find that $\Delta\theta \lesssim 2.5^{\rm o}$ and we note that deviations are greatest at small effective radii - $r_{\rm eff} \lesssim 5\% r_{200}$. In spite of these small deviations, we conclude that the potential is not rotating.

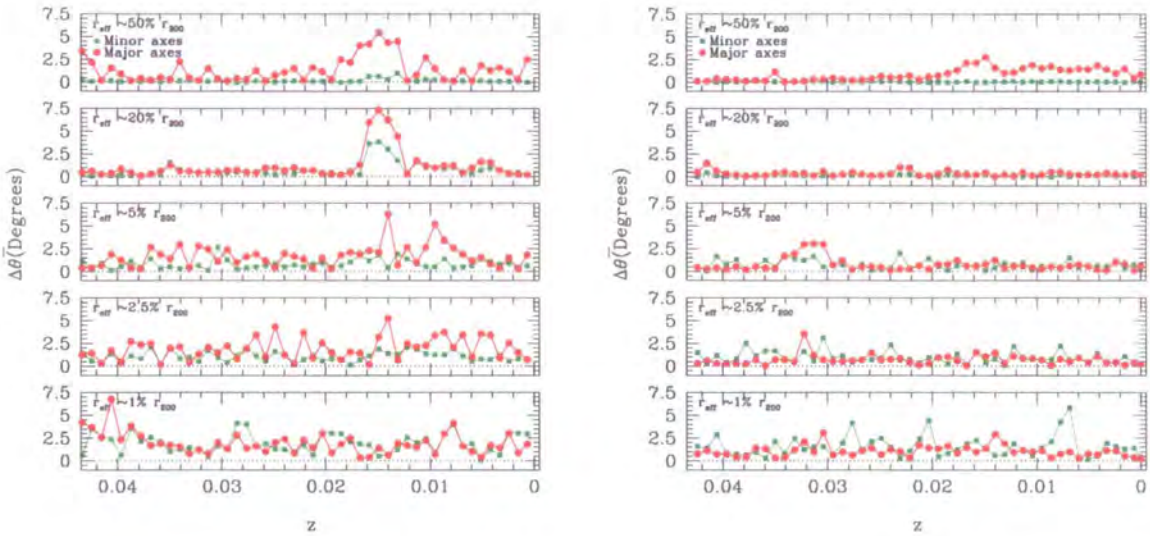

(a) dH01 (b) dH02

(c) dH03 (d) dH04

Figure 4.33: **Alignment of principal axes between** $0 \leq z \lesssim 0.04$ **.** We show the change in orientation ($\Delta\theta$, in degrees) of the major and minor axes between successive outputs as a function of redshift for volumes bounded by isopotential surfaces with effective radii (from top) of ($\sim 50\%, 20\%, 5\%, 2.5\%, 1\%$) r_{200}. Green filled squares and red filled circles represent the values of $\Delta\theta$ for the minor and major axes at a given redshift.

4.5 Conclusions

We began this chapter by raising a number of issues that we wished to address using a sample of four high resolution cosmological simulations of dark matter halos with masses of $M \sim 10^{10}\,\mathrm{M}_{\odot}$ at $z = 0$, comparable to those of dwarf galaxy halos, forming in the ΛCDM cosmology. In particular, we sought to

- characterise the spherically averaged mass profiles of these halos as a function of redshift, focusing on variations in their shape, concentration and inner slope;
- compare the shape of their mass profiles with the predictions of the NFW and Moore et al. models;
- determine their formation epochs and describe their formation histories;
- examine their spherically averaged kinematics, angular momentum content and shape;
- quantify their substructure content as a function of redshift;
- estimate the degree to which their gravitational potential can be considered symmetric and stable.

The average mass resolution of the simulations was chosen such that we could resolve each of our halos with ~ 1 million particles interior to r_{200} at $z = 0$, thus enabling us to obtain reliable estimates of the mass distribution within the central $\sim 1\% r_{200}$ according to the convergence criteria set out in chapter 2.

The main conclusions of this chapter can be summarised as follows;

- **The formation times of the dwarf halos in our sample are in good agreement with the predictions of extended Press Schechter theory for a ΛCDM cosmology.** We used extended Press Schechter (EPS) theory (Lacey & Cole (1993)) to construct the distribution of formation redshifts for a CDM halo with a virial mass of $M_{200} = 10^{10}\mathrm{M}_{\odot}$ at $z = 0$ forming in the ΛCDM cosmology with $\Omega_m = 0.3$, $\Omega_\Lambda = 0.7$, $h = 0.7$ and $\sigma_8 = 0.9$. Following the convention set out in Lacey & Cole (1993), we defined the formation redshift of a halo to be that redshift at which the mass of its most massive progenitor first exceeds half the mass of the halo at $z = 0$; we estimated the predicted median redshift of formation to be

$z_{\rm mode} \simeq 1.5$. According to our definition, the dwarf halos in our sample have formation redshifts between $1.1 \lesssim z \lesssim 2.7$, with a median of $z_{med} \simeq 1.8$, in reasonable agreement with the predicted value of $z_{med} \simeq 1.5$ and within the interquartile range of the distribution.

- **Dwarf galaxy halos are centrally concentrated systems with spherically averaged density profiles that are in good agreement with the best fitting NFW and Moore et al. models at redshifts in the range $0 \lesssim z \lesssim 3$.**

  We find that the best fitting NFW and Moore et al. models provide reasonably accurate descriptions of the simulated density profiles over the radial range $5\% r_{200} \lesssim r \lesssim r_{200}$ at $z = 0$. However, both models appear to underestimate the value of the density in the centres of the halos, at radii $\lesssim 5\% r_{200}$, and the discrepancy is particularly acute for the NFW profile, which can differ by up to a factor of $\sim 75\%$ at $\sim 1\% r_{200}$. On average, the deviations are smaller - $\sim 25\%$ for the NFW model and 10% for the Moore et al. model.

  At high redshifts, the best fitting NFW and Moore et al. models agree with the simulated profiles to better than 10% on average down to about $\sim 10\%$ of r_{200}. Interior to $\sim 10\% r_{200}$, both models underestimate the density, as at $z = 0$; we find that the predicted density can differ by as much as a factor of ~ 2 in the case of the NFW fit and 40% in the case of the Moore et al. fits at the innermost resolved point. On average, we find that the models tend to underestimate the density by $\sim 40\%$ in the case of the NFW model and 20% in the case of the Moore et al. model.

  However, we stress that **both the NFW and Moore et al. models tend to underestimate the density at small radii and overestimate it at intermediate radii** ($10\% r_{200} \lesssim r \lesssim 50\% r_{200}$), perhaps suggesting the need for a **modified density profile**?

- **The concentration of the most massive progenitor decreases with increasing redshift.** If we measure the slope of the most massive progenitor's density profile at a fixed fraction of the virial radius, we find that it decreases with increasing redshift - on average, the spherically averaged local overdensity at $r_{\rm min} \simeq 1.5\% r_{200}$ increases by a factor of $\sim 2 - 3$ between $z \simeq 1.5$ and $z = 0$; this suggests that the concentration of the most massive progenitor is lower at earlier times. Similarly, the radius at which the circular velocity peaks (normalised to the virial radius at a

given redshift) increases with increasing redshift, by a factor of ~ 3 between $z \simeq 1.5$ and $z = 0$ - another signature of a decrease in concentration.

We find that the median NFW concentration at $z = 0$ is $c_{200} \simeq 11$, but this falls to $c_{200} \simeq 5.9$ at $z \simeq 1.5$. However, we note that there is a large scatter in the best fit concentrations measured from the simulation data at all redshifts, in excess of the $1\,\sigma$ deviation of $\log \Delta c \sim 0.18$ measured by Bullock et al. (2001). We estimate that the maximum deviation relative to the mean concentration never exceeds $\log \Delta c \sim 0.4$ or $\sim 40\%$ (at $z \simeq 1.5$), and is typically $25 - 30\%$ for redshifts $0 \leq z \lesssim 1.5$.

If we consider the average concentration at any given redshift, we find that it is in good agreement with the predictions of EPS theory and the Bullock et al. and ENS models for concentration; we note that the mean curve never deviates by more than $1\sigma = \log \Delta c \sim 0.18$ from either of the ENS or Bullock et al. curves for redshifts in the range $0 \leq z \lesssim 1.5$.

- **Steep profiles of the type described by the Moore et al. appear to be inconsistent with the simulated data.** We find that the maximum asymptotic slope, $\alpha(r)$, defined by equation 4.45, decreases approximately linearly with decreasing radius, $\alpha(r) \propto r$, down to the innermost believable radius ($\sim 1\% r_{200}$ at $z = 0$, $\sim 3\% r_{200}$ at $z \simeq 3$). This behaviour would appear to **rule out very steep central slopes** and is in sharp contrast (especially at $z = 0$) with the prediction of the Moore et al. model, which achieves its asymptotic inner value of $\alpha = 1.5$ at a relatively large radius - between $\sim 3\% r_{200}$ at $z = 0$ and $\sim 10\% r_{200}$ at $z \simeq 3$. We also note that the apparent lack of curvature in the profiles suggests that we have **yet to see evidence for convergence to an asymptotic slope.**

- The mean radial velocity profiles show that **dwarf galaxy halos are in dynamical equilibrium** at redshifts in the range $0 \leq z \lesssim 3$, as indicated by $\overline{v_r} \simeq 0$ within r_{200}. We note the somewhat surprising result that **dwarf galaxy halos experience little or no mass infall at** $z = 0$; however, we find that this process becomes progressively more important with increasing redshift; for example, at $z \simeq 1.5(3)$, there is a well defined trough $|\overline{v_r}| \simeq 0.2\,V_{200}(0.4\,V_{200})$ in the average radial velocity profile, indicating appreciable infall.

  Perhaps more surprising is the result that **the velocity distribution of particles in the outer parts of the dwarf halos follow preferentially tangential orbits**

for redshifts in the range $0 \leq z \lesssim 3$. This is in marked contrast with the results of more massive systems (see next chapter).

- We find that **dwarf galaxy halos can be characterised as general triaxial ellipsoids** at all radii. The axis ratios of these ellipsoids decrease with increasing overdensity in a way that can be characterised as a power law profile $b/a(c/a) \propto \rho_s^{-\alpha}$ where $\alpha \simeq 0.07$, independent of redshift, and suggests that **the centres of dwarf galaxy halos are more elongated than their outer parts**. We also note that whereas there are equal numbers of prolate and oblate halos at early times, these systems appear to be **preferentially oblate at late times** ($z \lesssim 0.5$).

- In common with published results for galaxy and cluster mass halos, we find that our dwarf galaxy halos contain an abundance of substructures. The **bound mass fraction is small,** $m_f \simeq 2 - 10\% M_{200}$, although the precise value tends to be sensitive to the few most massive subclumps in the halo. In three of the four cases considered, m_f **increases with increasing redshift**, while in the the fourth case, the halo appears to be in the process of merging. We note that the **mass fraction appears to fluctuate in response to recent merging activity**. The **mass distribution function of subhalos can be approximated as a power-law**, $dn/dM \propto M^{-\alpha}$, with $\alpha \simeq 2$, which applies equally well at all redshifts. There is reasonable agreement between the number density profiles of the subhalos and the smooth component at $\sim r_{200}$ but the subhalo profile rapidly drops off for $r \lesssim r_{200}$, indicating that the **subhalos distribution is less concentrated (or *antibiased*) with respect to the underlying smooth halo mass distribution**.

- We find that the **gravitational potential of a dwarf galaxy halo is symmetric and stable at** $z \simeq 0$. As we have mentioned already, a stable, symmetric gravitational potential enhances the probability that the halo can support closed, non-intersecting orbits of the kind required for a gaseous disk to form and survive. We shall return to this subject in chapter 6.

The question of whether there are any systematic differences between the structure and kinematics of dwarf galaxy halos and those of more massive systems such as galaxy and cluster halos is dealt with in considerable detail in the next chapter.

Chapter 5

The Structure of ΛCDM Halos : Mass Dependence

5.1 Introduction

One of the principal aims of the thesis so far has been to describe in detail the properties of the kind of Cold Dark Matter halos that we might expect a typical isolated late-type dwarf galaxy to inhabit. We have placed particular emphasis on their central structure, probing scales that can be directly compared with observations. For this purpose, we have performed several high resolution N-body simulations that follow the formation and evolution of individual isolated dark matter halos with masses of order* $M \sim 10^{10}\,M_{\odot}$ in the ΛCDM cosmogony. The spatial resolution of our simulations has been such that we can reliably resolve the mass distribution within the central few kiloparsecs of the halos and can, in turn, accurately predict the shape of the dark matter rotation curve on sub-kiloparsec scales.

By performing high resolution simulations of dark matter halos on dwarf mass scales, we can gain important insights into the behaviour of the CDM model on a scale hitherto unexplored in numerical work. We have stressed the need to provide reliable model predictions for comparison with observations; this need is particularly acute on dwarf galaxy scales, where there is an apparent discrepancy between the mass profiles implied by rotation curve studies and predictions extrapolated from simulations of galaxy and cluster mass halos. However, it is equally important to establish whether or not the properties of dwarf mass halos are consistent with extrapolations from the results of simulations of

*Recall that we use units of $M_{\odot}$ when discussing general results but $h^{-1}M_{\odot}$ when commenting on the results of our simulations.

larger masses.

Several studies have addressed mass dependent trends in the structural properties of dark matter halos (e.g. Frenk et al. (1988); Warren et al. (1992); Navarro, Frenk & White (1996, 1997) (hereafter NFW); Cole & Lacey (1996); Fukushige & Makino (2001); Jing & Suto (2000, 2002)). Earlier studies such as Frenk et al. (1988) and Cole & Lacey (1996) focused on generating a large sample of halos by simulating large cosmologically representative volumes, but at the expense of relatively poor resolution, whereas more recent studies such as NFW (1996, 1997) and Jing & Suto (2000, 2002) have funnelled their computational resources into simulating individual halos at high resolution, at the expense of a smaller sample size ($\sim$ 10 halos). The high resolution studies have generally concentrated on the behaviour of the dark matter density profile at small radii (Jing & Suto (2000), Fukushige & Makino (2001)), although most recently Jing & Suto (2000) have studied the shapes of a sample of halos ranging in mass from $M \sim 10^{12}\mathrm{M}_{\odot}$ to $M \sim 10^{14}\mathrm{M}_{\odot}$. Furthermore, both Moore et al. (1999a) and Klypin et al. (1999a) have noted that high resolution simulations of individual galaxy mass halos contain a similar abundance of substructure to cluster mass halos.

There is good reason to suspect that some properties of dark matter halos will show a systematic variation with mass. In the hierarchical paradigm, we expect that low mass halos will be the first to form at high redshifts, and successive generations of more massive halos will be assembled through the successive merging and accretion of lower mass predecessors. Within this context, it seems reasonable to expect those properties that depend on the epoch of formation or those that are sensitive to the passage of time to exhibit a dependence on mass.

What kind of properties might we expect to systematically vary with mass? We might ask, for example,

- **Does the shape of the dark matter density profile depend on mass? Or is it universal?** We found in chapter 4 that while both the NFW and Moore et al. models provided reasonable descriptions of the spherically averaged mass profiles of our sample of dwarf galaxy halos, neither could account fully for the detailed shape over the entire radial range; in particular, we noted significant deviations in the

innermost parts. By determining how the maximum asymptotic slope, α, varies as a function of radius, we asserted that the inner slope of the density profile on dwarf galaxy scales is unlikely to be as steep as that proposed by Moore et al. , based on the profiles of the four halos in our sample. At $\sim 1\% r_{200}$, we found that $\alpha \simeq -1.2$, whereas we would expect a Moore et al. profile to have $\alpha \simeq -1.5$ at this radius. These results also indicate that the profiles are steeper than the corresponding NFW profile, which has a maximum slope of $\alpha \simeq 1.1$ at this radius, although it is difficult to draw any firm conclusions in this case precisely because α really only defines an upper limit. Perhaps more significantly, we found that the theoretical models fail to capture the general shape of the measured density profiles; α appears to show very little curvature compared to the behaviour of the corresponding NFW and Moore et al. models. At small radii, the profiles appear to be steeper than predicted by NFW but shallower than predicted by Moore et al. ; at intermediate radii, the profiles appear to be in agreement with the predictions of both models; and at large radii, $\alpha \sim 2.4$, slightly shallower than the expected behaviour of both theoretical models.

The question now arises, do we see similar behaviour in the spherically averaged mass profiles of more massive halos, or is this behaviour peculiar to dwarf galaxy halos? While there has been a substantial amount of work published in this area making use of the highest resolution cosmological N-body simulations performed to date (e.g. NFW (1996, 1997); Moore et al. (1998, 1999); Ghigna et al. (1998, 2000); Fukushige & Makino (1997, 2002, 2003); Jing & Suto (2000); Klypin et al. (2001)), these studies have focused on the asymptotic central slope of the density profile, with little attention paid to the overall shape of the profile.

- **Is there a relationship between the central density of a dark matter halo and its mass?** NFW (1996) noticed a correlation between characteristic overdensity, δ_c, and virial mass, M_{200}, when comparing halos of different masses in their sample. They found that more massive halos tend to have lower characteristic densities and lower concentrations, and related this observation to the redshift of collapse of the halo. In general, less massive halos are assembled at earlier times when the mean density of the Universe is higher, and it is this density that is imprinted on a halo's central density. We therefore expect less massive halos to have systematically steeper density profiles at a fixed fraction of the virial radius

r_{200} than their more massive counterparts, reflecting their higher concentrations. On the other hand, we expect that the profiles of all halos should appear similar when they are scaled appropriately, or in the parlance of NFW, we might expect that a universal density profile exists.

- **Is there a relationship between the kinematics of a dark matter halo and its mass?** We noted in chapter 4 that, on average, the radial velocity component of material surrounding a dwarf galaxy halo is positive and increasing, and there does not appear to be any significant mass infall beyond r_{200}. The velocity anisotropy, $\beta = 1 - \sigma_t^2/2\sigma_r^2$, indicates that the velocity distribution is preferentially radial within the central 80% of r_{200}, becomes increasingly isotropic towards r_{200}, preferentially tangential beyond r_{200} and finally turns over and becomes radial once again at $\sim 2\,r_{200}$. These results are in marked contrast with those found by previous studies of cluster masses, where it was noted that there is significant infall onto the halos, as characterised by a trough in the radial velocity profile beyond r_{200} corresponding to infalling material, and an almost linear increase in $\beta(r)$ out to $\sim 2\,r_{200}$, indicating that the velocity distribution is preferentially radial.

  Furthermore, we might ask whether a halo's shape or the distribution of its angular momentum is dependent on mass.

- **Does the amount of mass bound in substructure depend on halo mass? How is this mass distributed?** The hierarchical nature of mass assembly in the CDM model implies that as the mass of a halo increases, its formation epoch will be pushed to progressively later times. We found in chapter 4 that $\sim 5\%$ of the mass of a typical dwarf galaxy halo is bound to substructure halos. As we show in figure 5.1, according to extended Press Schechter theory, we expect a dark matter halo with a virial mass of $M \sim 10^{10}\mathrm{M}_\odot$ at $z = 0$ to have a median formation redshift of $z_f \simeq 1.5$. On the other hand, a halo with a mass of $M \sim 10^{15}\mathrm{M}_\odot$ identified at the same redshift has a median redshift of formation of $z_f \simeq 0.4$. For the ΛCDM cosmology, these redshifts correspond to approximately 2/3 and 1/3 of a Hubble time, or 8.9 and 4.5 billion years respectively. We found that dwarf galaxy halos are close to virial equilibrium, with $2T/|W| \sim 1.05$ when measured at $r_{\rm vir}$ (recall that $r_{\rm vir}$ corresponds to the radius of a spherical volume enclosing a mean overdensity of $\Delta_{\rm vir}\rho_{\rm crit}$, where $\Delta_{\rm vir} \simeq 97$ at $z = 0$ for the ΛCDM model), whereas we expect more massive systems to be less relaxed. We might therefore expect less massive systems

to contain, on average, a smaller fraction of their mass in substructure than their more massive brethren because they are more relaxed and contain fewer relatively massive subclumps, although we note that this assertion will be very sensitive to the object's detailed merging history and the orbital distribution of its subhalos. On the other hand, previous studies have found that the distribution of mass amongst subhalos is very similar for both galaxy and cluster mass halos (e.g. Moore et al. (1999), Klypin et al. (1999)), and we have no reason to suspect that dwarfs will differ in this respect.

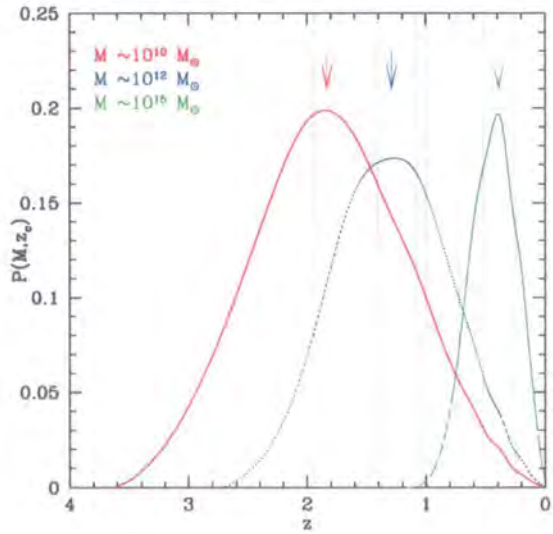

Figure 5.1: **Probability Distributions of Formation Redshifts predicted by Extended Press Schechter theory.** We can get an idea of the typical formation time and the expected spread in these times for a halo of a given mass forming in the ΛCDM cosmology (with $\Omega_m = 0.3$, $\Omega_\Lambda = 0.7$, $h = 0.7$ and $\sigma_8 = 0.9$) by making use of extended Press Schechter theory. In this figure, we have constructed distributions of formation times by generating several thousand realisations of the merger history (using the method outlined in Cole et al. (2000)) of a halo of a given mass and defined the redshift of formation, z_f, as the redshift at which the most massive progenitor first contains half the mass of the halo identified at redshift z. The curves are coloured according to mass scale - red, blue and green denote masses of order $M \sim 10^{10}\,\mathrm{M}_\odot$, $10^{12}\,\mathrm{M}_\odot$ and $10^{15}\,\mathrm{M}_\odot$ respectively. The three sets of vertical dotted lines correspond to the median, upper and lower quartiles, while arrows indicate the modes of the distributions.

We address all of these issues in this chapter by gathering together a sample of high resolution N-body simulations of individual dark matter halos spanning five orders of

magnitude in mass. We complement our sample of four dwarf mass halos with a further seven galaxy mass halos ($M \sim 2 \times 10^{12}\,\mathrm{M}_{\odot}$) and ten cluster mass halos ($M \sim 5 \times 10^{14}\mathrm{M}_{\odot}$). All of the halos in our sample contain of order 10^6 particles - the best resolved case contains over 4.2 million particles within r_{200} - and it is possible to reliably resolve the mass distribution down to a typical radius $r_{\mathrm{min}} \sim 1\% r_{200}$.

The outline of this chapter is as follows. In § 5.2, we present details of the simulations used and provide the gross characteristics of the halos in our sample. We describe the results of our analysis in some detail in § 5.3, encompassing the spherically averaged profiles, the shapes and the substructure content of the halos. Salient points arising from the results are discussed in § 5.4, and we present our conclusions in § 5.5.

5.2 The Simulations

We wish to investigate the structural and kinematic properties of dark matter halos spanning several orders of magnitude in mass, extending from dwarf galaxy ($M \sim 10^{10}\mathrm{M}_{\odot}$) to cluster ($M \sim 10^{15}\mathrm{M}_{\odot}$) mass halos. In particular, we would like to make a detailed analysis of the mass distribution in these objects, with special emphasis on the shape of the density and circular velocity profiles at radii of order $\sim 1\%$ the virial radius, r_{200}. As we have already seen in chapter 2, we require of order 10^6 particles within r_{200} if we are to reliably reproduce the mass distribution on these scales.

We have therefore assembled a sample of high resolution N-body simulations of individual dwarf, galaxy and cluster mass dark matter halos with typical (median) masses of $M \sim 8 \times 10^9\, h^{-1}\mathrm{M}_{\odot}$, $M \sim 2.3 \times 10^{12}\, h^{-1}\mathrm{M}_{\odot}$ and $M \sim 6 \times 10^{14}\, h^{-1}\mathrm{M}_{\odot}$ respectively. When choosing which halos to resimulate, we did not employ any selection criteria other than a mass cut at $z = 0$, except in the case of three of the galaxy mass halos - **gH01**, **gH02** and **gH03**. In these cases, we enforced relative isolation, that is, we ensured that the halos did not have any neighbours more massive than $2 \times 10^{12} h^{-1}\mathrm{M}_{\odot}$ within a distance of $1.5h^{-1}$ Mpc.

The simulations were run assuming a ΛCDM cosmological model in which $\Omega_{\Lambda} = 0.7$, $\Omega_0 = 0.3$ and $\sigma_8 = 0.9$. We have assumed $h = 0.7$ in all but three of the simulations - the galaxy halos **gH01**, **gH02** and **gH03** - in which $h = 0.65$. The majority of the simulations were carried out using **GADGET**, although two of the galaxy mass halos were run using

PKDGRAV (gH05 and gH06). Numerical parameters were set according to the convergence criteria of chapter 2; these parameters are presented in table 5.1.

Our highest resolution run, gH05, contains over $\sim 4.5 \times 10^6$ particles inside r_{200}, thus allowing us to reliably resolve the mass distribution within the central $0.5\% r_{200}$ of the halo, whereas our lowest resolution run, gH03, contains $\sim 3.4 \times 10^5$ particles corresponding to an innermost believable radius of $\sim 1.7\% r_{200}$. On average, our galaxy halos are better resolved than either our dwarf or cluster halos, but in practically all cases we can believably resolve to within $\sim 1\% r_{200}$. The minimum believable radius, $r_{\rm min}$, has been determined for each of the halos by applying the convergence criteria of chapter 2; we find that it is the number of particles that defines this limit, and so we compute the outermost radius at which the relaxation timescale, $t_{\rm relax} \lesssim 0.6\, t_0$, where t_0 defines the Hubble time. Values for $r_{\rm min}$ are given in table 5.1.

Projected maps of the dark matter density distribution at $z = 0$ in a sample of these objects are shown in figures 5.2 and 5.3. We have smoothed the mass (particles) in cubes centred on the halos and containing all material within $\sim 2\, r_{200}$ - corresponding to boxes of side $0.1h^{-1}$ Mpc, $1h^{-1}$ Mpc and $3h^{-1}$ Mpc on dwarf, galaxy and cluster mass scales respectively - and projected the smoothed distribution onto a mesh. Each mesh point is weighted according to the logarithm of its projected surface density, and so the "brighter" the mesh point, the higher the projected surface density[†]. Thus, as we might expect, the centres of the halos tend to be the brightest points in these maps, although it should be noted that there are many distinct bright regions in and around the halo, corresponding to substructure and orbiting halos outside of r_{200}.

Physical properties of the halos at $z = 0$ are given in table 5.2; we give values for the halo's virial mass, M_{200}; virial radius, r_{200}; the circular velocity at r_{200}, V_{200}; the number of particles within r_{200}, N_{200}; its spin parameter, λ; and the virial ratio, $2T/|W|$. Recall that it is our convention to define the virial radius as the radius enclosing a spherical volume whose mean overdensity is 200 times the critical density, $\rho_{\rm crit}$. When computing the spin parameter and the virial ratio for a given halo, we might consider using the more general overdensity criterion of $\Delta_{\rm vir}$ as determined for the spherical top-hat model (Lacey & Cole (1993), Eke et al. (1996)); $\Delta_{\rm vir} \simeq 97$ at $z = 0$ for a ΛCDM cosmology. For completeness, we quote values for λ and $2T/|W|$ computed at both the general $r_{\rm vir}$ and at r_{200}.

[†]A more detailed description of the procedure can be found in § 3.2.1 of chapter 3

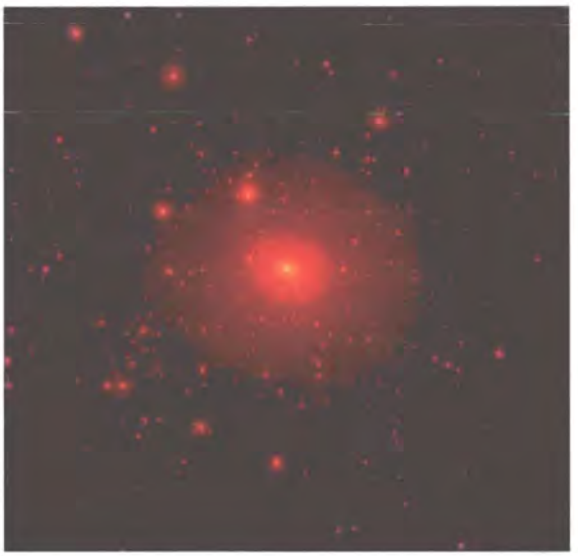

(a) Dwarf Halo dH01

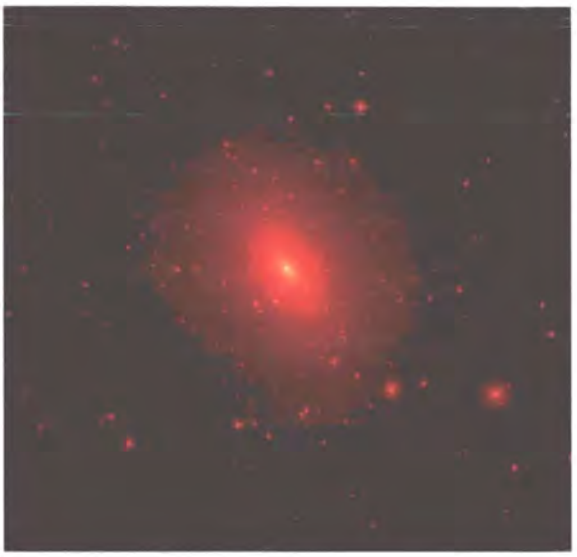

(b) Dwarf Halo dH02

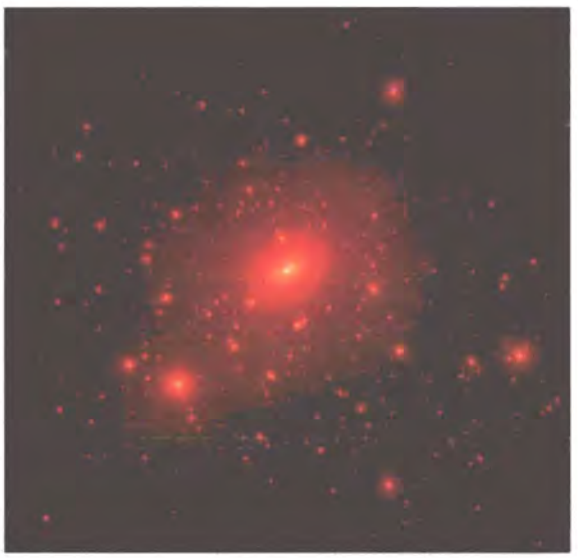

(c) Dwarf Halo dH03

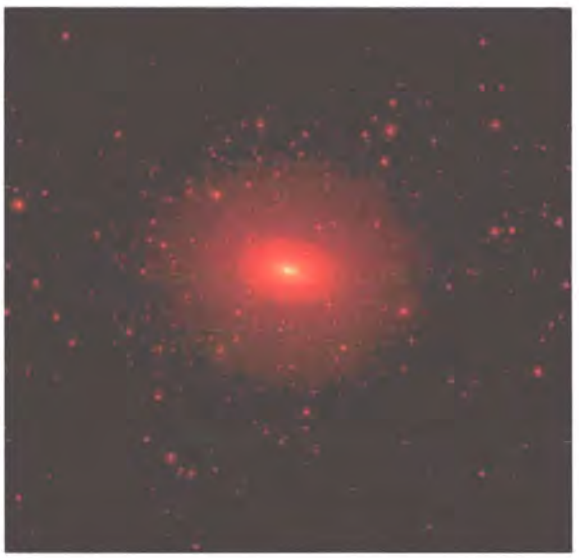

(d) Dwarf Halo dH04

Figure 5.2: **Projected maps of the dark matter density distribution in our four dwarf galaxy halos at** $z = 0$**.** In these figures, we have identified all the mass (particles) within a cube of $100\,h^{-1}$ kpc on a side, centred on the halo, and projected the smoothed distribution onto a two dimensional (1024^2) mesh. Particles were weighted according to their local density, determined using a SPH smoothing kernel computed over the nearest 32 neighbours. Each mesh point (or pixel) is weighted according to the logarithm of its projected mass density; the brighter the mesh point, the greater the projected density at that point.

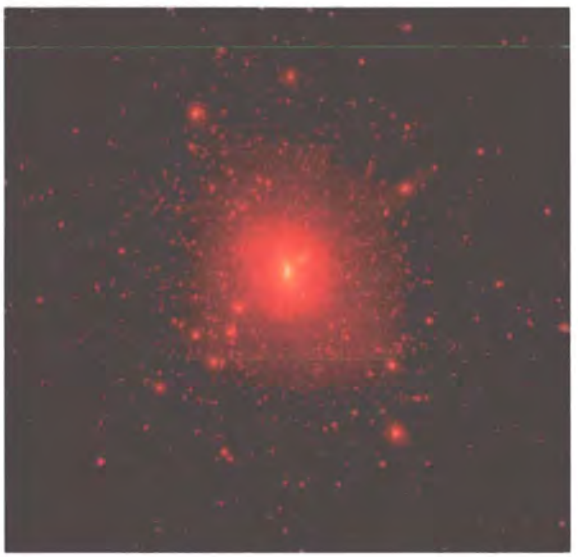

(a) Galaxy Halo gH01

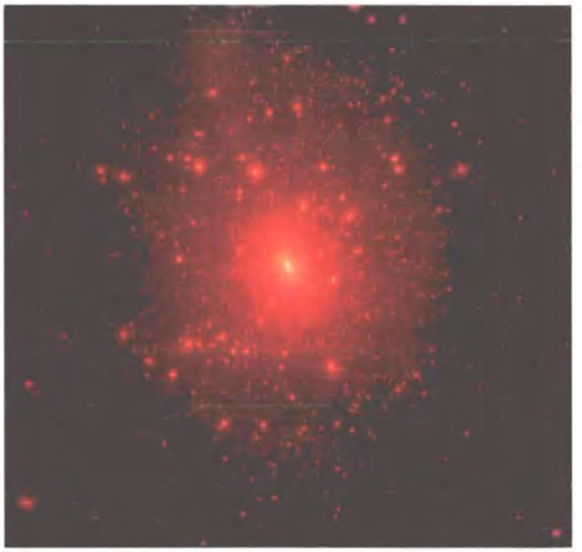

(b) Galaxy Halo gH04

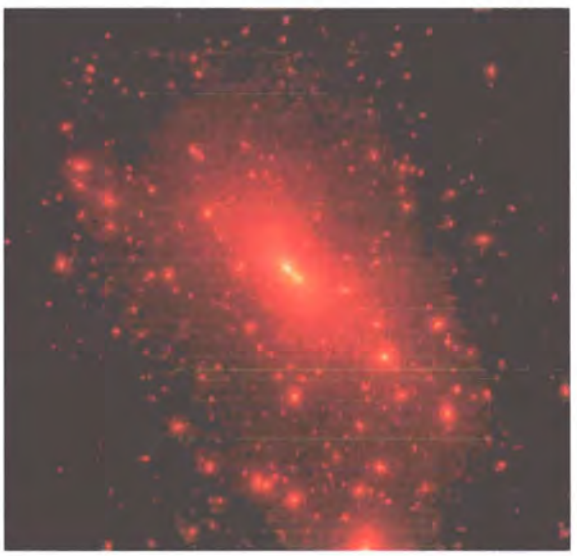

(c) Cluster Halo cl04

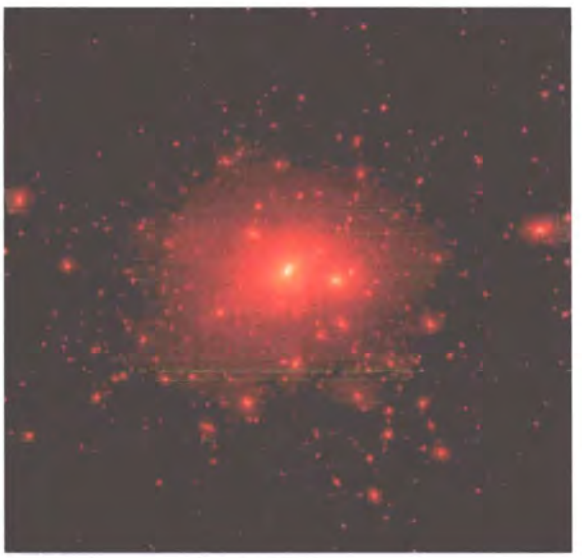

(d) Cluster Halo cl07

Figure 5.3: **Projected maps of the dark matter density distribution in a sample of our galaxy and cluster mass halos at** $z = 0$. As in the previous figure, we show projected dark matter density maps for two of our seven galaxy halos (`gH01` and `gH04`) and two of our ten cluster halos (`cl04` and `cl07`). In the case of the galaxy halos, we consider all the mass within a cube of side of $1\,h^{-1}$ Mpc, while in the case of the cluster halos, we look at a cube of side of $3\,h^{-1}$ Mpc.

Table 5.1: **Numerical Parameters used in the Simulations**. For each halo, we show (1) the size of the simulation box, L_{box} in units of h^{-1} Mpc, (2) the number of particles in the simulation box, N_{box}, (3) the number of particles in the high resolution region, N_{hres}, (4) the mass of the high resolution particles, m_{hres}, in units of $h^{-1}M_{\odot}$, (5) the gravitational softening of the high resolution particles, ϵ_{hres}, in units of h^{-1} kpc, (6) the minimum believable radius, r_{min}, expressed as a percentage of r_{200}, and (7) the starting redshift of the simulation, z_i. Halos gH05 and gH06 (indicated by *) were run using PKDGRAV.

	L_{box} [h^{-1} Mpc]	N_{box}	N_{hres}	m_{hres} [$h^{-1}M_{\odot}$]	ϵ_{hres} [h^{-1} kpc]	r_{min} [% r_{200}]	z_i
Dwarfs							
dH01	35.325	5741027	3422221	9.97×10^3	0.0625	1.05	74
dH02	35.325	5084492	2710686	1.18×10^4	0.0625	1.09	49
dH03	35.325	3837889	2462551	8.24×10^3	0.0625	1.02	49
dH04	35.325	3505274	1943130	9.57×10^3	0.0625	0.92	49
Galaxies							
gH01	32.5	8955682	8932352	6.5×10^5	0.15625	0.64	49
gH02	32.5	2105161	2097152	5.19×10^6	0.3125	1.25	99
gH03	32.5	2104432	2097152	6.92×10^6	0.3125	1.73	99
gH04	32.5	12443838	10297824	3.05×10^6	0.15625	0.6	49
gH05*	35.325	16785271	16777216	6.5×10^5	0.35	0.53	49
gH06*	35.325	16784496	16777216	8.65×10^5	0.35	0.76	49
gH07	35.325	18062707	16233892	2.64×10^5	0.35	0.61	49
Clusters							
cl01	479	10758109	8457516	5.12×10^8	5.0	1.1	36.0
cl02	479	10020750	7808951	5.12×10^8	5.0	1.13	36.0
cl03	479	16046774	13466254	5.12×10^8	5.0	1.22	36.0
cl04	479	10401965	8143738	5.12×10^8	5.0	1.38	36.0
cl05	479	11772412	9352943	5.12×10^8	5.0	1.19	36.0
cl06	479	11359299	9011020	5.12×10^8	5.0	1.16	36.0
cl07	479	11058731	8754054	5.12×10^8	5.0	1.01	36.0
cl08	479	12710381	10182210	5.12×10^8	5.0	1.31	36.0
cl09	479	10709813	8454580	5.12×10^8	5.0	1.21	36.0
cl10	479	9698988	7549542	5.12×10^8	5.0	1.1	36.0

Table 5.2: **Physical Properties of the Simulated Halos at $z = 0$** For each halo, we show (1) the virial mass, M_{200}, in units of $10^{10}h^{-1}\mathrm{M}_{\odot}$, (2) the virial radius, r_{200}, in units of h^{-1} kpc, (3) the circular velocity at r_{200}, V_{200}, in units of km/s, (4) the number of particles interior to r_{200}, N_{200}, (5) the dimensionless spin parameter, λ, and (6) the ratio of twice the kinetic energy to the potential energy of the halo, $2\mathrm{T}/|\mathrm{W}|$; we expect this ratio to approach unity if the halo is in virial equilibrium. Both λ and $2T/|W|$ have been evaluated at the virial radius, r_{vir}, but we also quote their values at r_{200} (in brackets) ; see text for further details.

	M_{200} $[10^{10}h^{-1}\mathrm{M}_{\odot}]$	r_{200} $[h^{-1}$ kpc]	V_{200} [km/s]	N_{200}	λ	$2T/\|W\|$
Dwarfs						
dH01	0.781	32.26	31.87	783309	0.0649 (0.0627)	1.06 (1.08)
dH02	0.923	34.11	34.14	778369	0.0325 (0.0307)	1.03 (1.06)
dH03	0.778	32.23	32.25	944050	0.0222 (0.0153)	1.07 (1.15)
dH04	0.959	34.54	34.58	1000702	0.0349 (0.0329)	1.07 (1.08)
Galaxies						
gH01	222.87	212.42	212.6	3429196	0.0317 (0.0433)	1.17 (0.47)
gH02	268.74	226.09	226.3	516877	0.0650 (0.0466)	1.06 (1.09)
gH03	237.12	216.85	217.1	342645	0.0043 (0.0070)	1.15 (1.21)
gH04	106.37	166.01	166.2	3481206	0.0377 (0.0326)	1.08 (1.11)
gH05	298.44	234.41	234.4	4537968	0.0687 (0.0693)	1.16 (1.18)
gH06	232.18	215.34	215.5	2682846	0.0086 (0.0129)	1.13 (1.22)
gH07	98.46	161.78	161.9	3726406	0.0571 (0.0571)	1.10 (1.10)
Clusters						
cl01	80730.8	1514.23	1515.7	1576325	0.0209 (0.0214)	1.16 (1.26)
cl02	75292.7	1479.44	1480.9	1470142	0.0172 (0.0156)	1.25 (1.41)
cl03	52046.4	1308.11	1309.4	1016243	0.0437 (0.0344)	1.27 (1.28)
cl04	37244.8	1170.04	1171.2	727230	0.0304 (0.0346)	1.19 (1.29)
cl05	54065.6	1324.81	1326.1	1055669	0.0185 (0.0300)	1.32 (1.38)
cl06	61725.2	1384.63	1385.9	1205227	0.0318 (0.0323)	1.26 (1.35)
cl07	83708.1	1532.63	1534.1	1634459	0.0173 (0.0200)	1.20 (1.28)
cl08	45677.0	1252.41	1253.6	891875	0.0392 (0.0339)	1.27 (1.41)
cl09	60319.9	1374.04	1375.4	1177789	0.0143 (0.0119)	1.31 (1.42)
cl10	82907.1	1527.72	1529.2	1618819	0.0173 (0.0151)	1.31 (1.37)

5.3 Results

5.3.1 Spherically Averaged Mass Profiles

One of the most fundamental questions that we can ask about the structure of a dark matter halo relates to the spatial distribution of its mass. Projected maps of the mass distribution, such as those shown in figures 5.2 and 5.3, indicate that dark matter halos, irrespective of their virial mass, are very centrally concentrated systems. This observation is consistent with the belief that divergent central densities - or *dark matter cusps* - are a generic prediction of the CDM model and the hierarchical merging paradigm (see § 1.5 and references therein).

Previous studies lead us to expect that the density profiles of dark matter halos have a universal shape, independent of mass and cosmological model (NFW 1996, 97; Cole & Lacey 1996), but the resolution of the simulations used was not adequate to reliably resolve the mass distribution within $\sim 10\% r_{200}$. Subsequent higher resolution studies of galaxy and cluster mass halos (e.g. Moore et al. 1998, 1999; Fukushige & Makino 1997, 2001, 2003; Jing & Suto 2000; Klypin et al. 2001) have focused on the inner asymptotic behaviour of the profiles, but have neglected the overall shape.

We would like to establish whether the concept of a universal dark matter density profile, independent of halo mass, is valid at higher resolution, and if so, whether or not the ubiquitous NFW and Moore et al. parameterisations can provide an adequate description of the dark matter distribution.

We begin by seeking mass dependent trends in the dark matter density and circular velocity profiles; in figures 5.4 and 5.5, we show spherically averaged mass profiles for the dwarf (solid red curves), galaxy (solid blue curves) and cluster mass halos (green solid curves) in our sample. Density and circular velocity profiles are plotted against radius expressed in physical units of kpc/h in figures 5.4(a) and 5.5(a), running from left to right in order of ascending mass scale. All the curves are plotted down to their innermost believable radius, corresponding to $\sim 1\%$ r_{200} or 0.3, 2 and 10 kpc/h for dwarf, galaxy and cluster mass halos respectively.

We expect lower mass halos to have higher concentrations and therefore higher central densities because these objects formed at redshifts when the mean density of the Universe was greater. This relationship between mass and central density is readily apparent in

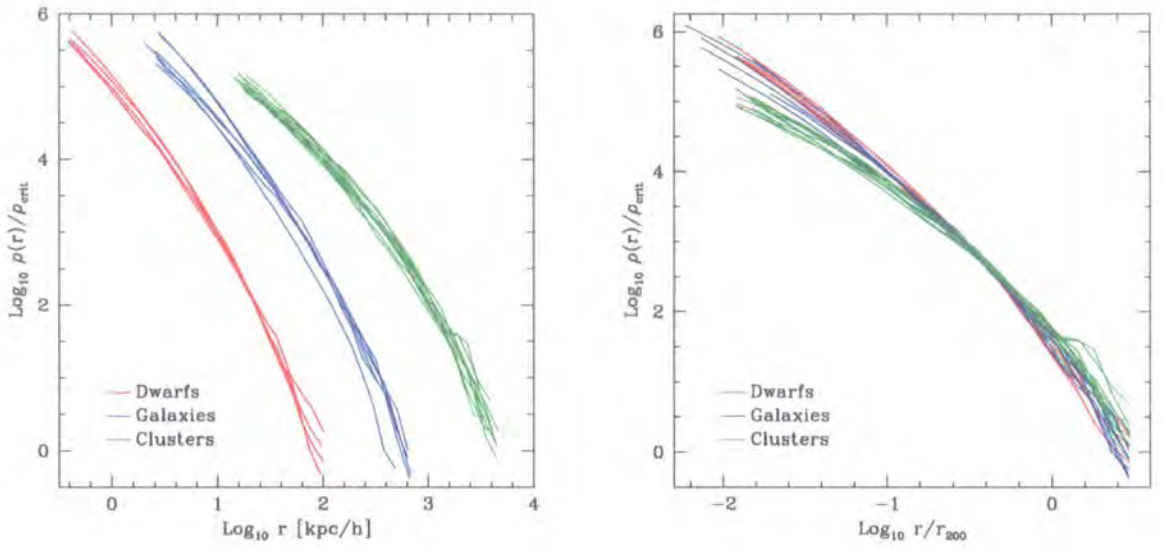

(a) Density Profiles

(b) Density Profiles (normalised)

Figure 5.4: **Spherically Averaged Mass Density Profiles.** We show the dark matter density profiles (figures 5.4(a) and (5.4(b)) for all the halos in our sample, coloured according to mass scale; the red solid curves correspond to dwarf mass halos ($M \sim 10^{10}\,\mathrm{M}_{\odot}$), blue solid curves correspond to galaxy mass halos ($M \sim 2 \times 10^{12}\,\mathrm{M}_{\odot}$) and green solid curves correspond to cluster mass halos ($M \sim 10^{15}\,\mathrm{M}_{\odot}$). Note that we express the radius in physical units of kpc/h in figure 5.4(a) whereas we normalise to the virial radius, r_{200} in figure 5.4(b).

the density profiles of our halos; although there is an appreciable spread - a factor of $\sim 2-3$ - at the innermost believable point in our simulations, we can see a systematic trend in the data. Halos of lower mass are systematically denser in their innermost parts; at $\sim 1\%\ r_{200}$, $\rho \sim 4 \times 10^5 \rho_{\rm crit}$ for dwarf halos, compared to $\rho \sim 10^5 \rho_{\rm crit}$ for clusters.

This trend can be seen most easily in figures 5.4(b) and 5.5(b), where again we plot density and circular velocity profiles for all the halos in our sample, but with the radius scaled by r_{200}. The density (circular velocity) profiles of the dwarf and galaxy mass halos are systematically steeper (shallower) than those of the clusters at the corresponding fraction of the virial radius. This is effectively a statement that lower mass halos have higher concentrations, and confirms what we might intuitively expect from the results of previous theoretical studies (e.g. NFW 1997, Bullock et al. 2001, Eke, Navarro & Steinmetz 2001). As an example, the density profile of a cluster mass halo with a NFW concentration $c = 5$ will have a slope of $\simeq -2.6$ at r_{200} and $\simeq -1.1$ at $1\%\ r_{200}$, compared to $\simeq -2.8$

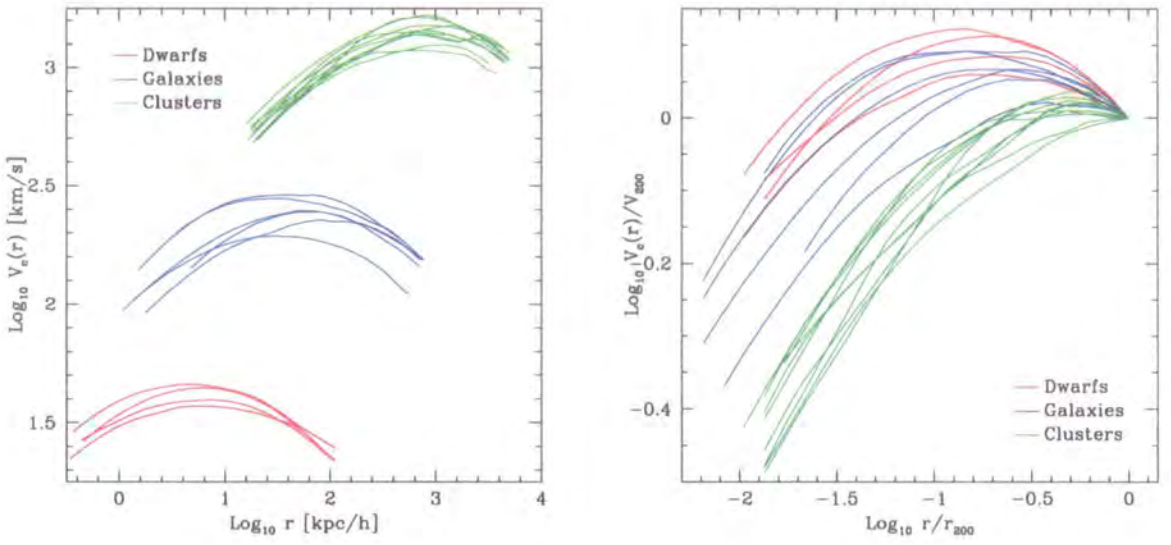

(a) Circular Velocity Profiles

(b) Circular Velocity Profiles (normalised)

Figure 5.5: **Spherically Averaged Circular Velocity Profiles.** We show the dark matter circular velocity profiles (figures 5.5(a) and 5.5(b)) for all the halos in our sample. As before, curves are coloured according to mass scale. Radii are expressed in physical units of kpc/h in figure 5.5(a) and in units of the virial radius, r_{200} in figure 5.5(b).

and $\simeq -1.2$ for a less massive halo with a concentration $c = 12$ at the same fractional radii.

Our example indicates that we should expect a typical dwarf mass halo to have a lower local density at r_{200} than a cluster mass halo by a factor of ~ 1.4, but a higher local density at 1% r_{200} by a factor ~ 3. However, we see a larger rms deviation in the simulation data than expected at these fractional radii; our high resolution dwarfs are less dense than a typical cluster by a factor of ~ 3 at r_{200}, and a factor of ~ 8, or nearly an order of magnitude denser at $\sim 1\%$ r_{200}. We might expect a spread at radii $\sim r_{200}$ because of mass infall and accretion, but the reason for the large discrepancy in central densities is not so obvious. Could this indicate that the central slope of the density profile, and in turn the shape of the circular velocity profile, may have a dependence on mass?

We can investigate whether or not the shape of halo profiles might depend on mass by finding a suitable scaling that will allow a direct comparison between objects of different masses. In effect, we are seeking a characteristic density and circular velocity (and the corresponding radii at which they occur) that can be used to normalise the profiles. Our

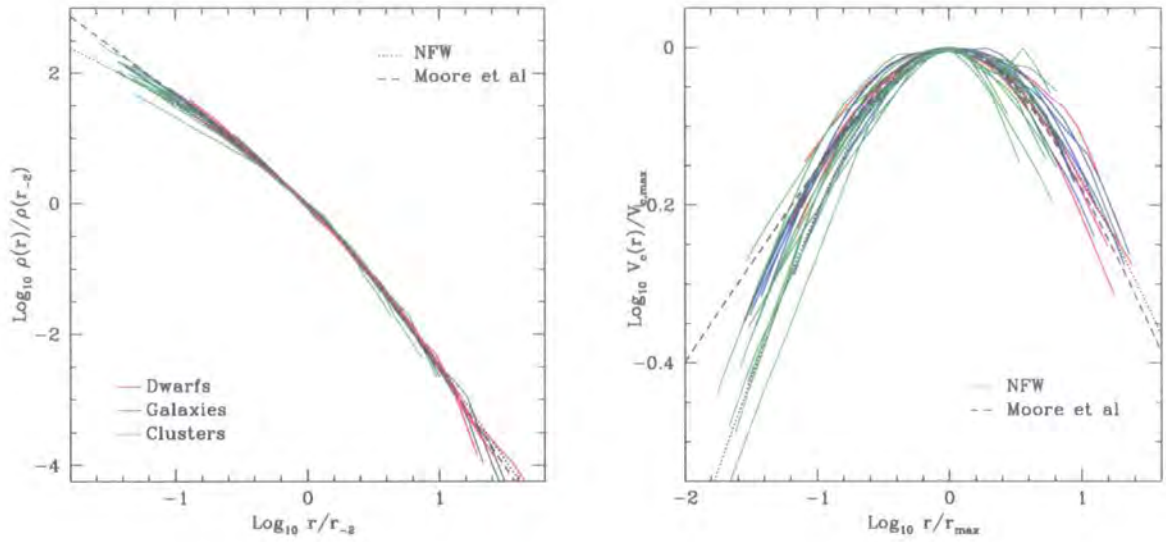

(a) Similarity of Density Profiles

(b) Similarity of Circular Velocity Profiles

Figure 5.6: **Similarity of Spherically Averaged Mass Profiles.** We wish to emphasise the similarity of the spherically averaged mass profiles and their independence from mass scale. In figure 5.6(a), we have normalised the density profiles by expressing radii in units of r_{-2}, the radius at which the slope of the logarithmic density profile is -2, and densities in units of ρ_{-2}, the spherically averaged density at this radius. We perform a similar scaling on the circular velocity profiles in figure 5.6(b) by expressing velocities in terms of the peak circular velocity, $v_{\rm c,max}$, and radii in terms of $r_{\rm max}$,the radius at which the peak occurs.

attempts to find such scalings for the density profile and circular velocity profile are presented in figures 5.6(a) and 5.6(b) respectively.

In the case of the density profile, we have decided to use the radius at which the logarithmic slope of the density profile is -2, r_{-2}, and the density at this radius, $\rho_{-2} = \rho(r_{-2})$, as the units of length and density. Recall that the radius r_{-2} defines the scale radius, r_s, in the case of a NFW profile; if the halos could be most appropriately described by NFW profiles, then we would expect the density at this radius to equal one quarter of the characteristic density of the halo, $\delta_c/4$. On the other hand, it would seem that the peak circular velocity, $v_{\rm c,max}$, and the radius at which this occurs, $r_{\rm max}$, are the most natural scalings for the circular velocity profiles.

It is relatively straightforward to determine r_{-2} and ρ_{-2} from the simulation data.

By locating the peak of the differential mass profile, ρr^2, we can estimate the radius at which the logarithmic slope of the density profile is $S(r) = -2$ by noting that,

$$\frac{d}{dr}(\rho r^2) = \frac{d\rho}{dr}r^2 + 2\rho r = 0 \Rightarrow S(r) = \frac{d\log\rho}{d\log r} = -2 \tag{5.1}$$

We define this radius to be r_{-2} and invert the ρr^2 profile to give the local density, ρ_{-2}, at that point. It should be noted that ρr^2 can be quite flat around its maximum, leading to an error in r_{-2} of as much as 50% or 0.2 dex, or a factor of ~ 2.5 or 0.4 dex in ρ_{-2}.

We estimate the values of $r_{\rm max}$ and $v_{\rm c,max}$ in a similar manner by locating the peak value of the circular velocity. While our method consistently finds $v_{\rm c,max}$ to $\sim 1\%$, the error in $r_{\rm max}$ can be as large as 0.1 dex or 25%, reflecting the flatness of $v_c(r)$ around the peak in some cases.

Normalised density profiles for all the halos in our sample are shown in figure 5.6(a); the expected behaviour of NFW (dotted curve) and Moore et al. (dashed curve) profiles are shown for comparison. Perhaps the main point to note in this plot is the remarkable similarity of the profiles, in spite of the wide range in mass spanned. There are no strong trends apparent in the data; indeed, *all the curves appear to be consistent with a single underlying profile.* It could be argued that the respective averages of the lower dwarf and galaxy mass profiles are slightly steeper than the average cluster mass profile interior to $\sim 0.4\,r_{-2}$. However, this is purely speculative because we do not have many low mass halos and, more importantly, there is a disparity in the range of radii that are reliably resolved on different mass scales. In general, cluster mass profiles (green curves) extend to smaller values of r/r_{-2} than those of either galaxy (blue curves) or dwarf (red curves) mass halos; this reflects the fact that r_{-2} occurs at progressively larger fractions of r_{200} as the mass of the halo increases, as we would expect.

We also show the normalised circular velocity profiles for all our halos in figure 5.6(b), with the predicted behaviour of the NFW (dotted curve) and Moore et al. (dashed curve) models shown for comparison. One of the first points to note in this plot is the apparently large scatter in the profiles. Although we expect the normalised profiles to agree close to $r/r_{\rm max} = 1$, at which point $v_c(r)/v_{\rm c,max} \simeq 1$, we find a large spread in circular velocities at both smaller and larger values of $r/r_{\rm max}$. At $0.1\,r_{\rm max}$, normalised circular velocities can differ by as much as 40% or ~ 0.15 dex, while at $10\,r_{\rm max}$, the spread is of order 25% or ~ 0.1 dex. The spread in $v_c(r)$ at large radii can be attributed to the presence of orbiting

substructure and mass infall. On the other hand, the behaviour at smaller radii probably represents an intrinsic scatter in the halo profiles.

If we separate our sample according to the mass of the halo, we find that the scatter appears to increase with increasing halo mass. For example, normalised circular velocities differ by $\sim$ 10% at $0.1\,r_{\rm max}$ on dwarf and galaxy mass scales, compared with 40% for cluster masses at the same normalised radius. Similarly, we find that normalised circular velocities differ by $\sim$ 5%, $\sim$ 10% and $\sim$ 15% at $0.25\,r_{\rm max}$ on dwarf, galaxy and cluster mass scales respectively. While this apparent trend might partially reflect disparity in the sample sizes, it is also likely that the larger scatter on cluster mass scales reflects their more recent formation.

Finally we note that the shapes of the average dwarf, galaxy and cluster mass profiles are remarkably similar. Values of $v_c(r)/v_{\rm c,max}$ on the three mass scales agree to better than 5% or 0.05 dex for all reliably resolved $r/r_{\rm max}$ in the region of overlap ($0.05 \lesssim r/r_{\rm max} \lesssim 5$). We might therefore conclude, on the basis of this evidence, that there exists a *single underlying mass profile* that describes dark matter halos on all mass scales.

These results strongly indicate that there exists a single *universal* profile that describes the spherically averaged mass profiles of dark matter halos spanning several orders of magnitude in mass. Do either the NFW or Moore et al. models provide an adequate description of this "universal" profile?

The density and circular velocity measured at the scaling radius should be sensitive to the structure of the halo, and so it seems reasonable to ask whether or not the values of ρ_{-2} and $v_{\rm c,max}$ determined from the simulation data are consistent with the predictions of the NFW and Moore et al. models.

We compare the values of r_{-2} and ρ_{-2} estimated for the halos in our sample with the predictions of the theoretical models in figure 5.7(a). The simulation data are represented by red asterisks (dwarf mass halos), blue filled triangles (galaxy mass halos) and green filled squares (cluster mass halos). Model concentrations are computed using both the Eke, Navarro & Steinmetz (2001; hereafter ENS) (long dashed curves) and the Bullock et al. (2001) (dotted curves) prescriptions, and we highlight the relationship between r_{-2} and ρ_{-2} predicted by the NFW (black curves) and Moore et al. (green curves) profiles.

A halo's *mean* concentration is uniquely determined by its virial mass in both the ENS and Bullock et al. prescriptions. We can express the halo's virial radius, $r_{\rm vir}$, in

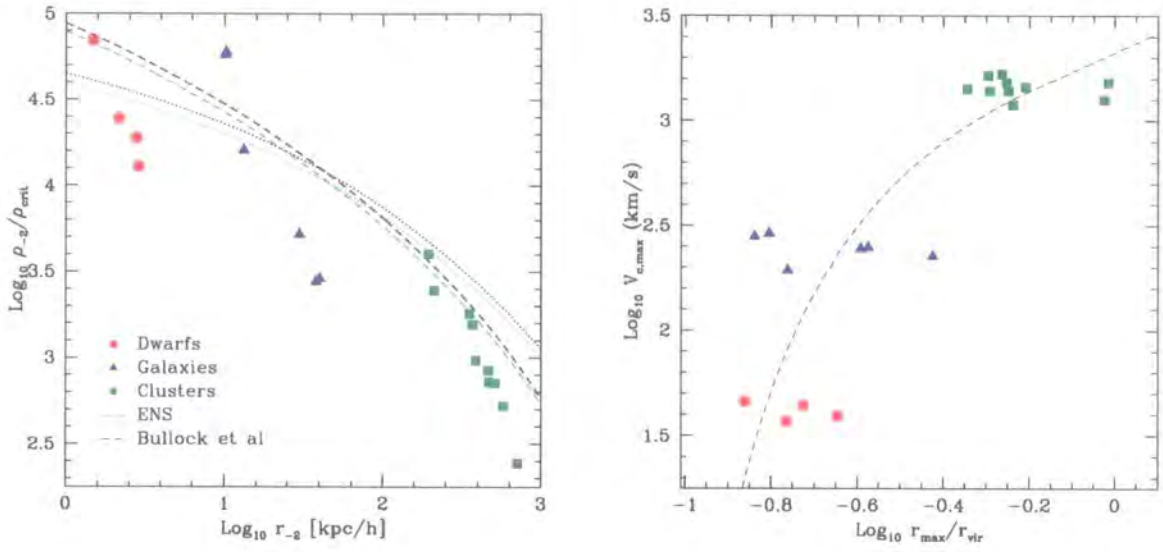

(a) Predicted variation of ρ_{-2} with r_{-2}

(b) Predicted variation of $v_{\rm c,max}$ with $r_{\rm max}$

Figure 5.7: **Expected variation of scaling parameters with halo mass.** We have computed the predicted variation of r_{-2}, ρ_{-2}, $r_{\rm max}$ and $v_{\rm c,max}$ with halo mass according to both the ENS (dashed lines) and Bullock et al. (dotted lines) prescriptions for both NFW (heavy black curves) and Moore et al (heavy green curves) profiles. In figure 5.7(a), we show how the density ρ_{-2} depends on the radius r_{-2}, which in turn reflects the concentration of the halo. Figure 5.7(b) illustrates the relationship between a halo's peak circular velocity, $v_{\rm c,max}$, and the radius at which this occurs, $r_{\rm max}$.

terms of its virial mass,$M_{\rm vir}$;

$$r_{\rm vir} = \left(\frac{1}{\Delta_{\rm vir}} \frac{1}{\rho_{\rm crit}} \frac{3}{4\pi} M_{\rm vir} \right)^{1/3}, \tag{5.2}$$

Note that $r_{-2} = r_s^{\rm N}$ for a NFW profile, while $r_{-2} = r_s^{\rm M}/2^{2/3}$ for a Moore et al. profile.[‡] Given the concentration ($c_{\rm vir}$), virial radius ($r_{\rm vir}$) and virial mass ($M_{\rm vir}$), it follows that we can compute the value of r_{-2}, expressed in units of the scale radius r_s. Furthermore,

$$\rho_{-2} = \frac{1}{4}\rho_{\rm crit}\delta_c = \frac{\Delta_{\rm vir}}{12} \frac{\rho_{\rm crit}\, c_{\rm vir}^3}{\ln(1+c_{\rm vir}) - c_{\rm vir}/(1+c_{\rm vir})} \tag{5.3}$$

for a NFW profile, while the corresponding expression for the Moore et al. profile is

$$\rho_{-2} = \frac{4}{3}\rho_{\rm crit}\delta_c = \frac{\Delta_{\rm vir}}{12} \frac{\rho_{\rm crit}\, c_{\rm vir}^3}{\ln(1+c_{\rm vir}^{3/2})}. \tag{5.4}$$

[‡]The superscripts N and M are used to differentiate the scale radii in the respective models. We require that both models agree on the radius at which the circular velocity peaks, and so $1.24\, r_s^{\rm M} = 2.16\, r_s^{\rm N}$ or $c^M = 0.574\, c^N$.

The simulation data do show a definite trend, with ρ_{-2} decreasing as r_{-2} (and consequently $M_{\rm vir}$) increases. On average, $\rho_{-2} \sim 3 \times 10^4\, \rho_{\rm crit}$ for dwarf masses, compared to $\rho_{-2} \sim 10^3\, \rho_{\rm crit}$ for cluster masses. However, we find significant scatter in the data, with ρ_{-2} varying by as much as a factor of ~ 30 (galaxy masses). If we compare the data with the predicted behaviour, it is clear that the values of r_{-2} measured from the simulations are systematically lower than would be expected if the halos were either NFW or Moore et al. models.

We also compare the values of $r_{\rm max}$ and $v_{\rm c,max}$ measured from the simulation data with the predictions of the theoretical models in figure 5.7(b). As before, simulation data are represented by red asterisks (dwarfs), blue filled triangles (galaxies) and green filled squares (clusters). The dashed curve corresponds to the expected variation of $v_{\rm c,max}$ with $r_{\rm max}$, assuming concentrations computed using the ENS formulation and structural parameters determined from the NFW profile.

Note that the peak circular velocity can be expressed in terms of the circular velocity at the virial radius, $V_{\rm vir}$, and the concentration, $c_{\rm vir}$.

$$v_{\rm c,max} = V_{\rm vir} \sqrt{\frac{g(f c_{\rm vir})}{g(c_{\rm vir})}} \tag{5.5}$$

The function $g(x)$ depends on the parameterisation used; for a NFW profile, $f = 2.16$ (because $r_{\rm max} = 2.16\, r_s^{\rm N}$) and

$$g(x) = \frac{\ln(1+x)}{x} - \frac{1}{1+x}, \tag{5.6}$$

while for a Moore et al. profile, $f = 1.24$ (because $r_{\rm max} = 1.24\, r_s^{\rm M}$) and

$$g(x) = \frac{\ln(1+x^{3/2})}{x} \tag{5.7}$$

Recall that we relate the NFW and Moore et al. concentrations by forcing the respective circular velocity profiles to agree upon $r_{\rm max}$. The peak circular velocities do not differ significantly ($\sim 2-3\%$) and so we do not show the variation of $v_{\rm c,max}$ with $r_{\rm max}$ predicted by the Moore et al. model.

We note that the simulation data are in reasonable agreement with the theoretical calculation (dashed curve), although there is an appreciable spread in $r_{\rm max}$ for a given value of $v_{\rm c,max}$. For example, on galaxy mass scales, we find that $r_{\rm max}$ can vary by as much as factor of 3 (or ~ 0.45 dex). The predicted value of $r_{\rm max}$ tends to be smaller than observed in our simulated dwarf halos, but larger on cluster mass scales. This indicates

that dwarfs have lower concentrations and clusters higher concentrations than one might expect if the dark matter halos of these objects can be described by NFW profiles.

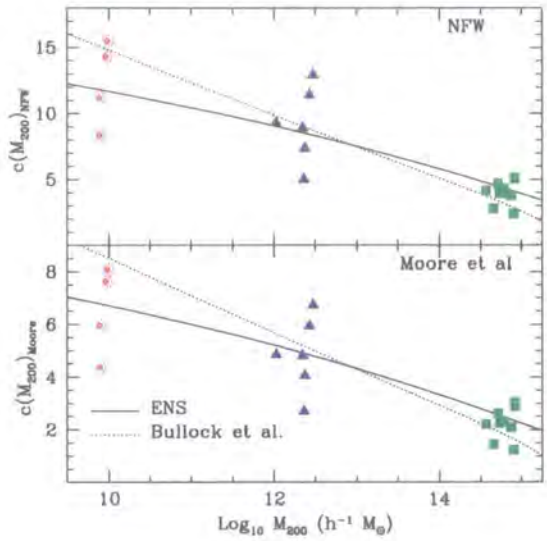

(a) Variation of c_{200} with M_{200}

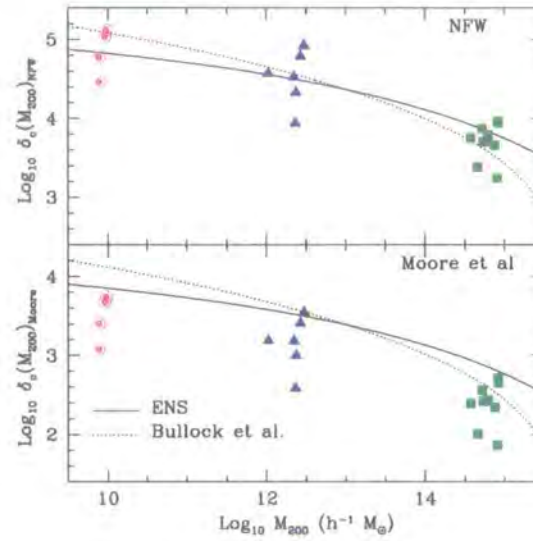

(b) Variation of δ_c with M_{200}

Figure 5.8: **The dependence of a halo's concentration, c_{200}, and characteristic density, δ_c, on its virial mass, M_{200}.** In figure 5.8(a), we plot the best fit concentrations assuming a NFW model (upper panel) and a Moore model (lower panel) against halo mass. In figure 5.8(b), we plot characteristic densities derived from these concentrations against halo mass. In both cases, red asterisks, blue filled triangles and green filled squares denote dwarf mass ($M \sim 10^{10}\,M_\odot$), galaxy mass ($M \sim 2 \times 10^{12} M_\odot$) and cluster mass ($M \sim 10^{15}\,M_\odot$) halos. We also show the predicted variation of concentration and characteristic density with halo mass, as derived from the Bullock et al. (light dotted curves) and ENS (light solid curves) prescriptions.

We take a more transparent approach in figures 5.8(a) and 5.8(b) where we compare best fit concentrations and characteristic overdensities for all the halos in our sample with the predictions of the NFW and Moore et al. models. Concentrations are obtained by fitting to the density profile (see § 4.4). The light dotted and solid curves highlight the expected variation of the concentration, c_{200}, and characteristic overdensity, δ_c, with virial mass, M_{200}. Concentrations have been computed using the ENS (solid curves) and Bullock et al. (dotted curves) prescriptions; note that we have corrected these concentrations, $c_{\rm vir} = r_{\rm vir}/r_s$, to obtain $c_{200} = r_{200}/r_s$.

We expect to find a correlation between both concentration and characteristic overdensity and the mass of the halo. We also expect to find a spread in measured concentration at any given mass scale. This will reflect not only variations in the halo's formation time and recent merging history, but also deviations from the idealised model profiles and intrinsic scatter in the profile itself. For reference, Bullock et al. (2001) found that $\Delta \log_{10} c_{\rm vir} = 0.18$ with little variation with halo mass.

Let us consider the distribution of best fit concentrations with halo mass (figure 5.8(a)); there are two important observations worthy of note here. The first is that there is a definite trend in the simulation data, with higher mass halos having lower concentrations; a typical cluster will have a concentration of $c_{200}^{\rm N} \simeq 5$ ($c_{200}^{\rm M} \simeq 2$), while a dwarf mass halo will have a concentration of $c_{200}^{\rm N} \simeq 12$ ($c_{200}^{\rm M} \simeq 7$). This is consistent with our earlier findings (e.g. figure 5.4) and previous studies (NFW 1997). The second is that there is a sizable spread in the best fit concentrations measured from the simulation data on all mass scales; we find that c_{200} can vary significantly, by as much as a factor of $2-3$. For example, we expect a typical galaxy mass halo to have a concentration of $c_{200}^{\rm N} \simeq 9$, but we find objects with measured concentrations as low as $c_{200}^{\rm N} \simeq 5$ and as high as $c_{200}^{\rm N} \simeq 12$.

If we now consider the performance of the theoretical models and pay particular attention to median value of the simulation data on each mass scale, we see that the Bullock et al. model overestimates the concentration of low mass halos but underestimates the concentration of more massive halos. On the other hand, the ENS model is in much better agreement with the data and seems to provide a good average fit, if slightly overestimating the concentration of the most massive objects. However, it is not possible to discriminate between the NFW and Moore et al. profiles on the basis of these data.

It should be noted that concentration is a relatively weak function of mass; the dwarf halos in our sample have a median concentration of $c_{200}^{\rm N} \simeq 11.2$ ($c_{200}^{\rm M} \simeq 5.9$), compared to $c_{200}^{\rm N} \simeq 4.3$ ($c_{200}^{\rm M} \simeq 2.2$) for the clusters. This corresponds to a change of a factor of ~ 3 over nearly five orders of magnitude in mass. On the other hand, we expect the characteristic overdensity, which varies as c^3, to show a much stronger dependence on mass; as we saw earlier, the central densities in cluster mass halos are typically a factor of several lower than in dwarf halos.

We show the distribution of characteristic overdensities (computed using the best fit concentrations) with halo mass in figure 5.8(b). If we concentrate on the ENS predictions (solid curves), we note that the Moore et al. model consistently overestimates the value

of δ_c on all mass scales by about 60% relative to the median of the data. This suggests that the Moore et al. profile is too steep at small radii. The NFW model provides a much better average fit to the data, although it does tend to slightly overestimate δ_c on cluster mass scales by about 25%.

We conclude that the data do show the expected trend, with lower mass halos having higher characteristic overdensities and concentrations, in broad agreement with the theoretical models. Our results favour the ENS prescription for predicting concentrations and the NFW model for halo structure, but the large spread in the simulation data - roughly a factor of ~ 10 in overdensity and a factor of $\sim 2-3$ in concentration - makes it difficult to be more discriminating. As we mentioned earlier, the scatter may reflect variations in formation epoch and dynamical state, and this intrinsic scatter may disguise the "true" underlying profile.

We can gain greater insight into the performance of the theoretical models by comparing profiles measured from the simulation data with both the NFW and Moore et al. parameterisations as a function of radius. Recall that both the NFW and Moore et al. models failed to accurately describe the behaviour of the measured density and circular velocity profiles shown in figure 5.6 at small radii. Our measured profiles appeared shallower than predicted by Moore et al. but steeper than expected if the profiles were as described by NFW. On the other hand, it is difficult to discriminate between the models and the data at intermediate to large radii. We might therefore expect to find good agreement between the data and the model fits beyond the central $\sim 10\% r_{200}$, but appreciable deviations within this radius.

We have computed the fractional deviation (or dispersion) between the measured profiles and the model fits as a function of radius; the results are shown in figures 5.9(a) and 5.9(b). Two sets of concentrations have been estimated for each halo; one by means of a weighted fit to the density profile (see figure 5.9(a), hereafter ρ-fit), the other by an unweighted fit to the circular velocity profile (shown in figure 5.9(b), hereafter v_c-fit). Our spherically averaged profiles are constructed from shells equally spaced in $\log_{10} r$. The weights ($\sigma_{\rm shell} \sim \delta\rho$) in our ρ-fits depend on the number of particles per shell ($N_{\rm shell}$) because the deviation $\sigma_{\rm shell}$ varies as $1/\sqrt{N_{\rm shell}}$; because the inner few bins contain relatively few particles (when compared to bins in the outer parts of the halo), the fractional error ($\delta\rho/\rho$) is relatively large and so we find that our weighted fits tend to place most emphasis on fitting intermediate to large radii, in contrast to unweighted fits which fit all

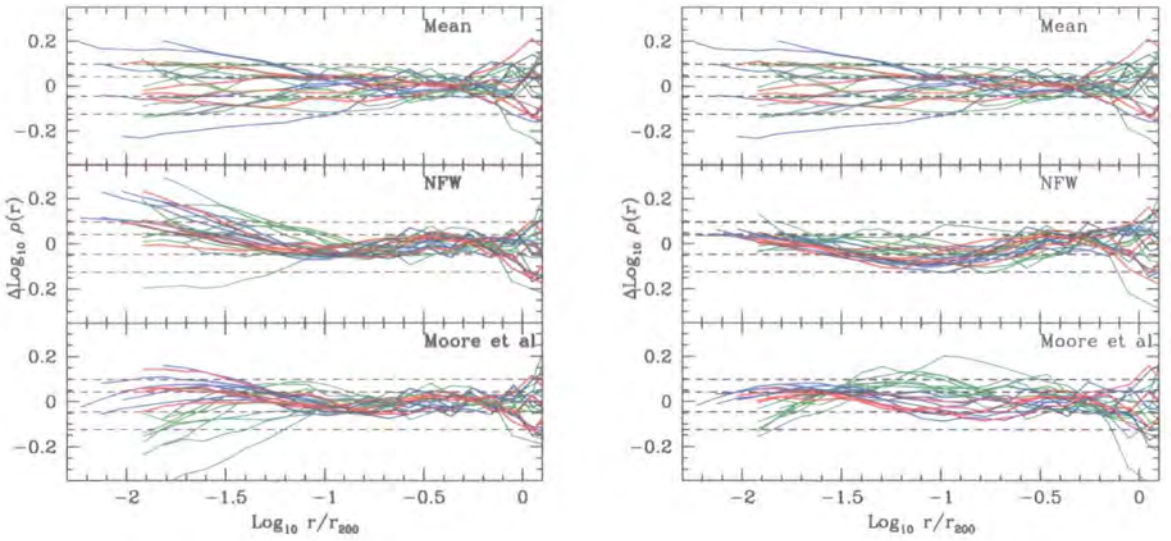

(a) Radial Variation of Residuals (Fit to $\rho(r)$)

(b) Radial Variation of Residuals (Fit to $v_c(r)$)

Figure 5.9: **Dispersion Profiles as Function of Radius.** We compare the measured density profile of each halo in our sample with the average profile (upper panels) determined from all halos on the appropriate mass scale and the best fitting NFW (middle panels) and Moore et al. profiles (lower panels) by computing dispersion profiles as a function of radius. Red curves correspond to dwarf mass halos, blue curves to galaxy mass halos and green curves to cluster mass halos. Figure 5.9(a) shows the radial variation of residuals computed using best fit concentrations determined from the density profiles ($\rho(r)$), while the profiles in figure 5.9(b) are based on concentrations determined from the circular velocity profiles ($v_c(r)$).

parts of the halo to the same level of accuracy.

For comparison, we show the scatter about the mean profile determined on the appropriate mass scale in the upper panels, while the middle and lower panels show the dispersion relative to the best fit NFW and Moore et al. profiles respectively. As before, we have colour coded the curves according to the mass of the halo - dwarf halos are red, galaxy halos are blue and cluster halos are green. Curves are truncated at the innermost believable radius (as determined by the convergence criteria presented in chapter 2).

We first consider the deviation of the measured profiles relative to the mean appropriate to that mass scale in the upper panels of figures 5.9(a) and 5.9(b). The first point to note here is that the scatter is uniform about the mean, as you would expect. The dwarf and cluster profiles never deviate by more than $\sim 25\%$ from their respective means

over the entire radial range. On the other hand, three of the six galaxies deviate by as much as $\sim$ 60%, although all agree to within $\sim$ 25% down to $\sim$ 10% r_{200}. The large deviations apparent close to $\sim r_{200}$ merely reflect the presence of interlopers and infalling substructure.

If we consider the deviations of the measured profiles from the best fitting NFW (middle panels) and Moore et al. (lower panels) models, we find that the v_c-fits tend to perform better than ρ-fits at small radii. Within $\sim$ 10% r_{200}, the measured profile can deviate by as much as a factor of $\sim$ 2 from the ρ-fit (see middle panel, figure 5.9(a)), compared to $\sim$ 25% relative to the v_c-fit. Both the best NFW and Moore et al. ρ-fits perform equally well down to the inner $\sim$ 10% r_{200}, deviating by $\sim$ 10% at most over this range. The Moore et al. model performs better on dwarf and galaxy scales within this radius (maximum deviation $\sim$ 40%) than the NFW profile, but both stumble on cluster mass scales, deviating by as much as a factor of $\sim$ 2. On the other hand, the v_c-fits perform less well at intermediate to large radii, deviating by as much as $\sim$ 60% on cluster mass scales, but outperform the ρ-fit within the central $\sim$ 10% r_{200}, in which case deviations are $\lesssim$ 25%.

We also note that these results indicate that the shape of the underlying density profile is sufficiently different from both the NFW and Moore et al. ρ- and v_c-fits to warrant the introduction of an alternative functional form. Both parameterisations appear to systematically overestimate the local density ($\rho(r)$) at intermediate radii and underestimate it at large radii *on all mass scales.* We can explore the shape of this modified profile in a more quantitative fashion by considering the radial dependence of the logarithmic slope, $S(r)$, and the maximum asymptotic slope, $\alpha(r)$.

Recall our definition of the logarithmic slope, $S(r)$,

$$S(r) = -\frac{d\log\rho(r)}{d\log r}. \tag{5.8}$$

It is straightforward to calculate analytic expressions for $S(r)$ for both the NFW and Moore et al. profiles; for a NFW profile,

$$S(r) = -\frac{1+3\,c^{\rm N}\,x}{1+c^{\rm N}\,x}. \tag{5.9}$$

The equivalent expression for a Moore et al. profile is given by

$$S(r) = -\frac{3}{2}\frac{1+2\,(c^{\rm M}\,x)^{3/2}}{1+(c^{\rm M}\,x)^{3/2}} \tag{5.10}$$

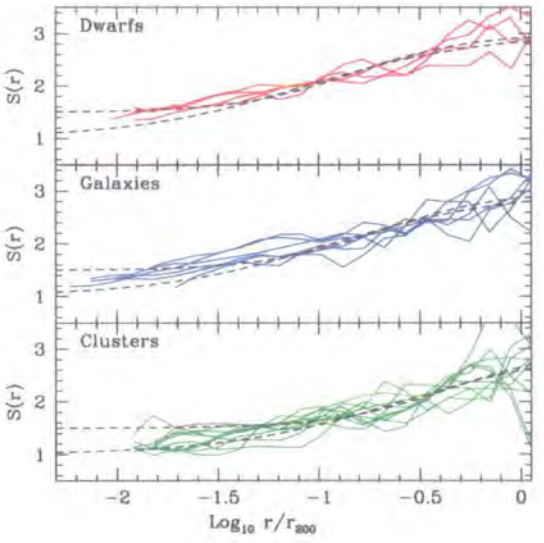

(a) Logarithmic Slope, $S(r)$: Mass Dependence

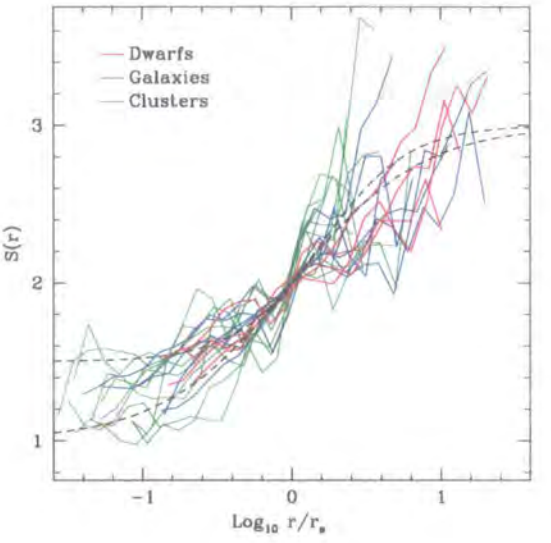

(b) Logarithmic Slope, $S(r)$: Universality

Figure 5.10: **Variation of the Logarithmic Slope, $S(r)$, as a function of radius.** We have computed the logarithmic slope of the density profile in concentric spherical shells for each halo in our sample, and we show its variation as a function of radius in figures 5.10(a) and 5.10(b). Our sample of halos is separated into dwarf (red curves, upper panel), galaxy (blue curves, middle panel) and cluster (green curves, bottom panel) mass objects in figure 5.10(a). We have expressed radii in units of r_{200}. Figure 5.10(b) assesses the similarity of the profiles by expressing radii in units of r_s, the scale radius of the halo. The upper and lower dashed lines highlight the behaviour of NFW and Moore et al. models respectively (see text for details).

Here, $c^{\rm N}$ and $c^{\rm M}$ are the NFW and Moore et al. concentrations, and $x = r/r_{200}$ is the normalised radius. It follows that $S(r) = -2$ and -2.25 at the NFW and Moore et al. scale radii respectively. We note that the explicit dependence on concentration in equations 5.9 and 5.10 can be removed if we normalise the radius by the scale radius, r_s, instead.

We investigate the behaviour of the logarithmic slope of the density profile as a function of radius in figures 5.10(a) and 5.10(b). Because we do not wish to smooth the data any more than is necessary, we choose to compute $S(r)$ by a simple differencing of consecutive shells.

The upper, middle and lower panels of figure 5.10(a) show the variation of the logarithmic slope with radius on the different mass scales - dwarf, galaxy and cluster mass

halos respectively. Heavy dashed curves indicate the behaviour of typical NFW (lower curves) and Moore et al. (upper curves) models at $z = 0$, with appropriate concentrations (for a halo of mass M) derived from the ENS formulation.

There are a few points worth noting here. $S(r)$ tends to be higher for lower mass objects at a fixed fraction of r_{200}, that is, the density profiles of lower mass halos are steeper at a fixed fractional radius, confirming our earlier observations (c.f. figure 5.4(b)). For example, we find that $S(r) \simeq 1.2$, 1.15 and 1.1 on dwarf, galaxy and cluster mass scales respectively at $r = 1.25\%$ of r_{200}.

Unfortunately, the measured profiles are quite noisy (as you might expect from a derivative of a differential quantity) and so it is difficult to draw any strong conclusions regarding the applicability of the NFW and Moore et al. parameterisations. However, we can seek general trends in the mean behaviour of $S(r)$ on each mass scale as a function of radius; in agreement with our previous findings, it would appear that neither the NFW nor Moore et al. profiles provide an accurate representation of the data. The mean curves on dwarf and galaxy scales show very little curvature - indeed, these curves shows an almost linear rise with log radius - while on cluster scales, the mean curve appears to gently curve upwards with increasing radius, albeit with shallower curvature than either the NFW or Moore et al. profiles.

These findings are strengthened by figure 5.10(b), which also highlights the similarity of the profiles by removing the dependence on concentration. We have plotted all the profiles, colour coded according to the mass scale of the halo, against radius normalised by the scale radius, r_s. The upper and lower dashed curves correspond to the expected behaviour of the Moore et al. and NFW profiles. Curves are truncated at the innermost believable radius (typically $\sim 1\% r_{200}$), and so cluster profiles (green curves) tend to probe smaller values of r/r_s than either dwarf or galaxy profiles because $r_s/r_{200} = 1/c$ is larger on these mass scales. Note that r_s has been computed by determining the location of the peak of ρr^2.

Neither the NFW nor Moore et al. models fully capture the general trends in $S(r)$ that we observe in the measured profiles - these differences are most pronounced at small values of r/r_s. However, the profiles are sufficiently similar (accounting for their inherent noisiness) to suggest that there might be an underlying universal or mass independent profile.

The maximum asymptotic slope, α, provides a more powerful constraint on the slope of

the density profile at a given radius. Recall that, if we assume that the halo is spherically symmetric and the local density can be described by a power-law, $\rho(r) \propto r^{-\alpha}$, then

$$\alpha = 3\left(1 - \frac{\rho(r)}{\overline{\rho(r)}}\right) \tag{5.11}$$

where $\rho(r)$ is the local density and $\overline{\rho(r)}$ is the mean interior density at radius r (§ 4.4); α represents an upper limit on the slope of the profile at that point. It is straightforward to calculate analytic expressions for $\alpha(r)$ for both the NFW and Moore et al. profiles; for a NFW model,

$$\alpha(x) = 3 - \left(\frac{c^{\rm N}x}{1+c^{\rm N}x}\right)^2 \frac{1}{\ln(1+c^{\rm N}x) - c^{\rm N}x/(1+c^{\rm N}x)}, \tag{5.12}$$

whereas the corresponding expression for the Moore et al. model is given by

$$\alpha(x) = 3 - \frac{3}{2}\left(\frac{(c^{\rm M}x)^{3/2}}{1+(c^{\rm M}x)^{3/2}} \frac{1}{\ln(1+(c^{\rm M}x)^{3/2})}\right) \tag{5.13}$$

In both cases, $x = r/r_{200}$ corresponds to the normalised radius.

The upper, middle and lower panels of figure 5.11(a) show the variation of $\alpha(r)$ with radius for dwarf, galaxy and cluster mass halos respectively. Heavy dashed curves indicate the behaviour of typical NFW (lower curves) and Moore et al. (upper curves) models at $z = 0$, with concentrations appropriate to the given mass scale.

In contrast to the noisy $S(r)$ profiles shown in figure 5.10(a), $\alpha(r)$ does not show the large fluctuations between shells that was characteristic of $S(r)$ - this reflects the fact that changes in the differential $\rho(r)$ are tempered by the steadying influence of the cumulative $\overline{\rho(r)}$. We note that lower mass objects tend to have steeper maximum possible slopes at a fixed fraction of r_{200}; at $r = 1.25\% r_{200}$, $\alpha(r) \simeq 1$, 1.1 and 1.2 on dwarf, galaxy and cluster mass scales respectively, as expected. This is consistent with our earlier findings for $S(r)$; however, $\alpha(r)$ allows us to derive more meaningful constraints on the slope of the density profile than $S(r)$ does.

If we compare our measured profiles and the predictions of the NFW and Moore et al. parameterisations, we see immediately that *steep inner profiles of the form favoured by Moore et al. appear inconsistent with the simulation data.* Indeed, the Moore et al. profile appears to achieve its asymptotic inner value at a relatively large radius (between $3-5\% r_{200}$), whereas the NFW profiles continues to become shallower as far in as $1\% r_{200}$.

On the other hand, we note that the detailed shapes of the measured profiles are not consistent with either the NFW or Moore et al. models; there is little curvature and the

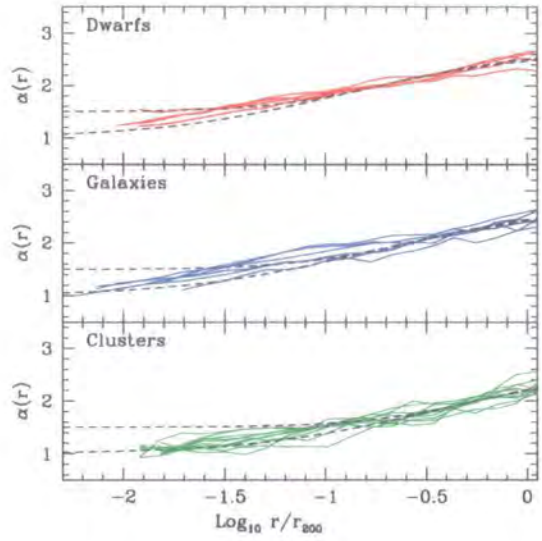

(a) Maximum Asymptotic Slope : Mass Dependence

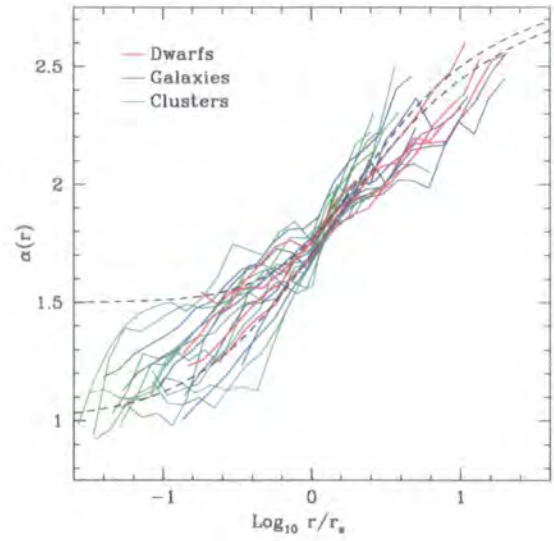

(b) Maximum Asymptotic Slope : Universality

Figure 5.11: **Variation of the Maximum Asymptotic Slope, $\alpha(r)$, as a function of radius.** We show the variation of $\alpha(r)$, the maximum asymptotic slope, as a function of radius for each halo in our sample in figures 5.11(a) and 5.11(b). As in figure 5.10, we separate our halo sample according to mass scale in figure 5.11(a); radii are expressed in units of r_{200}. As in figure 5.10(b), we make a direct comparison between profiles of different masses in figure 5.11(b) by normalising radii to individual scale radii, r_s. Upper and lower dashed lines indicate the behaviour of NFW and Moore et al. models respectively (see text for further details).

curves appear to show an almost linear rise with increasing radius. α lies close to the NFW prediction at small values of r/r_{200} ($\lesssim 1\% r_{200}$), is slightly larger than either model at intermediate values of r/r_{200} ($5\% r_{200} \lesssim r \lesssim 20\% r_{200}$) and in reasonable agreement with both models at large radii ($\sim r_{200}$). However, it should be stressed that α represents an upper limit on the slope at any given radius.

Finally, we highlight the similarity of the profiles in figure 5.11(b). As in figure 5.10(b), we have plotted all the profiles, colour coded according to the mass scale of the halo, against radius normalised by the scale radius, r_s; curves are truncated at the innermost believable radius. Upper and lower dashed curves correspond to the expected behaviour of the Moore et al. and NFW profiles.

Before considering the spherically averaged kinematics of the halos, it is worth recalling what we have learnt in this subsection

- The steepening of the central slope with mass should not be interpreted as representing a mass dependence in the shape of the density profile. Instead, it reflects the fact that dwarf halos are more centrally concentrated that cluster halos.

- The shapes of the density profiles of dark matter halos spanning several orders of magnitude in mass and forming in the ΛCDM cosmology are similar when suitably normalised. The profiles are sufficiently similar to suggest that their shape is not sensitive to the mass of the halo. This is an important result because it appears to confirm the universality of the dark matter density profile at *high spatial resolution*, at least with respect to the mass of the object.

- However, neither the NFW nor the Moore et al. profiles fully capture the behaviour of the spherically averaged mass profiles of the systems considered. It would appear that a broader profile is required.

- The central slope of the dark matter density profile at a fixed fraction of the virial radius cannot be as steep as predicted by the Moore et al. profile, but may be consistent with the NFW profile. We have found that the maximum slope at $1\% r_{200}$ increases from ~ -1.1 on cluster mass scales, through -1.2 on galaxy scales, up to ~ -1.3 on dwarf galaxy scales.

5.3.2 Spherically Averaged Kinematics

Our attention has so far focused on the spherically averaged mass distribution of the dark matter, with particular emphasis placed on the density and circular velocity profiles. We now consider the spherically averaged kinematical properties of the halos.

We have computed the mean behaviour of the radial velocity, v_r, and the velocity anisotropy, $\beta(r)$, as a function of radius for our dwarf, galaxy and cluster mass halos. Results are shown in figures 5.12 and 5.13; dwarf mass halos are shown in the upper left hand panels (red curves), galaxies in the upper right hand panel (blue curves) and cluster halos in the lower left hand panel (green curves). Average profiles - determined using all the halos on the appropriate mass scale - are shown in the lower right hand panel.

We compute v_r and $\beta(r)$ by averaging all particles in thin spherical shells centred on the centre of mass of the halo; velocities are defined relative to the bulk centre of mass

motion and are expressed in physical units, that is, we explicitly account for the Hubble component. The velocity anisotropy is defined by

$$\beta = 1 - \frac{1}{2}\frac{\sigma_t^2}{\sigma_r^2} \tag{5.14}$$

where σ_r and σ_t are the mean radial and tangential velocity dispersions respectively (c.f. § 4.4.3). If the velocity distribution is isotropic - $\sigma_t^2 = 2\sigma_r^2$ - then $\beta = 0$; on the other hand, if the distribution is radial/tangential, $\beta \to 1/-\infty$.

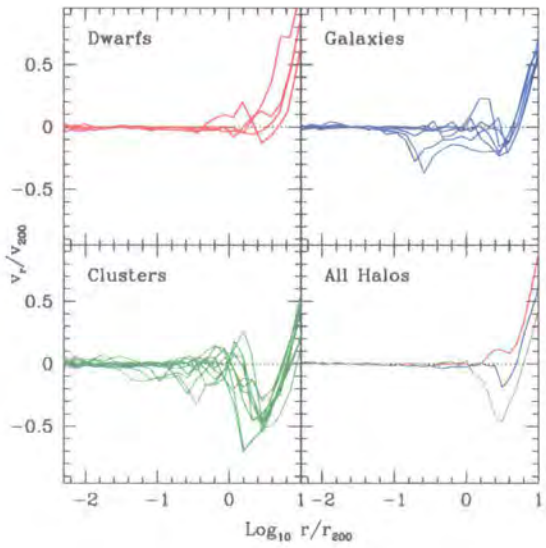

Figure 5.12: **Radial variation of radial velocity, v_r, at $z = 0$.** We show spherically averaged radial velocity profiles for dwarf (red curves, upper left hand panel), galaxy (blue curves, upper right hand panel) and cluster (green curves, lower left hand panel) mass halos at $z = 0$. The curves are truncated at the innermost believable radius, $r_{\rm min}$ (see text). The average behaviour on each of these mass scales is highlighted in the bottom right hand panel. We have expressed radial velocities in units of V_{200}, the circular velocity at r_{200}, and radii in units of r_{200}.

Figure 5.12 shows the behaviour of the mean radial velocity of the dark matter as a function of radius on dwarf, galaxy and cluster mass scales at $z = 0$. We express velocities in units of V_{200}, the halo's circular velocity at r_{200}, and radii in units of r_{200}; this allows us to directly compare the results for different mass halos.

If we start by considering the dwarf halos (upper left hand panel), we see that v_r is approximately zero within r_{200} in all cases, with very little scatter about the mean.[§] This

[§]The deviation apparent in one of the profiles at $\sim r_{200}$ corresponds to the passage of a companion

indicates that dwarf galaxy halos are probably dynamically relaxed systems, in agreement with the findings of § 4.4.3. On the other hand and somewhat surprisingly, $v_r \simeq 0$ between $r_{200} \lesssim r \lesssim 2\,r_{200}$ whereas we might have expected $v_r < 0$; this indicates that there is no appreciable infall of material onto the central halo. Beyond $2\,r_{200}$ (roughly corresponding to the turnaround radius), v_r grows rapidly as it joins the Hubble flow.

This apparent lack of infall contrasts sharply with the behaviour on galaxy (upper right hand panel) and cluster (lower left hand panel) mass scales. In common with the dwarfs, these systems are dynamically relaxed on average (blue and green curves respectively in lower right hand panel), albeit with a much larger scatter about the mean. The differences are most apparent at $\sim 3\,r_{200}$ where there are quite pronounced troughs (i.e. inward falling shells of material) in the radial velocity profiles. This imprint of infall is most significant on cluster mass scales, less so on galaxy scales. For an average cluster, $v_r < 0$ between $r_{200} \lesssim r \lesssim 8\,r_{200}$, that is, the influence of a "typical" cluster extends out to $\sim 10\,h^{-1}$ Mpc. Infall peaks at $\sim 3\,r_{200}$ or $\sim 3\,h^{-1}$ Mpc where $v_r \simeq 0.5\,V_{200}$ or ~ 500 km/s inwards. On galaxy scales, $v_r < 0$ between $2\,r_{200} \lesssim r \lesssim 4\,r_{200}$, or between $\sim 500 - 1000\,h^{-1}$ kpc. Infall peaks at $\sim 3\,r_{200}$ or $\sim 500\,h^{-1}$ kpc where $v_r \simeq 0.1\,V_{200}$ or ~ 20 km/s inwards.

We can gain a more complete understanding of the kinematics of material in and around the halo by considering the velocity anisotropy, β; we do so in figures 5.13(a) and 5.13(b), where we show how β varies both as a function of radius and of mass.

In figure 5.13(a), we show the radial variation of $\beta(r)$ with radius, separating the halos according to mass scale. The velocity distribution appears to be preferentially radial within $\sim r_{200}$ in almost all cases, irrespective of mass scale. We see a steady rise in $\beta(r)$ from the centre outwards, indicating that the orbits are becoming progressively more radial with increasing radius. Clusters tend to show a shallower rise, perhaps not too surprising considering their recent merging history - we might expect massive merging clumps spiralling into the centre of the halo to leave their imprint on the velocity distribution as material tidally stripped continues along its original orbit.

However, while $\beta(r)$ continues its almost linear rise out to and beyond r_{200} for both galaxies and clusters, we note that it begins to flatten at $\sim 10\%\,r_{200}$ on dwarf mass scales, forming a plateau out to $\sim 50\%\,r_{200}$, at which point orbits start to become more isotropic ($\beta(r) \sim 0$) and eventually tangential ($\beta(r) < 0$) at $\sim r_{200}$. This behaviour is con-

halo on the outward part of its journey.

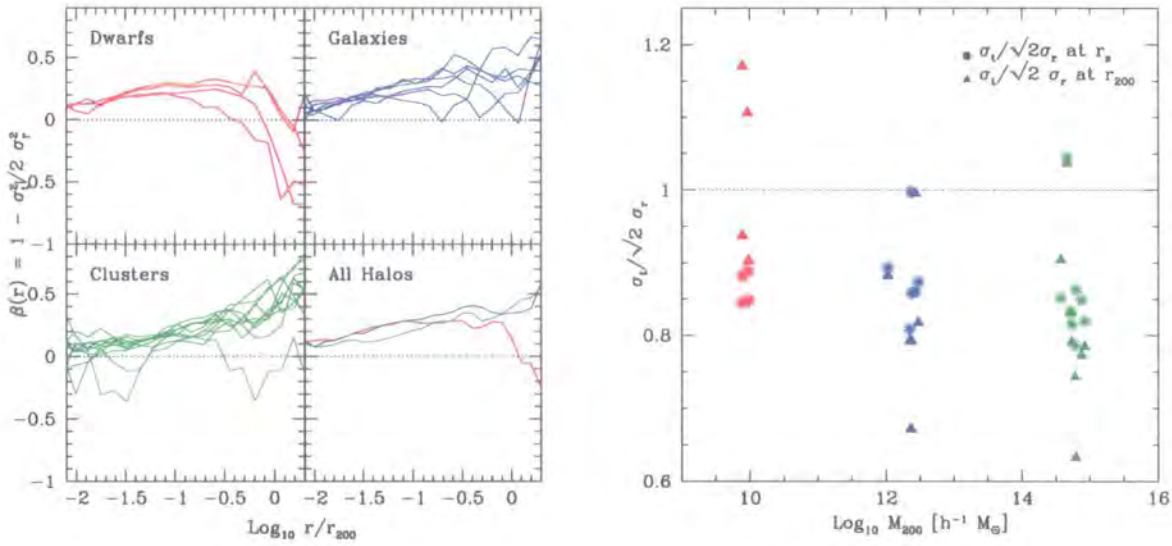

(a) Radial Dependence of $\beta(r)$

(b) Mass Dependence of $\beta(r)$

Figure 5.13: **Dependence of velocity anisotropy, β, on radius and mass at $z = 0$.** We have computed $\beta = 1 - 1/2\ \sigma_t^2/\sigma_r^2$ in a series of concentric spherical shells centred on the halo for all the halos in our sample.(a) Figure 5.13(a) illustrates the variation of β with radius on different mass scales; as in figure 5.12, we separate our sample into dwarfs (red curves, upper left hand panel), galaxies (blue curves, upper right hand panel) and clusters (green curves, lower left hand panel). Average profiles are shown in the lower right hand panel.(b) In figure 5.13(b), we plot the quantity $\sigma_t/\sqrt{2}\sigma_r$, evaluated at r_s and r_{200}, against virial mass for each of the halos. Asterisks and filled triangles indicate the values at r_s and r_{200} respectively. The light dotted line corresponds to the isotropic case.

sistent with the information about the radial velocity component derived from figure 5.12.

We could gauge the mass dependence of β by plotting its value at some characteristic radius against the mass of the halo. However, we have chosen to examine the related quantity $\sigma_t/\sqrt{2}\sigma_r$ measured at the scale radius, r_s, and the virial radius, r_{200}, for dependence on the virial mass of the halo, M_{200}; the result is shown in figure 5.13(b). The isotropic case (i.e. $\sigma_t^2 = 2\,\sigma_r^2$) is highlighted by the dotted line corresponding to $\sigma_t/\sqrt{2}\sigma_r = 1$; radial distributions have $\sigma_t/\sqrt{2}\sigma_r < 1$. Asterisks and filled triangles indicate the value of $\sigma_t/\sqrt{2}\sigma_r$ at r_s and r_{200} respectively.

Based on our analysis of figure 5.13(a), we expect to find most points below $\sigma_t/\sqrt{2}\sigma_r = 1$, that is, the velocity distribution is preferentially radial at both characteristic radii.

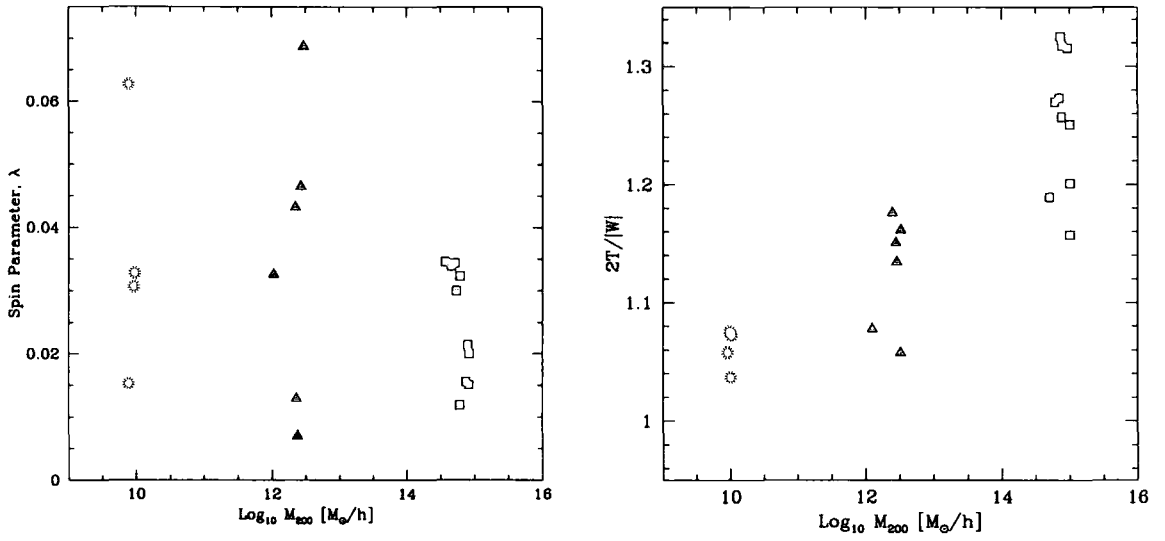

(a) Mass Dependence of λ

(b) Mass Dependence of 2T/|W|

Figure 5.14: **Dark Matter Halos are Supported by Anisotropic Velocity Dispersion.** This is borne out by the values of λ, the dimensionless spin parameter, plotted in figure 5.14(a); $\lambda \simeq 0.04$, irrespective of the virial mass of the halo. Figure 5.14(b) indicates that higher mass halos tend to be less relaxed than their less massive counterparts. As usual, red asterisks correspond to dwarf mass halos, blue filled triangles to galaxy mass halos and green filled squares to cluster mass systems.

There does not appear to be any strong trend with mass apparent in the measurements at r_s (asterisks); we find that, on average, $\sigma_t/\sqrt{2}\sigma_r \simeq 0.8 - 0.85$, independent of halo mass. On the other hand, measurements of $\sigma_t/\sqrt{2}\sigma_r$ at r_{200} appear to be systematically larger (i.e. more isotropic or tangential) than on larger mass scales. These observations confirm the trends seen in the lower right hand panel of figure 5.13(a), which stresses the mean behaviour of halo profiles on a particular mass scale. We find that $\beta \simeq 0.3$ at r_s in all cases; in contrast, $\beta \simeq 0.4$ (i.e. preferentially radial) on galaxy and cluster scales, whereas $\beta \simeq 0$ (i.e. isotropic) on dwarf scales.

Finally, we investigate whether our halos are supported by rotation or an anisotropic velocity dispersion in figure 5.14(a), where we show the dependence of the spin parameter, λ, on the mass of the halo. Recall that we can define a dimensionless spin parameter,

$$\lambda = \frac{J\,|E|^{1/2}}{GM^{5/2}} \tag{5.15}$$

where J, E and M are the total angular momentum, energy and mass of the virialised dark matter halo, and G is the gravitational constant. Physically, the spin parameter provides a measure of the size of a halo's net rotational velocity, derived from its spin angular momentum, relative to its circular velocity, and indicates whether the halo is supported by an anisotropic velocity dispersion tensor ("anisotropy pressure") or by rotation. Low values indicate that rotation is unimportant. Previous studies have found that λ is generally small with a median value $\lambda_{\rm med} \simeq 0.04$ (e.g. Cole & Lacey (1996)). Thus we conclude that dark matter halos are expected to be supported by anisotropy pressure.

We have computed λ for all the halos in our sample and the results are shown in figure 5.14(a); we show λ plotted as a function of the virial mass of the halo, $M_{\rm vir}$. Note that we have used $M_{\rm vir}$ instead of M_{200} in this instance for consistency with previous work; $M_{\rm vir}$ is defined as

$$M_{\rm vir} = \frac{4\pi}{3}\Delta_{\rm vir}\rho_{\rm crit}r_{\rm vir}^3 \tag{5.16}$$

where $\Delta_{\rm vir} \simeq 97$ at $z = 0$. We show values λ computed for both $M_{\rm vir}$ and M_{200} in table 5.2. For reference, we present values of the virial ratio, $2T/|W|$; these data are shown graphically in figure 5.14(b) and indicate that more massive objects tend to be less dynamically relaxed than their less massive brethren.

Perhaps the main point to note in this plot is that λ is comparable for all the halos in our sample, despite the masses spanning nearly five orders of magnitude. Indeed, we find $\lambda_{\rm med} \simeq 0.035$ on dwarf mass scales, compared to $\lambda_{\rm med} \simeq 0.037$ and $\lambda_{\rm med} \simeq 0.027$ on galaxy and cluster mass scales. However, we also note a large spread in values about this median, irrespective of mass; λ extends from ~ 0.02 to ~ 0.065 for dwarf masses, from ~ 0.005 to ~ 0.07 for galaxies and from ~ 0.015 to ~ 0.045 for clusters.

Although the values for the dwarf and galaxy mass halos are in good agreement with the findings of previous studies (e.g. Cole & Lacey (1996)), it is not entirely clear why $\lambda_{\rm med}$ on cluster mass scales is so low. No criteria other than the mass of the object were used in generating the initial conditions for the clusters, and other kinematic measures (such as v_r and $\beta(r)$) are consistent with published results; we tentatively conclude that it probably reflects the relatively small number of halos used.

In spite of this "minor mystery", we conclude that dark matter halos are supported by an anisotropic velocity dispersion tensor, irrespective of mass.

5.3.3 The Shapes of Dwarf, Galaxy and Cluster Mass Halos

We have so far concerned ourselves with computing spherically averaged properties for our sample of halos, but it is clear from projections of the particle distribution such as those shown in figures 5.2 and 5.3 that dark matter halos are generally aspherical. Previous studies (e.g. Frenk et al. (1988), Cole & Lacey (1996), Thomas et al. (1998), Jing & Suto (2002)) and the findings presented in § 4.4 indicate that dark matter halos can be better approximated as ellipsoids with axis ratios that vary as a function of radius.

This result becomes immediately apparent if we plot the distribution of particles within a given halo that have densities satisfying some threshold criterion. Following the convention set out in chapter 4, we define a series of thin shells of particles with progressively higher densities in the range $0.97\,\rho_s < \rho < 1.03\,\rho_s$, where

$$\begin{aligned} \rho_s &= \tilde{\rho}^{(n)}\rho_{\rm crit}\ , \\ \tilde{\rho}^{(n)} &= 20 \times 5^{n-1}\ ,\ n = 1, 7. \end{aligned} \tag{5.17}$$

These densities correspond to shells with effective radii of 100%, 80%, 40%, 20%, 5% and 2% of the virial radius, r_{200}, where we define the effective radius of the shell, $r_{\rm eff} = (abc)^{1/3}$. We show two dimensional projections of the particle distribution in three of these shells in figures 5.15 and 5.16 - (from top) $\rho_s = 500$, 2500 and 12500. For clarity, we determine the orientation of the principal axes for each shell and rotate the particle coordinates into this diagonalised frame so that projections are onto the principal planes. To accentuate their shape and ellipsoidal nature, we take thin slices through these rotated shells, with thicknesses corresponding to 10%, 5% and 2.5% of r_{200} for $\rho_s = 500$, 2500 and 12500 respectively. Furthermore, we show projections of ellipsoids with axis ratios computed for the particle distribution in each shell in the bottom panel.

Note that we have removed all bound substructure from the halo, using the method described in § 4.3.3 of chapter 4, because we wish to quantify the shape of the smooth component of the halo. Bound subclumps constitute a small fraction of the halo mass - between 5% and 10% (see § 5.3.4) - but typically have high central densities. As we saw in § 4.3.3, selecting particles according to density threshold resolves not only a shell of particles that belong to the parent but also many disjoint regions corresponding to subclumps. These disjoint regions bias our estimates of the shell's axis ratios and the orientation of its principal axes and so it is best to remove this problem at its source.

There are several points worth noting in figures 5.15 and 5.16. It is clear from both

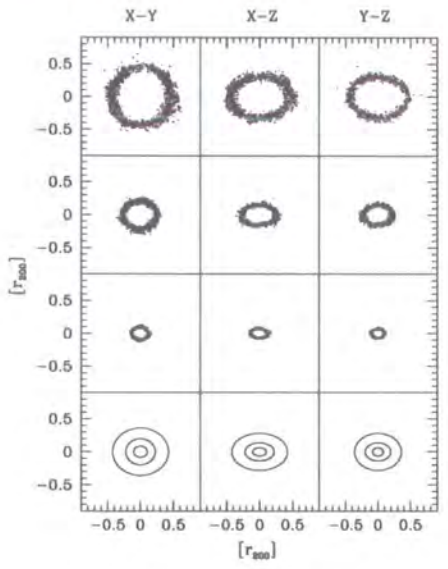

(a) Dwarf Halo dH01

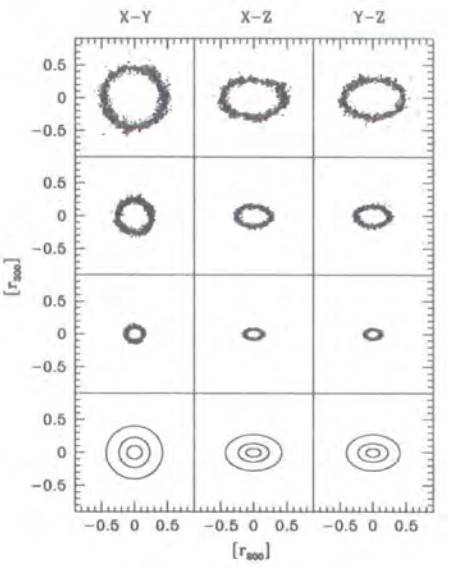

(b) Dwarf Halo dH02

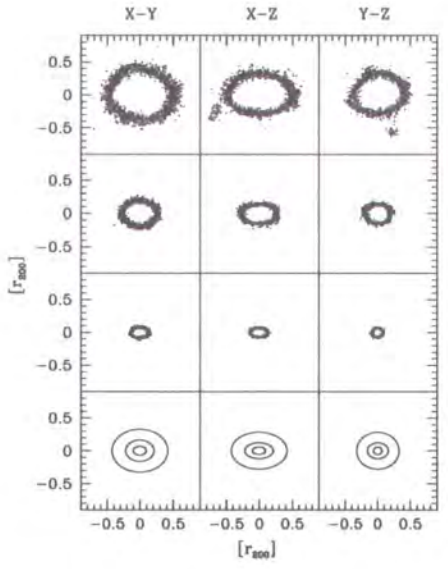

(c) Dwarf Halo dH03

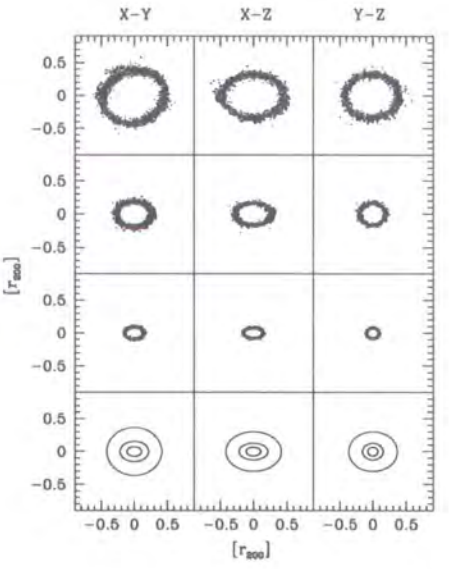

(d) Dwarf Halo dH04

Figure 5.15: **Two dimensional projections of isodensity shells in our sample of dwarfs.** Here we show two dimensional projections of the distribution of particles in shells satisfying the density thresholds (from top) $\rho_s = 500$, 2500 and 12500 times $\rho_{\rm crit}$. The particle coordinates have been rotated into the diagonalised frame and scaled by the virial radius, r_{200}, of the halo. We show the particle distribution as projected onto the major- intermediate (X-Y), major-minor (X-Z) and intermediate-minor (Y-Z) planes. We also show the corresponding ellipsoidal fits to the isodensity surfaces in the bottom set of panels.

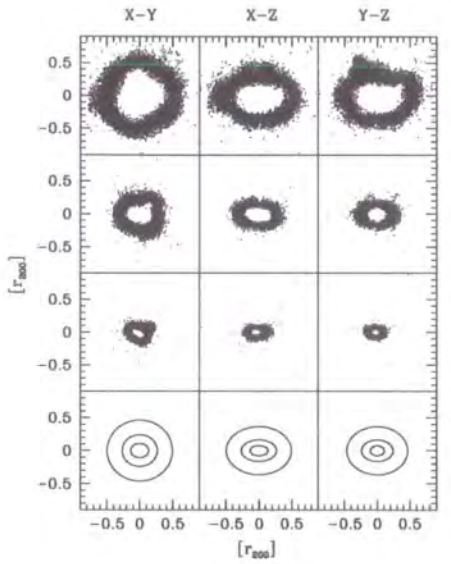

(a) Galaxy Halo gH01

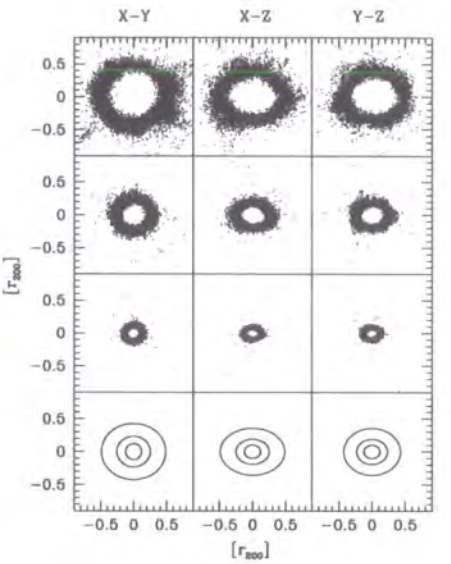

(b) Galaxy Halo gH04

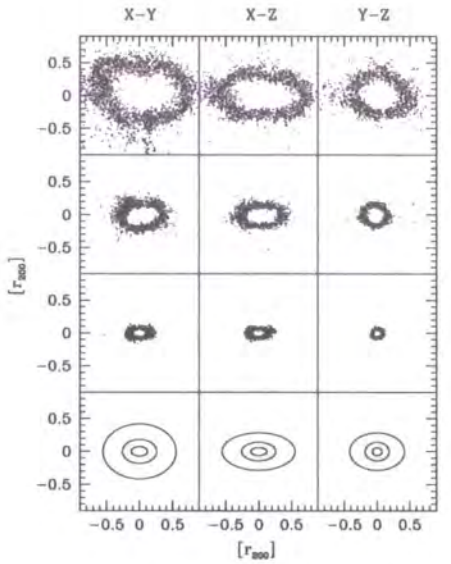

(c) Cluster Halo c104

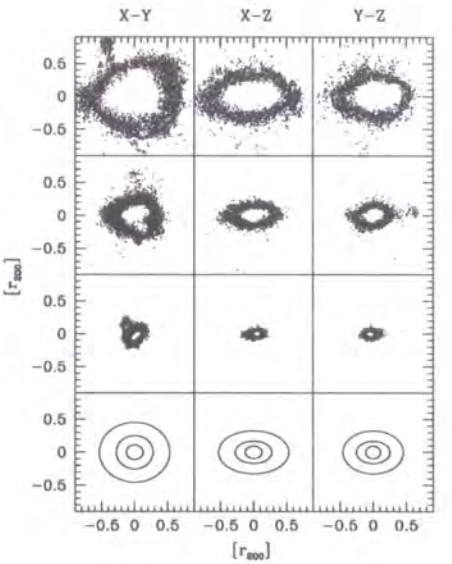

(d) Cluster Halo c107

Figure 5.16: **Two dimensional projections of isodensity shells in selected galaxy and cluster halos.** As in figure (5.15), we show two dimensional projections of the distribution of particles in three isodensity shells, where $\rho_s = 500$, 2500 and 12500 times $\rho_{\rm crit}$, as before. Particle coordinates have been rotated into the diagonalised frame and scaled by the virial radius, r_{200}. Ellipsoidal fits to the isodensity shells are shown in the bottom set of panels.

sets of figures that the ellipsoidal description is an appropriate one. None of the halos highlighted are highly flattened - the most extreme case, `cl04`, has a major-to-minor axis ratio of 2 : 1 - and it would appear that a typical dark matter halo can be characterised by an oblate spheroid, independent of mass scale. The isodensity surfaces of the dwarf mass halos in our sample are quite regular and axisymmetric in comparison with the larger mass halos. In particular, the cluster mass halos - `cl04` and `cl07` - show significant departures from axisymmetry. This trend probably reflects the fact that dwarfs are more relaxed systems than clusters - $2T/|W| \simeq 1.05$ for dwarf masses compared to $2T/|W| \simeq 1.4$ for clusters. Finally, axis ratios do not appear to change dramatically over the range of overdensities highlighted, although there appears to be a weak trend towards a decrease with increasing overdensity, at least in the case of the dwarfs and galaxies. This suggests that isodensity surfaces become more elongated closer to the centres of dwarf and galaxy halos, but not in clusters halos.

We can gain greater insight into the variation of a halo's shape with radius by calculating the ratio of the intermediate-to-major and minor-to-major axis ratios, b/a and c/a, for shells at progressively higher overdensities , ρ_s. Figure 5.17(a) nicely illustrates this variation by showing the behaviour of b/a (solid lines) and c/a (dashed lines) for a series of thin isodensity shells of increasing overdensity. Because we are interested in the possible mass dependence of this variation, we have split our sample according to mass scale. We show the results for dwarf (upper left hand panel), galaxy (upper right hand panel) and cluster (lower left hand panel) mass halos. The average behaviour of the axis ratios with overdensity are also shown for each mass scale in the bottom right hand panel.

The dwarf mass halos show a definite trend, with both b/a and c/a decreasing with increasing ρ_s. The intermediate-to-major axis ratios show quite a large scatter at any given overdensity; for example, b/a ranges from ~ 0.75 up to ~ 0.95 at $\rho_s = 1000$, and from ~ 0.5 up to ~ 0.8 at $\rho_s = 10^5$. On the other hand, the scatter in the minor-to-major axis ratios is much smaller at intermediate to high overdensities - $c/a \sim 0.6$ at $\rho_s = 1000$ and ~ 0.5 at $\rho_s = 10^5$ - although it does show a larger scatter at smaller overdensities, ranging from $c/a \sim 0.6$ up to ~ 0.8 at $\rho_s = 100$. The mean behaviour of b/a and c/a with ρ_s (red solid and dashed curves), shown in the bottom right hand panel, confirms this general trend. $b/a \sim 0.85$ and $c/a \sim 0.6$ at $\rho_s = 1000$, while $b/a \sim 0.65$ and $c/a \sim 0.5$ at $\rho_s = 10^5$.

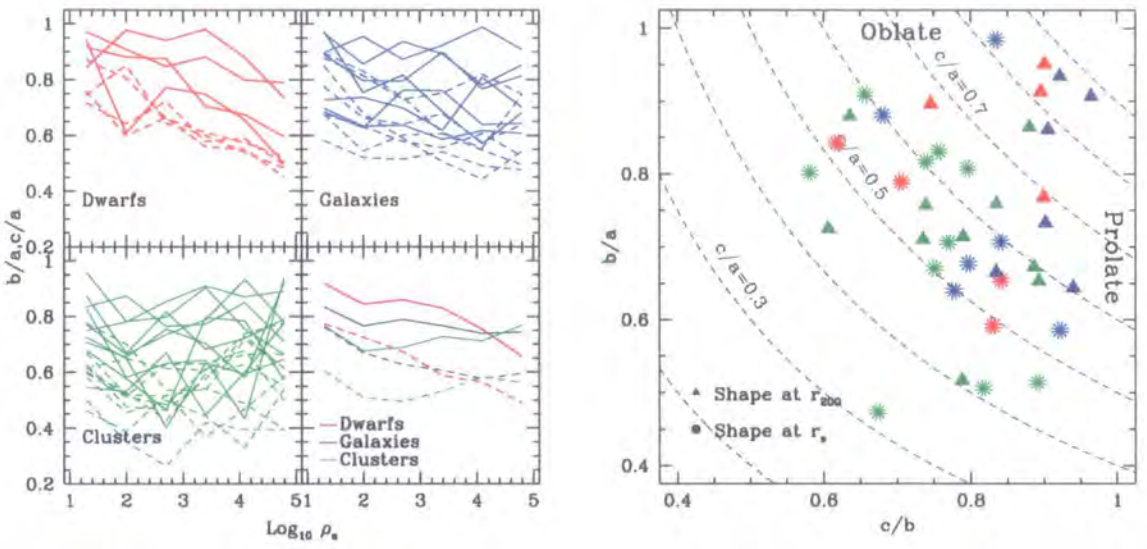

(a) Variation of Axis Ratios with Local Density

(b) Variation of Shape with Mass Scale

Figure 5.17: **Variation of Halo Shape with Overdensity, ρ_s, and Mass, M, at $z = 0$.** Figure 5.17(a) illustrates how the axis ratios of isodensity shells change as we probe higher densities, corresponding to smaller radii, within the bulk of the dark matter halo. We show the variation of b/a (heavy solid lines) and c/a (heavy dashed lines) as a function of increasing density threshold, ρ_s, for dwarf (upper left hand panel), galaxy (upper right hand panel) and cluster mass halos (lower left hand panel). We compare the results for the three mass scales in the lower right hand panel, where we plot the median curves for each set of halos in our sample. In figure 5.17(b), we show how a halo's shape depends on its mass by comparing b/a with c/b at the virial radius r_{200} (filled triangles) and the scale radius r_s (asterisks) for all the halos in our sample. Symbols are colour coded according to mass scale - red, blue and green denote dwarf ($M \sim 10^{10}\,M_{\odot}$), galaxy ($M \sim 2 \times 10^{12}\,M_{\odot}$) and cluster ($M \sim 10^{15}\,M_{\odot}$) mass scales. Lightly dashed curves indicate how the value of c/a varies for a given c/b and b/a.

In comparison, it is difficult to judge whether galaxy or cluster mass halos show any significant variation of axis ratios with overdensity whatsoever! The axis ratios for both galaxy and clusters masses show significant scatter; b/a varies between ~ 0.65 and ~ 0.95 at $\rho_s = 1000$ for galaxy halos, and ~ 0.5 and ~ 0.9 at the same overdensity for cluster halos. In a similar manner, c/a varies between 0.5 and 0.75 at $\rho_s = 1000$, and 0.35 and 0.65 at the same overdensity for clusters halos. It could be argued that the values of b/a measured for galaxy halos remain roughly constant over the range of overdensities investigated, while the corresponding values for galaxy clusters show a slight *increase* with increasing overdensity. Also, the measured values of c/a for galaxy halos appear to show a decrease with increasing overdensity, implying that the centres of dark matter halos in galaxies are more flattened than their outer parts. The measured values of c/a for cluster halos, on the other hand, also exhibit a tendency to increase with increasing overdensity.

These conclusions appear to be borne out by the mean curves plotted in the bottom right hand panel. b/a, as estimated from all the galaxy halos in our sample (blue solid curves), remains approximately constant from $\rho_s = 100$ up to $\rho_s = 10^5$, whereas the mean behaviour of the corresponding quantity for all the cluster halos (green solid curve) shows a slight increase over the same range. On the other hand, while c/a appears to decrease with increasing overdensity for the galaxy halos (blue dashed curves), it appears to increase with increasing overdensity for the cluster halos (green dashed curves).

Figure 5.17(b) provides extra insight into trends in the shapes of halos of different masses. We compare the distribution of axis ratios, b/a and c/b, as measured at the virial radius r_{200} (filled triangles) and the scale radius r_s (asterisks) for each halo. Prolate objects have $a = b > c$, whereas oblate objects have $a > b = c$. We find that our data are distributed uniformly about $b/a = c/b$, indicating that they can be characterised as general triaxial ellipsoids. If we consider the shapes of isodensity surfaces at r_s, we find that there are as many oblate dwarfs and clusters as prolate ones, but twice as many galaxies are prolate than oblate. On the other hand, the results at r_{200} suggest that there are equal numbers of oblate and prolate dwarfs, but both the galaxies and the clusters are preferentially prolate (100% and 80% respectively).

We conclude that dark matter halos can be characterised as general triaxial ellipsoids at all radii, but that galaxies and probably clusters appear to be preferentially prolate, whereas our dwarfs are as likely to be prolate as oblate.

5.3.4 Dark Matter Substructure within Dwarfs, Galaxies and Clusters

The mass and spatial resolution of our simulations should be more than adequate to resolve a wealth of substructure within the virialised regions of our sample of halos. Indeed, the numerous dense knots apparent in the projected dark matter density maps shown in figures 5.2 and 5.3 clearly indicate that substructure is plentiful within all our halos, irrespective of their mass. This basic observation is consistent with the findings of previous studies (e.g. Moore et al. (1999), Klypin et al. (1999)), which found that the substructure halo (or *subhalo*) population in galaxy mass objects is very similar to that found in cluster mass objects.

It is clear that our dwarf, galaxy and cluster mass halos contain a wealth of substructure, and so it is interesting to compare the properties of the respective populations. If there are systematic differences between the populations, they most probably reflect the correlation between the mass of the host and its formation redshift. As we noted in § 5.1, a typical cluster mass halo ($M \sim 10^{15}\,\mathrm{M}_{\odot}$) halo is predicted to form at a redshift of $z_f \sim 0.4$, whereas a typical dwarf mass halo ($M \sim 10^{10}\,\mathrm{M}_{\odot}$) has a redshift of formation $z_f \sim 1.5$. In other words, dwarf mass halos are on average ~ 3 times older than cluster mass halos (assuming a ΛCDM cosmology) and therefore processes such as tidal stripping and dynamical friction will have had ~ 3 times longer to take effect.

We would like to get some idea of the kind of properties of the subhalo population that might depend on the mass of the parent. As we mentioned in § 5.1, we have decided to focus our attention on the relative amount of mass in substructure (the *mass fraction*), the distribution of this mass amongst subhalos (the *mass distribution function*), the spherically averaged number density profile and typical subhalo concentrations.

Note that we have used the `SubFind` algorithm of Springel et al. (2000), described in detail in § 3.2.2, to identify bound substructures and to generate a catalogue of subhalos for each halo in our sample. Furthermore, we have restricted our analysis to only those subhalos containing more than N_{min}, the minimum number of particles, which we have set to 20 particles, and whose centre of mass of mass lies within the virial radius of the host.

We begin by examining whether or not a correlation exists between the mass of a halo and the fraction of this mass that is in substructure. In figure 5.18, we show how the fraction of mass bound in substructure within the virial radius, r_{200}, varies as a function of the virial mass, M_{200}, for all the halos in our sample. The simulation data - red asterisks,

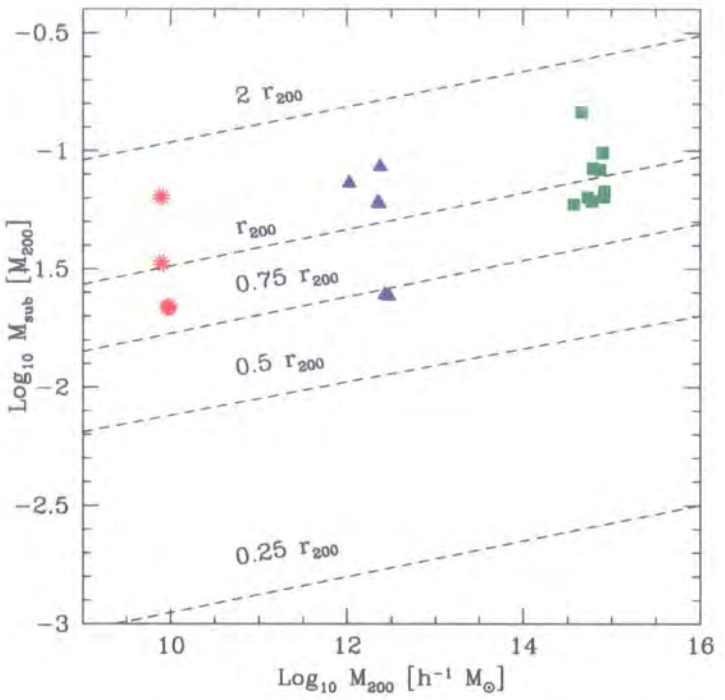

Figure 5.18: **Fraction of Virial Mass Bound in Substructure.** We have plotted an estimate of the fraction of a halo's mass bound in substructure against its virial mass for all the halos in our sample. Simulation data for the mass fraction within r_{200} are represented by red asterisks, blue filled triangles and green filled squares, corresponding to dwarf, galaxy and cluster mass halos respectively. Dashed lines indicate the typical variation of the mass fraction with halo mass at $(2, 1, 0.75, 0.5, 0.25)r_{200}$ (see text for further details).

blue filled triangles and green filled squares - represent dwarf, galaxy and cluster mass halos respectively. For comparison, we have also estimated the substructure mass fraction within 200%, 75%, 50% and 25% r_{200} for each of our halos. Dashed lines (determined by simple least squares fits to these data) indicate the typical variation of mass fraction with halo mass.

The main point to note here is that there does appear to be a correlation, albeit a weak one, between the amount of a halo's mass bound in substructure and its virial mass. The average mass fraction appears to increase with increasing halo mass - $M_{\rm sub} \sim 4\%\, M_{\rm vir}$ on dwarf scales, $\sim 5\%\, M_{\rm vir}$ for galaxy scales and $\sim 8\% M_{\rm vir}$ for cluster scales. However, it is difficult to judge how significant this trend is, given the number of lower mass halos in our sample.

We also note that the slope of the observed relationship between substructure mass

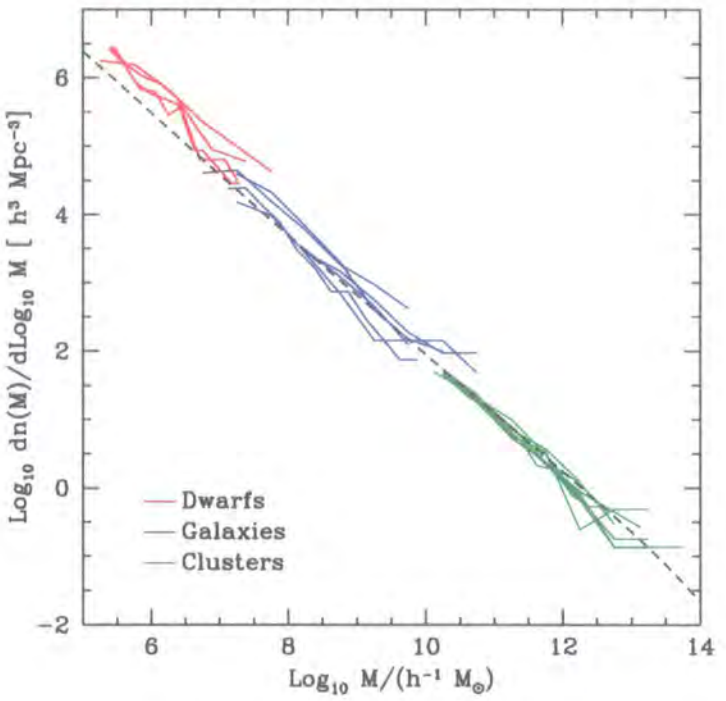

Figure 5.19: **Mass Distribution Functions (MDFs) of Subhalos at $z = 0$.** We show the $z = 0$ mass distribution functions for the dwarf (red curves), galaxy (blue curves) and cluster (green curves) mass halos in our sample. For an intriguing comparison, we also show the Sheth-Tormen best fit to the Jenkins et al. (2001) universal mass function (light dashed curve) (see text for details).

fraction and mass of host does not change significantly if we include all bound objects within $\sim 2\,r_{200}$ or only those subhalos within 0.75, 0.5 and $0.25\,r_{200}$ (dashed lines). This is reassuring; we expect subhalos to follow predominantly radial orbits (e.g. Ghigna et al. (1998)), independent of their spatial distribution and the mass of their host, and so the variation of enclosed mass fraction with radius should not depend on halo mass. However, the rapid decline in the abundance of substructure at small radii - e.g. a factor of ~ 10 decrease between 0.5 and $0.25\,r_{200}$ indicates that, even with several million particles within r_{200}, the effects of finite resolution (as described in chapter 3) is still a problem.

If we consider the abundance of subhalos with a given fractional mass relative to the host, we find similar numbers for all of the halos in our sample. For example, the number of objects with masses of order $\sim 0.001\,M_{\rm vir}$ agrees to within 20%, regardless of mass. However, we find that this relation is slightly steeper for lower mass halos, indicating that there are more relatively massive subhalos in higher mass systems. We might have

expected this - the more massive the host, the more recent its formation and the shorter the timescales over which dynamical friction and tidal stripping have had to operate.

We can gain further insight into this behaviour by investigating the mass distribution function (MDF), which we define as the number of subhalos per unit logarithmic mass interval per unit physical volume. We have constructed MDFs from the subhalo catalogues for each of the halos in our sample and the results are shown in figure [5.19].

Figure [5.19] is very interesting. We have scaled the subhalo abundances by the volume occupied by the halos to obtain the MDFs, and so the results for the dwarf, galaxy and cluster halos are both vertically and horizontally offset from each other. There is some scatter (mainly due to Poisson errors and, in the case of the galaxy halos, variations in the size of the halos) but it appears that the MDFs are drawn from an *underlying subhalo mass function that spans the entire range in mass.*

For a speculative comparison, we show results of fitting the Sheth-Tormen halo mass function - distinct from the subhalo mass functions we have been discussing - to the simulation data presented in Jenkins et al. (2001; hereafter J2001). Although we plot this function to mass scales as low as $\sim 10^5\,\mathrm{M}_\odot$, it should be noted that neither Sheth-Tormen nor any of the other mass functions discussed in J2001 have been tested on scales below $\sim 10^8\,\mathrm{M}_\odot$. With this important caveat in mind, we note good agreement between the MDFs on cluster and galaxy scales and the Sheth-Tormen model, but find that the dwarf MDFs are higher than predicted by the fit.

The spherically averaged number density profile provides a useful measure of the spatial distribution of the subhalos and we show results for all the halos in our sample in figures [5.20(a)] and [5.20(b)].

We show number density profiles in physical units in figure [5.20(a)], noting that all the profiles are steep in the outer parts (beyond r_{200}) but turn over and become shallower at smaller radii (interior to r_{200}). Dashed lines indicate the behaviour of the smooth component of a typical dark matter halo on the appropriate mass scale, where we have assumed that the density distribution can be described by a NFW profile. There is good agreement between the profiles of the subhalos and the smooth component at $\sim r_{200}$ but the subhalo profile rapidly drops off for $r \lesssim r_{200}$, indicating that subhalos are less concentrated (or *antibiased*) with respect to the underlying smooth halo mass distribution.

The similarity of the subhalo number density profiles is highlighted in figure [5.20(b)], where we show normalised profiles. Radii have been scaled by r_{200}. The profiles are noisy

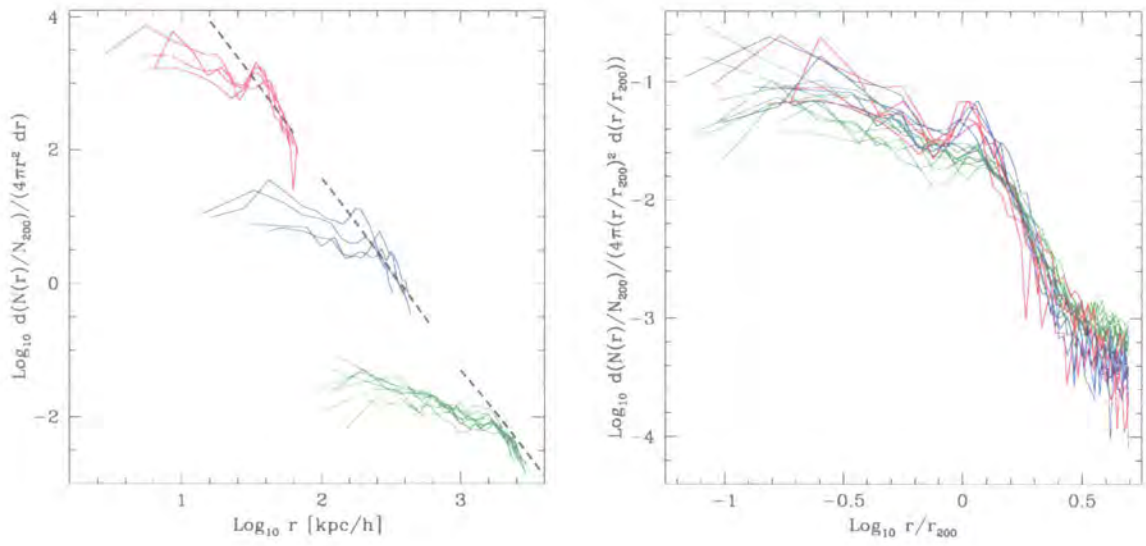

(a) Density Profiles of Substructure

(b) Density Profiles of Substructure (normalised)

Figure 5.20: **Number Density Profiles of Substructure Halos.** We show the spherically averaged number density profiles in physical units for all subhalos within r_{200} in figure [5.20(a)]. Dashed lines indicate the behaviour of the underlying halo profiles (see text). Normalised profiles are shown in figure [5.20(b)]; in this case, we include all subhalos within $\sim 3\,r_{200}$. As usual, red, blue and green curves indicate that the host is a dwarf, galaxy and cluster halo respectively.

but there are no obvious mass dependent trends in the data, leading us to conclude that the spherically averaged spatial distribution of substructure and infalling halos within $\sim 3\,r_{200}$ does not depend on the mass of the host.

The conventional measure of concentration, $c = r_{\rm vir}/r_s$, cannot be applied to subhalos because it is generally not possible to define $r_{\rm vir}$ in the dense environment of their host. Instead we choose to look at the distribution of peak circular velocities, $v_{\rm c,max}$, and the radius at which the peak occurs, $r_{\rm max}$. We expect more concentrated systems to have a smaller $r_{\rm max}$ for a given value of $v_{\rm c,max}$. As has been shown in previous studies (e.g. Ghigna et al. 1998, 2000), the peak circular velocity of a substructure halo is a robust quantity that can be used to identify the object over many orbital timescales, changing by as little as $\sim 20\%$ over several billion years during which time $\sim 80-90\%$ of the halo's mass has been lost (Ghigna et al. 2000).

We have calculated $r_{\rm max}$ and $v_{\rm c,max}$ from the simulation data for a subset of the

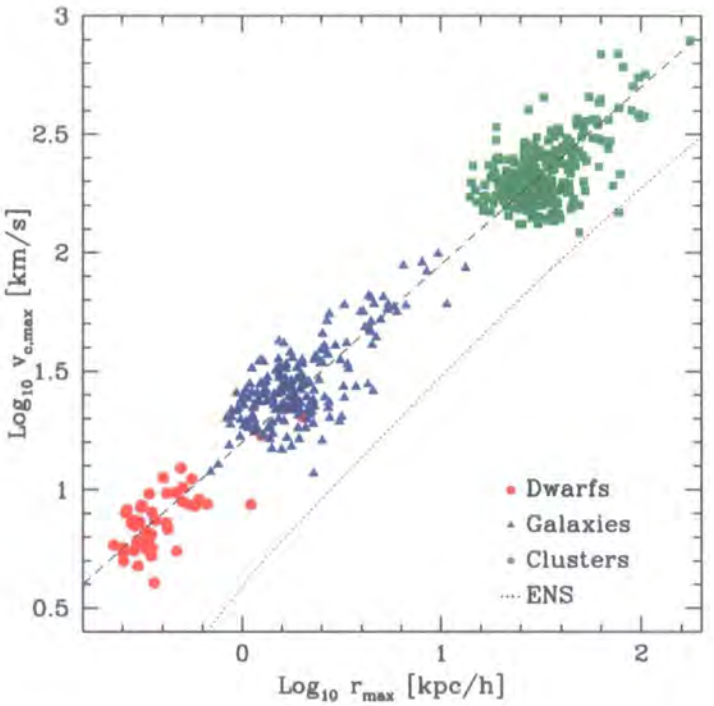

Figure 5.21: **Distribution of substructure peak circular velocities, $v_{c,max}$, and the radii at which they occur, r_{max}.** We show the distribution of peak circular velocities, $v_{c,max}$, and the radii at which they occur, r_{max}, computed for all the subhalos in our sample containing more than 500 particles, corresponding to masses of $\sim 5 \times 10^6 M_\odot$, $\sim 10^9 M_\odot$ and $\sim 3 \times 10^{11} M_\odot$ on dwarf (red asterisks), galaxy (blue filled triangles) and cluster (green filled squares) mass scales respectively. The light dotted line corresponds to the expected relation between $v_{c,max}$ and r_{max} for isolated halos if we assume that the mass distribution of halos can be described by NFW profiles with concentrations computed using the ENS prescription. The light dashed line corresponds to the mean relation measured from the simulation data.

substructure halos in our sample; for the sake of clarity, we restrict our analysis to halos resolved with more than 500 particles. These data are shown in figure [5.21], where the red asterisks represent subhalos identified in dwarf mass halos, blue filled triangles represent the population found in galaxy mass halos and the green filled squares correspond to subhalos found in cluster mass halos. For comparison, we also show the predicted distribution of $r_{\rm max}$ and $v_{\rm c,max}$ for isolated halos at $z = 0$, where we have assumed that the mass distribution can be characterised by the NFW profile, and representative concentrations are estimated using the ENS formulation (light dotted line).

The main point to note in this figure is that there is a definite trend in the data; $r_{\rm max}$ and $v_{\rm c,max}$ are strongly correlated, as we might have anticipated, with larger values of $v_{\rm c,max}$ having correspondingly larger values of $r_{\rm max}$. In other words, the more massive subhalos tend to be less concentrated than their less massive counterparts.

If we compare typical values of $r_{\rm max}$ and $v_{\rm c,max}$ for our subhalos with model predictions for isolated halos, we find that $v_{\rm c,max}$ is a factor of ~ 3.5 lower on average for a given $r_{\rm max}$ for isolated halos. This disparity indicates that subhalos with a given *bound* mass tend to be much more concentrated than their isolated counterparts with an equivalent virial mass. We expect subhalos to be tidally stripped as they orbit in the potential of their larger host, although the degree of mass loss will be sensitive to their exact trajectory. However, it has been noted that orbits are mostly radial (Ghigna et al. 1998), and so we expect tidal stripping to be very effective at removing mass from the outer parts of halos. If $r_{\rm max}$ and $v_{\rm c,max}$ are insensitive to this mass loss, it follows that the peak circular velocity of a typical subhalo with a given bound mass will tend to be greater than would be expected for an equivalent isolated halo. Therefore, when comparing the simulation data with model predictions, we should account for this discrepancy by using the concentration of the halo *before* it was tidally stripped.

5.4 Discussion

We began this chapter by raising a number of issues relating to the mass dependence of the structure, kinematics and substructure content of dark matter halos. In some cases, it was possible to draw on the findings of previous studies (e.g. NFW (1996, 1997); Cole & Lacey (1996); ENS (2001)) to help guide our understanding of the problem involved and to enable us to predict the kind of behaviour we might expect to observe. For example,

Bullock et al. (2001) and ENS (2001), building on the pioneering work of NFW (1997), developed a prescription for predicting the concentration of a dark matter halo based on its mass and the cosmogony in which it formed. In other cases, either previous work has focused on one particular aspect of the analysis (e.g. the central asymptotic slope of the spherically averaged density profile, as in the studies of Fukushige & Makino (1997) and Jing & Suto (2000)), or the analysis would not have been possible given the limited resolution of the simulations.

In order to address these issues, we have analysed a sample of twenty high resolution dark matter halos at $z = 0$ with masses ranging from $M \sim 10^{10}h^{-1}\mathrm{M}_{\odot}$, characteristic of isolated dwarf galaxy halos, to $M \sim 10^{15}h^{-1}\mathrm{M}_{\odot}$, typical of cluster mass systems. The average mass resolution has been such that we can resolve our halos with ~ 1 million particles interior to r_{200} at $z = 0$, implying that we can obtain reliable estimates of the mass distribution within the central $\sim 1\% r_{200}$.

We now discuss in some detail in the following subsections each of the issues raised in the introduction, summarising the results presented in the previous section and placing them in context with respect to previous studies.

5.4.1 The Inner Slope and Shape of the Dark Matter Density Profile

In the hierarchical paradigm, dark matter halos are assembled predominantly through a sequence of mergers interspersed with mass accretion events, and so we expect violent relaxation to be an important mechanism in shaping the global halo structure. Cosmological simulations that follow the formation and evolution of individual dark matter halos have shown that the structure is approximately isothermal, that is, $\rho(r) \propto r^{-\alpha}$ where $\alpha = 2$ in the isothermal case (see § 1.5); the density profile is shallower than isothermal ($\alpha \simeq 1 - 1.5$) in the central parts of the halo, but somewhat steeper ($\alpha \simeq 3$) at large radii (e.g. NFW (1996, 1997); Moore et al. (1998, 1999)). Indeed, the results of cosmological simulations indicate that the mass profiles of dark matter halos are *universal* (NFW (1996, 1997)), although attempts to constrain the asymptotic behaviour at small radii and high overdensities suggest some scatter in the shape in the innermost parts (e.g. Moore et al. (1998, 1999)). We briefly review these results before discussing our results from § 5.3 in the context of these previous studies.

The highly influential and widely cited studies of Navarro, Frenk & White (1996, 1997) crystallised the concept of a *universal* dark matter density profile. They used a resimu-

lation technique to follow in detail the formation and evolution of individual dark matter halos spanning several orders of magnitude in mass in a host of hierarchical cosmologies. By considering only those systems in dynamical equilibrium, they found that the shape of the density profile of a dark matter halo could be characterised, in an *average sense*, by the functional form,

$$\rho(r) = \frac{\delta_c \, \rho_{\rm crit}}{r/r_s \, (1 + r/r_s)^2} \, ; \tag{5.18}$$

they asserted that this shape is independent of halo mass, cosmological parameters and cosmogonical model. A similar result was reported by Cole & Lacey (1996), who analysed the structure of a large sample of halos forming in simulations of $\Omega = 1$ hierarchical cosmologies with scale-free (i.e. $P(k) \propto k^n$, where $n = -2, -1$ and 0) initial conditions.

However, if we apply the convergence criteria presented in chapter 2, we find that the simulations used by both NFW and Cole & Lacey are insufficient to place strong constraints on the shape of the dark matter density profile at small radii, and so these studies could not have resolved the central asymptotic behaviour of equation 5.18 (as noted by Cole & Lacey (1996) in their discussion). The best resolved halos contained between $\sim 5,000 - 10,000$ particles within the virial radius, and so applying our convergence criteria reveals that numerical effects would have compromised the structure of their halos within the central $\sim 10\% \, r_{200}$.

Subsequent higher resolution studies (e.g. Fukushige & Makino (1997, 2001, 2003); Moore et al. (1998, 1999); Ghigna et al. (1998, 2000); Jing & Suto (2000); Klypin et al. (2001)) focused primarily on the central asymptotic behaviour and paid little attention to the overall shape of the profile. In general, the simulation techniques were similar to those used by NFW, i.e. follow the formation and evolution of an individual system over a Hubble time, but particular emphasis was placed on increasing the number of particles inside r_{200} at $z = 0$ - typically of order $\sim 10^6$. According to our convergence criteria, approximately 1 million particles are required within the halo to reliably resolve its central $\sim 1\% \, r_{200}$, assuming reasonable softenings and timesteps have been used. Therefore these studies could probe the structure of dark matter halos on scales as small as $\sim 1\% \, r_{200}$.

Fukushige & Makino (1997) followed the clustering of particles within an isolated sphere centred upon a density peak in a SCDM cosmology and reported that the profile appeared steeper than the $\rho(r) \propto r^{-1}$ implied by NFW, equation (5.18)[¶]. Moore et al. (1998) resimulated two cluster mass halos ("Virgo" and "Coma") in a SCDM cosmology

[¶]Although doubts have been raised regarding their use of isolated boundary conditions.

and found that the central profile in their highest resolution run (containing over 3 million particles within r_{200}) reached an asymptotic slope $r^{-1.4}$ at $\sim 1\% r_{200}$ (c.f. $r^{-1.1}$ at the corresponding radius for a NFW profile with a concentration $c = 5$). These cluster mass halos were supplemented in Moore et al. (1999) by six high resolution Galaxy mass halos (the "Local Group"), again run in the context of the SCDM cosmological model, each of which contained ~ 1 million particles within r_{200} at $z = 0$. Based on these data, Moore et al. (1999) offered the following modified functional form for the shape of the dark matter density profile;

$$\rho(r) = \frac{\delta_c \, \rho_{\rm crit}}{(r/r_s)^{3/2} \, (1 + (r/r_s)^{3/2})} \tag{5.19}$$

Differences between this Moore et al. profile and the NFW profile (equation (5.18) only become apparent within the central $\sim 5\% r_{200}$ (c.f. § 1.5). Further studies by Ghigna et al. (1998, 2000) (both of which focused on the substructure content of high resolution cluster resimulation), Fukushige & Makino (2001, 2003) and Klypin et al. (2001) have reported good agreement between the density profiles of their simulated halos and the Moore et al. profile, equation (5.19).

On the other hand, Jing & Suto (2000) reported that the value of the central asymptotic slope appeared to depend on the mass of the halo, based on analysis of a sample of twelve high resolution dark matter halos with masses ranging from $\sim 2 \times 10^{12} - 5 \times 10^{14} h^{-1} \mathrm{M}_{\odot}$. They found that lower mass halos had steeper central slopes than more massive counterparts - at $\sim 1\% r_{200}$, they measured slopes of $-1.5, -1.3$ and -1.1 on galaxy, group and cluster masses respectively. However, as we noted in § 5.3, lower mass halos tend to have higher central densities and therefore their profiles are steeper than those of more massive halos at a fixed fraction of the virial radius. Klypin et al. (2001) reflected on Jing & Suto's findings and noted that their results were "consistent with NFW profiles" and that the apparent dependence of slope on mass was "simply a manifestation of the well-studied $c_{\rm vir}(M)$ relation".

Constraining the Inner Slope

We presented density profiles for each of our sample of dwarf, galaxy and cluster mass halos in figure 5.4. It is clear from this figure that lower mass halos have systematically higher densities within the central $\sim 10\% r_{200}$ than is the case for more massive systems; this reflects the correlation between a halo's concentration, c, and its virial mass, $M_{\rm vir}$, as

was first noted by NFW (1997). In addition, the profiles of lower mass systems are also systematically steeper.

This behaviour is highlighted in figure 5.10(a), where we plotted the variation of the logarithmic slope, $S(r)$, as a function of radius, normalised to r_{200}. If we measure $S(r)$ at, say, $1\% r_{200}$, we find that it appears to increase with decreasing virial mass - $S(r) \simeq -1.1$ on cluster scales, compared to $S(r) \simeq -1.4$ on dwarf scales. This is precisely the kind of behaviour that Klypin et al. (2001) asserted was "a manifestation of the ... $c_{\rm vir}(M)$ relation" in the Jing & Suto (2000) findings and should be borne in mind when comparing our results for the central asymptotic slope with the findings of previous studies - we *expect* the slopes of, say, dwarf and cluster mass halos to differ at a fixed fraction of r_{200}. On the other hand, if we plot the radial variation of $S(r)$ with radii expressed in units of r_s, the scale radius, as shown in figure 5.10(b), we find that, in spite of the large scatter, there is no obvious systematic difference in the logarithmic slope at a fixed fraction of r_s for different mass halos.

Previous published high resolution studies have considered the shape of the dark matter density profile in cluster and galaxy mass halos forming in the SCDM cosmogony; all have claimed to resolve the innermost $\lesssim 1\% r_{200}$ and all find steep asymptotic profiles, with $\rho(r) \propto r^{-1.4} - r^{-1.5}$, implying a logarithmic slope of $S(r) \simeq -1.4 - 1.5$. Although our simulations differ slightly in detail (insofar that we have assumed the ΛCDM cosmological model) from earlier studies, we find that our clusters generally have shallower central slopes - $\rho(r) \propto r^{-1.1}$ or $S(r) \simeq -1.1$ - while our galaxy mass halos appear to be consistent - $\rho(r) \propto r^{-1.4}$ or $S(r) \simeq -1.4$. However, $S(r)$ is a noisy quantity and so it is difficult to place strong constraints on the inner slope, even with results from a large sample of halos.

On the other hand, the maximum asymptotic slope, $\alpha(r)$, provides a more stringent constraint on the slope - it sets an upper limit to the slope of the profile at a given radius - and so we evaluated it as a function of radius in figure 5.11(a). On all mass scales, we find that the average value of α is smaller, i.e. the profile is shallower, than predicted by the Moore et al. profile - at $\sim 1\% r_{200}$, the slope can be no steeper than ~ 1.1, ~ 1.2 and ~ 1.3 on cluster, galaxy and dwarf mass scales respectively. Furthermore, the scatter in α is smaller than in the case of $S(r)$ (as we anticipated), and so *our results give us confidence to rule out the kind of steep central profiles favoured by the Moore et al. parameterisation.*

Characterising the Shape

The majority of high resolution studies have focused on constraining the shape of the dark matter density profile within the innermost parts of a halo. Provided the halo is in virial equilibrium, NFW and Moore et al. fits to the density profile at radii beyond $\sim 10\% r_{200}$ are generally indistinguishable - differences only become apparent at smaller radii. If dark matter halos can be characterised by either the NFW or Moore et al. profiles, it follows that the behaviour of the central asymptotic slope can be used to discriminate between models, in principle at least. However, there is no a priori reason to believe that the spherically averaged mass profiles of dark matter halos can be best described by either NFW or Moore et al. profiles. Indeed, it is conceivable that the shape of the profile might depend on the mass of the halo.

We investigated the shape of the dark matter density profile and its possible mass dependence in figures 5.6(a), 5.6(b) and 5.9(a). The comparatively low resolution studies of NFW (1996, 97) crystallised the concept of a universal dark matter density profile, which did not depend on the mass of the halo or the cosmological in which it formed. Subsequent higher resolution studies concentrated on the central asymptotic slope whilst seemingly tacitly assuming a universal profile. However, our results strongly suggest that *the spherically averaged mass profiles of dark matter halos are similar, independent of the virial mass of the halo.* This is demonstrated in figures such as 5.6(a), which shows our sample of density profiles scaled by their characteristic densities, ρ_{-2}, and 5.6(b), which shows the circular velocity profile scaled by the peak circular velocity, $v_{\rm c,max}$. However, it is also clear from these figures that neither the NFW nor the Moore et al. profiles can accurately describe the shape of the mean profile, and a modified mass profile should be sought instead.

Properties of this modified profile can be inferred from figures such as 5.9, which shows how the fractional deviation - $\Delta \log \rho$ - between the best fitting models and the measured profiles varies as a function of radius. Fits to the density profile (ρ-fits) generally performed much better at intermediate-to-large radii - $\Delta\rho/\rho \lesssim 10\%$ for $r \gtrsim 10\% r_{200}$) - compared to corresponding fits to the circular velocity profile (v_c-fits), which found $\Delta\rho/\rho \sim 20\%$ for $r \gtrsim 5\% r_{200}$. In contrast, v_c-fits performed much better with the central $\sim 10\% r_{200}$.

This suggests that both the NFW and Moore et al. parameterisations provide a good fit to the density profiles of simulated dark matter halos for $r \gtrsim 5 - 10\% r_{200}$. However,

the differences in the performance of ρ- and v_c-fits indicate genuine shortcomings on the part of the parameterisations in describing the structure of high resolution halos on scales $\sim 1\% r_{200}$. A modified profile that could plausibly describe all of our halos should exhibit less "curvature" (i.e. the rate of change of the slope should be lower) than either NFW or Moore et al. . A possibility is the profile proposed by Taylor-Navarro (2001) with a logarithmic slope given by the expression

$$S(r) = \frac{0.75 + 2.625\, x^{1/2}}{1 + 0.5\, x^{1/2}}. \tag{5.20}$$

This expression was deduced by assuming that the phase space density can be approximated as a power law - $\rho/\sigma^3 \propto r^{-\alpha}$ - and using the solution of the second Jeans equation to determine the power law exponent, α. One might also consider "fleshing out" the sample of halos on dwarf and galaxy mass scales and test a variety of analytical formulae on the average curves. Perhaps a simple modification of the NFW profile will suffice?

5.4.2 The Relationship between Mass and Concentration

As we mentioned earlier, we expect a halo's central density and consequently its concentration to increase with decreasing halo mass. This correlation, evident in the density profiles of figure 5.4, was first noted by NFW (1997) and reflects the relationship between concentration and the mean density of the universe at the redshift of collapse. Attempts have been made to construct a physically motivated model that can predict both the mass and redshift dependence of this relation, most notably by NFW (1997), Bullock et al. (2001) and ENS (2001).

The NFW (1997) and Bullock et al. (2001) prescriptions are similar in spirit - they relate the amplitude of the power spectrum to concentration - but differ in their exact implementation. Both methods require two free parameters; one to derive a characteristic collapse epoch for some fixed fraction (adjustable parameter) of the halo mass at z, the other to relate this collapse epoch to a characteristic density (or concentration). On the other hand, the ENS (2001) formulation constrains the concentration by using both the amplitude and the shape of the power spectrum. This method requires a single free parameter, which relates an effective amplitude for the power spectrum on a scale M, incorporating both the amplitude and shape, to the collapse epoch via a free parameter; this collapse epoch can then be used to derive the concentration from known cosmological parameters.

We have investigated our simulation data for the expected trend with mass and compared the results with the predictions of these models. Recall figure 5.8 in which we show how concentrations (c_{200}) and characteristic overdensities (δ_c) derived from best NFW and Moore et al. fits to the data vary as a function of virial mass. It is clear from this figure that there is a trend, with lower mass halos having higher *fitted* concentrations on average than their more massive counterparts, as expected. Based on these results, we conclude that typical dwarf and cluster mass halos forming in a ΛCDM cosmology have NFW concentrations at $z = 0$ of $c \simeq 12$ and 5 respectively. However, we note that the data do show a large *rms* scatter and we find that concentrations on a given mass scale can vary by as much as a factor of ~ 2. Although the masses of halos on a particular mass scale can vary by as much as a factor of ~ 3, we do not expect the concentration to differ by more than $\sim 5\%$ on dwarf galaxy scales and $\sim 40\%$ on cluster scales. However, we note that the masses of our dwarf halos differ by at most 20% but concentrations differ by as much as a factor of 2.

These results are consistent with the findings of Klypin et al. (2000), who considered the formation of four high resolution ΛCDM galaxy halos with virial masses of $M \sim 10^{12}h^{-1}\mathrm{M}_{\odot}$, and found NFW concentrations between $\sim 8 - 13$. We agree with Klypin et al. (2001) and conclude that the scatter in concentrations reflects real differences in the merging histories of their halos.

We also note that our data appear to favour the ENS rather than the Bullock et al. prescription for halo concentrations. The Bullock et al. $c_{\mathrm{vir}} - M_{\mathrm{vir}}$ relation appears to be too steep relative to the mean of the data, overestimating it on dwarf scales and underestimating it on cluster scales. In contrast, the ENS relation predicts a concentration that is consistent with the mean on dwarf and galaxy scales, if a little too high ($\sim 20\%$) for cluster masses.

5.4.3 Halo Kinematics

We have determined the radial variation of the spherically averaged radial velocity (v_r) and velocity anisotropy (β) and evaluated the dimensionless spin parameter (λ) for each of the halos in our sample. The results have proven to be quite interesting, with some very real differences apparent in the kinematics of material in the peripheries and surrounding environs of halos on different mass scales.

If we consider the average behaviour of the radial velocity profile on a given mass scale

(c.f. figure 5.12), dark matter halos are dynamically stable - in the sense that $v_r \simeq 0$ - within $r \lesssim r_{200}$, irrespective of mass. On the other hand, we see real differences between masses beyond r_{200}; there is a well defined trough in v_r at $\sim 2\,r_{200}$ - $|v_r|_{\rm max} \simeq 0.5\,V_{200}$ or $\sim$ 500 km/s- on cluster mass scales, indicating strong mass infall; a dip in v_r at $\sim 2\,r_{200}$ (equivalent to $0.1\,V_{200}$ or $\sim$ 20 km/s) on galaxy mass scales; and little or no mass infall on dwarf scales. By $\sim 6\,r_{200}$, the average v_r of material surrounding the halo has started to climb steeply as it joins with the Hubble flow.

Complementary information was gleaned from the average behaviour of the velocity anisotropy profile, $\beta(r)$ (c.f.figure 5.13). In this case, both galaxy and cluster mass halos exhibit similar behaviour - a steady rise in $\beta(r)$ with radius, indicating that particle orbits are initially close to isotropic within the centres of the halos but become gradually more eccentric with increasing radius. A similar result was reported by Tormen et al. (1998) in their analysis of nine *medium resolution* cluster mass halos forming in a SCDM[‖] cosmology. However, although our dwarf halos show an initial rise in $\beta(r)$ within the central $\sim 10\%\,r_{200}$, the profiles then flatten off before turning over close to r_{200}, at which point $\beta < 0$, indicating that particle orbits are predominantly tangential (or *circular*) in the outer parts and surrounding environs. This peculiar behaviour in $\beta(r)$ is consistent with our observation that dwarf halos experience negligible mass infall.

The values for the dimensionless spin parameter, λ, (illustrated in figure 5.3.2) confirm earlier findings and show that dark matter halos are supported by anisotropy pressure, irrespective of mass scale. We find that the median value on dwarf and galaxy mass scales is $\lambda_{\rm med} \simeq 0.035$ and slightly lower for cluster masses ($\lambda_{\rm med} \simeq 0.027$), but with a large rms scatter for all masses ($\sim 0.02 - 0.03$). These values for the galaxies and dwarfs are in reasonable agreement with previous studies, but the clusters appear to be slightly lower than reported. For example, Cole & Lacey (1996) found a median value of $\lambda_{\rm med} \simeq 0.04$) in their simulations of a scale-free cosmogony and noted a weak trend in their data for lower λ at higher halo mass. More recently, Vitvitska et al. (2002) found in high resolution simulations run in the ΛCDM cosmology that $\lambda_{\rm med} \simeq 0.044$.

[‖]The power spectrum used in these simulations mimicked that of CDM in relevant scales

5.4.4 Halo Shapes

The results of § 5.3.3 indicate that the mass distribution within the virial radius of a typical dark matter halo forming in the ΛCDM cosmology can be approximated by series of concentric triaxial ellipsoidal isodensity shells. We have used a method similar in spirit to that used by Jing & Suto (2002) and described in § 4.3.3 to isolate these isodensity shells and to determine their axis ratios by diagonalising the moment of inertia tensor of material in these shells.

We found that isodensity surfaces in dwarf galaxy halos at $z = 0$ (c.f. figure 5.15) are regular and axisymmetric when compared with those of larger mass halos at similar overdensities (c.f. figure 5.16). In particular, we found that the cluster mass halos in our sample showed significant departures from axisymmetry at low overdensities (i.e. close to r_{200}), as we might expect from systems that have recently formed.

Estimates of the axis ratios of a series of thin isodensity shells within r_{200} indicate that the axis ratios of both dwarf and galaxy mass halos decrease with increasing overdensity (i.e. decreasing radius). We saw in figure 5.17(a) that, on average, b/a (c/a) falls from ~ 0.85 (~ 0.7) at $\sim r_{200}$ to ~ 0.8 (~ 0.6) at $\sim 5\% r_{200}$ for dwarf galaxy halos, and from ~ 0.75 (~ 0.65) at $\sim r_{200}$ to ~ 0.75 (~ 0.6) at $\sim 5\% r_{200}$ for galaxy halos. On the other hand, b/a (c/a) rises from ~ 0.65 (~ 0.5) at $\sim r_{200}$ to ~ 0.7 (~ 0.6) at $\sim 5\% r_{200}$ for cluster mass halos. These results suggest that isodensity shells in the centres of typical cluster mass halos are *rounder* than those found on the peripheries, whereas both dwarf and galaxy mass halos become slightly flattened.

Furthermore, an "average" dwarf galaxy halo can be described as an oblate spheroid, in contrast to an "average" galaxy or cluster mass halo, which are more appropriately described as prolate spheroids. This result is in good agreement with the conclusion drawn from the distribution of axis ratios (b/a against c/b), which shows that the isodensity surfaces in galaxy and cluster mass halos are preferentially prolate whereas the dwarfs are as likely to be prolate as oblate.

How do these results compare with the conclusions drawn from previous work? Several studies have analysed the shapes of a statistical sample of dark matter halos drawn from large cosmological simulations. Frenk et al. (1988) examined the structure of their best resolved halos forming in the SCDM model and found that these systems were generically triaxial with a mean $c/a \simeq 0.5$, but with a slight preference for prolate configurations.

They also reported a weak tendency for the innermost parts of their halos to be more spherical than their outer parts. Both Warren et al. (1992) and Cole & Lacey (1996) investigated the shapes of halos forming in a scale-free cosmology; Warren et al. (1992) noted that halos tended to be more prolate than oblate with a mean $c/a \simeq 0.5$ at small radii, and that they became rounder with increasing radius. Similarly, Cole & Lacey (1996) found that halos were generically triaxial with a slight preference for prolate configurations, with average values for the axis ratios of $b/a \simeq 0.8$ and $c/a \simeq 0.6$ at the virial radius of the halo (which they defined to be r_{178}). In common with Frenk et al. (1988) but in contrast to Warren et al. (1992), they found that halos became gradually more elongated with increasing radius. Thomas et al. (1998) analysed the internal structure of halos forming in simulations of four different CDM cosmologies and reported a mean c/a that varied between 0.43 and 0.5, decreasing in the high-Ω runs.

On the other hand, Dubinski & Carlberg (1991) analysed the structure of halos forming in high resolution simulations that followed the collapse of individual isolated density peaks. The objects that formed were found to be strongly triaxial, generally more prolate than oblate, and with average axis ratios of $b/a \simeq 0.71$ and $c/a \simeq 0.5$ at $\sim 50\% r_{200}$. In contrast with Frenk et al. (1988) and Cole & Lacey (1996), they reported a tendency for halos to be more *elongated* in their centres.

Most recently, Jing & Suto (2002) have analysed a sample of twelve high resolution simulations ($\sim 10^6$ particles inside r_{200}) of galaxy, group and cluster mass halos and found average axis ratios of $b/a = 0.74$ and $c/a = 0.58$ measured at a shell overdensity of $\rho_s = 2500$ ($\sim 20\% r_{200}$). They also noted that, on average, the axis ratios of their halos decreased with increasing overdensity - in other words, the centres of their halos are more elongated than their outer parts.

If we compare our results with those of Jing & Suto (2002), with whom we differ only in the fact that we have split our sample of halos according to mass, we find essentially no difference in the conclusions reached. Averaging the results for all of the halos, we find $b/a \simeq 0.75$ and $c/a \simeq 0.57$ at a shell overdensity of $\rho_s = 2500$, in excellent agreement with Jing & Suto's values of $b/a \simeq 0.78$ and $c/a \simeq 0.54$. Furthermore, we also find that the axis ratios decrease with increasing overdensity and the functional form for this variation proposed in Jing & Suto (2002) fits our data well.

On the other hand, we note that our results are in good quantitative agreement with those of Dubinski & Carlberg (1991), and in reasonable qualitative agreement with those

of Warren et al. (1992). Cole & Lacey (1996) reported axis ratios that are in very good agreement with ours. However, Frenk et al. (1988) and Cole & Lacey (1996) found that their best resolved halos (containing $\sim 10^3$ particles within the virial radius) became rounder with decreasing radius, contrary to our own conclusion that they should become more elongated. While it is possible that this discrepancy reflects differences in the precise methods used to determine shapes, it is more likely that they have been compromised by limited numerical resolution.

5.4.5 Dark Matter Substructure

High resolution studies of individual galaxy and cluster dark matter halos such as those of Moore et al. (1999) and Klypin et al. (1999) have indicated that the substructure content of these systems appears strikingly similar. The results of the previous section would appear to reinforce this basic picture; dwarf, galaxy and cluster mass halos contain similar amounts of substructure - of order $\sim 10\%$ of the virial mass of the halo - with no significant differences in the mass and spatial distributions of the subhalos when suitably normalised.

Unfortunately there have been few detailed, systematic studies of the global properties of substructure halos with which we may compare our results. This is partly because of the significant implications of the "substructure problem" (that is, the apparent overabundance of substructure halos in CDM halos relative to the observed satellite population of our own Galaxy (c.f. Moore et al. (1999), Klypin et al. (1999)); partly because of the computational expense involved (such simulations require of order several million particles); and partly because of uncertainties relating to the impact of numerical resolution on subhalo properties (although see chapter 3).

The "substructure problem" has spawned a cottage industry; some studies focused on quenching star formation and producing a population of "dark" satellites (e.g. Benson et al. 2001, Somerville 2001); others modified the dark matter physics, seeking to suppress the formation of, or disrupt, the putative subhalos (e.g. Moore et al. (2000), Yoshida et al. (2000)); whilst others sought to reconcile theory and observations by claiming that the comparison between simulations and data on which the original claims were based were misleading (e.g. Font & Navarro (2001), Stoehr et al. (2002)).Issues relating to numerical resolution and its impact on substructure - in particular, the "overmerging problem" (c.f. chapter 3) - have been investigated generally in idealised studies by, e.g. , Moore et al. (1996), Tormen et al. (1998), Klypin et al. (1999), Hayashi et al. (2002) and Ghigna et

al. (2000), and in the SCDM cosmology by Ghigna et al. (1998), who also investigated the convergence of these properties with increased mass and force resolution.

We have used our simulations, which have a typical mass and force resolution comparable to those of Ghigna et al. (1998), to investigate the properties of dark matter substructure in halos forming in the ΛCDM cosmology and to determine whether these properties might depend on mass. We decided to restrict our study to the examination of a few choice "global" measures of the subhalo population. In particular, we have considered the fraction of a halo's mass bound to substructure (m_f), the distribution of subhalo masses (MDF), the spherically averaged spatial distribution ($n(r)$) and the subhalo's concentration, as inferred from the $v_{c,max} - r_{max}$ relation. The main findings of our results are discussed below.

- **The Bound Mass Fraction** Previous studies, such as Tormen et al. (1998), Moore et al. (1998) and Ghigna et al. (1998,2000), have led us to expect a bound mass fraction of about 10%, although factors such as the underlying cosmological model and merging history will affect the precise value. We found that m_f ranged between $\sim$ 2% and $\sim$ 12%, with a weak trend for less massive hosts to have lower values of m_f; the median value of dwarf scales is $\sim 4\% M_{200}$, compared to $\sim 8\% M_{200}$. However, there is an appreciable scatter in the data, with 1σ deviations on dwarf and cluster mass scales of $\Delta(\log m_f) \sim 50\%$ and $\sim 30\%$ respectively. Subhalo mass fractions will be affected by the intrinsic spread in formation times, detailed merging histories and, to a lesser extent, the orbital distribution of the substructure**.

- **The Subhalo Mass Function** We have found that the mass function of subhalos can be well described by a power law, $dn/dM \propto M^{-\alpha}$, with $\alpha \simeq 2$, irrespective of the virial mass of the host. This result is in excellent agreement with that of Ghigna et al. (2000) for a galaxy cluster forming in the SCDM cosmology. The similarity also highlights that the "substructure problem" (if there is one) on galaxy mass scales is just as serious on dwarf galaxy scales, and suggests that even the smallest dark matter halos will possess an abundance of substructure.

  We note also that the MDFs of individual halos appear to be drawn from an underlying power law distribution whose logarithmic slope is similar to that of the general *universal* halo mass function described in Jenkins et al. (2001), although we stress

**Indeed, it can be affected by a change in numerical resolution (see chapter 3), but we do not expect this to be important in this instance, given the number of particles used.

that we have extrapolated the Jenkins et al. mass function shown in figure 5.19 below the mass limit ($\sim 10^8\,M_\odot$) used in that particular paper.

- **The Spatial Distribution of Subhalos** Measurements of the spatial distribution of subhalos in all the halos in our sample indicate that substructure is spatially antibiased with respect to the underlying smooth dark matter component of the halo at $z = 0$. This is apparent in the spherically averaged number density profiles, shown in figure 5.20, in which it is apparent that the ratio of the number density of halos to dark matter particles in spherical shells falls rapidly within $r \lesssim r_{200}$. This corresponds to the definition of the bias parameter, $b(r)$, introduced in Ghigna et al. (2000). The cluster number density profiles appear a little flatter than either the galaxy or dwarf profiles, but this simply reflects that differences between the kinematics of the subhalos and the underlying dark matter are negligible - 3-d velocity dispersion supports the shape of the density profile, and both the halos and dark matter particles have similar velocity dispersions.

- **Subhalo concentrations** The $v_{c,max} - r_{max}$ relation contains important information about how concentrated halos are and can, in principle, help to discriminate between various mass profiles. We have found that, for a given value of r_{max}, $v_{c,max}$ is greater than we might expect for an isolated halo with a similar r_{max} at $z = 0$. This is equivalent to Ghigna et al. 's observation that halos in their SCDM galaxy cluster had higher concentrations than those in the field (Ghigna et al. (1998)).

  Subhalos are tidally stripped as they orbit in the dense environment of their host. Ghigna et al. (1998) noted that subhalos follow very eccentric orbits (with an apo-to-pericentre ratio of $\sim 6 : 1$) and so we expect them to experience significant mass loss at each pericentre. If it is the case that r_{max} and $v_{c,max}$ are robust quantities in spite of this mass loss - Ghigna et al. (2000) suggest that they are - we expect these halos to appear more concentrated than a "field" halo with an equivalent mass.

5.5 Conclusions

The main conclusions of this chapter can be summarised as follows;

- **Cuspy dark matter density profile appear to be a generic prediction of the CDM model.** All of the halos in our sample have divergent central densities. We

have determined the maximum possible slope of the density profile at the innermost believable radius, which is typically $\sim 1\% r_{200}$, and find median values of ~ -1.3, ~ -1.2 and ~ -1.1 on dwarf, galaxy and cluster masses respectively. The scatter is small with a typical 1σ deviation of $\sim 10\%$. The fact that lower mass halos are steeper at a fixed fraction of the virial radius is merely a manifestation of the $c_{\rm vir}(M)$ relation, as becomes apparent when we normalise radii by the scale radius, r_s. We conclude from our results that **steep profiles of the type described by the Moore et al. parameterisation can be ruled out.**

- **The shape of the spherically averaged mass profile of high resolution dark matter halos appears to be independent of virial mass.** We have demonstrated that, when appropriate scalings are found, the spherically averaged density and circular velocity profiles of halos spanning several orders of magnitude in mass are very similar. However, it would appear that **neither the NFW nor the Moore et al. profiles fully capture the details of this shape.**

- We confirm the results of previous studies (e.g. NFW 1997, Bullock et al. 2001, ENS 2001) that found that **concentrations of dark matter halos are correlated with virial mass.** Typical NFW concentrations at $z = 0$ for halos forming in the ΛCDM cosmology range from $c_{200} \simeq 12$ on dwarf galaxy scales, $c_{200} \simeq 8$ on galaxy scales to $c_{200} \simeq 4$ on cluster mass scales. However, there is a **scatter in concentration on any given mass scale**, which probably reflects differences in the formation times and detailed merging histories of individual halos. We find a 1σ variation of $\Delta(\log c_{200}) \sim 0.25, 0.3$ and 0.2 on dwarf, galaxy and cluster mass scales respectively.

- We have found that *average* **dark matter halos are dynamically stable systems**, as indicated by $\overline{v_r} \simeq 0$ within r_{200}, irrespective of virial mass. Particle orbits are initially close to isotropic, that is, $\sigma_t^2 \simeq 2\,\sigma_r^2$, but become more eccentric (or radial) with increasing radius. Close to r_{200}, **genuine differences between dwarf mass halos and galaxy and cluster mass systems** become apparent. The orbits of particles in galaxy and cluster mass halos continue to become more eccentric with radius ($\beta(r) \to 1$) out to and beyond r_{200}, while particle orbits in dwarfs remain mildly radial for radii $0.3\,r_{200} \lesssim r \lesssim r_{200}$ before rolling over and becoming predominantly tangential at $r \simeq r_{200}$. This result is consistent with our observation that **dwarf galaxy halos experience little or no mass infall** whereas material

surrounding both galaxy and cluster halos show clear signs of infall.

- Typical dark matter halos can be approximated as **triaxial ellipsoids**, irrespective of virial mass. If we separate our sample according to mass, we find that our dwarf and galaxy mass halos become more elongated with increasing overdensity (or decreasing radius), whereas the change in shape of clusters is negligible. On average, dwarf galaxy halos are oblate, whereas galaxy and cluster mass halos are prolate.

- All of the halos in our sample contain substantial amounts of substructure, with a **typical bound mass fraction of order** $\sim 10\% M_{200}$**, irrespective of the virial mass of the host**, although there is a weak trend for more massive halos to have slightly higher mass fractions than their lower mass counterparts. On a given mass scale, we have found appreciable scatter with a 1σ deviation in mass fraction which varies between $\Delta(\log m_f) \sim 20\%$ and 30% on cluster and galaxy masses respectively. The **mass distribution function of subhalos can be characterised by a power-law**, $dn/dM \propto M^{-\alpha}$, with $\alpha \simeq 2$, which applies equally well on all mass scales. The number density of subhalos decreases rapidly with respect to the underlying smooth component of the dark matter halo within r_{200}, that is, **subhalos are spatially antibiased with respect to the dark matter**.

Chapter 6 | *Conclusions*

The Cold Dark Matter model has proven to be an impressively successful framework within which cosmological structure formation can be understood. Although the precise details of the model have changed over the last twenty years - the critical density Standard CDM model was dispelled in favour of the low matter density ΛCDM model - the basic premise, that the dominant contribution to the matter component of the Universe comes from non-baryonic Cold Dark Matter, remains. Many of the predictions of the ΛCDM model are in excellent agreement with a number of key observations, as highlighted in chapter 1. However, the model's impressive successes on large ($\gtrsim$ Mpc) scales must be qualified by the challenges it has encountered on small ($\lesssim$ Mpc) scales, in the centres of galaxies.

As we noted in Chapter 1, the structure of the innermost parts of galactic dark matter halos should be sensitive to the nature of the dark matter, and observational constraints on this structure should provide crucial evidence that can be used to establish the validity of the CDM paradigm. Divergent central halo densities are a generic prediction of all Cold Dark Matter models (Navarro, Frenk & White (1997)) (hereafter NFW); high resolution cosmological simulations make the robust prediction that *simulated* dark matter halos forming in CDM cosmologies have central density cusps, which asymptotically approach $\rho \propto r^{-\alpha}$ where $1 \lesssim \alpha \lesssim 1.5$ at progressively smaller radii (e.g. NFW (1996, 1997), Moore et al. (1998, 1999), Ghigna et al. (1998, 2000), Jing & Suto (2000), Klypin et al. (2001)).

This prediction would appear to be in stark contrast with results derived from high resolution rotation curve studies of nearby dark matter dominated dwarf and low surface brightness (LSB) galaxies, which suggest that *real* dark matter halos have finite central density cores (e.g. de Blok et al. (2001a), Bolatto et al. (2002), Weldrake et al. (2003), Simon et al. (2003)). Although some authors have found that, even with high spatial resolution, the data are insufficient to discriminate between cuspy halos of the kind predicted by CDM and halos with finite central densities (Swaters et al. (2000)), others are more strident and argue that the disparity between observations and simulations signals a fundamental flaw in the CDM model.

However, as stressed in Chapter 1, it would be premature to discard CDM without fully investigating the predictions of the model on the relevant mass scales and questioning the validity of assumptions that are made when comparing these predictions with observations. Recent studies by Swaters et al. (2003), de Blok et al. (2003) and Weldrake et al. (2003) have examined the sensitivity of results of mass decomposition of rotation curves to systematic errors made in observations and assumptions made in constructing mass models, but we note that these studies offer conflicting results.

In contrast, the results presented in chapter 2 indicate that we now have a good understanding of the impact our choice of numerical parameters can have on the mass distribution of simulated CDM halos. We found that, provided the gravitational softening is chosen such that particle discreteness effects are negligible, we can reproduce the spherically averaged circular velocity to better than 10% accuracy at radii where

- the timestep is much shorter than the local orbital timescale;
- the accelerations do not exceed a characteristic acceleration imprinted by the gravitational softening;
- enough particles are enclosed so that the collisional relaxation timescale is longer than the age of the universe.

In particular, we found that it is the number of particles that offers the most stringent criterion for convergence; of order $\sim$ 1 million particles are needed to resolve the kind of overdensities ($\sim 10^6$) that we expect to measure at $\sim 1\% r_{200}$.

These convergence criteria have allowed us to provide a sample of high resolution simulations of dark matter halos with masses $M \sim 10^{10} M_{\odot}$, comparable to those of dwarf galaxy halos, forming in the ΛCDM cosmology. The mass and force resolution of these simulations has been sufficient to reliably resolve the spherically averaged mass profile within the central few kiloparsecs of the halos and can, in turn, be used to accurately predict the shape of the dark matter rotation curve on sub-kiloparsec scales, $\sim 1\% r_{200}$.

We have performed extensive analysis of the structure and kinematics of our sample of dwarfs, paying particular attention to variations with redshift (in chapter 4) and mass (in chapter 5). The principal results of this analysis can be briefly summarised as follows;

- The median redshift of formation of our sample of dwarf galaxy halos is in good agreement with the predictions of extended Press Schechter theory for a ΛCDM

cosmology (Chapter 4).

- Cuspy dark matter density profiles are a robust prediction of the CDM model on all mass scales (Chapters 4 and 5).

- When suitably scaled, the shape of the spherically averaged mass profile of high resolution dark matter halos appears to be independent of virial mass and redshift (Chapter 5).

- However, it would appear that neither the NFW nor the Moore et al. profiles fully capture the details of this shape (Chapters 4 and 5).

- Furthermore, steep central profiles of the type favoured by the Moore et al. model can be ruled out (Chapters 4 and 5).

- We find genuine differences in the spherically averaged kinematics of our dwarf halos when compared to more massive systems at $z = 0$; dwarf galaxy halos experience little or no mass infall, and particle orbits are preferentially tangential in the outer parts of the halos, close to r_{200}. This is in marked contrast with the behaviour of more massive systems - both galaxy and cluster mass halos show clear signs of mass infall, and particle orbits become increasingly radial with increasing radius (Chapter 5).

- The isodensity shells of dark matter halos can be well approximated as triaxial ellipsoids, independent of virial mass. Dwarf and galaxy mass halos become increasingly elongated as we probe smaller radii, whereas the change in shape of clusters is negligible. On average, dwarf galaxy halos are oblate, whereas galaxy and cluster mass halos are prolate (Chapter 5).

- Dark matter halos contain a substantial amount of substructure. Typically, $\sim 3 - 10\%$ of a halo's virial mass is bound to substructure halos although there is a weak trend for more massive halos to have slightly higher mass fractions than their lower mass counterparts. We also note that the mass fraction increases with increasing redshift, and that there appears to be a correlation with the merging activity of the parent halo (Chapters 4 and 5).

- The mass distribution function of subhalos can be characterised by a power-law, $dn/dM \propto M^{-\alpha}$, with $\alpha \simeq 2$, which applies equally well on all mass scales (Chapter 5).

- We find that the gravitational potential of dwarf galaxy halos at $z \simeq 0$ is both symmetric and stable. Such a stable, symmetric gravitational potential enhances the probability that these halos can support closed, non-intersecting orbits of the kind required for a gaseous disk to form and survive. By exploring the phase space of simulated CDM halos, we can constrain the kind of rotation curves we might expect to measure if real dark matter halos can be described by the structures we find in simulations. Needless to say, this is an interesting avenue for further study (Chapter 4).

These results are of obvious theoretical interest - but what of their astrophysical implications? In particular, what bearing will these findings have on the validity of the ΛCDM model?

One of the key motivating factors for this thesis was the desire to place robust constraints on the distribution of dark matter in dwarf galaxy halos on scales that could be directly compared with observational data, such as those derived from rotation curve studies. To this end, the results extend the findings of earlier studies such as NFW (1996, 97) and Moore et al. (1999)) by showing that the mass profiles of dwarfs are similar to those of higher mass halos, and establish conclusively that *the density profiles of CDM halos are cuspy.* Therefore, we might conclude that the discord that has existed between theory and observation, as originally highlighted by Flores & Primack (1994) and Moore (1994), has been exacerbated. Comparison is no longer constrained by finite numerical resolution (chapter 2) or uncertainties about the structure of halos on the relevant mass scales (chapters 4 and 5), suggesting that the disparity signals a genuine "small scale" crisis for the CDM paradigm.

Such a straightforward interpretation implicitly assumes that the mass profiles inferred from rotation curve studies of dark matter dominated systems constitute a true reflection of the underlying halo's mass distribution. However, as we noted earlier, there is sufficient disagreement between different authors about the ability of high resolution rotation curve data to discriminate between cuspy profiles and profiles with finite central densities (e.g. Swaters et al. (2003); de Blok et al. (2003)) to question this assumption. Furthermore, Hayashi et al. (2003a) recently performed an analysis of overlapping data drawn from de Blok et al. (2001a), de Blok & Bosma (2002) and Swaters et al. (2003) and find that $\sim 2/3$ of LSB galaxies are consistent with circular velocity profiles expected of CDM

halos. Although the remaining $\sim 1/3$ appear to be incompatible with CDM's predictions*, these authors argue that the discrepancies simply reflect differences between the circular velocity and gas rotation speed that are likely to arise in gaseous disks embedded within triaxial CDM halos.

Nevertheless, let us assume that the inferred dark matter profiles represent an accurate reflection of the underlying halo mass distribution. In this case, it seems reasonable to question whether or not the structure of the dark matter halo could have remained unaffected - effectively decoupled - from the baryons during the formation history of the galaxy. Astrophysical processes, such as gravitational scattering by black holes (e.g. Merritt & Cruz (2001), Milosavljevic & Merritt (2001)) and the transfer of angular momentum between a stellar bar and the dark matter halo (Weinberg & Katz (2002)) may lower the central dark matter density, but it has been argued that these effects are incompatible with observations (e.g. Merritt & Milosavljevic (2002), Sellwood (2003)) or are unlikely to be important in dark matter dominated systems. However, it is difficult to discount at present the possibility that *some* astrophysical process could effectively erase the dark matter cusp.

Recently, Dekel et al. (2003, 2003a) have argued that efficient energy injection into the progenitor clumps during the hierarchical assembly of a halo could potentially result in a dark matter halo with a core in the mass distribution at the present day, based on their consideration of the tidal disruption and compression of subhalos. As yet, there is little work in the literature exploring how altering the structure of progenitors early in the merging hierarchy will impact on the structure of the final halo (see Merritt & Cruz (2001) for an example), but the most plausible mechanisms require the inclusion of baryons.

In other words, it seems clear that we require a deeper understanding of both the finer details of galaxy formation and the strength of the coupling between the dark matter and baryons before we can *confidently* predict the form of the mass profile on the scales observed in dark matter dominated systems †.

*Their rotation curves feature a transition between the rising and flat parts that appears to be too sharp.

†Such a sentiment echoes that of James Binney at the recent IAU meeting (Sydney, July 2003) on "Dark Matter in Galaxies" (Binney (2003)).

On the other hand, there is a signature of a CDM halo's structure that can be reliably constrained observationally, measured in high resolution N-body simulations, and that can, in principle, allow us to determine whether the ΛCDM model is a valid one - namely, the shape of a halo's dark matter distribution. There exist a variety of dynamical tracers that can be used to probe the distribution of dark matter through its gravitational potential in our own Galaxy and others; streams of stellar debris stripped from tidally disrupted satellite galaxies whose orbits are decaying; "polar" rings of neutral HI; warps in both the stellar and gaseous disks. Furthermore, the advent of instruments sensitive enough to detect galaxy-galaxy lensing will allow a direct measurement of the shape of the dark matter distribution in the halo.

As noted by Merrifield (2003), there is sound observational evidence to suggest that galaxy and cluster mass halos are triaxial, in good agreement with the predictions of CDM (e.g. Dubinski & Carlberg (1991), Warren et al. (1992)). Alternatives such as Warm Dark Matter are predicted to produce rounder halos than those that form in CDM cosmologies (e.g. Bullock (2001b)), while theories that modify gravity, such as MOND, predict perfectly spherical halos (Sellwood (2003)). The results presented in this thesis are consistent with the findings of previous studies and as such are consistent with observations.

In summary, it is not clear whether the key prediction of this thesis - that the mass profiles of dwarf galaxy halos are similar to those of more massive systems when suitably scaled - can be used to discount the ΛCDM model on the basis of the discord between mass profiles derived from rotation curve studies and those measured in high resolution simulations. However, it is clear that we require a more detailed understanding of galaxy formation if we wish to confidently predict the mass distribution on those scales where baryons dominate the dark matter. Until such a theory exists, we should seek alternative measures of halo structure that are sensitive to the nature of the dark matter, for example, the shape of the mass distribution, as discussed. Such explorations shall constitute the basis of future work.

"It is alright, everything is alright, the struggle is finished, and I have won the victory over myself...".

Appendix A

The Generation of Cosmological Initial Conditions

A.1 The Generation of Cosmological Initial Conditions

Periodic boundary conditions are usually adopted in cosmological simulations for reasons of convenience. The assumption of periodicity implies that the simulation volume as a whole has to have precisely the mean density, a requirement that places restrictions on the size of the region and on the redshifts at which a particular simulation may be considered reliable. On the other hand, with periodic boundaries the density field can be expanded as a sum over a discrete set of periodic plane waves. For a simulation volume which is cubic, the Fourier transform of the density field has the form of a cubic grid in Fourier space. The discrete nature of the power spectrum thus makes it easy to set up Gaussian density fields.

The aim of our initial conditions generating procedure is to provide a particle realisation of a Gaussian density field with the chosen power spectrum, $P(k)$, on scales and at redshifts where linear theory is applicable. Our procedure follows closely that described in Efstathiou et al. (1985), where further details may be found. As in Efstathiou et al. (1985), we use the Zel'dovich approximation to perturb particles from a uniform cubic grid,

$$\mathbf{x}(t) = \mathbf{q} - b(t)\psi(\mathbf{q}), \tag{A.1}$$

where $\mathbf{x}$ is the comoving Eulerian coordinate of the particle, $\mathbf{q}$ is the Lagrangian coordinate denoting the particle's unperturbed position in the grid, $b(t)$ is the linear growth factor, and ψ is a function that describes the spatial structure of the density field. The function

ψ can be expressed in terms of the acceleration field at time t,

$$\psi(\mathbf{q}) = -\frac{\mathbf{F}(\mathbf{q},t)}{ma^2(a\ddot{b}+2\dot{b}\dot{a})}, \tag{A.2}$$

where $\mathbf{F}$ is the force field, $a(t)$ is the expansion factor, m is the particle mass, and a dot denotes a time derivative.

In practise, a realisation of the desired fluctuation distribution is created in Fourier space, with random phases and normally distributed amplitudes for the real and imaginary components of each mode. We then multiply by an appropriate Green's function, and transform back to obtain the potential on a spatial mesh. This potential is differenced to obtain $\mathbf{F}(\mathbf{q},t)$ which, together with equation A.1 and equation A.2, gives the displacement field required to generate the desired density fluctuations from a uniform distribution.

Once the displacements from the unperturbed positions have been computed, velocities are assigned to the particles assuming that only growing modes are present. The peculiar velocity is then simply proportional to the displacement vector,

$$\dot{\mathbf{x}} = -\dot{b}\,\psi(\mathbf{q}) \tag{A.3}$$

In cases such as CDM, where there is significant power on all scales, it is important to avoid unrealistically large initial velocities that may result from large amplitude fluctuations on small scales. Thus we assign peculiar velocities only after recalculating the accelerations using the perturbed particle positions and using equation A.2 to re-estimate $\psi(\mathbf{q})$.

We use a cubic grid distribution of particles to represent a uniform density distribution for all simulations reported here, but it is also possible to use a 'glass' for the unperturbed configuration. As discussed by White (1994), this is a better choice for highly aspherical perturbations, and avoids artifacts that arise from the existence of 'preferred' (Cartesian) directions in cubic grids. This is especially important when attempting to simulate very low mass halos in CDM cosmogonies, since on those scales the mass fluctuation spectrum is nearly 'flat' ($P(k)$ approaches k^{-3}) and collapse proceeds almost simultaneously on many different mass scales in a network of sheets and filamentary structures.

A.2 Mass Refinement Technique

As discussed above, simulations of periodic boxes are only reliable provided that the box is large enough so that perturbations on scales comparable to the box size are still linear

by the present time. This sets a minimum size for periodic boxes designed to be run to $z = 0$ in a ΛCDM universe. For example, in the case considered in § 2.2.2, the size of the periodic box is $L_{\rm box} = 32.5\,h^{-1}$ Mpc ($M_{\rm box} = 9.533 \times 10^{15}\,\Omega_0\,h^{-1}\,M_\odot$), and the variance at $z = 0$ is already $\sigma(M_{\rm box}) \approx 0.3$, at the limit of what may be used to obtain a good representation of large scale structure in this cosmogony. Clearly boxes smaller than $32.5\,h^{-1}$ Mpc cannot capture the correct statistical properties of the dark matter distribution at $z = 0$. Our original low-resolution simulation was carried out with 128^3 particles.

Even if 512^3 particles were used in such a box (at the limit of what is possible with today's largest supercomputer if many thousands of timesteps are needed) the mass per particle in a $32.5\,h^{-1}$ Mpc box would be $m_p = 7.1 \times 10^7\,\Omega_0\,h^{-1} M_\odot$, and a galaxy-sized, $10^{12}\,h^{-1} M_\odot$ halo would only contain slightly more than 10,000 particles. A dwarf galaxy halo would have fewer than 1,000 particles. Clearly, a different technique is required in order to improve the mass and spatial resolution of the calculation while at the same time accounting properly for the effects of large scale structure.

The technique most widely adopted so far selects a few systems identified from the final configuration of the periodic box and re-simulates the whole box, with coarser resolution everywhere except in the selected regions. This technique has been used in a number of cosmological simulations (see, e.g., Katz & White 1993, Navarro & White 1994, Evrard, Summers & Davis 1994, Moore et al. 1998), and has become common in high-resolution simulation work targeted at individual systems. The price one pays with this procedure is that to build a statistically significant sample of halos entails running many different simulations and there is always the possibility of introducing biases during the selection procedure. Having identified a halo in the periodic box for resimulation, all particles within $\sim 2\,r_{200}$ from its centre are traced back to the initial conditions and their positions on the original cubic grid are recorded. A box of size $L_{\rm sbox}$ enclosing all of these particles is then defined.

A displacement field is generated for $N_{\rm sbox} = 256^3$ particles in this new box using a two-step procedure that allows for inclusion of fluctuations from the original periodic box. In the first step, displacements for the $N_{\rm sbox}$ particles are calculated using the *same* Fourier representation as in the original box, except for the contribution from wavelengths shorter than a characteristic scale, $d_{\rm lcut}$. Typically, $d_{\rm lcut}$ is chosen to be the shortest wavelength in the original box, $d_{\rm lcut} = 2L_{\rm box}/N_{\rm box}^{1/3} = 2 \times 32.5/128\,h^{-1}{\rm Mpc} \sim 0.5\,h^{-1}$ Mpc, which is

the Nyquist wavelength of the low-resolution particle grid. We truncate the waves at a boundary which is cubical in Fourier space.

It is important to ensure that the displacements due to the long wavelength Fourier components are applied to the high resolution particles in a sufficiently smooth fashion to avoid introducing significant spurious power. Computing the displacements by simple finite differencing of the potential, as is the case for the large periodic simulation box, is inadequate in this context unless an impractically large mesh is deployed. A better way is to compute the individual components of the displacement field one at time, using the appropriate Green's functions, and to interpolate the displacement components themselves, by trilinear interpolation to the individual particle positions. The use of trilinear interpolation ensures that the displacement field is continuous–which in itself is sufficient to avoid spurious non-linear features being introduced. The larger the mesh used the more accurate is the interpolation. For the simulations reported here a 512^3 mesh was used and proved satisfactory.

In the second step, fluctuations are generated on scales smaller than $d_{\rm lcut}$, down to the Nyquist frequency of the high-resolution box. The new displacement field is periodic within $L_{\rm sbox}$, and can be vector added to the large-box displacements in order to obtain final perturbed positions for all particles within the high-resolution box. Trilinear interpolation is once again used to assign the short wave components of the displacement field to the particles. Peculiar velocities proportional to the displacements are then assigned using the Zel'dovich approximation and assuming that only growing modes are present.

Following this procedure, a realisation of the displacement field of 256^3 particles is created and stored for each halo. Finally, the high-resolution box is inserted in the large periodic box after removal of all overlapping particles.

Not all particles in the small box will end up near the system of interest, so the location on the original grid of selected particles is used to identify an 'amoeba-shaped' region within the cube that is retained at full resolution. Regions exterior to the 'amoeba' are coarse-sampled using particle masses which increase with distance from the region of interest (figure 2.2). The sampling is typically done by binning together cubes of 2^{3n} neighbouring particles from the initial grid (where n is an integer). This allows us to concentrate numerical resources within our selected object without compromising the contribution from larger scales to the tidal field acting on the system. Because of the

non-spherical nature of the collapse of dark halos, accurate simulation of the formation of a single system incurs a significant overhead. Even after all this optimisation, at most 1 in 3 particles in the amoeba region ends up within the virial radius of the system considered.

The success of our procedure may be gauged by computing the power spectrum from the displaced particle positions and comparing it with the theoretical power spectrum that we are trying to generate. Figure 2.1 shows the desired theoretical power spectrum, the power spectrum measured from the parent simulation, and the power spectrum measured from a high-resolution box created in the manner outlined above. The power spectra are shown at $z = 49$. In this case, the high resolution box is $5.08\,h^{-1}$ Mpc on a side and is sampled with 256^3 particles, with individual masses of $6.5 \times 10^5\,h^{-1}M_\odot$. The power spectrum of the small box is actually determined for a cube of $4.3\,h^{-1}$ Mpc excised from the middle of the high resolution region. The excised region would contain 216^3 particles if it had precisely mean density. The density field is assigned to a 432^3 mesh using a cloud-in-cell assignment scheme and periodic boundary conditions forced. Forcing periodicity does not significantly distort the power spectrum for modes small compared to the fundamental mode of the cube. The power spectrum is then computed from the Fourier transformed density field. The power from individual modes is binned in shells of constant cubical wavenumber ($k_{cubical} = \max(|k_x|, |k_y|, |k_z|)$). Plotting the power spectrum using the cubical wavenumber highlights discrepancies more sharply than the more usual spherical binning. The good agreement between the theoretical power spectrum and that measured in our realisations gives us confidence that our simulations faithfully follow the formation of a dark matter halo in the ΛCDM cosmogony.

Bibliography

The following abbreviations are used in this bibliography:

MNRAS: Monthly Notices of the Royal Astronomical Society

ApJ: The Astrophysical Journal

ApJ: The Astrophysical Journal Letters

ApJSS: The Astrophysical Journal Supplement Series

AJ: The Astronomical Journal

A&A: Astronomy and Astrophysics

Ap&SS: Astrophysics and Space Science

ARA&A: Annual Reviews of Astronomy and Astrophysics

J. Comp. Phys.: Journal of Computational Physics

J. Phys. USSR: Journal of Physics (USSR)

PhRvD: Physical Review D, Journal

PhRvL: Physical Review Letters

Aarseth S. J. **1985**, in *Multiple Time Scales*, ed. J. U. Brackbill & B. I. Cohen, p. 377, Orlando: Academic Press

Alam S. M. K., Bullock J. S. & Weinberg D. H. **2002**, ApJ, 572, 34

Arfken G. B. & Weber H. J. **2000**, *Mathematical Methods for Physicists*, Academic Press

Babcock H. W. **1939**, Lick Observatory, 498, 41

Bahcall N. A. & Fan X. **1998**, ApJ, 504, 1

Bahcall N. A., Ostriker J. P., Perlmutter S. & Steinhardt P. J. **1999**, Science, 284, 1481

Balbi A., Ade P., Bock J., Borrill J., Boscaleri A., de Bernardis P., Ferreira P. G., Hanany S., Hristov V., Jaffe A. H., Lee A. T., Oh S., Pascale E., Rabii B.,

Richards P. L., Smoot G. F., Stompor R., Winant C. D. & Wu J. H. P. **2000**, ApJ, 545, L1

Bardeen J. M., Bond J. R., Kaiser N. & Szalay A. S. **1986**, ApJ, 304, 15

Barnes J. & Hut P. **1986**, Nature, 324, 446

Battaner E., Garrido J. L., Membrado M. & Florido E. **1992**, Nature, 360, 652

Becker R. H., Fan X., White R. L., Strauss M. A., Narayanan V. K., Lupton R. H., Gunn J. E., Annis J., Bahcall N. A., Brinkmann J., Connolly A. J., Csabai I., Czarapata P. C., Doi M., Heckman T. M., Hennessy G. S., Ivezic Z., Knapp G. R., Lamb D. Q., McKay T. A., Munn J. A., Nash T., Nichol R., Pier J. R., Richards G. T., Schneider D. P., Stoughton C., Szalay A. S., Thakar A. R. & York D. G. **2001**, AJ, 122, 2850

Begeman K.G. **1989**, A&A, 223, 47

Bell E. F. & de Jong R. S. **2000**, MNRAS, 312, 497

Benson A. J., Lacey C. G., Baugh C. M., Cole S. & Frenk C. S. **2002**, MNRAS, 333, 156

Bertschinger E. **1985**, ApJS, 58, 39

Bertschinger E. **2001**, ApJS, 137, 1

Bertschinger E. & Gelb J. M. **1991**, Computers and Physics, 5, 164

Binney J. **1977**, ApJ, 215, 483

Binney J. & Tremaine S. **1987**, *Galactic Dynamics*, Princeton University Press

Binney J. & Merrifield M. **1998**, *Galactic Astronomy*, Princeton Univeristy Press

Binney J. **2003**, in *Dark Matter in Galaxies*, Proceedings of the IAU Symposium 220, ed. S. Ryder, D. J. Pisano, M. Walker & K. C. Freeman (astro-ph/0310219)

Blais-Ouellette S., Carignan C., Amram P. & Côté S. **1999**, AJ, 118, 2123

Blais-Ouellette S., Amram P. & Carignan C. **2001**, AJ, 121, 1952

Blumenthal G. R., Faber S. M., Primack J. R. & Rees M. J. **1984**, Nature, 311, 517

Bode P., Ostriker J. P. & Turok N. **2001**, ApJ, 556, 93

Bolatto A. D., Simon J. D., Leroy A. & Blitz L. **2002**, ApJ, 565, 238

Borriello A. & Salucci P. **2001**, MNRAS, 323, 285

Bond J. R., Centrella J., Szalay A. S. & Wilson J. R. **1983**, in *Formation and Evolution of Galaxies and Large Scale Structures*, ed. J. Audouze & J.T.T. Van, p. 87

Bond J. R., Cole S., Efstathiou G. & Kaiser N. **1991**, ApJ, 379, 440

Bosma A. **1978**, Ph.D. Thesis, University of Groningen

Bosma A. **1981**, AJ, 86, 1825

Broeils A. H. **1992**, A&A, 256, 19

Bullock J. S., Kolatt T. S., Sigad Y., Somerville R. S., Kravtsov A. V., Klypin A. A., Primack J. R. & Dekel A. **2001**, MNRAS, 321, 559

Bullock J. S., Kravtsov A. V. & Weinberg D. H. **2001a**, ApJ, 548, 33

Bullock J. S. **2001**, in *The Shapes of Galaxies and their Dark Halos*, ed. P. Natarajan, Proceedings of the Yale Cosmology Workshop (astro-ph/0106380)

Burke B. F. & Graham-Smith F. **1997**, *An Introduction to Radio Astronomy*, Cambridge University Press

Burkert A. **1995**, ApJ, 447, L25

Burkert A. & Silk J. **1997**, ApJ, 488, L55

Burles S., Nollett K. M. & Turner M. S. **2001**, ApJ, 552, L1

Caldwell R. R., Dave R. & Steinhardt P. J. **1998**, Ap&SS, 261, 303

Caldwell R. R., Doran M., Müller C. M.; Schäfer G. & Wetterich C. **2003**, ApJ, 591, L75

Carroll S. M. & Mersini L. **2001**, PhRvD, 64, l4008

Carignan C. & Freeman K. C. **1988**, ApJ, 332, L33

Carignan C. & Beaulieu S. **1989**, ApJ, 347, 760

Carlberg R. G. **1994**, ApJ, 433, 468

Cole S. & Lacey C. **1996**, MNRAS, 281, 716

Cole S., Lacey C., Baugh C. & Frenk C.S. **2000**, MNRAS, 319, 168

Coles P. & Lucchin F. **1995**, *Cosmology: The Origin and Evolution of Cosmic Structure*, John Wiley & Sons

Croft R. A. C., Weinberg D. H., Pettini M., Hernquist L. & Katz N. **1999**, ApJ, 520, 1

Crone M. M., Evrard A. E. & Richstone D. O. **1994**, ApJ, 434, 402

Danziger I. J. **1997**, *Dark and Visible Matter in Galaxies*, ed. M. Persic & P. Salucci, p. 28, ASP Conference Series 117

David L. P., Durisen R. H. & Steiman-Cameron T. Y. **1984**, ApJ, 286, 53

David L. P., Durisen R. H. & Steiman-Cameron T. Y. **1985**, ApJ, 295, 65

Davis M., Efstathiou G., White S. D. M. & Frenk C. S. **1985**, ApJ, 292, 371

Davis D. S. & White R. E. III **1996**, AJ, 470, L35

De Bernardis P., Ade P., Bock J., Bond J. R., Borrill J., Boscaleri A., Coble K., Crill B. P., De Gasperis G., Farese P., Ferreira P. G., Ganga K., Giacometti M., Hivon E., Hristov V., Iacoangeli A., Jaffe A. H., Lange A. E., Martinis L., Masi S., Mason P., Mauskopf P. D., Melchiorri A., Montroy T., Netterfield C. B., Pascale E., Piacentini F., Pogosyan D., Prunet S., Rao S., Romeo G., Ruhl J. E., Scaramuzzi F., Sforna D. & Vittorio N. **2000**, Nature, 404, 955

De Bernardis P., Ade P., Bock J., Bond J. R., Borrill J., Boscaleri A., Coble K., Contaldi C. R., Crill B. P., De Troia G., Farese P., Ganga K., Giacometti M., Hivon E., Hristov V., Iacoangeli A., Jaffe A. H., Jones W. C., Lange A. E., Martinis L., Masi S., Mason P., Mauskopf P. D., Melchiorri A., Montroy T., Netterfield C. B., Pascale E., Piacentini F., Pogosyan D.; Polenta G., Pongetti F., Prunet S., Romeo G.; Ruhl J. E. & Scaramuzzi F. **2002**, ApJ, 564, 559

de Blok W. J. G., McGaugh S. S. & van der Hulst J. M. **1996**, MNRAS, 283, 18

de Blok W. J. G. & McGaugh S. S. **1996**, ApJ, 469, L89

de Blok W. J. G. & McGaugh S. S. **1997**, MNRAS, 290, 533

de Blok W. J. G., McGaugh S. S., Bosma A. & Rubin V. C. **2001**, ApJ, 552, L23

de Blok W. J. G., McGaugh S. S. & Rubin V. C. **2001a**, AJ, 122, 2381

de Blok W. J. G., McGaugh S. S. & Rubin V. C. **2001b**, AJ, 122, 2396

de Blok W. J. G. & Bosma A. **2002**, A&A, 385, 816

de Blok W. J. G., Bosma A. & McGaugh S. S **2003**, MNRAS, 340, 657

Dekel A., Devor J. & Hetzroni G. **2003**, MNRAS, 341, 326

Dekel A., Arad I., Devor J. & Birnboim Y. **2003a**, ApJ, 588, 680

de Lucia G., Kauffmann G., Springel V. & White S. D. M. **2003**, MNRAS, in press (astro-ph/0306205)

Dubinski J. & Carlberg R. G. **1991**, ApJ, 378, 496

Efstathiou G., Davis M., Frenk C. S. & White S. D. M. **1985**, ApJS, 57, 241

Efstathiou G., Frenk C. S., White S. D. M. & Davis M. **1988**, ApJ, 327, 507

Efstathiou G., Moody S., Peacock J. A., Percival W. J., Baugh C., Bland-Hawthorn J., Bridges T., Cannon R., Cole S., Colless M., Collins C., Couch W., Dalton G., de Propris R., Driver S. P., Ellis R. S., Frenk C. S., Glazebrook K., Jackson C., Lahav O., Lewis I., Lumsden S., Maddox S., Norberg P., Peterson B. A., Sutherland W. & Taylor K. **2002**, MNRAS, 330, L29

Eisenstein D. J. & Hut P. **1998**, ApJ, 498, 137

Eke V. R., Cole S. & Frenk C. S. **1996**, MNRAS, 282, 263

Eke V. R., Cole S., Frenk C. S. & Patrick Henry J. **1998**, MNRAS, 298, 1145

Eke V. R., Navarro J. F. & Steinmetz M. **2001**, ApJ, 554, 114

Ettori S. & Fabian A. C. **1999**, MNRAS, 305, 834

Evrard A. E., Summers F. J. & Davis M. **1994**, ApJ, 422, 11

Faber S. M. & Lin D. N. C. **1983**, ApJ, 266, L17

Fillmore J. A. & Goldreich P. **1984**, ApJ, 281, 1

Finzi A. **1963**, MNRAS, 127, 21

Flores R., Primack J. R., Blumenthal G. R. & Faber S. M. **1993**, ApJ, 412, 443

Flores R. A. & Primack J. R. **1994**, ApJ, 427, L1

Font A., Navarro J. F, Quinn T. & Stadel J. **2001**, ApJ, 563, L1

Frenk C. S., White S. D. M., Efstathiou G. & Davis M. **1985**, Nature, 317, 595

Frenk C. S., White S. D. M., Davis M. & Efstathiou G. **1988**, ApJ, 327, 507

Frenk C. S., Evrard A. E., White S. D. M. & Summers F. J. **1996**, ApJ, 472, 460

Fukushige T. & Makino J. **1997**, ApJ, 477, L9

Fukushige T. & Makino J. **2001**, ApJ, 557, 533

Fukushige T. & Makino J. **2003**, ApJ, 588, 674

Gelb J.M. & Bertschinger E. **1994**, ApJ, 436, 467

Ghigna S., Moore B., Governato F., Lake G., Quinn T. & Stadel J. **1998**, MNRAS, 300, 146

Ghigna S., Moore B., Governato F., Lake G., Quinn T. & Stadel J. **2000**, ApJ, 544, 616

Gnedin O. Y. & Zhao H. **2002**, MNRAS, 333, 299

Gott J. R. III, Weinberg D. H. & Melott A. L. **1987**, ApJ, 319, 1

Grego L., Carlstrom J. E., Reese E. D., Holder G. P., Holzapfel, W. L., Joy M. K., Mohr J. J., Patel S. **2001**, ApJ, 552, 2

Gunn J. E. & Gott J. R. III **1972**, ApJ, 176, 1

Gunn J. E. 1977, ApJ, 218, 592

Hamilton A. J. S, Matthews A., Kumar P. & Lu E. **1991**, ApJ, 374, L1

Hayashi E., Navarro J. F., Taylor J. E., Stadel J. & Quinn T. **2003**, ApJ, 584, 541

Hayashi E., Navarro J. F., Power C., Jenkins A., Frenk C. S., White S. D. M., Springel V., Stadel J. & Quinn T. **2003**, preprint (astro-ph/0310576)

Hernquist L. **1987**, ApJS, 64, 715

Hernquist L. & Katz N. **1989**, ApJS, 70, 419

Hernquist L. **1990**, ApJ, 356, 359

Hernquist L., Bouchet F. R. & Suto Y. **1991**, ApJS, 75, 231

Hernquist L. & Ostriker J. P. **1992**, ApJ, 386, 375

Hernquist L., Sigurdsson S. & Bryan G. L. **1995**, ApJ, 446, 717

Hoffman Y. & Shaham J. **1985**, ApJ, 297, 16

Huss A., Jain B. & Steinmetz M. **1999**, ApJ, 517, 64

Jenkins A., Frenk C. S., White S. D. M., Colberg J. M., Cole S., Evrard A. E., Couchman H. M. P. & Yoshida N. **2001**, MNRAS, 321, 372

Jernigan J. G. & Porter D. H. **1989**, ApJS, 71,871

Jing Y. P. **1998**, ApJl, 503, L9

Jing Y. P. & Suto Y. **2000**, ApJ, 529, L69

Jing Y. P. & Suto Y. **2002**, ApJ, 574, 538

Jobin M. & Carignan C. **1990**, AJ, 100, 648

Kalnajs A. J. **1987**, in *Dark Matter in the Universe*, Proceedings of the IAU Symposium, pp. 289-296

Katz N. **1991**, ApJ, 368, 325

Katz N. & White S. D. M. **1993**, ApJ, 412, 455

Klypin A., Gottlöber S., Kravtsov A. V. & Khokhlov A. M. **1999**, ApJ, 516, 530

Klypin A., Kravtsov A. V., Valenzuela O. & Prada F. **1999a**, ApJ, 522, 82

Klypin A., Kravtsov A. V., Bullock J. S. & Primack J. R. **2001**, ApJ, 554, 903

Knebe A., Kravtsov A. V., Gottlöber S. & Klypin A. A. **2000**, MNRAS, 317, 630

Krauss L. M. & Chaboyer B. **2003**, Science, 299, 65

Kravtsov A. V., Klypin A. A., Bullock J. S. & Primack J. R. **1998**, ApJ, 502, 48

Kull A. **1999**, ApJ, 516, L5

Lacey C. & Cole S. **1993**, MNRAS, 262, 627

Lake G. & Feinswog L. **1989**, AJ, 98, 166

Lake G., Schommer R. A. & van Gorkom J. H. **1990**, AJ, 99, 547

Levine S. E. & Sparke L. S. **1994**, ApJ, 428, 493

Lifshitz E. M. **1946**, J. Phys. USSR, 10, 116.

Maoz D. & Rix H. **1993**, ApJ, 416, 425

Merrifield M.. **2001**, in *The Shapes of Galaxies and their Halos*, ed. P. Natarajan, Proceedings of the Yale Cosmology Workshop (astro-ph/0106380)

Merrifield M.. **2003**, in *Dark Matter in Galaxies*, Proceedings of the IAU Symposium 220, ed. S. Ryder, D. J. Pisano, M. Walker & K. C. Freeman (astro-ph/0310497)

Merritt D. & Cruz F. **2001**, ApJ, 551, L41

Merritt D. & Milosavljevic M. **2002**, in *Dark Matter in Astro- and Particle Physics*, Proceedings of the International Conference, DARK 2002, ed. H. V. Klapdor-Kleingrothaus & R. D. Viollier (astro-ph/0205140)

Milgrom M. **1983**, ApJ, 270, 365

Milosavljevic M. & Merritt D. **2001**, ApJ, 563, 34

McGaugh S. S & de Blok W. J. G. **1998**, ApJ, 499, 41

Mo H.J. & White S. D. M **1996**, MNRAS, 282, 347

Mohr J.J., Mathiesen B. & Evrard A. E. **1999**, ApJ, 517, 627

Moore B. **1994**, Nature, 370, 629

Moore B., Katz N. & Lake G. **1996**, ApJ, 457, 455

Moore B., Quinn T., Governato F., Stadel J. & Lake G. **1998**, ApJ, 499, L5

Moore B., Ghigna S., Governato F., Lake G., Quinn T., Stadel J. & Tozzi P. **1999**, ApJ, 524L, 19

Moore B., Quinn T., Governato F., Stadel J. & Lake G. **1999a**, MNRAS, 310, 1147

Moore B., Gelato S., Jenkins A., Pearce F. R. & Quilis V. **2000**, ApJ, 535, L21

Moore B. **2001**, in the Proceedings of the 20th Texas Symposium, ed. J. C. Wheeler & H. Martel. (astro-ph/0103100)

Navarro J. F. & White S. D. M. **1993**, MNRAS, 265, 271

Navarro J. F. & White S. D. M. **1994**, MNRAS, 267, 401

Navarro J. F., Frenk C. S. & White S. D. M. **1995**, MNRAS, 275, 720

Navarro J. F., Frenk C. S. & White S. D. M. **1996**, ApJ, 462, 563

Navarro J. F., Eke V. R. & Frenk C. S. **1996**, MNRAS, 283, L72

Navarro J. F., Frenk C. S. & White S. D. M. **1997**, ApJ, 490, 493

Navarro J. F. & Steinmetz M. **2000**, ApJ, 538, 477

Netterfield C. B., Ade P., Bock J., Bond J. R., Borrill J., Boscaleri A., Coble K., Contaldi C. R., Crill B. P., de Bernardis P., Farese P., Ganga K., Giacometti M., Hivon E., Hristov V., Iacoangeli A., Jaffe A. H., Jones W. C., Lange A. E., Martinis L., Masi S., Mason P., Mauskopf P. D., Melchiorri A., Montroy T., Pascale E., Piacentini F., Pogosyan D., Pongetti F., Prunet S., Romeo G., Ruhl J. E. & Scaramuzzi F. **2002**, ApJ, 571, 604

Noordermeer E., Sparke L. S. & Levine S. E. **2001**, MNRAS, 328, 1064

O'Meara J. M., Tytler D., Kirkman D, Suzuki N., Prochaska J. X., Lubin D. & Wolfe A. M. **2001**, ApJ, 552, 718

Oort J. H. **1940**, ApJ, 91, 273

Ostriker J. P. & Peebles P. J. E. **1973**, ApJ, 186, 467

Ostriker J. P., Peebles P. J. E. & Yahil A. **1974**, ApJ, 193, L1

Page T. **1952**, ApJ, 116, 63

Page T. **1960**, ApJ, 132, 910

Peacock J. A. & Dodds S. J. **1996**, MNRAS, 280, L19

Peacock J. A. **1999**, *Cosmological Physics*, Cambridge University Press

Peacock J. A., Cole S., Norberg P., Baugh C. M., Bland-Hawthorn J., Bridges T., Cannon R. D., Colless M., Collins C., Couch W., Dalton G., Deeley K, De Propris R., Driver S. P., Efstathiou G., Ellis R. S., Frenk C. S., Glazebrook K., Jackson C., Lahav O., Lewis I., Lumsden S., Maddox S., Percival W. J., Peterson B. A., Price I., Sutherland W. & Taylor K. **2001**, Nature, 410, 169

Peebles P. J. E. **1967**, ApJ, 147, 859

Peebles P. J. E. **1980**, *The Large-scale Structure of the Universe*, Princeton University Press

Peebles P. J. E. **1993**, *Principles of Physical Cosmology*, Princeton University Press

Peebles P. J. E. **2000**, ApJ, 534, L127

Pen U. **1997**, ApJL, 490, L127

Percival W. J., Baugh C. M., Bland-Hawthorn J., Bridges T., Cannon R. D., Cole S., Colless M., Collins C., Couch W., Dalton G., De Propris R., Driver S. P., Efstathiou G., Ellis R. S., Frenk C. S., Glazebrook K., Jackson C., Lahav O., Lewis I., Lumsden S., Maddox S., Moody S., Norberg P., Peacock J. A., Peterson B. A., Price I., Sutherland W. & Taylor K. **2001**, MNRAS, 327, 1297

Perlmutter S., Aldering G., Goldhaber G., Knop R. A., Nugent P., Castro P. G., Deustua S., Fabbro S., Goobar A., Groom D. E., Hook I. M., Kim A. G., Kim M. Y., Lee J. C., Nunes N. J., Pain R., Pennypacker C. R., Quimby R., Lidman C., Ellis R. S., Irwin M., McMahon R. G., Ruiz-Lapuente P., Walton N., Schaefer B., Boyle B. J., Filippenko A. V., Matheson T., Fruchter A. S., Panagia N., Newberg H. J. M. & Couch W. J. **1999**, ApJ, 517, 565

Porter D. H. **1985**, Ph.D. Thesis, University of California at Berkeley

Press W. H. & Schechter P. **1974**, ApJ, 187, 425

Press W. H., Teukolsky S. A., Vetterling W. T. & Flannery B. P. **1995**, *Numerical Recipes in C*, Cambridge University Press, Cambridge

Pryke C., Halverson N. W., Leitch E. M., Kovac J., Carlstrom J. E., Holzapfel W. L. & Dragovan M. **2002**, ApJ, 568, 46

Quinn P. J., Salmon J. K. & Zurek W. H. **1986**, Nature, 322, 329

Quinn T., Katz N., Stadel J. & Lake G. **1997**, preprint (astro-ph/9710043)

Riess A. G., Filippenko A. V., Challis P., Clocchiatti A., Diercks A., Garnavich P. M., Gilliland R. L., Hogan C. J., Jha S., Kirshner R. P., Leibundgut B., Phillips M. M., Reiss D., Schmidt B. P., Schommer R. A., Smith R. C., Spyromilio J., Stubbs C., Suntzeff N. B. & Tonry J. **1998**, AJ, 116, 1009

Riess A. G., Nugent P. E., Gilliland R. L., Schmidt B. P., Tonry J., Dickinson M., Thompson R. I., Budavári T., Casertano S., Evans A. S., Filipenko A. V., Livio M., Sanders D. B., Shapley A. E., Spinrad H., Steidel C. C., Stern D., Surace J. & Veilleux S. **2001**, ApJ, 560, 49

Roberts M. S. & Rots A. H. **1973**, A&A, 26, 483

Roberts M. S. & Whitehurst R. N. **1975**, ApJ, 201, 327

Rogstad D. H. & Shostak G. S. **1972**, ApJ, 176, 315

Romanishin W., Krumm N., Salpeter E., Knapp G., Strom K. M. & Strom S. E. **1982**, ApJ, 263, 94

Rubin V. C. & Ford W. K., Jr. **1970**, ApJ, 159, 379

Rubin V. C., Thonnard N. & Ford W. K., Jr. **1980**,ApJ, 238, 471

Saha P. **1993**, MNRAS, 262, 1062

Salmon J. K. & Warren M. S. **1993**, J. Comp. Phys., 111, 136

Sellwood J. **1985**, MNRAS, 217, 127

Sellwood J. A. & Kosowsky A. **2001**, in *Gas and Galaxy Evolution*, ed. J. E. Hibbard, M. Rupen & J. H. van Gorkom, ASP Conference Proceedings, Vol. 240 (astro-ph/0009074)

Sellwood J. **2003**, ApJ, 587, 638

Sheth R. K. & Tormen G. **1999**, MNRAS, 308, 119

Silk J., **1977a**, ApJ, 214, 152

Silk J., **1977b**, ApJ, 214, 718

Simon J. D., Bolatto A. D., Leroy A. & Blitz L. **2003**, ApJ, in press (astro-ph/0307154)

Somerville R. S. **2002**, ApJ, 572, L23

Smith S. **1936**, ApJ, 83, 23

Sommer-Larsen J., Gelato S. & Vedel H. **1999**, ApJ, 519, 501

Spergel D. N. & Steinhardt P. J. **2000**, PhRvL, 84, 3760

Springel V., Yoshida N. & White S. D. M. **2001**, New Astronomy, 6, 79

Springel V., White S. D. M., Tormen G. & Kauffmann G. **2001a**, MNRAS, 328, 726

Stadel J. **2001**, Ph.D. Thesis, University of Washington.

Steiman-Cameron T. Y. & Durisen R. H. **1982**, ApJ, 263, L51

Steiman-Cameron T. Y. & Durisen R. H. **1984**, ApJ, 276, 101

Steiman-Cameron T. Y., Kormendy J. & Durisen R. H. **1992**, AJ, 104, 1339

Stoehr F, White S. D. M., Tormen G. & Springel V. **2002**, MNRAS, 335, L84

Strauss M. **2000**, in *Cosmic Flows Workshop*, ed. S. Courteau & J. Willick, ASP Conference Series, Vol. 201 (astro-ph/9908325)

Summers F. J., Davis M. & Evrard A. E. **1995**, ApJ, 454, 1

Swaters R. A. **1999**, Ph.D. Thesis, University of Groningen

Swaters R. A., Madore B. F. & Trewhella M. **2000**, ApJ, 531, L107

Swaters R. A., Madore B. F., van den Bosch F. C. & Balcells M. **2003**, ApJ, 583, 732

Syer D. & White S. D. M. **1998**, MNRAS, 293, 337

Taylor J. E. & Navarro J. F. **2001**, ApJ, 563, 483

Thacker R. J. & Couchman H. M. P. **2001**, ApJ, 555, L17

Thomas P. A., Vine S. & Pearce F.R. **1994**, MNRAS, 268, 253

Thomas P. A., Colberg J. M., Couchman H. M. P., Efstathiou G., Frenk C. S., Jenkins A., Nelson A. H., Hutchings R. M., Peacock J. A., Pearce F. R. & White S. D. M. **1998**, MNRAS, 296, 1061

Tormen G., Bouchet F. & White S. D. M. **1997**, MNRAS, 290, 411

Tormen G., Diaferio A. & Syer D. **1998**, MNRAS, 297, 648

Tremaine S. & Gunn J. E. **1979**, PhRvL, 42, 407

van den Bergh S. **1999**, PASP, 111, 657

van den Bosch F. C., Lewis G. F., Lake G. & Stadel J. **1999**, ApJ, 515, 50

van den Bosch F. C. & Swaters R. A. **2001**, MNRAS, 325, 1017

van den Bosch F. C., Robertson B. E., Dalcanton J. J & de Blok W. J. G. **2001a**, AJ, 119, 1579

van Driel W. & van Woerden H. **1997**, *Dark and Visible Matter in Galaxies*, ed. M. Persic & P. Salucci, pp. 144, ASP Conference Series 117

van Waerbeke L., Mellier Y., Radovich M., Bertin E., Dantel-Fort M., McCracken H. J., Le Fèvre O., Foucaud S., Cuillandre J.-C., Erben T., Jain B., Schneider P., Bernardeau F. & Fort B. **2001**, A&A, 374, 757

Vitvitska M., Klypin A. A., Kravtsov A. V., Wechsler R. H., Primack J. R. & Bullock J. S. **2002**, ApJ, 581, 799

Vogt S. S., Mateo M., Olszewski E. W. & Keane M. J. **1995**, AJ, 109, 151

Warren M. S., Quinn P. J., Salmon J. K. & Zurek W. H. **1992**, ApJ, 399, 405

Wechsler R. H., Bullock J. S., Primack J. R., Kravtsov A. V. & Dekel A. **2002**, ApJ, 568, 52

Weinberg, M. D. **1998**, MNRAS, 297, 101

Weinberg, M. D. & Katz N. **2002**, ApJ, 580, 627

Weldrake D. T. F, de Blok W. J. G. & Walter F. **2003**, MNRAS, 340, 12

White S. D. M. & Rees M. **1978**, MNRAS, 183, 341

White S. D. M. **1979**, MNRAS, 189, 831

White S. D. M., Davis M. & Frenk C. S. **1984**, MNRAS, 209, 27

White S. D. M., Davis M., Efstathiou G. & Frenk C. S. **1987**, Nature, 330, 451

White S. D. M. & Zaritsky D. **1992**, ApJ, 394, 1

White S. D. M. **1994**, *Formation and Evolution of Galaxies*, Lectures given at Les Houches, August 1993 (astro-ph/9410043).

Whitehurst R. N. & Roberts M. S. **1973**, ApJ, 175, 347

Yoshida N., Springel V., White S. D. M. & Tormen G. **2000**, ApJ, 544, L87

Zaritsky D. & White S. D. M. **1994**, ApJ, 435, 599

Zentner A. R. & Bullock J. S. **2002**, PhRvD, 66, d3003

Zwicky F. **1937**, ApJ, 86, 217